Magnetic Properties of La-Cr-O and Nd-Cr-O Based Orthochromites

A Thesis Submitted

By

Tribedi Bora

In Partial Fulfillment of the Requirements for the Award of the Degree of

Doctor of Philosophy in Physics

Department of Physics
Indian Institute of Technology Guwahati
Guwahati-781039, India

October, 2014

Magnetic Properties of La-Cr-O and Nd-Cr-O Based Orthochromites

A Thesis Submitted

By

Tribedi Bora

Roll No: 09612102

In Partial Fulfillment of the Requirements for the Award of the Degree of

Doctor of Philosophy in Physics

Department of Physics
Indian Institute of Technology Guwahati
Guwahati-781039, India

October, 2014

Statement

The work contained in the thesis entitled **"Magnetic Properties of La-Cr-O and Nd-Cr-O Based Orthochromites"** has been carried out by me under the supervision of Prof. S. Ravi, Department of Physics, Indian Institute of Technology Guwahati. This work has not been submitted elsewhere for the award of any degree.

22nd October, 2014

(Tribedi Bora)
Department of Physics
Indian Institute of Technology Guwahati
Guwahati – 781039, India

Certificate

It is certified that the work contained in the thesis entitled **"Magnetic Properties of La-Cr-O and Nd-Cr-O Based Orthochromites"** by Ms. Tribedi Bora, a PhD student of the Department of Physics, Indian Institute of Technology Guwahati for the award of the degree of *Doctor of Philosophy* has been carried out under my supervision. This work has not been submitted elsewhere for the award of any degree.

22nd October, 2014

(S. Ravi)
Professor, Department of Physics
Indian Institute of Technology Guwahati
Guwahati – 781 039, India

Dedicated

to

My Family

Acknowledgements

This thesis is the result of a very nice, revealing and fruitful research time during 2009-14 at IIT Guwahati. It gives me immense pleasure to acknowledge all those who supported directly or indirectly and made this thesis possible.

First and foremost, I wish to express my sincere thanks to my supervisor, Prof. S. Ravi, taking me as his PhD student and providing me the opportunity and a well established experimental lab to conduct my doctoral research. I owe a deep sense of gratitude for his encouragement and persistence guidance. His simple, down to earth and tolerance behavior are always inspiring me. He helped in my study to large extent from basic knowledge of Physics to material science, experimental techniques, orthochromites, CMR materials, spintronics, magnetism, *etc*. I am very fortunate that I have carried out my research under him. His constant support and broad scientific experience have made my research possible. I will remain grateful to him for teaching Physics to me.

I would like to thanks my Doctoral Committee (DC) members, Prof. A. Perumal (Chairman), Dr. D. Pamu, and Dr. V. Manivannan for their evaluations and valuable suggestions at constant interval to improve the quality of my work.

I would like to thanks my collaborators, Dr. M. Kar from IIT Patna, Dr. B. Samanataray from SINP Kolkata, Dr. P. Saravanan from DMRL Hyderabad and Dr. N. Harish Kumar from IIT Madras, for helping me in taking SEM images.

I also take this opportunity to thank my lab-mates whose presence has made the work environment interesting and fruitful. So, in no particular order, I offer my thanks to former and present research group members, Dr. Manoranjan Kar, Dr. Pramoda Kumar Nayak, Dr. Sandeep Kumar Srivastava, Dr. B. Samantaray, Dr. Sunita Mohanty, Bipul Deka, Ranganadha Gopalarao, Junmoni Barman, Bibhuti Bhushan Dash, Pratap Behera and Aakansha for their assistance, advice and cooperation. My special thanks to Dr. B. Samantaray and Dr. Sunita Mohanty for their help and discussions during my starting PhD days.

I am very much thankful to Head of Department Prof. S. Basu for his help towards departmental facility. I would like to thank former HOD Prof. S. Ravi for his cooperation in

all regards. I am also thankful to all faculty members of Physics department. My special thanks go to Dr. Sidananda Sarma for helping me to carry out experiments and Mr. Basab Bijoy Purakayasthya for interfacing instruments with LabView. I am also thankful to other staff members of my department.

I am thankful to Central Instrumental Facility (CIF), IIT Guwahati, for enabling me to avail several sophisticated instruments to perform the experiments during my PhD tenure. Department of Science and Technology for facilitating Vibrating Sample Magnetometer and TTRAX III diffractometer are gratefully acknowledged.

I am grateful to Dr. Amal Medhi, IISER Thiruvanthapuram, who has inspired me towards the subject of Physics. I am also thankful to my college teachers for their constant encouragement.

My special thanks to my batch-mates Dr. Akhilesh Kumar Singh, Bhargab Deka, Dr. Padam Rajendar, Dr. T. Santhosh Kumar, Bhagaban Kishan, Souvik Paul, Indrajeet Kumar, Mukesh Singh, Dr. Enamulla Khan, Poulami Ghosh, Dr. Deepanwita Dutta and Shyni P.C. for having very good friendship. I am thankful to my seniors as well as juniors Dr. Biswanath Dutta, Dr. Poloumi Dey, Dr. Meera, Dr. Arpita Nath, Dr. Rahul Das, Himanshu Jha, Ranjan Bhuyan, Dr. Manirupa Saha, Anabil Gayan, Arnab Das, Mahesh, Deepanjali Goswami and all research scholars of my department for pleasant memories had with them. I would like to give heartiest thanks to Shashi, Dr. Tejasha Kalita, Dr. Biju Prava Saharia, Dr. Annu, Dr. Namita Behera and Bharti for their continuous support and encouragements.

I am grateful to my family members and relatives for their continuous encouragement and moral support. I would like to offer my thanks to them for their affection, tolerance and support for which I could reach the present stage.

Last but not the least, I am grateful to Indian Institute of Technology Guwahati and Ministry of Human Resource and Development for giving the financial support to carry out the present thesis work. Department of Science and Technology, New Delhi and Board of Research in Nuclear Science Mumbai are acknowledged for financial support through research projects for various experimental facilities.

Lastly I would like to thank Almighty God who has given me the strength to believe my passion and pursue my dreams.

Tribedi Bora

IIT Guwahati, India, 22nd October 2014

Abstract

Magnetic materials are expected to play a major role in shaping the future electronic devices and circuits, where not only the type and concentrations of charge carriers but also their magnetic spins are going to act as controlling parameters in the electronic circuits. Such increased degree of freedom is likely to improve the efficiency, miniaturization, reduction in power consumption, speed and non-volatile memory, *etc*. In an attempt to tune and understand the magnetic properties in this direction, our studies are focused on magnetic orthochromites. The usefulness of these magnetic orthochromites for electronic application is established by the fact that these materials exhibit high magnetization reversal, exchange bias behavior and high electronic conductivity at high temperature. The discovery of large magnetization reversal and tunable exchange bias behavior has opened up the possibility of potential application in magnetic storage and magnetic switches. These materials have also potential applications as electrode in the magneto hydrodynamic generator or interconnector in the solid oxide fuel cell due to their high electronic conductivity under elevated temperatures.

The orthochromites can be described by the chemical formula as $RCrO_3$ where R is the trivalent rare earth element. Three types of magnetic interaction are possible, such as, Cr^{3+}-Cr^{3+}, R^{3+}-R^{3+} and R^{3+}-Cr^{3+}. Mainly, Cr^{3+}-Cr^{3+} interaction gives rise to G-type antiferromagnetism (AFM) along with a weak ferromagnetic behavior. The presence of canted ferromagnetic component was explained by considering the anisotropy exchange interaction which holds the interacting spins in perpendicular direction. The magnetic properties of $GdCrO_3$ were explained in terms of paramagnetic moment of Gd ions under the effective internal field (H_I) due to AFM ordered Cr^{3+} ions. The values of canted Cr moment (M_{Cr}) and H_I are reported to be 400 emu/mol and 5.5 kOe respectively. Magnetization reversal has been observed in $La_{1-x}Pr_xCrO_3$ compounds.

In orthovanadate $LaVO_3$, MR was reported due to the first order magnetostriction transition and the associated discontinuous change in the unquenched orbital angular momentum. The magnetization reversal in YVO_3 single crystal was explained by using a model where the competition between the single ion anisotropy and Dzyaloshinsky-Moriya (DM) interaction was invoked. $SmVO_3$ and $NdVO_3$ also show the MR behavior. The

observed MR in double perovskite Sr_2YbRuO_6 was explained by using the argument of the reversal of the residual ferromagnetic (FM) component of magnetization triggered by DM interaction. Some of the perovskite manganites such as $La_{1-x}Gd_xMnO_3$ and $Nd_{1-x}Ca_xMnO_3$ exhibit MR due to the *4f -3d* interaction. The origin of the MR in molecular magnets is generally due to the different temperature dependences magnetic sublattices.

$LaCrO_3$ and $NdCrO_3$ are the well known orthochromites having G-type antiferromagnetic structure with Néel temperatures 290 K and 214 K. In addition to AFM transition, $NdCrO_3$ exhibits spin reorientation transition of Cr^{3+} ions at T_{SRT} = 35 K. The interest in these series is due to the fact of isoelectronic configuration of Cr^{3+} with Mn^{4+} ions. The Mn^{4+} ions are known to play a major role in colossal magnetoresistance materials such as alkaline earth doped $LaMnO_3$. Divalent alkaline earth doped $LaCrO_3$ shows the weakening of AFM transition along with a low temperature weak ferromagnetic behavior due to the presence of Cr^{4+} ions. Two magnetic transitions was observed in $La_{0.7}Te_{0.3}CrO_3$ such as paramagnetic to antiferromagnetic at 282 K followed by antiferromagnetic to ferromagnetic at 150 K. Predominant AFM behavior in $La_{1-x}Ce_xCrO_3$ for x upto 0.2 and decrease in T_N values with increase in Ce concentration along with a large irreversibility between zero field cooled (ZFC) and field cooled (FC) magnetization curve have been reported. Signature of MR was reported in $LaCr_{0.5}Fe_{0.5}O_3$ and $NdMn_{0.15}Cr_{0.85}O_3$ compounds. The nature of the magnetic interaction present in the above two series is yet to be understood. In order to understand the crystal structure and magnetic properties of the above two systems, we have taken up the preparation of transition elements (Fe, Mn) doped La-Cr-O and Nd-Cr-O based orthochromites and as well as Ce doped $LaCrO_3$ samples.

Five series of samples were prepared for the present thesis work

i. $LaCr_{1-x}Fe_xO_3$ (x = 0.0 to 1.0)
ii. $LaCr_{1-x}Mn_xO_3$ (x = 0.0 to 1.0)
iii. $NdCr_{1-x}Fe_xO_3$ (x = 0.0 to 1.0)
iv. $NdCr_{1-x}Mn_xO_3$ (x = 0.0 to 0.7)
v. $La_{1-x}Ce_xCrO_3$ (x = 0.0 to 0.20)

The first four series deal with Cr site doping with transition elements and the last series deals with Ce doping at La site. Here two parent compounds $LaCrO_3$ and $NdCrO_3$ have been taken for substitutional studies, the former one contains non magnetic rare earth ion and

the latter one contains magnetic rare earth ion. The main goal is to study the crystal structure and magnetic properties to understand the magnetic interactions between Cr and other transition elements (Fe and Mn) and as well as Cr and Nd ions.

The above samples were characterized by using X-ray diffraction (XRD), Scanning electron micrographs (SEM) and Energy-dispersive spectrum (EDS). To determine the crystal structure, XRD patterns were recorded at room temperature by using the Rigaku make TTRAX III diffractometer. To understand the magnetic properties of these samples we have studied the dc magnetization as a function of temperature and field by using a Lakeshore make vibrating sample magnetometer of model no. 7410.

The present thesis consists of six chapters, namely

I. Introduction
II. Experimental details
III. $LaCr_{1-x}M_xO_3$ (M = Fe and Mn) series
IV. $NdCr_{1-x}M_xO_3$ (M = Fe and Mn) series
V. $La_{1-x}Ce_xCrO_3$ series
VI. Conclusions

In chapter I, the discovery of magnetization reversal and exchange bias in orthochromites are reviewed briefly. Brief introduction to crystal structure, crystal field effect and Jahn-Teller distortion and their effect on magnetic properties are presented. The details of various types of magnetic ordering, magnetic interactions, and magnetic anisotropy are discussed. The different mechanisms responsible for various magnetic properties are also discussed. The past studies on rare earth and transition element doped La and Nd based orthochromites are reviewed with special emphasize on their crystal structure and magnetic properties.

The chapter II is dedicated to the experimental techniques where the methods of material preparation and characterization technique are discussed. The working principle of various sophisticated equipments such as X- ray diffractometer, scanning electron microscope and vibrating sample magnetometer are presented.

Chapter III deals with the preparation, characterization and the detailed analysis of magnetic properties of $LaCrO_3$ system substituted by Fe and Mn at Cr site.

$LaCr_{1-x}Fe_xO_3$ compounds were prepared in single phase form for x = 0 to 1.0. The lattice parameters are found to systematically increase with increase in Fe concentration. Magnetization reversal has been observed for x = 0.05, 0.10, 0.15, 0.45 and 0.50 samples. The exchange bias behavior has been observed for x = 0.45 and 0.50 samples. With increase in Fe concentration, the compensation temperature was found to increase from 38 K for x = 0.05 sample to 105 K for x = 0.50 sample due to the decrease in canted ferromagnetic component of Cr^{3+} ions. For $x \geq 0.6$ samples, AFM transition was observed due to the presence of superexchange AFM interaction in Fe^{3+}-O^{2-}-Fe^{3+} networks.

The temperature variations of magnetization of x = 0.05, 0.10, 0.15, 0.45 and 0.50 samples at different applied magnetic fields were analyzed to study the magnetization reversal behavior. The origin of magnetization reversal behavior was found to be due to the a) competition between the canted ferromagnetic component of the Cr^{3+} ions and the paramagnetic component Fe^{3+} ions under the influence of negative internal field due to the AFM ordered Cr^{3+} ions for x = 0.05, 0.10 and 0.15 samples and b) competition between the single ion anisotropy and Dzyloshinsky-Moriya interaction for x = 0.45 and 0.50 samples.

The single phase samples of $LaCr_{1-x}Mn_xO_3$ were prepared for x = 0.0 to 1.0. The crystal structure was found to be orthorhombic for x = 0.0 to 0.5 but for $x \geq 0.6$, it undergoes transition into rhombohedral structure. The x = 0.15 and 0.20 samples show magnetization reversal as well as a clear tunable exchange bias behavior with higher compensation temperature T_{comp} (95 K for x = 0.15 and 147 K for x = 0.20) compared to that of Fe doped samples. The value of negative magnetization was found to be much larger than that of Fe doped series. The origin of magnetization reversal behavior was explained by considering the competition between the canted ferromagnetic component of the Cr^{3+} ions and the paramagnetic component Mn^{3+} ions under the influence of negative internal field due to the AFM ordered Cr^{3+} ions.

The tunable exchange bias phenomenon was explained by considering the anisotropic exchange interaction between the ferromagnetic component of Cr^{3+} and the paramagnetic component of Mn^{3+} ions under the influence of negative internal field. The maximum and minimum values of the exchange bias for x = 0.15 sample are found to be 2.6 kOe at 60 K and -2.1 kOe at 140 K respectively.

With increase in Mn concentration *i.e.* $x \geq 0.30$, presence of ferromagnetic transition was observed and its T_C was found to increase from 128 K for $x = 0.40$ to 244 K for $x = 1.0$ sample. The observed magnetization behavior was explained on the basis of exchange interaction in Mn^{3+}-O^{2-}-Mn^{4+} and Cr^{3+}-O^{2-}-Mn^{3+} networks.

Isothermal magnetization was measured as a function of field in the vicinity of ferromagnetic transition of $x = 0.70$ sample. They were analyzed in terms of modified Arrott plot method and the estimated critical exponents $\beta = 0.325 \pm 0.006$, $\gamma = 1.247 \pm 0.066$ and $\delta = 4.823 \pm 0.004$ are comparable to that of 3D Ising model. The critical exponent values are found to be consistent with the Widom scaling relation and the universal scaling hypothesis.

Chapter IV contains the study of magnetic properties of $NdCrO_3$ by Fe and Mn substitutions at Cr site.

$NdCr_{1-x}Fe_xO_3$ samples were found to be crystallized in orthorhombic structure for $x = 0$ to 1.0 and lattice parameters systematically increase with increase in Fe concentration. The temperature variation of magnetization plots show the presence of magnetization reversal with large negative magnetization value and tunable exchange bias for $x = 0.05$, 0.10, 0.15 and 0.20 samples. The compensation temperature was found to increase with Fe concentration from 158 K for $x = 0.05$ sample to 198 K for 0.15 samples. Magnetization reversal behavior was explained in terms of competition between the canted ferromagnetic component of the Cr^{3+} ions and the paramagnetic components of Nd^{3+} ions and Fe^{3+} ions under the influence of negative internal field due to the AFM ordered Cr^{3+} ions. Below the compensation temperature, bipolar switching mechanism was observed. Samples with $x \geq 0.3$ show antiferromagnetic transition. These behaviors are attributed to the super exchange AFM interaction in Fe^{3+}-O^{2-}-Fe^{3+} and Cr^{3+}-O^{2-}-Cr^{3+} networks.

$NdCr_{1-x}Mn_xO_3$ compounds were prepared in single phase form for $x = 0$ to 0.7. The studies of crystal structure and magnetic property would be presented. The $x = 0.10$, 0.15 and 0.20 samples exhibit the magnetization reversal properties along with low temperature spin reorientation and tunable exchange bias behavior. Below the compensation temperature, bipolar magnetization switching behavior and magneto caloric effect have been observed. The compensation temperature was found to increase from 111 K to 157 K for the variation of x from 0.10 to 0.20. The magnetization reversal behavior was found to be due to the competition between the canted ferromagnetic component of the Cr^{3+} ions and the

paramagnetic components of Nd^{3+} ion and Mn^{3+} ions under the influence of negative internal field due to the AFM ordered Cr^{3+} ions. For $x \geq 0.3$, FM transition has been observed. The measured magnetization data were explained based on the ferromagnetic interaction in Mn^{3+}-O^{2-}-Cr^{3+} and Mn^{3+}-O^{2-}-Mn^{4+} networks and antiferromagnetic superexchange interaction in Cr^{3+}-O^{2-}-Cr^{3+} networks.

Effect of Ce substitution in the La site of $LaCrO_3$ is discussed in chapter V.

All Ce substituted $LaCrO_3$ samples are found to be in single phase form and their unit cell volume was found to decrease with increase in Ce concentration upto $x = 0.10$ sample. As the doping concentration is increased, the ferromagnetic transition temperature increases from 40 K for $x = 0.05$ to 135 K for $x = 0.15$ and on the other hand, the Néel temperature is found to decrease. Thus, Ce doping gives rise to short range double exchange FM interaction in Cr^{3+}-O^{2-}-Cr^{2+} networks. All the doped samples exhibit FM like hysteresis loop but without any saturation below the FM transition temperature. Onset of large coercivity along with peak like structure was observed as the sample is cooled through the FM transition. The observed FM is explained in terms of short range double exchange ferromagnetic interaction in Cr^{2+}-O^{2-}-Cr^{3+} networks.

A brief summary of results and discussions obtained from the measurement and analysis of experimental data of all the five series are presented in chapter VI. The transition elements doped La-Cr-O based compounds show the magnetization reversal and tunable exchange bias behavior around compensation temperature. On the other hand, transition elements doped Nd-Cr-O exhibit the large magnetization reversal along with higher magnetic compensation temperature. In addition to that Nd-Cr-O series exhibit spin reorientation at low temperature. The magnetic properties of Ce doped La-Cr-O based compound are explained in terms of short range double exchange FM interactions. Future scopes of research in this area are also given briefly.

List of Abbreviations used in this Thesis

AFM Antiferromagnet

CCR Close Cycle Refrigerator

CMR Colossal Magnetoresistivity

DE Double Exchange

DE-FM Double Exchange Ferromagnetism

DM Dzyaloshinsky -Moriya

EB Exchange bias

EDS Energy Dispersive Spectra

FC Field Cooled

FM Ferromagnet (ic)

JT Jahn-Teller

MAP Modified Arrot Plot

MCE Magnetocaloric Effect

MR Magnetization reversal

PID Proportional–Integral–Derivative

PM Paramagnet (ic)

RF Radio Frequency

SE Superexchange

SEM Scanning Electron Micrograph

VSM Vibrating Sample Magnetometer

XRD X-ray Diffractometer

ZFC Zero-Field Cooled

Table of Contents

Content **Page No.**

List of Figures

Page No.

Chapter 1:

Chapter 2:

Chapter 3:

Chapter 4:

Chapter 5:

Chapter 6:

List of Tables

Page No.

Chapter 1:

Chapter 3:

Chapter 4:

Chapter 5:

Chapter 1

Introduction

Chapter1: Introduction

The pioneering discovery of giant magneto-resistance in magnetic multilayer by Fert and Grünberg [1] revolutionized the information storage and retrieval and hence the information technology. It is the direct example of spin valve and (magneto-electronic) spintronic devices, where the magnetic field can control the electrical transport. Subsequent to the discovery of giant magneto-resistance in magnetic multilayer, colossal magneto-resistance was discovered in rare earth manganites with alkaline earth doping, $R_{1-x}A_xMnO_3$ (R : rare earth, A: alkaline earth) compounds [2, 3]. Recent research works on magnetic materials suggest that magnetic materials are expected to play a major role in future electronic circuits, where not only the type and concentrations of charge carriers but also their magnetic spin are going to act as controlling parameters in electronic circuits [4]. Such increased degree of freedom is likely to improve the efficiency, miniaturization, reduction in power consumption, speed and non volatile memory, *etc*. Exchange bias behavior and magnetization reversal play a major role in controlling the properties of spin valve and spintronic devices. So, the research interest continues in understanding the above properties, not only in multilayer thin films but also in bulk magnetic materials such as spinels, orthochromites, orthovanadates, manganites, intermetallic alloys, *etc*. The present thesis is devoted to study such properties in orthochromites.

Orthochromites are one of the important class of magnetic materials, which exhibit antiferromagnetic transition along with canted ferromagnetic component and in addition to that they exhibit very interesting properties such as magnetization reversal, exchange bias phenomena and multiferroicity. Such important properties have significant role in technological applications like spintronic devices, magnetic random access memory, *etc*. Notwithstanding to the above magnetic properties, these materials are the subject of study towards the development of electrode material in solid oxide electrolyte fuel cell due to their high electrical conductivity at elevated temperature.

Rare earth orthochromites $RCrO_3$ (R = rare earth elements) having perovskite structure contain either magnetic or non magnetic R ion and Cr^{3+} ion. The magnetic ordering is controlled by the nature of magnetic interaction in Cr^{3+}-O^{2-}-Cr^{3+}, R^{3+}-O^{2-}-Cr^{3+} and R^{3+}-O^{2-}-

R^{3+} networks. Magnetic interaction in Cr^{3+}-O^{2-}-Cr^{3+} networks gives rise to G-type antiferromagnetic ordering and along with canted weak ferromagnetic behavior. Moreover, some of the orthochromites having magnetic rare earth ion exhibit low temperature spin reorientation transition because of antiferromagnetic interaction between R^{3+} and canted Cr^{3+} ions. Substitution of divalent alkaline earth elements (Sr, Ca) at rare earth site yields mixed valent chromites, $(R_{1-x}A_x)(Cr^{3+}_{1-x}Cr^{4+}_{x})O_3$ having weak ferromagnetic behavior [5, 6]. On the other hand, partial or complete substitution of magnetic rare earth elements (Pr, Ce, Gd, Yb, Nd, Tm) in the R site unravels the underlying competing magnetic interaction and metastable magnetic ground state such that novel properties like magnetization reversal and tunable exchange bias phenomena can be exploited. This property plays important roles in the development of thermally assisted magnetic random access memories and other spintronics devices [7-11].

In this chapter, the crystal structure and magnetic properties of orthochromites are reviewed.

1.1 Crystal Structure

Study of crystal structural parameters such as type of lattice symmetry, unit cell, lattice constant, bond angle, bond length, cation and anion occupancy values, *etc.* is essential to interpret and understand the magnetic properties of crystalline materials. So, a brief review of crystal structure of orthochromites and other related properties; crystal field effect and Jahn-Teller distortion are discussed.

The orthochromites, $RCrO_3$ generally exhibit distorted perovskite structure. The ideal perovskite structure for ABO_3 type of compound is shown in Fig. 1.1. The A site ions occupy the vertices of the cube, the B site ion occupies the body center position of the cube and O ions occupy the six face centered positions. This structure contains BO_6 octahedral coordination with B-O-B angle of 180°. The unit cell dimension is equivalent to the B-B bond length. But, in general $RCrO_3$ compounds deviate from cubic structure due to lattice distortion induced by various factors such as ionic size mismatch, crystal field effect, Jahn-Teller effect, *etc.*

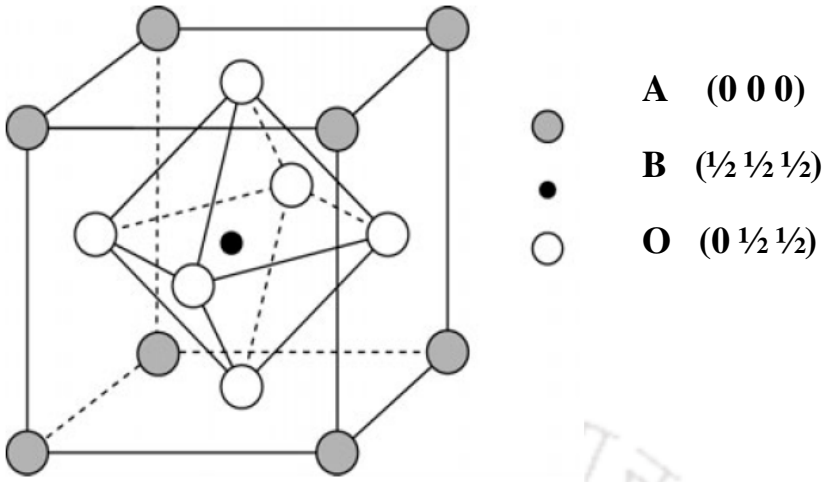

Figure 1.1: Crystal structure of cubic perovskite with chemical formula ABO_3.

The lattice distortion can be calculated from the Goldsmith tolerance factor [12], $t=(r_A+r_O)/\sqrt{2}(r_B+r_O)$ where r_A, r_B and r_O are the ionic radii of A, B and oxygen ions respectively. For the cubic system, $t \sim 1$, if the value of t differs from 1 then we can say that sample is distorted from the ideal cubic structure. In $La_{1-x}Sr_xCrO_3$ system, the average radius of A site ions (La, Sr) increases with increase in x value and it leads to increase in t value. So, the lattice distortion stabilizes the structure in orthorhombic or rhombohedral symmetry [5]. Enhancement of t value towards 1 (0.882 to 0.907) and hence the reduced lattice distortion has been reported in La substituted $NdCrO_3$ [13].

Most of the $RCrO_3$ compounds (R = La, Nd, Gd, Y, Yb, Sm, Ce and Tm) exhibit distorted perovskite structure with orthorhombic symmetry. Typical crystal structure of $RCrO_3$ compound with orthorhombic symmetry is shown in Fig. 1.2(a), where we can see the reduced crystal symmetry compared to the ideal cubic structure due to the tilting of CrO_6 octahedra. The general atomic positions are given in Table 1.1. The crystal structure of orthochromites such as $LaCrO_3$ and $GdCrO_3$ are found to follow the *Pbnm* space group with four formula units per unit cell (Z = 4) and with typical lattice parameters, a = 5.487 Å, b = 5.511 Å and c = 7.750 Å [14] and, a = 5.3142, b = 5.5239 Å and c = 7.6063 Å [15] respectively. $LaCrO_3$ exhibits orthorhombic structure at room temperature and undergoes a structural transition from orthorhombic to rhombohedral cell at 240 ˚C to 280 ˚C and at 1650 ˚C it further transforms to cubic structure [16]. On the other hand, Ca and Mn doped $RCrO_3$

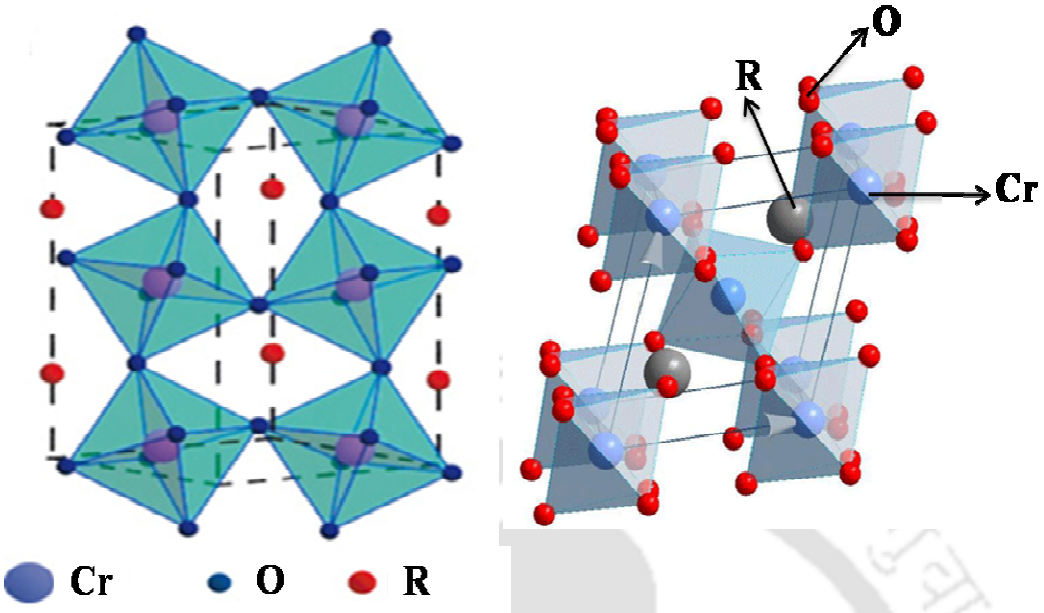

(a) **(b)**

Figure 1.2: Crystal structure of chromites (a) in orthorhombic and (b) in rhombohedral symmetry [5].

Table 1.1: Atomic positions of $RCrO_3$ in *Pbnm* space group.

Ion	Number of Position	Wyckoff Notation	Point Symmetry	(*x*, *y*, *z*)
R	4	c	m	(*x*, *y*, ¼) ≅ (0.99, 0.03, ¼)
Cr	4	b	$\bar{1}$	(½, 0,0) ≅ (½, 0,0)
O_1	4	c	m	(*x*, *y*, ¼) ≅ (0.07, 0.49, ¼)
O_2	8	d	1	(*x*, *y*, *z*) ≅ (0.72, 0.28, 0.04)

compounds form in rhombohedral crystal structure. The typical rhombohedral crystal structure is shown in Fig. 1.2(b). Here each Cr ion is octahedrally coordinated with O ions. The rotation of CrO_6 octahedra along the three fold rotational axis of the ideal cubic structure gives rise to rhombohedral symmetry. Here, the structural parameters are generally referred in hexagonal co-ordinate system. The general atomic positions in rhombohedral structure

($R\bar{3}c$ space group) is given in Table 1.2. The typical lattice parameters of $LaCrO_3$ at 600 K are reported to be $a = b = 5.531$ Å and $c = 13.363$ Å [17].

Table 1.2: Atomic positions of $RCrO_3$ in $R\bar{3}c$ space group given in hexagonal coordinate system.

Ion	Number of Position	Wyckoff Notation	Point Symmetry	(*x*, *y*, *z*)
R	6	a	3	0 0 ¼
Cr	6	b	1	0 0 0
O	18	e	1	0.55 (*x*) 0 ¼

Unlike the case of orthorhombic cell, there is no buckling of CrO_6 octahedra and hence the Cr-O bond lengths are identical in all the three directions. The Cr-O-Cr bond angle is found to be slightly larger than that of orthorhombic cell. The *Z* value is 6.

1.2 Crystal Field Effect

Crystal field is an average electric field produced by neighboring atoms in the crystal. The magnetism in transition elements originates from their unfilled *d*-shell electrons. So, here we discuss about crystal field effect in *d*-orbital due to the neighboring ions. The size and the nature of the crystal field depend on the symmetry of the local environment. Basically *d* orbital has five degenerate energy levels and is divided into two sub orbitals namely t_{2g} (d_{xy}, d_{yz} and d_{zx}) and e_g ($d_{x^2-y^2}$ and d_{z^2}) as shown in Fig. 1.3(a). t_{2g} orbital contains three energy levels d_{xy}, d_{yz} and d_{zx} and e_g orbital contains two levels $d_{x^2-y^2}$ and d_{z^2}. Crystal field effects in octahedral and tetrahedral environments are discussed because in most of the compounds such coordinations exist between *3d* orbitals of transition elements surrounded by the *2p* orbitals of oxygen ions. The electronic configurations in *2p* orbitals are oriented along *x*, *y* and *z* axes and are referred as p_x, p_y and p_z respectively. Due to the crystal field effect, the *d* orbital energy is no longer degenerate. In octahedral environment, e_g electrons overlap predominantly with neighboring *p*-orbitals of oxygen ion compared to that of t_{2g} orbital

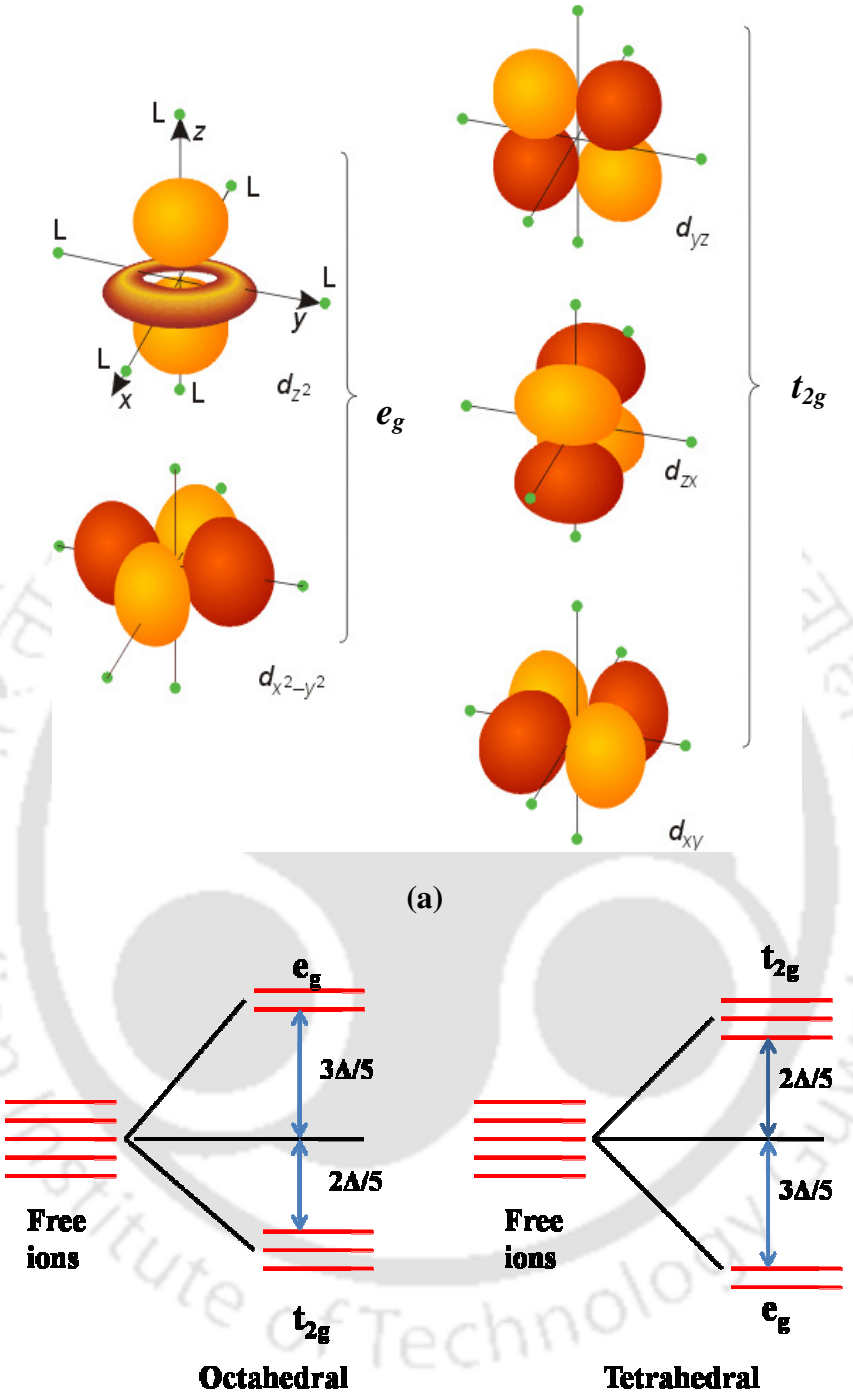

Figure 1.3: (a) The electronic distribution of *3d* orbitals. In the cubic crystal field, this fivefold degeneracy is lifted and separated into two e_g levels ($d_{x^2-y^2}$ and d_{z^2}) and three t_{2g} levels (d_{xy}, d_{yz} and d_{zx}) (Reproduced from Tokura *et al.* [18]). (b) Crystal field effect in octahedral and tetrahedral environments.

electrons and as a result e_g levels are lifted up compared to t_{2g} levels. The energy level diagram of octahedral environment is shown in Fig. 1.3(b). But in the case of tetrahedral environment, t_{2g} levels are lifted up because they overlap predominantly with neighboring *p*-orbitals [19].

The crystal field effect is mainly observed in transition elements, where their *3d* valence electrons are close to the outermost shell and thus they are exposed to the electronic configuration of neighboring ions. In general, the effective magnetic moment (μ_{eff}) of an ion can be calculated by using the relation $\mu_{eff} = g\sqrt{J(J+1)}$ in the unit of μ_B but it does not match with experimental values for most of the transition elements. This is due to the large crystal field effect, which dominates over the Hund's spin-orbit coupling energy in *3d* transition elements and hence the orbital angular momentum is quenched ($L = 0$). Hence, μ_{eff} is calculated using the relation $\mu_{eff} = g\sqrt{S(S+1)}$. Here J and S refer quantum numbers corresponding to total and spin angular momentum of electrons respectively. Another interesting series of elements having strong magnetic moments is rare earth series, where the magnetism originates from *4f* shell. Unlike transition elements, here the *4f* levels are deep inside from the outermost orbital with negligible overlapping with the electronic configuration of neighboring ions and hence they do not show any crystal field effect. In this class of materials μ_{eff} can be calculated using the general relation, $\mu_{eff} = g\sqrt{J(J+1)}$.

In some of the *3d* transition elements for a specific valence state of an ion, electrons are asymmetrically occupied within the degenerate t_{2g} or e_g orbital. The degeneracy within e_g or t_{2g} orbital is spontaneously lifted by further distorting the lattice such that the overall energy is reduced. This effect is called Jahn-Teller effect. Distortion occurs in two ways, one by elongation and another by compression. In the case of elongation in octahedral environment, the overlapping with neighboring oxygen *p*-orbital is reduced in one of the e_g orbital (d_{z^2}), while it is enhanced in another e_g orbital ($d_{x^2-y^2}$). So, $d_{x^2-y^2}$ level is lifted up compared to d_{z^2} level. Similarly in t_{2g} orbital, d_{xy} level is lifted up compared to d_{yz} and d_{zx} levels. On the otherhand, if there is a compression, d_{z^2} level is lifted up compared to $d_{x^2-y^2}$ level in e_g orbital and similarly d_{yz} and d_{zx} levels are lifted up with respect to d_{xy} level in t_{2g}

orbital. Cr^{3+} ion is not a Jahn-Teller active ion but Mn^{3+} is a Jahn-Teller active ion. The Jahn-Teller distortion in Mn^{3+} ion in octahedral environment is shown in Fig. 1.4.

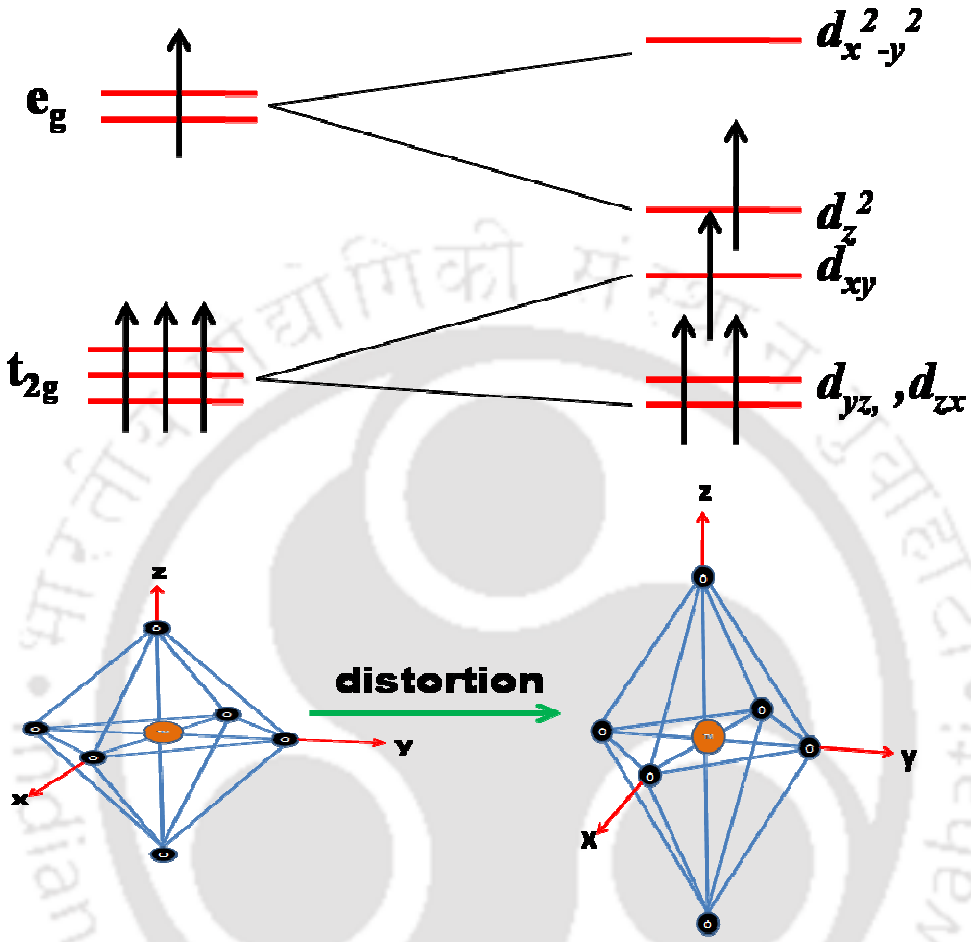

Figure 1.4: The Jahn-Teller distortion leads to a further splitting of both the t_{2g} and e_g states in Mn^{3+} ions.

1.3 Magnetic Ordering

Magnetic materials are broadly classified as: Diamagnet, Paramagnet, Ferromagnet, Antiferroamagnet and Ferrimagnet.

In diamagnetic substance, the induced magnetic moments orient opposite to the direction of applied magnetic field. The interaction between the applied magnetic field and the atomic moment due to electrons can be understood by considering the Lenz's law in electrodynamics. When a magnetic field is applied to a material having closed shell

electronic configuration, the direction of motion of electrons rearrange such that magnetic moment is induced in a direction opposite to the applied field. The diamagnetic moment will persist as long as magnetic field is applied [20].

The susceptibility of diamagnetic material having *N* number of atoms per unit volume and *Z* number of completely filled electrons per atom can be written as,

$$\chi = -\frac{\mu_0 N Z e^2}{6m} \overline{r}^2 \tag{1.1}$$

where, μ_0 is the permeability of free space, e is the charge of electron, m is the mass of the electron and $\overline{r}^2$ is the mean square radius of the electron orbit. This equation is called as Langevin's equation for diamagnetic susceptibility. The diamagnetic susceptibility is generally small of the order of 10^{-5} (cgs unit) and is mostly independent of temperature. The only type of material known to exhibit strong diamagnetism is superconductor.

The examples of diamagnetic substances are He, Ne, Ar, *etc.* having closed shell electronic configuration, polyatomic gases H_2, N_2, *etc* with closed shell electrons due to the nature of molecule formation and ionic solids like, NaCl with closed shell electrons due to electron transfer during ionic bonding. Formation of covalent bonding leads to closed shell configuration in C, Si and Ge.

In a paramagnetic substance, the magnetic dipoles (atomic moment) tend to align along the applied field direction, so the magnetic susceptibility is always positive. Here, the presence of unpaired electrons gives rise to magnetic moment and in the absence of magnetic field, they are oriented in random directions; so the net magnetic moment is zero. As the magnetic field is applied the magnetic moments tend to orient in the applied field direction but thermal energy does not allow them to completely orient along field direction. With increase in applied field or decrease in temperature, the degree of alignment increases and the net magnetic moment also increases. Opposite trend is observed with decrease in applied field or increase in temperature. So, magnetization of paramagnetic material is directly proportional to *B/T* [19].

The paramagnetic susceptibility as per the classical approach is given as,

$$\chi = \frac{\mu_0 N \mu^2}{3k_B T} \tag{1.2}$$

where N is the number of magnetic dipoles (magnetic ions) per unit volume each having magnetic moment of μ. The equation (1.2) demonstrates that the magnetic susceptibility is inversely proportional to the temperature and is known as Curie's Law.

By considering the quantum mechanical approach, the magnetic susceptibility at low magnetic field becomes,

$$\chi = \frac{N\mu_0 g^2 \mu_B^2 J(J+1)}{3k_B T} \tag{1.3}$$

where, g is Landé g factor and it is written as, $g = \frac{3}{2} + \frac{S(S+1) - L(L+1)}{2J(J+1)}$.

Basically salts of transition element, salts and oxides of the rare earths and the rare earth elements are the examples of the strong paramagnetic substances [21].

Ferromagnetic substances exhibit spontaneous magnetization even in the absence of external magnetic field due to the presence of strong exchange forces (molecular field) between the magnetic moments.

According to the molecular field theory, the magnetic moments align parallel to each other due to the presence of molecular field $B_m = \lambda M$. Here, λ is a positive constant and M is the magnetization of the material. Such ferromagnetic behavior is observed below the transition temperature T_C. For $T > T_C$, mostly they behave like a paramagnet with susceptibility,

$$\chi = \frac{C}{T - \theta_C} \tag{1.4}$$

where C and θ_C are Curie constant and Curie temperature respectively. The above equation

is known as Curie-Weiss law. Here $C = \mu_0 N g^2 \mu_B^2 J(J+1)/3k_B$ or $C = \mu_0 N \mu^2 / 3k_B$. Some common ferromagnetic materials are Fe, Co and Ni. Typical θ_C values of Fe, Ni and Co are 1043 K, 1394 K and 631 K [21] respectively.

In an antiferromagnetic substance, the magnetic moments are aligned antiparallel such that the net magnetic moment is zero below certain temperature known as Néel temperature (T_N) and above that it mostly behaves like paramagnet. The magnetic susceptibility in the paramagnetic region of such substance is written as,

$$\chi = \frac{C}{(T + T_N)} \tag{1.5}$$

The examples of antiferromagnetic materials are MnF_2, MnO, CoO, FeO, Cr_2O_3, α-Fe_2O_3 with respective Néel temperature of 67 K, 116 K, 292 K, 116 K, 307 K and 950 K respectively [21].

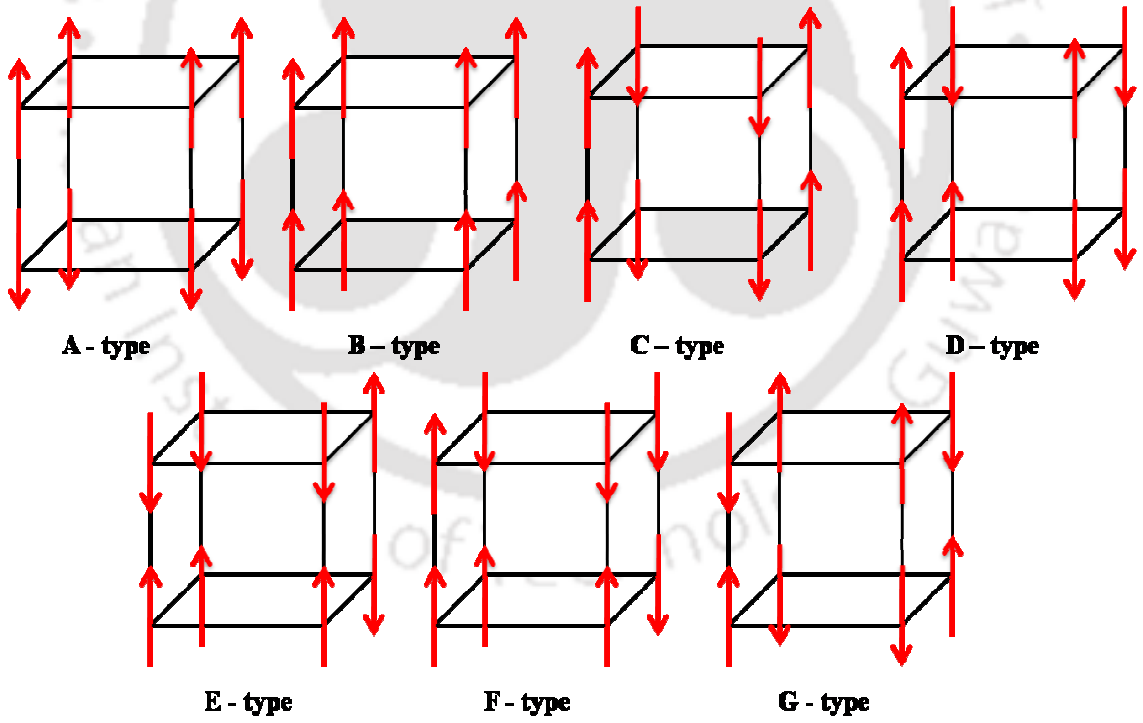

Figure 1.5: Different type of antiferromagnetic arrangement in a magnetic unit cell. The B type structure leads to ferromagnetism. The arrows refer the orientation of magnetic spin.

The antiferromagnetic ordering is possible based on different type of magnetic unit cell structures as shown in Fig. 1.5 except for B type, which is a FM one. In A-type structure, the magnetic ions are coupled ferromagnetically in each (001) plane but with alternate planes aligned in opposite spin orientation and the example is $LaMnO_3$. So, there is an antiferromagnetic interaction between the planes. B-type structure is a ferromagnetic one with all six nearest magnetic ions coupled ferromagnetically. In C-type structure, the atoms in (101) and ($\bar{1}10$) planes are ferromagnetically aligned. Each atom has two ferro and four antiferromagnetic nearest neighbors such that there is a net antiferromagnetic unit cell.

In G-type structure each ion is coupled antiferromagnetically to all its six nearest neighbors. Hence the atoms of positive and negative spins are arranged periodically, for example: $LaCrO_3$, $LaFeO_3$, $GdCrO_3$, *etc* [14, 22]. The other types of magnetic structures, D, E and F are shown in Fig. 1.5.

Ferrimagnetism is a special type of antiferromagnetism when the magnitudes of sub lattice magnetizations are not equal to each other and therefore a net magnetization is observed. Here, the molecular field differs at different sub lattices. The temperature dependence of sublattice magnetizations differ and as a result in certain temperature range one of the sublattices magnetization dominates over the other and the domination is reversed in some other temperature range. Because of this, the magnetization may pass through zero at certain temperature known as magnetic compensation temperature, T_{comp}. Most of the ferrimagnetisms are electrical insulators and they are useful for many of the practical applications. Some of the ferrimagnetic materials are $MnFe_2O_4$, $NiFe_2O_4$, $CoFe_2O_4$, Fe_3O_4, *etc*, [21].

1.4 Magnetic Interactions

Different types of magnetic interactions at microscopic scale are responsible for long range magnetic ordering. Some of the important magnetic interactions are briefly described.

1.4.1 Magnetic Dipole Interaction

The magnetic dipole interaction is one of the direct magnetic interactions, where the energy associated with two magnetic dipoles μ_1 and μ_2 separated by a distance r can be written as [19]

$$E = \frac{\mu_o}{4\pi r^3}\left[\vec{\mu}_1.\vec{\mu}_2 - \frac{3}{r^2}(\vec{\mu}_1.\vec{r})(\vec{\mu}_2.\vec{r})\right] \quad (1.6)$$

This interaction is significant at very low temperature and plays a major role in materials undergoing magnetic ordering at milliKelvin temperature. The magnetic dipolar interaction is too weak to account for the ordering of most of the magnetic materials. There is a built in anisotropy in the dipolar interaction which can orient the spins either parallel (FM) or anti-parallel (AFM). If the spins are oriented along r, they couple ferromagnetically and if they are oriented perpendicular to r, they couple antiferromagnetically.

1.4.2 Direct Exchange Interaction

If the electrons of the neighboring magnetic atoms interact directly without any intermediate non-magnetic ion then the interaction is called as direct exchange interaction. The direct exchange interaction is not an important mechanism in controlling the magnetic properties of most of the materials due to insufficient overlapping of electron distribution between the neighboring atoms. The Pauli's exclusion principle keeps the electrons with parallel spins away from each other to reduce the Coulomb repulsion. So, mostly antiparallel spin configuration is favored in direct exchange interaction. The wave functions of the magnetic '*d*' or '*f*' electrons decrease exponentially in space, thereby too small overlap of wave functions and hence weak direct exchange interaction.

1.4.3 Super Exchange Interaction

The indirect exchange between two magnetic ions through a non magnetic intermediate ion is called super exchange interaction and it is a long range interaction. According to Kramers' model [23], interaction between the cations having more than half filled *d*-shells gives rise to the antiferromagnetic interaction, while such interaction among

cations having less than half filled *d*-shells gives rise to ferromagnetic interaction. On the other hand, Slater [24], Goodenough and Loeb [25] and Goodenough [26] proposed that the antiferromagnetic interaction is allowed among less than half filled *d*-shell cations. The mechanism related to super exchange interaction is as follows:

When core spins of magnetic cations are antiparallel to each other with allowed empty higher energy levels across an intermediate non-magnetic ion like oxygen, antiferromagnetic interaction is facilitated due to the strong Hund's coupling. To satisfy the Hund's rule, out of two valence electrons of oxygen, the up spin electron spends some time with the cation in one side having up spin configuration and the down spin electron spends some time with other cation having down spin configuration. In this process, each cation-anion pair has ferromagnetic (parallel) alignment of electrons and the net cation-cation interaction is antiferromagnetic. This is depicted in Fig. 1.6(a) for Mn^{4+}-O^{2-}-Mn^{4+} pair. The above covalent bonding is not permissible if the core spins are aligned parallel.

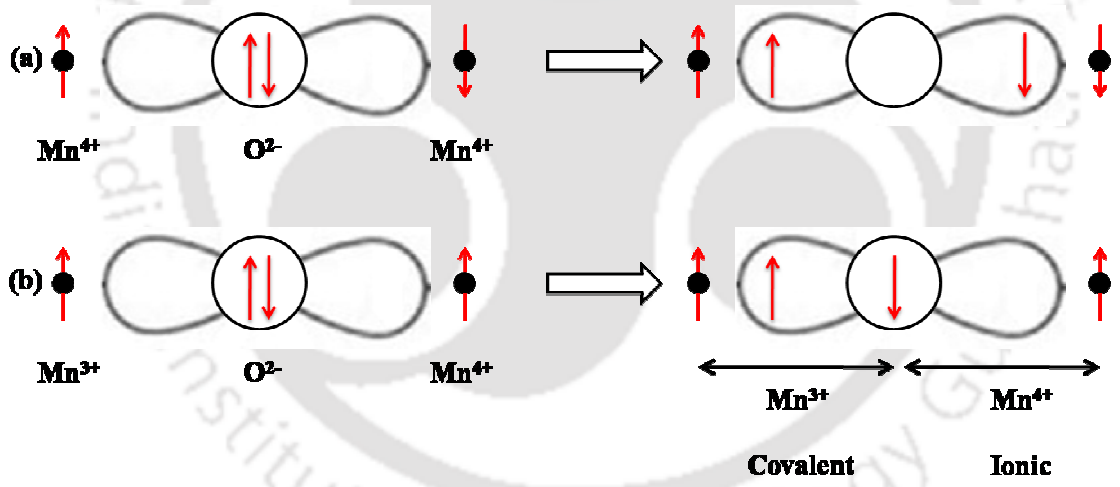

Figure 1.6: Schematic diagram showing the arrangement of spins and orbitals in (a) an antiferromagnetic superexchange interaction and (b) a ferromagnetic superexchange interaction.

According to Goodenough [26], the superexchange interaction also gives rise to ferromagnetism provided the cation-anion-cation is asymmetric , *i.e.* covalent bond one side and ionic bond another side as depicted in Fig. 1.6(b) for Mn^{3+}-O^{2-}-Mn^{4+} pairs. Here core spins of cations are parallel to each other. Out of two valence electrons of O^{2-}, the spin up

electron form covalent bonding with left side cation (Mn^{3+}) having spin up electron, while the spin down electron of oxygen forms ionic bond with right side cation (Mn^{4+}). The direct exchange between oxygen and the right side cation is antiferromagnetic. So, overall ferromagnetic interaction prevails between Mn^{3+} and Mn^{4+} ions.

Thus according to Goodenough [26], the superexchange interaction in Mn^{3+}-O^{2-}-Mn^{3+} and Mn^{4+}-O^{2-}-Mn^{4+} networks lead to antiferromagnetism (AFM), while the interaction in Mn^{3+}-O^{2-}-Mn^{4+} networks lead to ferromagnetism (FM). The superexchange interaction mainly promotes the insulating behavior. According to Kanamori [27], Cr^{3+}-O^{2-}-Cr^{3+}, Fe^{3+}-O^{2-}-$Fe^{3+}$are antiferromagnetic in nature.

1.4.4 RKKY Interaction

In metals, conduction electrons are the mediator of the exchange interaction between the magnetic ions. A localized magnetic moment of an ion, spin polarizes the conduction electrons and this polarization couples to the neighboring localized magnetic moment at a distance *r* away. This interaction is an indirect one, because it does not couple directly. The coupling takes the form of an *r*-dependent exchange interaction $J_{RKKY}(r)$ given by [19]

$$J_{RKKY}(r)\alpha\frac{\cos(2k_F r)}{r^3} \tag{1.7}$$

where k_F is the radius of the spherical Fermi surface. This interaction has oscillatory dependence of the distance between the magnetic ions and it is in long range. Such interaction gives rise to either ferromagnetic or antiferromagnetic coupling depending on the distance between the magnetic ions.

1.4.5 Double Exchange Interaction

In 1951, Zener presented a theory of indirect magnetic exchange between *3d* atoms [28, 29]. According to Zener model, carrier electrons can hop between two ions only if the electron spins of the two ions are parallel, and Zener showed that FM interactions are energetically favored when conduction electrons are present. To describe the exchange interaction between Mn^{3+} and Mn^{4+} ions via an oxygen ion, Zener introduced the concept of

double exchange, *i.e.* simultaneous transfer of an electron from Mn^{3+} to oxygen and from oxygen to Mn^{4+}. Two simultaneous motions are involved in this process, and so it is called double exchange (DE) interaction. The movement of electron can be shown as, $Mn^{3+}_{1\uparrow}O_{2\uparrow,3\downarrow}Mn^{4+} \rightarrow Mn^{4+}O_{1\uparrow,3\downarrow}Mn^{3+}_{2\uparrow}$, where the electron spins are labeled as 1, 2 and 3. Anderson and Hasegawa [30] presented the DE mechanism in detail by visualizing a second order process in which the electron transfer takes as follows $Mn^{3+}_{1\uparrow}O_{2\uparrow,3\downarrow}Mn^{4+} \rightarrow Mn^{3+}_{1\uparrow}O_{3\downarrow}Mn^{3+}_{2\uparrow} \rightarrow Mn^{4+}O_{1\uparrow,3\downarrow}Mn^{3+}_{2\uparrow}$.

Double exchange always gives rise to ferromagnetism; if the spins of the *d*-electrons of two manganese ions are parallel, the configurations Mn^{3+}-O^{2-}-Mn^{4+} and Mn^{4+}-O^{2-}-Mn^{3+} will be degenerated as shown in Fig. 1.7(a). If the manganese spins are not parallel, the electron transfer becomes more difficult due to strong onsite Hund's coupling as shown in Fig. 1.7(b). The electron transfer is also more difficult if the Mn-O-Mn bond is considerably bent; when the angle is 180° the overlap of the manganese *d*-orbitals and the oxygen *p*-orbital is the largest and the interactions is the strongest, and will decrease on deviation from this angle.

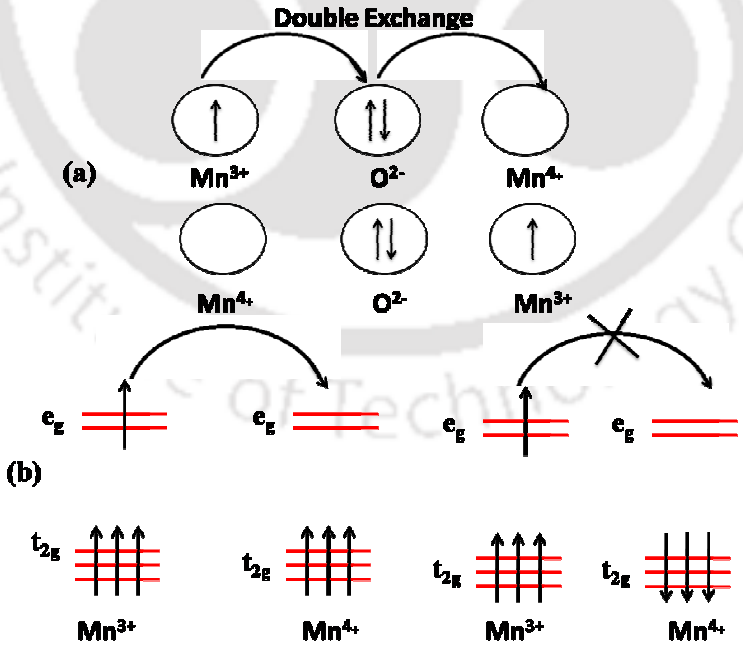

Figure 1.7: (a) Sketch of double exchange mechanism which involves two Mn ions and one O ion. (b) The mobility of e_g electrons improves if the localized spins are polarized.

1.4.6 Dzyaloshinsky-Moriya (DM) Interaction

Some of the antiferromagnetic crystals exhibit weak ferromagnetic behavior such as α-Fe_2O_3, Cr_2O_3, $MnCO_3$, $CoCO_3$ *etc*. The magnitude of their spontaneous magnetization is very small in such case and is in order of 10^{-2}-10^{-5} of the nominal value. The origin of the weak ferromagnetism was explained by Néel and Li. Néel suggests [31] that the magnetite impurities or imperfection can gives rise the weak ferromagnetism and Li [32] proposed that the uncompensated magnetic moments at the walls separating the antiferromagnetic domains give rise to weak ferromagnetism.

Another mechanism proposed by Dzyaloshinsky-Moriya [33, 34] is that the tilting of the magnetic moments of antiparallel spins towards each other gives rise to a net magnetic moment. However, such a canted spin arrangement is allowed only if the original magnetic structure when the spins were antiparallel is not disturbed. The exchange energy between the magnetic moments at this canted configuration can be written as follows,

$$H_{DM} = \vec{D}.(\vec{S}_1 \times \vec{S}_2) \tag{1.8}$$

Where $\vec{S}_1$ and $\vec{S}_2$ are the spins of two interacting magnetic ions and D is DM constant. The $\vec{D}$ vanishes when the crystal field has an inversion symmetry, *i.e.* with respect to the middle point (centre) connecting the two magnetic ions. In general $\vec{D}$ lies either parallel or perpendicular to the line connecting the two spins, depending on the symmetry. The DM interaction tries to align $\vec{S}_1$ and $\vec{S}_2$ at right angle to each other in a plane perpendicular to $\vec{D}$. The microscopic origin of canting of spins can be explained by considering two mechanisms. The first one is due to the occupation of magnetic ions in two different nonequivalent crystal sites such that they experience different crystal field. The crystal field effect along with the spin-orbit coupling leads to the non parallel easy directions for the non equivalent ions with crystalline anisotropy. This mechanism leads to canted antiferromagnetism. Second one originates from spin-orbit coupling along with the superexchange interaction. In case of low symmetric crystal, an antisymmetric superexchange interaction is the reason for the presence of weak ferromagnetism [20].

1.5 Magnetic Anisotropy

Several factors affect the shape of the magnetization curves including coercivity, remanent magnetization, saturation magnetization, *etc*. One such factor is the magnetic anisotropy. Several type of anisotropies exist as given below:

I. Crystal anisotropy or magnetocrystalline anisotropy
II. Shape anisotropy
III. Stress anisotropy
IV. Exchange anisotropy

1.5.1 Crystal Anisotropy

The magnetic properties are not generally isotropic with respect to crystallographic orientation. It is easy to magnetize the sample to its full saturation value if the field is applied along a specific crystallographic axis and such axis is called magnetic easy axis. On the other hand, in certain crystallographic orientation it would be very difficult to completely magnetize the sample and such direction is called hard axis. Spontaneous domain magnetization remains aligned along the easy direction in the absence of external field. Therefore crystal anisotropy is considered as a force which tends to hold the magnetization in certain equivalent crystallographic direction in a crystal. The energy associated in the crystal having magnetization orientation away from the easy axis is given as,

$$E_a = K_0 + K_1(\alpha_1^2\alpha_2^2 + \alpha_2^2\alpha_3^2 + \alpha_3^2\alpha_1^2) + K_2(\alpha_1^2\alpha_2^2\alpha_3^2) + ... \quad (1.9)$$

Here K_0, K_1 and K_2 are constants for a particular crystal at a particular temperature and, α_1, α_2 and α_3 are the direction cosines of the magnetization with respect to crystallographic axes *a*, *b* and *c*. If K_2 is zero, the direction of easy magnetization can be determined from the sign of K_1. If K_1 is positive, then $E_{100}<E_{110}<E_{111}$ with <100> as the easy axis as observed in iron, cubic ferrite containing cobalt, *etc*. If K_1 is negative, $E_{111}<E_{110}<E_{100}$, here the easy axis is <111> and the examples are nickel, cubic ferrite, *etc*. If K_2 is not zero, then the direction of easy magnetization axis is determined by both K_1 and K_2 [21].

The anisotropy associated with a single crystallographic axis (which is the easy axis) is called uniaxal anisotropy and the energy can be written as,

$$E_a = K_0' + K_1' \cos^2\theta + K_2' \cos^4\theta + ... \quad (1.10)$$

where θ is the angle between the magnetization and the easy axis. The above equation can be written in terms of powers of $sin\theta$. The equation becomes,

$$E_a = K_0 + K_1 \sin^2\theta + K_2 \sin^4\theta + ... \quad (1.11)$$

If K_1 and K_2 are positive, then E_a will be minimum when $\theta = 0$ *i.e.* for the magnetization lying along the easy axis and the examples are cobalt, barium ferrite and many rare earth transitional metal intermetallic compounds. If K_1 and K_2 are negative, then E_a will be minimum when $\theta = 90^\circ$ so here magnetization lie in an easy plane which is perpendicular to the easy axis. The anisotropic energy is generally larger for low symmetric crystals. For example, cubic Fe and Ni have $K_1 = 4.8\times10^4$ Jm^{-3} and -5.7×10^3 Jm^{-3} respectively but for hexagonal Co $K_1 = 5\times10^5$ Jm^{-3}. The magnitude of crystal anisotropy sharply decreases with increase in temperature and it vanishes at Curie temperature. Anisotropy gives rise to the enhanced coercive field [21].

The spin-orbit coupling of electrons in magnetic materials plays a major role in shaping the crystal anisotropy [21]. Electrons in the crystal are subjected to four different type of coupling namely spin-spin coupling, orbit-lattice, spin-orbit and spin-lattice coupling. The spin-spin coupling is very strong which forces the neighboring spins to be either parallel or antiparallel with each other. The energy associated with this coupling is isotropic and it depends on the angle between the spins rather than the crystallographic orientation. So, it does not contribute any crystal anisotropic energy. In most of the ferromagnetic materials, orbital moments are quenched, so the orientation of the orbits are fixed with the crystal lattice so the orbit-lattice interaction is very strong and even large applied magnetic field can't change them. The spin-orbit coupling is relatively weak, so when an external magnetic field is applied the spin and orbital moments of an electron try to align along the field direction but since the orbit is strongly coupled to the lattice, it resists the spin axis to rotate. The energy required to rotate the spin from its easy axis is called anisotropic energy.

In antiferromagnetic compounds, the crystal anisotropy arises mainly due to [20] i) the crystal field acting on single ion, ii) the anisotropic exchange interaction and iii) dipole-dipole interaction. When the crystal field is acting on a magnetic ion, the orbital magnetic moment is quenched, so the orientation of the electronic orbit is fixed strongly with the lattice. So the spin-orbit coupling gives rise to the anisotropy in the crystal. In addition to that the direct or indirect exchange interaction and the spin-orbit coupling produce the anisotropic exchange interaction. In antiferromagnetic compounds, spin-orbit coupling of the anions is also involved. The anisotropic dipole-dipole interaction also contributes to the crystal anisotropy.

1.5.2 Shape Anisotropy

The shape of a polycrystalline magnetic sample can produce magnetic anisotropy. As we know for polycrystalline sample having no preferred orientation so the presence of crystal anisotropy is rare. If the sample is spherical in shape then the magnetization produced by the applied field will be uniform in all the directions. But, if it is non-spherical then it is easy to magnetize along the longer axis due to the small demagnetization factor compared to shorter axis. The demagnetization field H_d is created whenever magnetic poles are produced in the material. H_d depends directly on the magnetization of the material and a shape and dimension dependent parameter known as demagnetization factor N_d. It is written as

$$\vec{H}_d = -N_d \vec{M} \tag{1.12}$$

The sum of the demagnetization factors along the three orthogonal axes of an ellipsoid is a constant:

$$N_a + N_b + N_c = 1 \text{ (SI) } or\ 4\pi \text{ (cgs)} \tag{1.13}$$

For spherical sample, all the three demagnetization factors are equal so, $N_{sphere} = 4\pi/3$ (cgs) or 1/3 (SI). The energy related with the demagnetization field of a specimen is called as magnetostatic energy (E_{ms}) and it can be written in the unit of J/m^3 as

$$E_{ms} = \frac{1}{2}\mu_0 N_d M^2 \tag{1.14}$$

1.5.3 Stress Anisotropy

Under the influence of stress the domain structure changes and gives rise to magnetic anisotropy. Stress can produce easy axis magnetization. So, stress anisotropy is a uniaxial anisotropy and the stress anisotropy energy or magnetoelastic energy can be written as

$$E_\sigma = K_\sigma \sin^2\theta \tag{1.15}$$

where K_σ is the stress anisotropy constant and θ is the angle between magnetization and the axis of stress. The axis of the stress behaves like easy axis if K_σ is positive or hard axis if K_σ is negative.

1.5.4 Exchange Anisotropy

Exchange anisotropy is generally observed in layered system or compounds having interfaces between ferromagnet and antiferromagnet. When such a system is cooled through the Néel temperature (T_N) of the antiferromagnet in the presence of static magnetic field then anisotropy is developed at the interface between FM and AFM and such anisotropy is called exchange anisotropy. Due to the exchange anisotropy, the center of hysteresis loops shift from the origin towards either negative or positive field axis and is called exchange bias phenomenon (EB). The exchange bias was first discovered by Meiklejohn and Bean in 1956 in Co particle coated with CoO layer [35]. The pinning of the FM spins by the hard AFM spins at interface gives rise to unidirectional exchange anisotropy and its energy can be written as,

$$E = -K_u \cos\theta \tag{1.16}$$

where K_u is the unidirectional anisotropy constant and θ is the angle between the magnetization and the direction of cooling field.

1.6 Critical Exponents in Magnetic Transition

The study of critical phenomena in the second order magnetic phase transition, *i.e.* close to FM transition temperture (T_C) in amorphous and crystalline ferromagnets has been

the field of interest for a long time to understand the type of magnetic interactions [19]. The famous Landau theory for the second order magnetic phase transition assumed that the Gibb's free energy is a function of the order parameter and temperature dependent coefficients [36]. The Gibb's free energy G is written in terms of powers of order parameters. The magnetization M is taken as the order parameter. The expression for G as per Landau theory is given as,

$$G(T,M) = G_0 - MH + aM^2 + bM^4 + ... \quad (1.17)$$

Here, the coefficients a and b are temperature dependent parameters. The condition for the minimum free energy in isothermal system, without any external influence can be written as ($\partial G/\partial M = 0$), and it gives rise to,

$$\frac{H}{M} = 2a + 4bM^2 \quad (1.18)$$

According to equation 1.18, a plot of M^2 versus H/M should be a straight line with a positive slope [37]. So, for a second order magnetic phase transition, M^2 versus H/M plot is expected to be a straight line, with a positive slope [38]. The spontaneous magnetization $M_s(0, T)$, the inverse susceptibility $\chi_0^{-1}(T)$ and the isothermal magnetization at the critical temperature $M(H, T=T_C)$ follow the power law behavior as given below [39],

$$M_S(T) \alpha |\varepsilon|^{-\beta} \qquad \varepsilon < 0 \quad (1.19)$$

$$\chi_0^{-1}(T) \alpha |\varepsilon|^{\gamma} \qquad \varepsilon > 0 \quad (1.20)$$

$$M(H, T = T_C) \alpha H^{\frac{1}{\delta}} \qquad \varepsilon = 0 \quad (1.21)$$

Here β, γ and δ are critical exponents corresponding to M_S, χ_0 and isothermal magnetization at T_C and $\varepsilon = (T - T_C)/T_C$ is the reduced temperature. According to Arrott and Noakes [40], the mean-field relation (equation 1.18) can be modified for a more general case as given below,

$$\left(\frac{H}{M}\right)^{\frac{1}{\gamma}} = \frac{(T - T_C)}{T_1} + \left(\frac{M}{M_1}\right)^{\frac{1}{\beta}} \tag{1.22}$$

where, T_1 and M_1 are material dependent constants. For the critical exponent values corresponding to the mean-field model, *i.e.*, $\beta = 0.5$ and $\gamma = 1$, equation (1.22) reduces to equation (1.18).

In the mean-field model (or molecular field model), the magnetic spins interact with one another through a molecular field proportional to the average magnetization. Here, the exchange interaction, J_{ij} between all the spins $\vec{S}_i$ and $\vec{S}_j$ is identical and independent of displacement. This model is appropriate, whenever the interaction is in long range. Chamberlin [41] has proposed the mean-field cluster model to explain the existence of long range interaction in different substances.

For highly anisotropic materials, the critical exponents generally follow the Ising model. This model deals with only one component of the spins. In highly anisotropic materials, a stronger magnetic coupling is seen in one of the components of spin compared to other two components. The γ value corresponding to three dimensional Ising model is 1.25.

Heisenberg model is an isotropic model, where all components of spins play an equal role in magnetic interactions. The magnetic interaction energy between spins $\vec{S}_i$ and $\vec{S}_j$ of atoms present at nearest neighboring positions i and j can be written as $U = -2J(\vec{S}_i \cdot \vec{S}_j)$ where, J is the exchange integral and is related to the overlap of the charge distributions of the atoms *i, j*. Such interaction takes place mostly with nearest neighbor magnetic ions and known as short range interaction.

The list of critical exponents γ, β and δ predicted by different theoretical models are given as follows [39, 42].

3-D Heisenberg model	$\gamma = 1.336$,	$\beta = 0.365$	$\delta = 4.80$
3-D XY model	$\gamma = 1.30$,	$\beta = 0.34$	$\delta = 4.80$

3-D Ising model	$\gamma = 1.241,$	$\beta = 0.325$	$\delta = 4.82$
Mean-field model	$\gamma = 1.00,$	$\beta = 0.50$	$\delta = 3.00$
Tricritical mean-field	$\gamma = 1.00,$	$\beta = 0.25$	$\delta = 5.00$

The above critical exponents are related to each other by the Widom scaling relation [43],

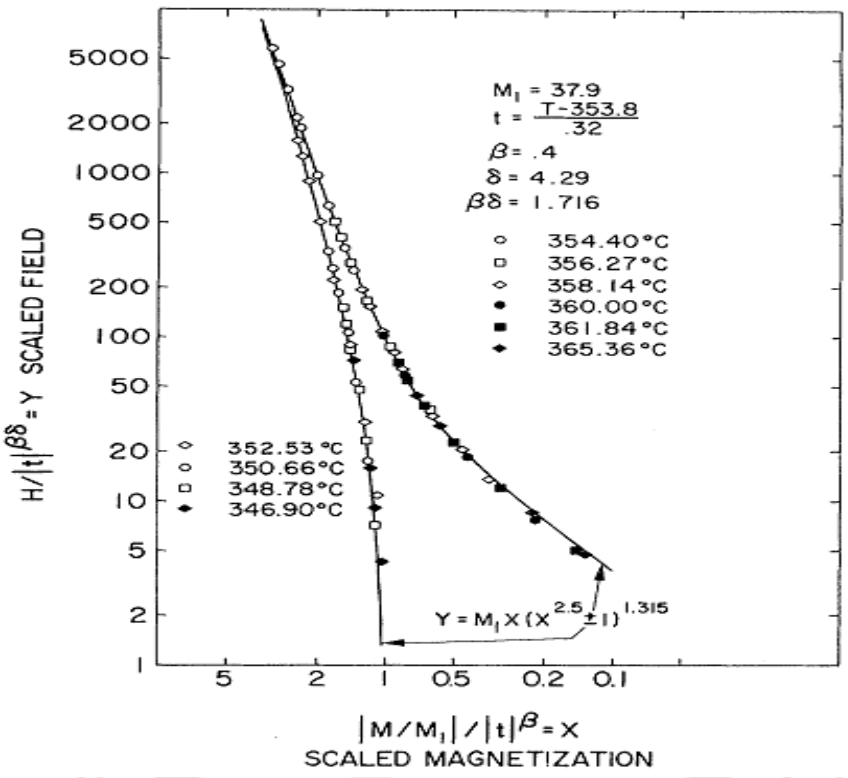

Figure 1.8: Scaling law for nickel sample using the data of Weiss and Forrer. The left side and right side curves correspond to $T < T_C$ and $T > T_C$ respectively. 't' denotes the reduced temperature $\varepsilon = (T - T_C)/T_C$ and M_1 is a constant. (Reproduced from Green *et al.* [44])

$\delta = 1 + \gamma/\beta$ and follow the static scaling hypothesis. The static scaling hypothesis predicts that $M(H, \varepsilon)$ is an universal function of ε and H as given below,

$$M(H,\varepsilon)|\varepsilon|^{-\beta} = f_{\pm}(H|\varepsilon|^{-(\beta+\gamma)}) \qquad (1.23)$$

where, f_+ and f_- are regular analytical functions for $\varepsilon > 0$ and $\varepsilon < 0$, respectively. According

to equation (1.23), plots of $M\ (H,\ \varepsilon)|\varepsilon|^{-\beta}$ versus $H|\varepsilon|^{-(\beta+\gamma)}$ would lead to universal curves, one for temperatures $T > T_C\ (\varepsilon > 0)$ and the other for $T < T_C\ (\varepsilon < 0)$. A typical scaling hypothesis plot for Ni sample reported by Green *et al.*[44] from the experimental data of Weiss and Forrer [45] is shown in Fig. 1.8. They have used the critical exponent values of $\beta = 0.4$, $\gamma = 1.315$ with Curie temperature $T_C = 353.8$ °C.

1.7 Magnetization Reversal

Magnetization reversal (MR) is a phenomenon of change in sign of magnetization for a fixed applied field direction, either due to the change in the magnitude of applied field or temperature. MR was first predicted by Néel in ferrimagnetic material in 1948 [46]. Other than that, MR was reported in canted antiferromagnetic [15, 47-50] and also in ferromagnetic compounds [51] .

Typical *M-T* plot of cobalt vanadate exhibiting MR is shown in Fig. 1.9. According to Menyuk [52], it exhibits a ferrimagnetic transition at T_C = 158 K. On decreasing the temperature, the spontaneous magnetic moment rises rapidly to a broad maximum at T = 139 K, then decreases to zero net moment at a compensation temperature T_{comp}= 70 K. In the presence of small applied field, the net magnetization below 70 K is opposite to the direction of applied field. This complicated magnetic behavior was explained by considering the competing magnetic interactions in Co^{2+}-O^{2-}-Co^{2+} and Co^{2+}-O^{2-} -V^{4+} and V^{4+}-V^{4+} networks.

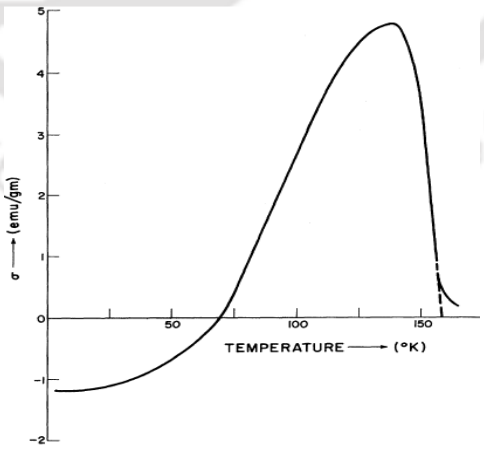

Figure 1.9: Temperature dependence of magnetization of Co_2VO_4 in an external field of 700 Oe [52].

In orthochromite materials, magnetization reversal can occur due to several reasons such as: i) ferrimagnetic ordering between two sublattices, ii) core-shell structure, iii) structural transition, iv) extrinsic effects like weak ferromagnetic clustering or magnetic impurity, v) paramagnetic moments under the influence of negative internal magnetic field and vi) competition between single ion anisotropy and Dzyloshinsky-Moriya interaction. They are briefly discussed as follows:

i) Ferrimagnetic ordering between two sublattices: In ferrimagnetic materials such as spinal oxide, the magnetization reversal was first predicted by Néel [46] due to the different temperature dependences of antiferromagnetically coupled sublattice magnetization. Here one sublattice magnetization may dominate over the other below certain temperature and, vice-versa can happen at higher temperature and, this process can lead to magnetization passing through zero value and changing sign below certain temperature known as compensation temperature (T_{comp}). At T_{comp}, $M \cong 0$.

ii) Core-shell configuration: Manna *et al.* [53] first proposed that the magnetization reversal can be possible in nano structured material due to the presence of core-shell configuration. They have discussed based on magnetization measurement in nano structured $La_{0.20}Ce_{0.80}CrO_3$ material. The core consists of predominant long range AFM due to Cr^{3+} ions along with canted FM component M_{Cr}. In addition to that the core contains paramagnetic moment M_{Ce} due to Ce^{3+} ions under the influence of negative internal field due to AFM ordered Cr^{3+} ions. The shell behaves like a diluted AFM with disordered surface shell magnetization M_{shell}. The net magnetization can be written as $M_{net} = M_{shell} + M_{Cr} - M_{Ce}$, when $T > T_{comp}$ M_{Ce} is weak so the total magnetization is positive but for $T < T_{comp}$, M_{Ce} is more and antiparallel to both M_{shell} and M_{Cr}, so the net magnetization become negative and magnetization reversal is observed.

iii) Structural transition: Nguyen *et al.*[48] have reported that the structure of $LaVO_3$ compound changes from room temperature orthorhombic to low temperature monoclinic by anomalously decreasing the ratio $c/\sqrt{2}\,a$ below certain temperature T = 138 K which produces two different inequivalent crystallographic V site [54]. That gives rise to different

extents of quenching of orbital magnetic moment and make them magnetically inquivalent [55]. This may give rise the magnetization reversal in this compound below 138 K.

vi)) Extrinsic effects: It was proposed by Belik *et al.* [56] in $BiFe_{0.6}Mn_{0.4}O_3$ that presence of magnetic impurity such as Fe-Mn, Fe-Cr and Mn-Cr or sample inhomogeneities or surface effect produces magnetization reversal.

v) Paramagnetic moment under the negative internal magnetic field: In orthochromites $RCrO_3$, when the A site is substituted partially or completely by magnetic rare earth ions, such as Pr, Ce, Yb, Gd, *etc.* the magnetization reversal is observed. The negative internal magnetic field due to the antiferromagnetically (AFM) ordered Cr^{3+} ions and its influence on the substituted ions gives rise to magnetization reversal. By considering the competition between the paramagnetic behavior of substituted ions under the influence of predominant negative internal magnetic field (H_I) due to AFM ordered Cr^{3+} ions and the weak ferromagnetic (FM) component of Cr^{3+} ions, Cook *et al.* [22] proposed the following expression for magnetization,

$$M = M_{Cr} + \frac{C(H + H_I)}{(T - \theta_C)} \qquad (1.24)$$

where M_{Cr} is the canted magnetization due to the Cr^{3+} ions, H_I is the internal magnetic field, $C = x\ C_0$, where C_0 is the Curie constant of substituted ion and x is the substituted element concentration.

vi) Single ion anisotropy and Dzyloshinsky-Moriya interaction: Single ion anisotropy and Dzyloshinsky-Moriya (DM) interaction both produce the canting in the antiferromagnetic materials. YVO_3 compound exhibits distorted perovskite structure due to the titling of VO_6 octahedra and such arrangement gives rise to the canted spin structure. Due to the tilting, the intermediate oxygen ion is not at the inversion center of two V ions and it leads to an antisymmetric interaction known as DM interaction. In addition to that, the tilting of VO_6 and the corresponding staggered V-O bonds lead to the staggering of single ion magnetic anisotropy axis. Ren *et al.* [57] have derived the expression for the net magnetization for H perpendicular to the easy axis by considering the contributions from single ion anisotropy, DM interaction and AFM interaction.

According to them, the net energy of the system is

$$\frac{E}{N} = J\vec{S}_1.\vec{S}_2 + \vec{D}.(\vec{S}_1 \times \vec{S}_2) - 2AS_Z^2 + \frac{E_f}{N} \qquad (1.25)$$

The first term is the Heisenberg exchange interaction with AFM coupling constant J between the two spins $\vec{S}_1$ and $\vec{S}_2$, the second term is due to the DM interaction, and the third term corresponds to single ion magnetic anisotropy with an anisotropy constant, A and the component of spin along the local easy axis, S_Z. The last term does not depend upon the canting angle. By taking θ as a spin canting angle with respect to the easy axis and γ as the canting angle due to single ion anisotropy as shown in Fig 1.10.

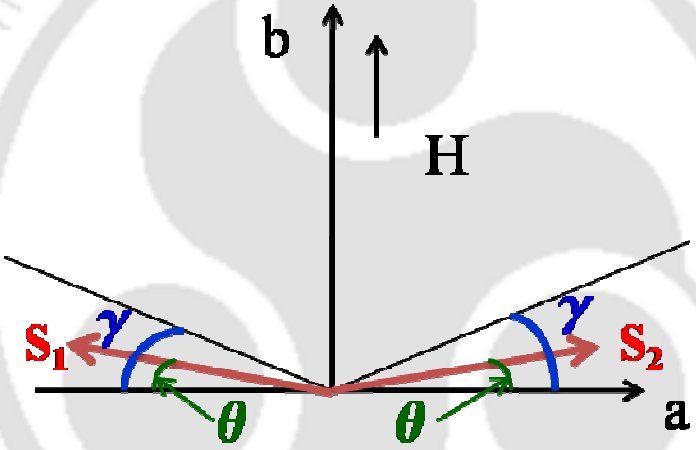

Figure 1.10: The schematic diagram of canting angle.

The equation (1.25) can be written as,

$$\frac{E}{N} = -J\left|\langle S\rangle\right|^2 \cos 2\theta + D\left|\langle S\rangle\right|^2 \sin 2\theta - 2AS^2 \cos^2(\theta - \gamma) + \frac{E_f}{N}$$

By minimizing the energy term and by assuming $\theta - \gamma << 1$ such that sine and cosine functions can be replaced by the first term of the Taylor expansion

$$\theta = \frac{2AS^2\gamma - D\left|\langle S\rangle\right|^2}{2J\left|\langle S\rangle\right|^2 + 2AS^2} \qquad (1.26)$$

By choosing the reduced constants $\xi=\frac{A}{J}$ and $\gamma=\frac{D}{2J}$, the expression for θ becomes

$$\theta=\frac{S^2\xi\gamma-\gamma_D\left|\langle S\rangle\right|^2}{\left|\langle S\rangle\right|^2+S^2\xi} \tag{1.27}$$

The net moment of the canted AFM system ($M_{net}=2Ng\mu_B\left|\langle S\rangle\right|\sin\theta$) by taking $sin\theta \cong \theta$ can be written as

$$M_{net}=2Ng\mu_B\left|\langle S\rangle\right|\frac{S^2\xi\gamma-\gamma_D\left|\langle S\rangle\right|^2}{\left|\langle S\rangle\right|^2+S^2\xi} \tag{1.28}$$

Here $\left|\langle S\rangle\right|=\frac{g\mu_B S(S+1)B}{3k_BT}$ as per the mean field model.

1.8 Exchange Bias

Exchange bias (EB) is a manifestation of anisotropic exchange interaction at the interface between the ferromagnetic (FM) and the antiferromagnetic (AFM) regions [7, 58-61]. Such EB effect is seen as a shift in the magnetic hysteresis loop along the field axis. Exchange bias effect was first observed in core-shell structure of FM Co and AFM CoO in 1956 [35]. The EB effect has been studied in wide variety of hetero-structured systems such as oxidized FM particles, bilayer and multilayer of FM/AFM, FM/Ferrimagnet, FM/spin-glass (SG), *etc* [7]. Bulk materials like binary alloys, intermetallic alloys and oxide materials are also known to exhibit EB [61]. The recent research interest in EB effect is driven by its role on potential applications in magnetic read heads [8] and spintronics devices [11, 62]. EB effect is observed in manganites and cobalites, for example, rare earth doped $CaMnO_3$ [63-66], alkaline earth and transition element doped $LaMnO_3$ [67, 68] and $La_{0.82}Sr_{0.18}CoO_3$ [69].

The shifting of the hysteresis loop can be quantitatively described by the exchange bias field (H_{EB}) using the relation,

$$H_{EB} = \frac{(H_+ + H_-)}{2} \tag{1.29}$$

The effective coercive field, H_c^{eff} can be obtained using the relation,

$$H_c^{eff} = \frac{(H_+ - H_-)}{2} \tag{1.30}$$

Here H_+ and H_- are the field values corresponding to the loop crossing the $M = 0$ axis during the ascending and descending branches of *M-H* loop. The exchange bias effect can be described in presence of field cooled condition by the alignment of AFM spins parallel to the FM spins at the FM-AFM interface. An additional torque comes into picture on FM spins due to the coupling of the AFM and FM spins at the interface. Depending on the strength of the AFM anisotropy, the observed *M-H* loops shows two different characteristic behavior: i) shifting of hysteresis loop along the field axis if the AFM anisotropy is large and ii) hysteresis with large coercivity if the AFM anisotropy is small.

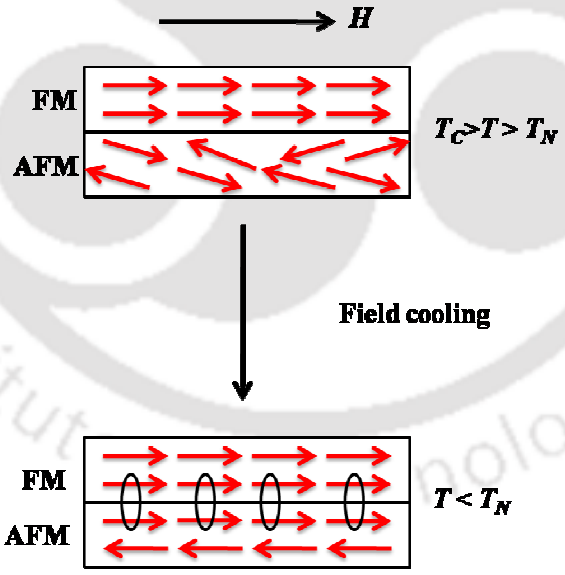

Figure 1.11: Schematic spin configurations of a FM-AFM couple before and after field cooling procedure [60].

Spin configuration of a FM and AFM couple under field cooled condition below T_N is shown in Fig. 1.11. If a magnetic field is applied at a temperature $T_N < T < T_C$, the FM spins

will align along the field direction but the spins in AFM material are in random direction. When the system is cooled through T_N, at FM-AFM interface, spins of FM and AFM interact with each other such that spins of top most layer of AFM adjacent to FM align parallel to the spins of FM while the remaining layers follow the regular antiparallel alignment to fulfill the AFM ordering.

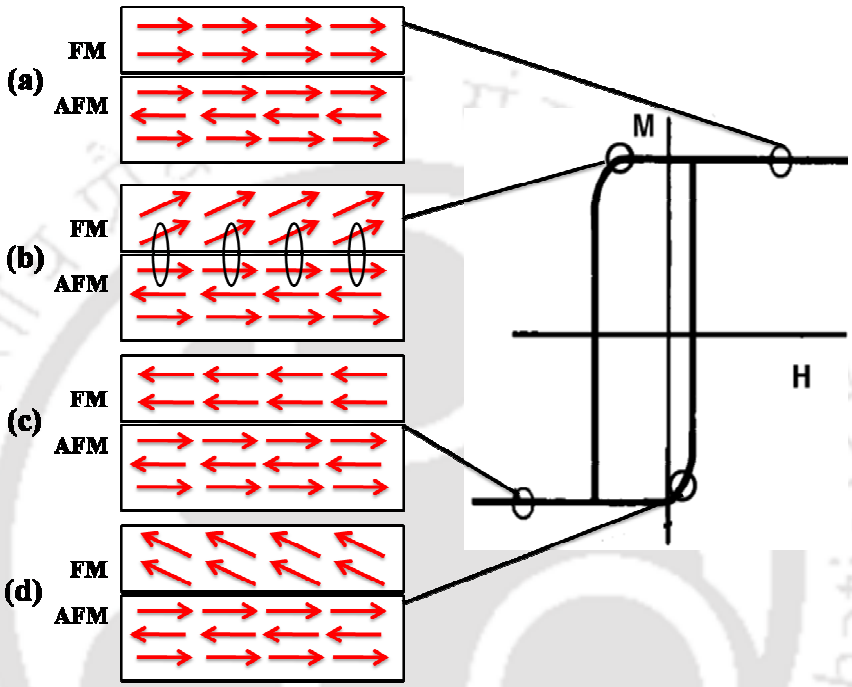

Figure 1.12: Schematic diagram of the spin configuration of an FM-AFM couple at different stages of a shifted hysteresis loop for a system with large AFM magnetic anisotropy [60].

Different stages of hysteresis loop for a system of FM-AFM couple having strong AFM anisotropy is shown in Fig. 1.12. Under field cooled condition, spins of FM and AFM lie parallel to each other at the interface (Fig. 1.12(a)). Upon reversing the magnetic field, the FM spins try to align along the reversed field direction but they are retarded due to the presence of strong AFM anisotropy. So, the FM spins experience microscopic torque due to AFM anisotropy and as a result larger negative field is required to align the FM spins compared to the case of isolated FM substance. Stages (b) and (c) in Fig. 1.12 depict the above behavior. Hence the coercive field in the negative field branch will increase (Fig. 1.12 (c)). On the other hand, while changing the magnetic field in the positive direction the FM spins will align easily along the direction of field as compared to uncoupled FM system and

whatever torque exerted by the AFM spins that will be in the same direction as applied field. Therefore the coercive field in the positive field branch will be reduced (Fig. 1.12 (d)). The net effect will be shifting of the hysteresis loop along the magnetic field axis [60]. In the above process we have considered FM coupling at the interface that gives rise to shifting of *M-H* loop along negative field axis. If the coupling at the interface is AFM, one would expect shifting the loop along positive field axis.

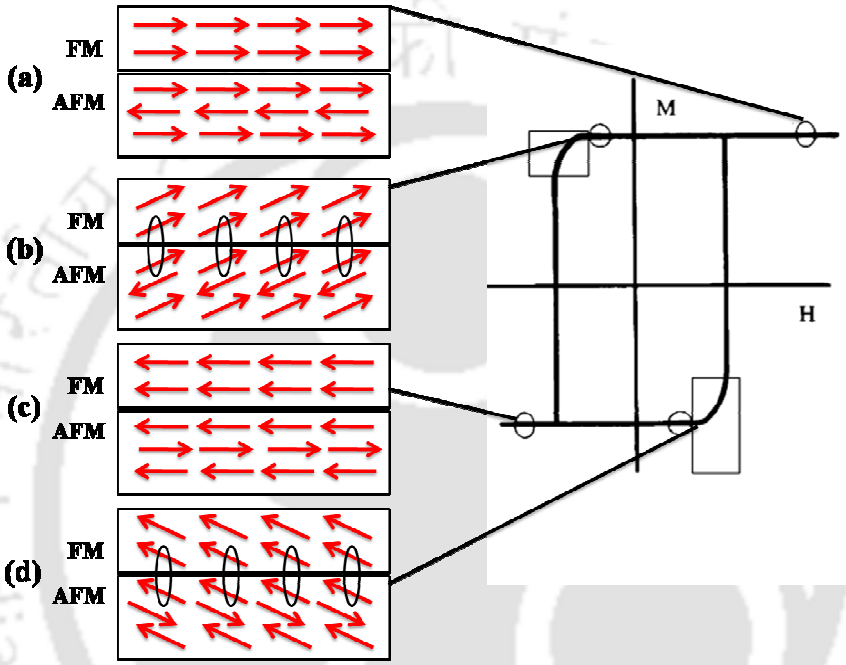

Figure 1.13: Schematic diagram of the spin configuration of an FM-AFM couple at different stages of a shifted hysteresis loop for a system with low AFM magnetic anisotropy [60].

If AFM magnetic anisotropy is low then there is a different situation. After field cooling, the spins of FM and AFM align in the field direction (Fig. 1.13 (a)). While reversing the magnetic field FM spin starts to rotate and also due to the low AFM magnetic anisotropy, the AFM spins also align along the field direction (Fig. 1.13 (b)). The extra energy associated with the creation of an irreversible twist in the AFM structure translates into an enhanced coercivity. Analogous behavior is observed after the saturation in the negative field (Fig. 1.13 (c) and (d)). In this case, although no loop shift is observed, the magnetic field required to reverse magnetization in both positive and negative branches becomes larger, *i.e.* hysteresis

loop becomes broader [60].

In most of the reports, the EB field (H_{EB}) is found to be either positive or negative but the tunable sign reversal of H_{EB} is quite rare [60, 61]. Magnetic field induced sign reversal of H_{EB} has been reported in FeF_2/Fe bilayer [70], Sr_2YbRuO_6 [71], $NdMnO_3$ [72] and $La_{1-x}Pr_xCrO_3$ [73]. The sign of H_{EB} can be reversed by using external parameters like temperature and field. The sign reversal of H_{EB} by varying the temperature was reported in $Sm_{0.975}Gd_{0.025}Cu_4Pd$ [74] and $La_{0.20}Ce_{0.80}CrO_3$ [53].

1.9 Magnetic Materials with Negative Magnetization and Exchange Bias Field

The magnetization reversal as well as tunable exchange bias phenomena has been reported in ferrimagnetic, ferromagnetic and antiferromagnetic materials. They are reviewed as follows

1.9.1 Ferrimagnetic Compounds

As we have already mentioned, the magnetization reversal in ferrimagnetic material was first predicted by Néel [46]. Following the Néel prediction, magnetization reversal in cobalt vanadate [52] with magnetic compensation at T_{comp} = 70 K was also explained. Magnetization reversal in LiFeCr spinels was explained in terms of exchange interaction between the magnetic moments on tetrahedral and octahedral sites and their antiparallel alignment [75]. Magnetization reversal in Prussian blue analogs or molecular magnets such as $[Ni^{II}_xMn^{II}_{1-x}]_{1.5}[Cr^{III}(CN_6)]$ for x = 0.38 to 0.42 and $[Ni^{II}_{0.22}Mn^{II}_{0.60}Fe^{II}_{0.18}]_{1.5}[Cr^{III}(CN_6)].7.6H_2O$ compounds have been studied and they were explained by considering different temperature dependence of sublattices magnetization having positive and negative values [76, 77]. Kageyama *et al.* [78, 79] observed magnetization reversal in $Ni(HCOO)_2.2H_2O$ due to two magnetic sublattices arising out of non equivalent Ni sites in the monoclinic $P2_1/c$ structure and their orientation opposite to each other. Yusuf *et al.* [80] studied the bipolar switching of magnetization in $Cu_{0.73}Mn_{0.77}[Fe(CN)_6].zH_2O$ molecular

magnet. They have observed the positive and negative magnetocaloric effects below its magnetic ordering temperature.

1.9.2 Ferromagnetic Intermetallic Alloys

For the first time, Adachi *et al.* [51] reported the magnetic compensation in ferromagnetic intermetalic alloys of $SmAl_2$. The unique temperature dependence of the total magnetic moment is due to the different temperature dependence of spin moment and orbit moment of Sm^{3+} ions. Kulkarni *et al.* [81] and Venkatesh *et al.* [82] observed the magnetization reversal and tunable exchange bias behavior in $Nd_{0.75}Ho_{0.25}Al_2$ single crystal and in ferromagnetic $Sm_{1-x}Gd_xAl_2$ intermetallic compounds. The reversal in the orientation of magnetic moment of different sub components of rare earth ions and conduction electron polarization gives rise to magnetization reversal.

1.9.3 Antiferromagnets

$LaCrO_3$ is one of the well known perovskite materials having orthorhombic crystal structure at room temperature along with an antiferromagnetic transition around T_N = 290 K. The material with G-type antiferromagnetic structure is also known to exhibit weak ferromagnetism [83]. Ueda *et al.* [84] reported ferromagnetism in $LaFeO_3$-$LaCrO_3$ superlattice structure with T_C around 375 K and the saturation magnetization close to 2 μ_B. Substitution of alkaline earth elements such as Sr and Ca are known to introduce structural transformation from orthorhombic to rhombohedral at room temperature [5, 16, 85, 86]. In addition to that such substitution reduces the antiferromagnetic transition temperature and influences the large change in magnetic hysteresis and related parameters.

A few authors have studied the effect of electron doping in $LaCrO_3$ *i.e.* by doping tetravalent elements like Te or Ce in place of La [87-89]. Te substitution gives rise to two magnetic transitions, *i.e.* antiferromagnetic transition at 282 K followed by low temperature ferromagnetic transition at 105 K. They originate from AFM superexchange interaction in Cr^{3+}-O^{2-}-Cr^{3+} and ferromagnetic interaction in Cr^{3+}-O^{2-}-Cr^{2+} networks respectively. Shukla *et al.* [89] reported the decrease in T_N value from 281.5 K to 257 K with increase in Ce^{3+}

concentration in $La_{1-x}Ce_xCrO_3$ ($0 \leq x \leq 1$). They have observed the interesting negative magnetization for $x \geq 0.8$ samples with T_{comp} = 70 K.

Substitution at La site of $LaCrO_3$ by using other rare earth elements and mostly by magnetic rare earths has been carried out by several researchers [49, 90] and such substitutions have yielded rich magnetic properties like magnetization reversal, exchange bias phenomenon, *etc*. Khomchenko *et al.* [50] observed the negative magnetization along with AFM at T_N = 268 K for $La_{0.75}Nd_{0.25}CrO_3$ compound due to the antiparallel coupling between the paramagnetic moment of Nd^{3+} ion and the moment due to Cr^{3+} ions. The values of spontaneous magnetization and H_C are reported to be around 0.02 μ_B/f.u. and 5.5 kOe at 5 K. Systematic decrease in lattice parameters with Nd substitution has been reported by Chakraborty *et al.* [91].

The negative magnetization has been reported in Pr doped $La_{1-x}Pr_xCrO_3$ with T_{comp} values in the range of 17 K to 230 K for x = 0.10 to 0.80 due to antiparallel coupling between Pr^{3+} and Cr^{3+} moments [49, 92]. The M_{Cr}, H_I and θ values for x = 0.5 sample for H = 20 Oe to 1000 Oe were reported to be 20 emu/mol to 70 emu/mol, -4 kOe to -13 kOe and -7 K respectively. Manna *et al.* [53] have observed the negative magnetization below T_{comp} = 45 K along with tunable exchange bias behavior in nanocrystalline $La_{0.2}Ce_{0.8}CrO_3$ because of the presence of the core-shell structure. Yoshii *et al.* [73] performed a systematic magnetization study in $La_{1-x}Pr_xCrO_3$ series for x = 0.7 to 0.85. A large negative magnetization was observed at ~ 5 K for x = 0.85 sample which is 300 times larger than that of positive magnetization. The M_{Cr} and H_I values for x = 0.85 sample are reported to be in the range of 15 emu/mol to 40 emu/mol and -2.8 kOe to -3 kOe for H = 20 Oe to 2 kOe respectively. The exchange bias behavior was observed for x = 0.85 sample. Sharma *et al.* [90] have observed the magnetization reversal in $La_{0.5}Gd_{0.5}CrO_3$ compound below T_{comp} = 75 K due to the antiparallel coupling between the Gd^{3+} moment and Cr^{3+} moment. The M_{Cr}, H_I and θ values for 100 Oe were reported to be 42 emu/mol, -511 Oe and -0.6 K respectively.

A few authors have studied the substitution of other transition elements in place of Cr in $LaCrO_3$. Azad *et al.* [93] have studied the structural and magnetic properties of $LaFe_{0.5}Cr_{0.5}O_3$ by recording neutron diffraction patterns and temperature dependent magnetization measurements. Antiferromagnetic transition with T_N ~ 265 K along with

negative magnetization for $T \leq 200$ K was reported. The ordered AFM magnetic moment from neutron powder diffraction data was found to be 2.79 (4) μ_B. Vijaynandhini *et al.* [94] reported negative magnetization in $(La_{1-x/2}Bi_{x/2})(Fe_{0.5}Cr_{0.5})O_3$ $(0 \leq x \leq 1)$ with $T_{comp} = 110$ K. Presence of ferromagnetism along with metal-insulator transition have been observed by a few groups in La(Cr, Mn)-O [17, 95-97].

Other than $LaCrO_3$, a few other rare earth chromites such as $GdCrO_3$ and $NdCrO_3$ have been studied in literature. One such report is in the parent compound $GdCrO_3$ by Cook *et al.* [22], where magnetization reversal was explained by considering the antiparallel coupling of the Gd^{3+} and Cr^{3+} ions. The negative internal field H_I and canted FM component of Cr ions M_{Cr} are reported to be 5.5 kOe and 400 emu/mol. Yoshii *et al.* [15] have also observed magnetization reversal with H_I and M_{Cr} values of -1.9 kOe and 100 emu/mol in $GdCrO_3$. Jaiswal *et al.* [98] studied the magnetic, dielectric and Raman spectroscopy of $GdCrO_3$ nanoparticles. They have also observed the magnetization reversal.

$NdCrO_3$ is an orthorhombic perovskite compound having G-type antiferromagnetic structure with Néel temperature $T_N \sim 220$ K and in addition to that it exhibits spin reorientation transition at around $T_{SRT} = 35$ K [99-102]. Troyanchuk *et al.* [103] have studied the magnetic properties of $NdMn_{1-x}Cr_xO_3$ system *i.e.* by substituting Cr for Mn in the composition range $x = 0.0$ to 0.85. For $x = 0.85$, they have observed magnetization reversal at around 160 K and it has been explained in terms of two sublattice model involving Nd ions and transition element (Mn/Cr) ions. Liu *et al.* [104] studied the structural, electrical and thermal expansion properties of Sr doped $NdCrO_3$. With increase in Sr concentration, unit cell volume decreases, on the other hand electrical conductivity and thermal expansion coefficient increases. Samantaray *et al.* [105] and Hong *et al.* [72] observed the magnetization reversal in $NdMnO_3$ below 13 K because of antiferromagnetic coupling between Nd^{3+} and Mn^{3+}.

Low temperature spin reorientation transition has been also reported in $TmCrO_3$ and $SmCrO_3$ [106, 107]. $YbCrO_3$ is one of the interesting compounds having strong anisotropic exchange interaction between the Cr^{3+} and Yb^{3+} ions. The presence of one *4f* hole in the Yb^{3+} ion, and the spreading of *4f* orbital give rise to a strong anisotropic exchange interaction in $YbCrO_3$. Su *et al.* [108] reported the magnetization reversal below $T_{comp} = 18.3$ K and

antiferromagnetic transition at 118 K. They have explained magnetization reversal by considering the paramagnetic effect of $Yb^{3+}$and its antiparallel coupling with the Cr^{3+} ions. Magnetization reversal along with two compensation temperatures one at 28 K and another 6.7 K was reported in $TmCrO_3$ [109]. The magnetization reversal was reported to be due to the antiparallel coupling between the Tm^{3+} and the Cr^{3+} ions. The second compensation temperature is due to the spin reorientation of Cr^{3+} from G_yF_z to the mixture of G_yF_z and G_zF_x. Yin *et al.* [110] reported the magnetization reversal, bipolar magnetization switching and, both normal and inverse magnetocaloric behavior in $x = 0.1$ and 0.5 samples of $SmCr_{1-x}Fe_xO_3$ ($0 \leq x \leq 0.5$) series.

Magnetization reversal and exchange bias behavior in $YFe_{0.5}Cr_{0.5}O_3$ was interpreted in terms of competition between the single ion anisotropy and DM interaction [111, 112]. At $T > T_{comp}$, DM interaction dominates so positive EB was observed and for $T < T_{comp}$, single ion anisotropy dominates so negative EB was observed. Dasari *et al.* [113] have quantitatively explained the magnetization in $YFe_{1-x}Cr_xO_3$ compound based on detailed theoretical calculation involving the competition between the Fe-Fe, Cr-Cr pairs versus the Fe-Cr pair induced by the DM interaction.

Interesting magnetic behaviors have been reported in a few orthovanadates. Shirakawa *et al.* [114] studied the anomalous diamagnetism in $LaVO_3$ compound and observed the structural transformation from cubic to orthorhombic around T_{comp}. Mahajan *et al.* [55] investigated the magnetic property of $LaVO_3$ and explained the observed magnetization reversal around 139 K by considering the inequivalent magnetic sites of V^{3+} ions and the quenching of their orbital magnetic moments at different extent. Nguyen *et al.* [48] also explained the magnetization reversal in $LaVO_3$ below 138 K. Ren *et al.* [47, 57] observed the magnetization reversal in YVO_3 below 95 K due to the competition between single ion anisotropy and DM interaction. $SmVO_3$ and Ca doped $NdVO_3$ compounds show the magnetization reversal and they were explained by considering the molecular field theory [115-117]. Tung *et al.* [118] proposed the presence of low temperature random spin along with infinite AFM networks in RVO_3 compounds (R = La, Y, Nd, Sm, Gd and Er) to explain the finite coercivity.

Singh *et al.* [71] reported magnetization reversal below T_{comp} = 33.5 K as well as exchange bias in Sr_2YbRuO_6, where Yb and Ru both are magnetic elements. They have explained exchange bias on the basis of three components: i) residual ferromagnetism from Ru, ii) residual magnetization from Yb moment and iii) reorientation in Ru and Yb moments triggered by DM interaction.

1.10 Motivation

During the beginning of my PhD work, as per the literature summary it was found that orthochromites show very interesting magnetic properties such as magnetization reversal and exchange bias phenomenon. In $LaCrO_3$, most of the reports were devoted to substitution at rare earth site. In order to look for magnetization reversal and to understand the mechanism, we have taken up transition element doping at Cr site. Moreover, $NdCrO_3$ is an interesting orthochromites having magnetic rare earth element. To our knowledge, the work on transition element doping at Cr site is limited and the magnetization reversal has not been studied in detailed. These compounds are very interesting due to the isoelectronic configuration of Cr^{3+} and Mn^{4+} ions. The Mn^{4+} ions are known to play a major role in colossal magneto resistive materials such as alkaline earth doped $LaMnO_3$ [2]. In order to understand the crystal structure and magnetic properties of the above two systems, we have taken up the preparation of transition elements (Fe, Mn) doped La-Cr-O and Nd-Cr-O based orthochromites and as well as Ce doped $LaCrO_3$ samples.

Five series of samples were prepared for the present thesis work

i. $LaCr_{1-x}Fe_xO_3$ (x = 0.0 to 1.0)
ii. $LaCr_{1-x}Mn_xO_3$ (x = 0.0 to 1.0)
iii. $NdCr_{1-x}Fe_xO_3$ (x = 0.0 to 1.0)
iv. $NdCr_{1-x}Mn_xO_3$ (x = 0.0 to 0.7)
v. $La_{1-x}Ce_xCrO_3$ (x = 0.0 to 0.20)

The first four series deal with Cr site doping with transition elements and the last series deals with Ce doping at La site. Here two parent compounds $LaCrO_3$ and $NdCrO_3$ have been taken for substitutional studies, the former one contains non-magnetic rare earth ion and

the latter one contains magnetic rare earth ion. The main goal is to study the crystal structure and magnetic properties to understand the magnetic interactions between Cr and other transition elements (Fe and Mn) as well as between Cr and Nd ions.

The above samples were characterized by using X-ray diffraction (XRD) patterns, Scanning electron micrographs (SEM) and Energy-dispersive X- ray Analysis (EDAX). To determine the crystal structure, XRD patterns were recorded at room temperature by using the Rigaku make TTRAX III diffractometer. To understand the magnetic properties of these samples we have studied the dc magnetization as a function of temperature and field by using a Lakeshore make Vibrating sample magnetometer of model no. 7410.

The transition elements (Fe and Mn) doped La-Cr-O based compounds show the magnetization reversal and tunable exchange bias behavior at around compensation temperature. The transition elements doped Nd-Cr-O exhibit the large magnetization reversal along with higher magnetic compensation temperature. In addition to that Nd-Cr-O series exhibit spin reorientation at low temperature. The magnetic properties of Ce doped La-Cr-O based compound are explained in terms of short range double exchange FM interactions.

Chapter 2

Experimental Techniques

Chapter 2: Experimental Techniques

Different types of experimental facilities were used during the course of my research work. It is essential to understand the working principle of these instruments in order to handle them properly, record the data efficiently and accurately such that maximum information can be extracted by appropriate analysis. Experimental techniques that were followed during the material preparation, structural characterization, magnetic measurements, microstructural characterization, *etc*. are discussed in this chapter. In this thesis work, samples were prepared by the standard sol-gel technique followed by annealing at different temperatures using different type of furnaces such as homemade and commercial models. Samples have been characterized by using various techniques: X-ray diffractometer (XRD) to record diffraction pattern for studying crystal structure and phase purity; Vibrating sample magnetometer (VSM) to measure temperature and field variations of magnetization for studying the magnetic properties, Scanning electron microscope (SEM) to study the microstructural morphology and Energy Dispersive X-ray Spectroscopy (EDS) to carry out compositional analysis. They are discussed in detail as follows.

2.1 Sample Preparation

In general polycrystalline samples are prepared by solid state or sol-gel routes. But at room temperature solids (in atomic scale) do not react with each other due to the lack of diffusion between the constituent elements, so the heat treatment is needed to overcome the kinetic barriers. Before starting the heat treatment, samples are pressed in pellet form for good contact between the particles. Heat treatment was done for several days and it was repeated to get good homogeneity throughout the sample. Heat treatment can be divided into two stages: presintering and sintering. The starting materials are usually single cation oxides, carbonates, nitrates or hydroxides which decompose to form oxides when heated. This is called presintering.

The sintering process mainly reduces the total interfacial energy. The total interfacial energy of compact powder can be express as γA where γ is the specific surface (interface) energy and A is the total surface (interface) area of the compact powder. The change in the interfacial energy can be written as [119]

$$\Delta(\gamma A) = A\Delta\gamma + \gamma\Delta A$$

where the reduction of interfacial energy $\Delta\gamma$ is due to the densification and the reduction of the area is due to the expansion of grain size. In the solid state route, the replacement of solid/vapour interface by solid/solid interface gives the reduction of the interfacial energy. The schematic diagram of the sintering process is shown in Fig. 2.1

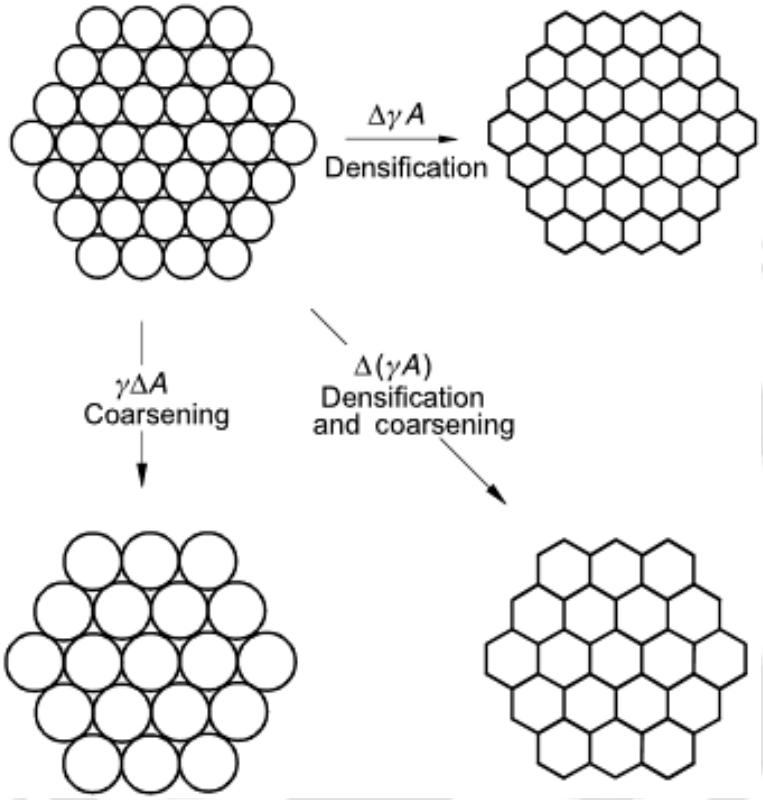

Figure 2.1: Different stages of sintering process [119].

The sintering process depends on the two types of variables: material variable and process variable. Material variable is related to the chemical composition of the material, powder size, powder shape, degree of powder agglomeration, *etc.* and such variables control the nature of grain growth and densification of the materials. The other variable is related to the sintering process such as temperature, time, heating and cooling rate of the samples, *etc.*

In this thesis work, the samples were prepared mainly by sol-gel technique.

The samples were prepared from the following starting compounds such as, lanthanum oxide (La_2O_3, 99.9 %), neodymium oxide (Nd_2O_3, 99.9%), chromium nitrate ($Cr(NO_3)_3.9H_2O$, 98%), ferric nitrate ($Fe(NO_3)_3.9H_2O$, 99%), manganese acetate ($C_4H_6MnO_4.4H_2O$, 99.5%) and cerium nitrate ($Ce(NO_3)_3.6H_2O$, 99.99%).

The starting compounds as per stoichiometric ratio were weighed using an electronic balance supplied by Mettler Toledo model no. AG135 with an accuracy of ± 0.01 mg. They were dissolved in either nitric acid or distilled water to convert them into metal nitrates. Excess amount of citric acid was added to the solution to convert them into citrate form, since citric acid is a chelating agent which can bind up only metal ions and remove the non metallic ions. By adding ethylene glycol, the solution was converted into dense gel form. The heating of gel using a hot plate gives rise to sudden combustion with an evolution of fumes and the final product is a fine powder. These precursor powders were presintered at 600 ˚C for 12 h. These powders were pressed into pellets by using 13 mm cylindrical die and a hydraulic press supplied by Techno Search instruments, Thane, India with a maximum load of 6 Ton/cm^2. The final sintering in cylindrical pellet form was carried out at 1100 ˚C for 24 h for all the samples. The advantages of sol-gel technique are as follows: (1) In sol-gel technique, the mixing of the starting materials at the molecular level is possible due to the dispersion of the materials in a solvent. (2) Dopant elements are evenly dispersed to achieve uniform doping on a molecular level. (3) The required temperature for sintering is relatively small compared to the case of solid state route and the diffusion of components is in the nanometer range.

2.2. High Temperature Furnaces

High temperature furnaces were used for material preparation. Homemade muffle furnaces with a maximum operating temperature of 1200 ˚C and commercial high temperature furnaces with the maximum operating temperature of 1400 ˚C were used for sintering the samples. The commercial furnaces were supplied by N. R. Enterprises and Bysakh & Company, Kolkata, India. The furnace supplied by N. R. Enterprises was powered by a thyristor unit of 30 A rating. The temperature was controlled using Honeywell make PID programmable temperature controller model no. DC 1040 with 16 segment programming feature. The platinum versus platinum-rhodium (Platinum + 10 % Rh) thermocouple was used for sensing the temperature. The heating elements were based on Si-carbide rods.

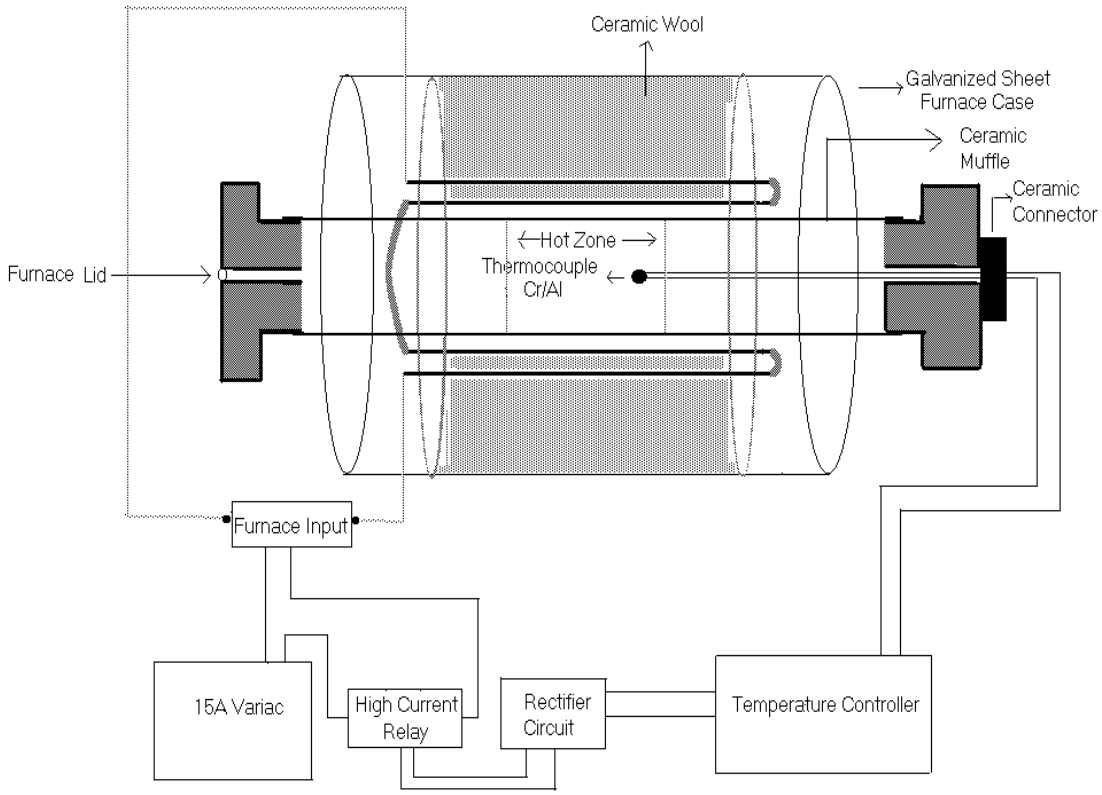

Figure 2.2: Block diagram of the furnace with maximum operating temperature of 1200 ˚C.

The temperature was controlled to an accuracy of ± 1 ˚C. The furnace could be operated up to a maximum temperature of 1400 ˚C. The other furnace supplied by Bysakh & Co. contains (1) a thyristor unit with a rating of 35 A, (2) a PID programmable temperature controller (model no. PRC-300) with 16 segment programming feature, (3) a platinum versus platinum-rhodium (Platinum + 13 % Rh) thermocouple wire and (4) Si-carbide rods based heating elements. The maximum operating temperature is 1450 ˚C.

The homemade furnace (1200 ˚C) was fabricated using a cylindrical alumina muffle with an inner diameter of 5.8 cm and 50 cm length. Six Si-carbide rods of 45 cm length each are used as heating element. The muffle loaded with heating elements is housed in a cylindrical container of 50 cm diameter and 50 cm length and it is made up of galvanized aluminum sheet. High temperature ceramic bricks and ceramic wools are used as thermal insulation. Chromel-Alumel (Cr-Al) thermocouple and a commercial on/off type temperature controller are being used for temperature measurement and controlling. The input power to the furnace is regulated using a variac (dimmerstat) of 15 A capacity. An external on/off

relay (15 A capacity) controls the power supply to the heater wire. The relay is triggered using the temperature controller. The block diagram of the furnace is shown in Fig. 2.2. The furnace could be operated up to a maximum temperature of 1200 ˚C. The temperature could be controlled with an accuracy of ± 5 ˚C.

2.3 X-Ray Diffraction

To know the crystal structure and the phase purity of prepared samples powder X-ray diffraction (XRD) technique is used. XRD patterns were recorded at room temperature by using Rigaku make TTRAX III (Theta Theta Rotating Anode X-ray) Diffractometer by employing Cu-Kα radiation of wavelength λ = 1.5406 Å. The X-ray generator was maintained around 55 kV voltage and 220 mA current to produce X-rays. The powder x-ray diffraction based on the principle of Bragg-Brentano geometry is used as shown in Fig. 2.3. Both X-ray generator and detector are placed at equidistance from the sample holder. The scanning was done from 20˚ to 70˚ in 2theta angle with a scan speed of 3˚/min and the step size was maintained around 0.005˚ to 0.03˚.

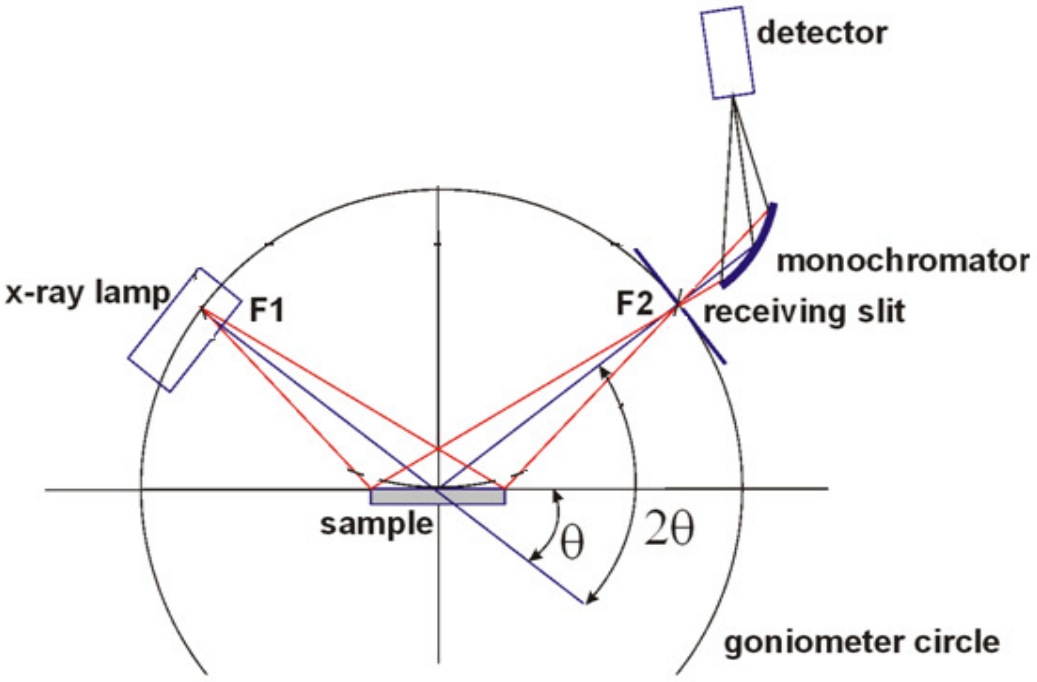

Figure 2.3: Ray diagram of X- ray diffractometer

XRD patterns were refined by Rietveld technique and using Fullprof software. The background was refined using a polynomial function. Pseudo-Voigt function was chosen for peak shape refinement. The global parameters, such as coefficients of background polynomial, scaling factor, half width parameters (*u*, *v*, *w*) and lattice parameters (*a, b, c*) were mainly varied during the refinement. In addition to that nuclear structure variables such as fractional atomic co-ordinates (*x*, *y*, *z*), isotropic displacement (temperature) parameters and occupancy values were varied. Here, occupancy is the chemical occupancy normalized to the multiplicity of the general position of the group. The occupancy of oxygen was taken as 1 for all the refinements and it was not varied during the refinement. The quality of the refinements are known based on the values of reliability factors such as, R_p, R_{wp}, R_{exp}, R_{Bragg}, R_F and χ^2 and they are defined as follows [120].

Profile factor,
$$R_p = 100\frac{\sum_{i=1,n}\left|y_i - y_{c,i}\right|}{\sum_{i=1,n} y_i} \quad (2.1)$$

Here y_i is the observed point (experimental) and $y_{c,i}$ is the calculated point and n represents the number of data points.

Weighted profile factor,
$$R_{wp} = 100\left[\frac{\sum_{i=1,n}\omega_i\left|y_i - y_{c,i}\right|^2}{\sum_{i=1,n}\omega_i y_i^2}\right]^{1/2} \quad (2.2)$$

Here $\omega_i = \frac{1}{\sigma_i^2}$, σ_i^2 is the variance of observation y_i.

Expected weight factor,
$$R_{\exp} = 100\left[\frac{n-p}{\sum_{i=1,n}\omega_i y_i^2}\right]^{1/2} \quad (2.3)$$

Here $(n - p)$ is the number of degrees of freedom. n is the total number of experimental points and p is the number of refined parameters.

Reduced chi-square, $$\chi^2 = \left[\frac{R_{wp}}{R_{\exp}}\right]^2 \quad (2.4)$$

Bragg factor, $$R_B = 100\frac{\sum_h \left|I_{obs,h} - I_{calc,h}\right|}{\sum_h I_{obs,h}} \quad (2.5)$$

Here h represents the particular hkl Bragg peak. The $I_{obs,h}$ is the observed integrated intensities and $I_{calc,h}$ is the calculated intensities.

Crystallographic R_F factor, $$R_F = 100\frac{\sum_h \left|F_{obs,h} - F_{calc,h}\right|}{\sum_h F_{obs,h}} \quad (2.6)$$

Here $F_{obs,h}$ and $F_{calc,h}$ are the observed and calculated structural factors respectively.

2.4. Scanning Electron Microscope (SEM)

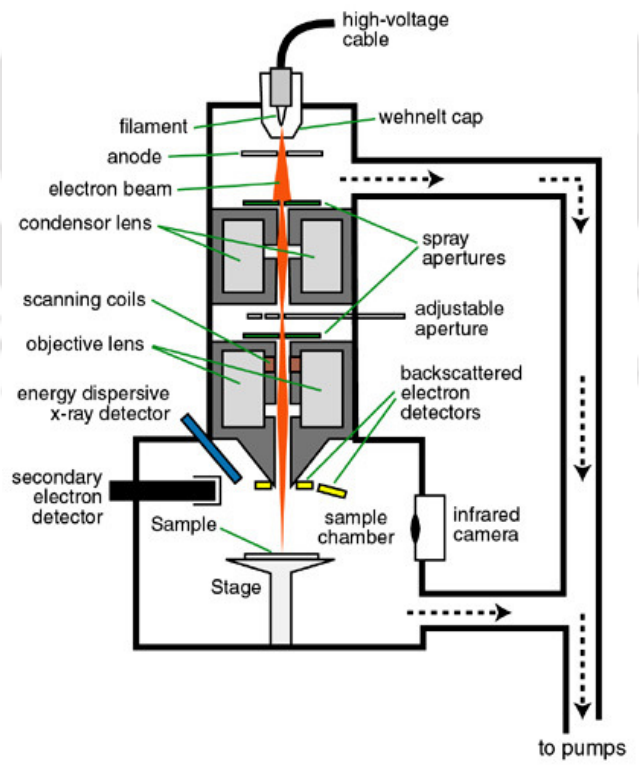

Figure 2.4: Schematic view of scanning electron microscope.

Recording of microstructural images and compositional analysis have been carried out by using LEO Scanning Electron Microscope (SEM, Leo 1430VP) equipped with Oxford energy dispersive spectrometer (EDS). Basic principles of SEM and EDS analysis are given briefly as follows.

The scanning electron microscope (SEM) is a type of electron microscope that uses electrons to form an image of objects and to study surface morphology, fractured components, foreign particles and residues, *etc*. The schematic view of SEM is shown in Fig. 2.4. The thermionically emitted electrons from a tungsten filament are drawn towards anode and were focused by two successive condenser lenses into a beam with a narrow spot size (~ 50 Å). The shorter wavelength of electrons permits image magnifications of up to 100,000 times in SEM. Pair of scanning coils located at the objective lens deflect the beam either linearly or in raster fashion over a rectangular area of specimen surface.

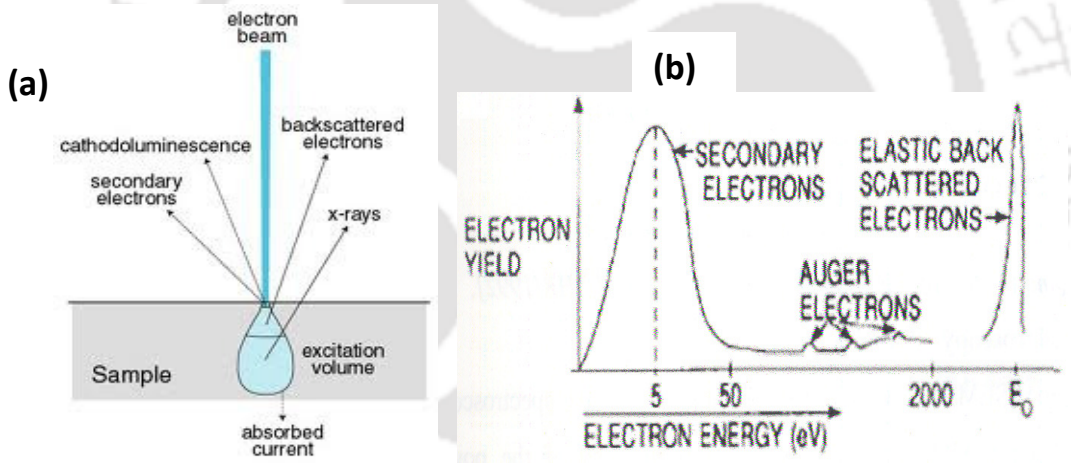

Figure 2.5: (a) Electrons and photons signals emanating from tear-shaped interaction volume during electron beam impingement on specimen surface, and (b) Energy spectrum of electrons emitted from the specimen surface.

These primary bombarding of electrons on the surface of the specimen dislodge electrons from the specimen. Fig. 2.5 shows the interaction of electrons with the surface of the sample. Upon electron impingement on the surface, the interaction volume assumes a tear shape. These dislodged electrons are known as secondary electrons which are attracted and collected

by a positively biased grid or detector and then translated into signals. These signals are then amplified, analyzed, and translated into images of the topography being inspected.

Apart from secondary electrons, the back scattered electrons (BSE), characteristic X-rays, light (cathode-luminescence), specimen current and transmitted electrons are produced by SEM. These types of signal require specialized detectors and all such detectors are not present in a single machine. The primary electron beam results in the emission of BSE from the specimen. BSE possess more energy than secondary electrons and have a definite direction. As such, they cannot be collected by a secondary electron detector, unless the detector is directly in their path of travel. All emissions above 50 eV are considered to be BSE. BSE imaging is useful in distinguishing one material from another, since the yield of the collected BSE increases monotonically with the specimen's atomic number Z (~ 0.05 $Z^{1/2}$). Backscattered imaging can distinguish elements with atomic number difference of at least 3.

Energy dispersive X-ray spectroscopy (EDS, EDX or EDXRF) is an analytical technique used for the elemental analysis or chemical characterization of a sample. Its characterization capabilities originate from the fact that each element has a unique atomic structure, which emits its unique characteristic X-ray. To stimulate the emission of characteristic X-rays from a specimen, a high energy beam of charged particles such as electrons or protons, or a beam of X-rays, is focused into the sample being studied. At rest, an atom within the sample contains ground state (or unexcited) electrons in discrete energy levels or electron shells bound to the nucleus. The incident beam may excite and eject an electron from an inner shell and it results in a hole or electron vacancy in the shell. An electron from an outer higher-energy shell then fills the hole, and the difference in energy between the higher-energy shell and the lower energy shell is released in the form of an X-ray. The atoms of every element releases X-rays with unique amounts of energy during the above process. Thus, by measuring the value of energy of X-rays being released by a specimen during electron beam bombardment, the identity of the atoms present in the specimen can be established. Thus, we get the EDS spectrum as an output and it is just a plot of how frequently an X-ray is received for each energy level. An EDS spectrum normally displays peaks corresponding to the energy levels for which the X-rays had been received.

Each of these peaks is unique to an atom, and therefore corresponds to a single element. The intensity of the peaks depends on the concentration of the elements present.

In the present work, a thin solid pellet was mounted on carbon coated tape. In case of conducting sample, the direct SEM and EDS measurements could be carried out without any metal coating. But our samples are semiconductor so, the electrons will get trapped in the surface and creates charge segregation which will not allow the further bombardment of electrons, and hence the electrons cannot reach the detector. So a coating of metal layer serves our purpose.

2.5. Vibrating Sample Magnetometer (VSM)

DC magnetization as a function of temperature and field was measured by using the Lakeshore make Vibrating sample magnetometer (VSM) (model no. 7410).

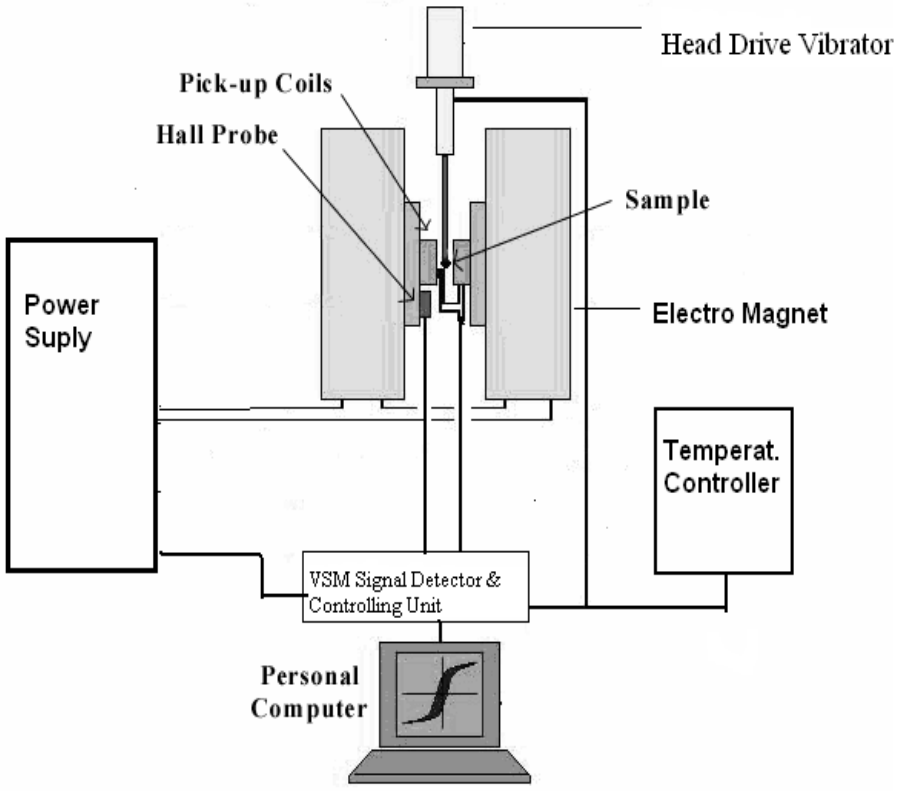

Figure 2.6: Block diagram of the vibrating sample magnetometer.

The vibrating sample magnetometer (VSM) has become a widely used instrument for measuring the magnetic properties of a large variety of magnetic materials. The vibrating sample magnetometer (VSM) developed originally by Foner [121] has however, been the most successful for low temperature and high magnetic field studies of most of the magnetic materials. It has a flexible design and combines high sensitivity with ease of sample mounting and exchange. Samples can be changed rapidly even at any operating temperature. Using a vibrating sample magnetometer, one can measure the DC magnetic moment as a function of temperature, magnetic field and time. So, it allows performing susceptibility and magnetization studies. Magnetic moments as small as 5×10^{-5} emu are measurable with a VSM [121].

The temperature variations of zero field cooled (ZFC) and field cooled (FC) magnetization (M) were measured by using the Lakeshore, model no. 7410 vibrating sample magnetometer. The temperature variation down to 25 K was achieved using an OXFORD make CCR cryostat (model X 74019-044) along with the temperature controller. The magnetic field was produced by using a 10 $^{//}$ electromagnet. The magnetization loop was measured by varying B up to 1.5 T. Calibration of the vibrating sample magnetometer was done by measuring the magnetic moment of a standard pure Ni sample. Block diagram of the vibrating sample magnetometer is shown in Fig. 2.6.

The VSM is based upon Faraday's law, according to which an emf is induced in a conductor by a time-varying magnetic flux. If a sample of any magnetic material is placed in a uniform magnetic field, a dipole moment will be induced. If the sample vibrates with sinusoidal motion, there is some magnetic flux change. This induces a voltage in the pick-up coils, which is proportional to the magnetic moment of the sample. Voltage, $V(t)$ can be detected to a high resolution and accuracy by means of suitable VSM signal detector (*e.g.* Lock in Amplifier).

Chapter 3

$LaCr_{1-x}M_xO_3$ (M = Fe and Mn) series

Chapter 3: $LaCr_{1-x}M_xO_3$ (M = Fe and Mn) series

$LaCrO_3$ is one of the important perovskite chromites which exhibits G-type antiferromagnetic (AFM) transition around 290 K along with a weak ferromagnetism due to spin canting [14, 16, 83, 84]. The interest in this series is not only due to its high electrical conductivity at elevated temperatures and its corresponding application as an electrode material in solid oxide electrolyte fuel cell [5, 6, 85, 88, 91, 122] but also due to the fact of isoelectronic configuration of Cr^{3+} and Mn^{4+} ions. The Mn^{4+} ions are known to play a major role in colossal magneto-resistance materials such as alkaline earth doped $LaMnO_3$ [2]. $LaCrO_3$ is known to exhibit magnetization reversal (MR) when La is partially or completely replaced by magnetic rare earth ions: Pr, Ce, Yb and Gd [15, 49, 53, 73, 90, 92, 108]. Azad *et al.* [93] have shown negative magnetization in $LaCr_{0.5}Fe_{0.5}O_3$ under the field cooled condition. The magnetization reversal (MR) in Bi and Fe doped $LaCrO_3$ was interpreted in terms of probable interaction between two types of weak ferromagnetic (FM) clusters in antiferromagnetic (AFM) matrix [94]. The work on Fe or Mn doping in the Cr site is limited. In order to understand the crystal structure and magnetic properties, we have prepared Fe and Mn doped $LaCrO_3$ compounds. These materials show interesting magnetic properties such as magnetization reversal, tunable exchange bias behavior, antiferromagnetic transition, ferromagnetic transition, *etc.*

3.1 $LaCr_{1-x}Fe_xO_3$ compounds (x = 0.0 to 1.0)

This section deals with the effect of Fe substitution at Cr site of $LaCrO_3$. The preparation, characterization and the result obtained from the dc magnetization along with the analysis are presented.

3.1.1 Sample Preparation and Characterization

Polycrystalline samples of $LaCr_{1-x}Fe_xO_3$ (x = 0.00, 0.05, 0.10, 0.15, 0.20, 0.30, 0.45, 0.50, 0.60, 0.70 and 1.00) were prepared by the standard sol-gel route. High purity (99.9 %) La_2O_3, $Cr(NO_3)_3.9H_2O$ and $Fe(NO_3)_3.6H_2O$ were taken as starting materials as per the stoichiometric ratio. Uniform mixture of the stoichiometric ratio of the starting compounds

was obtained by dissolving them either in nitric acid or distilled water. Excess amount of citric acid was added to convert them into citrates. By adding ethylene glycol and slow evaporation, the uniform solution was converted into a gel. On further heating the gel fine precursor powder was obtained. The powder was presintered at 600 ˚C for 12 h and the final sintering in pellet form was carried out at 1100 ˚C for 24 h.

The parent compound and all the Fe doped $LaCrO_3$ compounds are found to be in single phase form as per the XRD patterns. The XRD patterns for x = 0.00 to 1.00 are shown in Fig. 3.1. We can clearly see the shifting of (112) peak position towards lower 2θ value for $x > 0.20$ samples as shown in Fig. 3.2. No appreciable shifting of (112) peak is observed for $x \leq 0.20$. The XRD patterns of all samples were successfully refined by taking *Pbnm* space group in orthorhombic cell. The typical XRD pattern along with Rietveld refinement for x = 0.20 and 0.60 samples are shown in Fig. 3.3. The room temperature lattice parameters, reliability factors and unit cell volume are given in Table 3.1. We can see that the lattice parameters increase systematically with increase in Fe concentration and this can be easily explained in terms of Fe^{3+} ions (0.645 Å) having larger ionic radii replacing the Cr^{3+} (0.615 Å) ions. Thus the doped Fe^{3+} ions indeed get substituted at Cr sites.

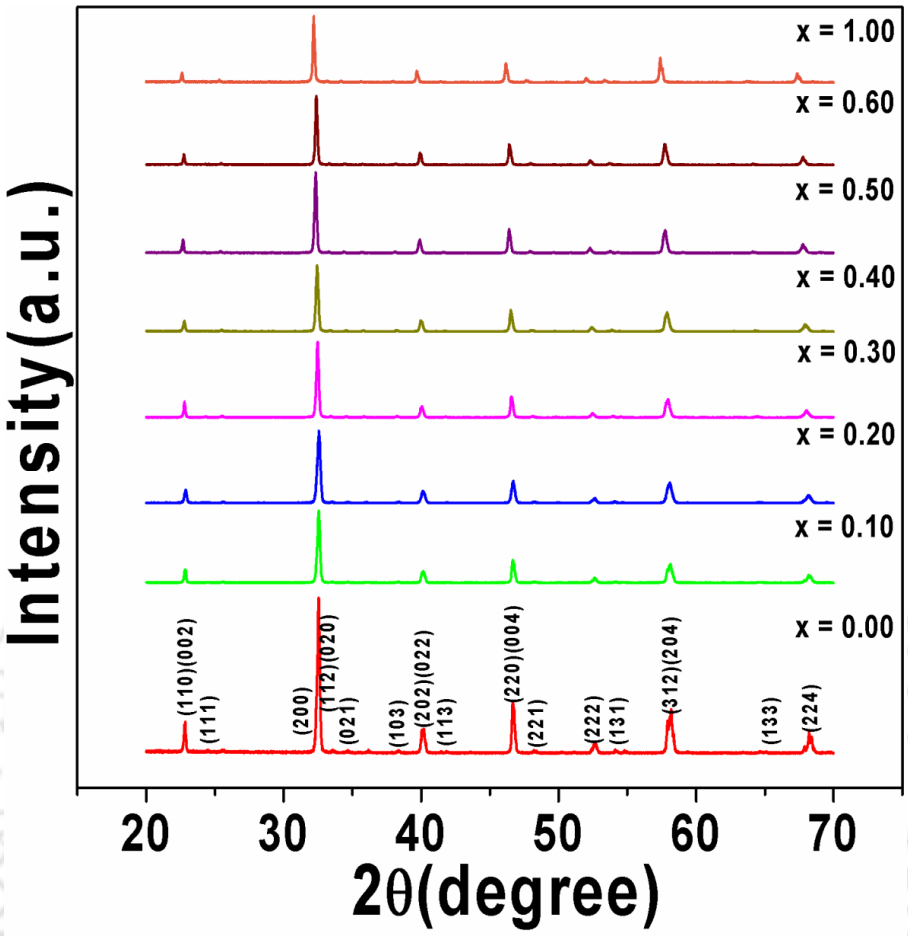

Figure 3.1: XRD patterns of $LaCr_{1-x}Fe_xO_3$ compounds for x = 0.00 to 1.00.

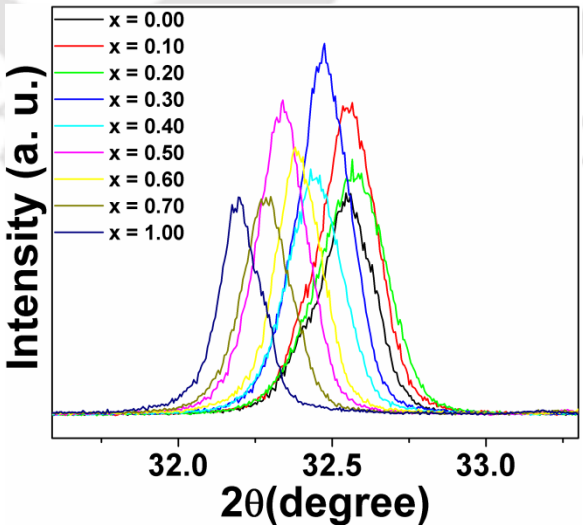

Figure 3.2: Expanded view of (112) peak of XRD patterns for $LaCr_{1-x}Fe_xO_3$ samples.

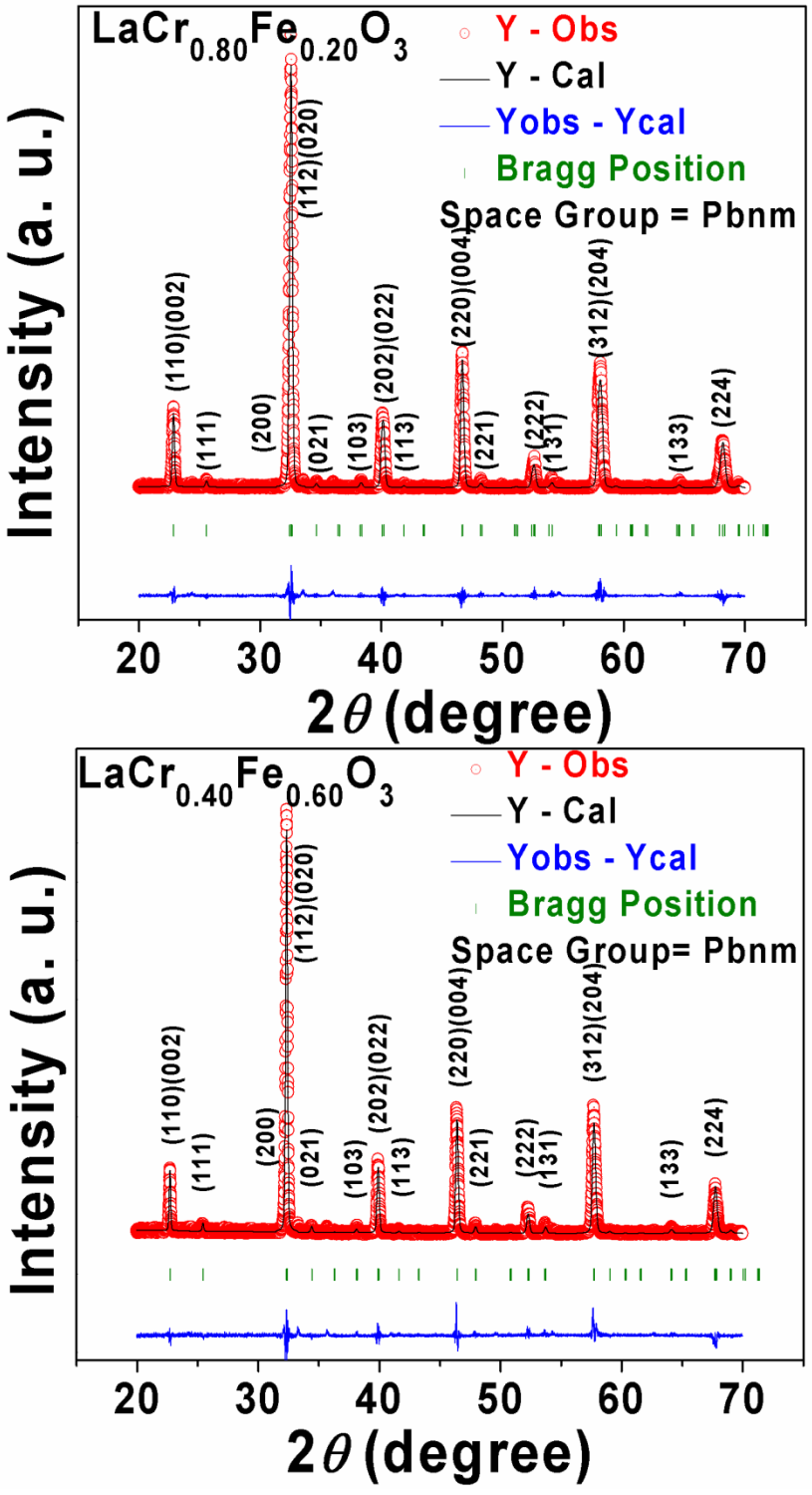

Figure 3.3: XRD patterns along with Rietveld refinement for x = 0.20 and 0.60 samples. The circles represent experimental data and solid line represents Rietveld refined data. The bottom line shows the difference between experimental and refined data. The marked 2θ positions are allowed Bragg peaks.

Table 3.1: Parameters obtained from the Rietveld analysis of XRD patterns for the samples $LaCr_{1-x}Fe_xO_3$ (0.00 to 1.00). R_F, R_{Bragg}, R_P, R_{exp} and χ^2 are the reliability factors.

Sample/ Parameters	***x* = 0.00**	***x* = 0.05**	***x* = 0.10**	***x* = 0.15**	***x* = 0.20**	***x* = 0.30**	***x* = 0.40**	***x* = 0.45**	***x* = 0.50**	***x* = 0.60**	***x* = 0.70**	***x* = 1.00**
Space group	*Pbnm*	*Pbnm*	*Pbnm*	*Pbnm*	*Pbnm*	*Pbnm*	*Pbnm*	*Pbnm*	*Pbnm*	*Pbnm*	*Pbnm*	*Pbnm*
***a* (Å)**	5.5118 (0.0002)	5.5148 (0.0002)	5.5177 (0.0002)	5.5205 (0.0002)	5.5245 (0.0002)	5.5264 (0.0002)	5.5282 (0.0004)	5.5337 (0.0004)	5.5352 (0.0004)	5.5411 (0.0003)	5.5436 (0.0008)	5.5543 (0.0003)
***b* (Å)**	5.4757 (0.0002)	5.4792 (0.0002)	5.4848 (0.0002)	5.4897 (0.0002)	5.4938 (0.0002)	5.5006 (0.0002)	5.5071 (0.0003)	5.5127 (0.0003)	5.5173 (0.0003)	5.5269 (0.0004)	5.5330 (0.0005)	5.5646 (0.0003)
***c* (Å)**	7.7540 (0.0004)	7.7587 (0.0004)	7.7682 (0.0003)	7.7751 (0.0004)	7.7793 (0.0004)	7.7902 (0.0004)	7.8001 (0.0007)	7.8026 (0.0007)	7.8096 (0.0007)	7.8190 (0.0011)	7.8269 (0.0015)	7.8529 (0.0004)
***Volume* (Å^3)**	234.03 (0.02)	234.44 (0.02)	235.09 (0.01)	235.63 (0.01)	236.10 (0.02)	236.81 (0.01)	237.47 (0.03)	238.02 (0.03)	238.50 (0.03)	239.46 (0.05)	240.07 (0.06)	242.72 (0.02)
R_F (%)	6.89	6.04	4.72	3.86	4.66	4.05	5.95	4.78	5.51	6.90	7.08	8.37
R_{Bragg} (%)	6.93	6.24	5.36	4.37	5.28	4.43	6.82	5.80	6.27	7.73	8.63	11.0
R_P (%)	14.2	13.2	12.8	11.3	12.2	12.6	13.7	13.4	13.7	14.9	15.4	18.2
R_{exp} (%)	4.97	4.73	4.68	4.66	4.87	4.57	4.96	4.88	4.84	4.82	5.13	5.36
χ^2	21.1	19.9	22.6	20.3	19.9	22.6	20.6	21.1	22.0	21.3	20.8	22.8
La/Cr/Fe Occupancy	0.912 /0.919 /0.000	0.933 /0.928 /0.028	0.939 /0.875 /0.075	1.015 /0.849 /0.149	0.955 /0.781 /0.181	0.980 /0.692 /0.292	0.875 /0.352 /0.552	0.940 /0.526 /0.426	0.934 /0.472 /0.472	0.911 /0.373 /0.573	0.933 /0.277 /0.677	0.973 /0.000 /1.00

The morphology of all the samples has been studied by scanning electron microscope. The typical SEM micrographs for x = 0.20, 0.50 and 0.60 samples are shown in Fig. 3.4. The surface morphology is found to be quite uniform for all the samples. The average particle size is found to be in the order of 470 nm to 650 nm. The elemental analysis of the prepared compounds has been carried out by recording EDS spectra. Typical EDS spectrum for x = 0.20 sample is shown in Fig. 3.4. The chemical composition determined from the EDS analysis is found to be comparable to the nominal starting composition. The cationic ratio values determined from EDS analysis for all the samples are given in Table 3.2

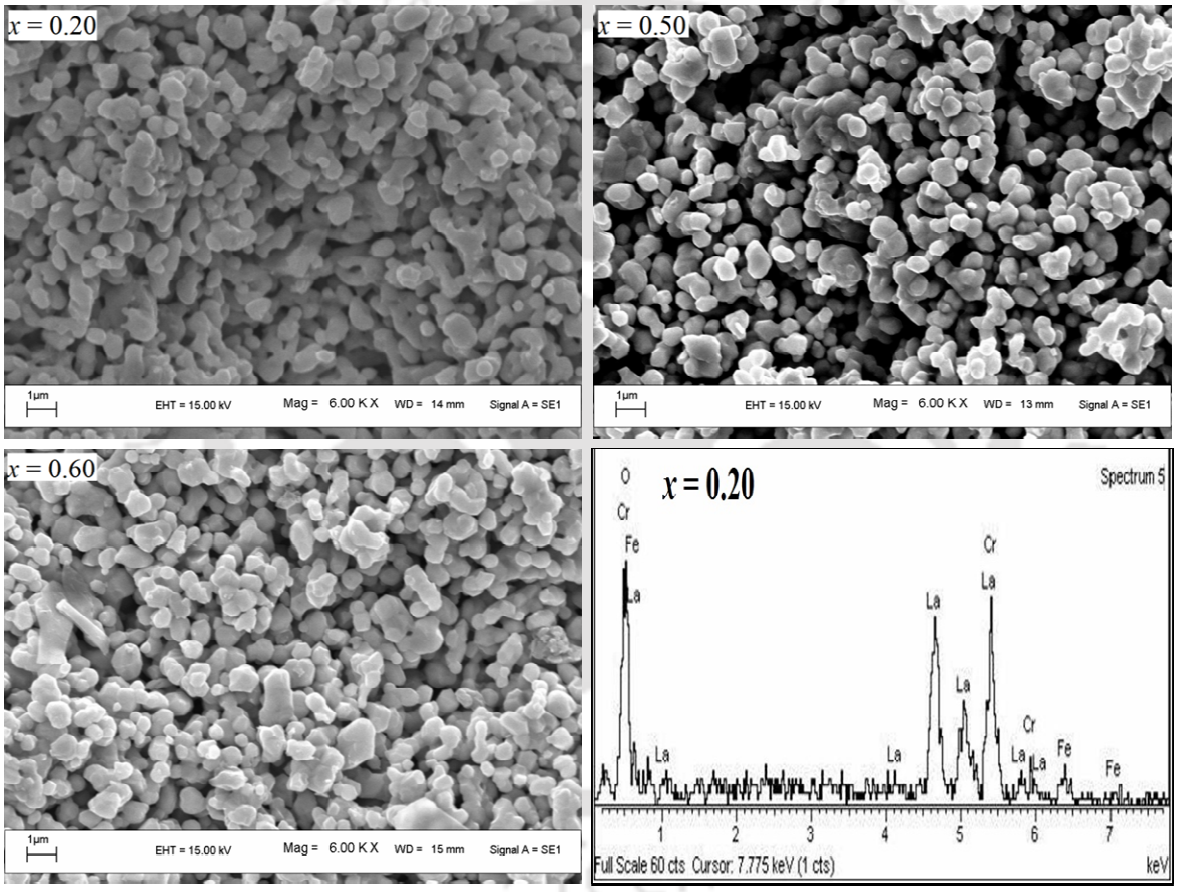

Figure 3.4: SEM images recorded for x = 0.20, 0.50 and 0.60 samples along with EDS spectrum for x = 0.20.

Table 3.2: The cationic ratio determined from EDS analysis for x = 0.00 -1.00 samples.

Samples	Calculated Cationic Ratio from EDS Analysis		
	La	**Cr**	**Fe**
***x* = 0.00**	0.92	1.07	0.00
***x* = 0.05**	0.95	0.93	0.07
***x* = 0.10**	0.91	0.86	0.14
***x* = 0.15**	0.94	0.84	0.16
***x* = 0.20**	0.96	0.80	0.20
***x* = 0.40**	0.96	0.62	0.38
***x* = 0.50**	0.97	0.53	0.47
***x* = 0.60**	0.96	0.40	0.60
***x* = 0.70**	0.95	0.30	0.70
***x* = 1.00**	0.99	0.00	1.00

3.1.2 Magnetic Properties

Magnetization (M) versus temperature (T) plots in zero field cooled (ZFC) and field cooled (FC) conditions for x = 0.00 to 1.00 samples are shown in Fig. 3.5 for the applied field H = 2000 Oe. The x = 0.00 sample exhibits a clear antiferromagnetic (AFM) transition at T_N = 289 K and for $T < T_N$, M value is found to decrease continuously. The FC curve shows irreversibility for $T < T_N$ with enhanced magnetization and it can be understood in terms of spin canted weak ferromagnetism (FM). The x = 0.05 sample shows a drastic change in M versus T behavior, especially under the FC condition. Even though M_{FC} (T) > M_{ZFC} (T) at just below T_N, M_{FC} value is found to decrease continuously with decrease in temperature

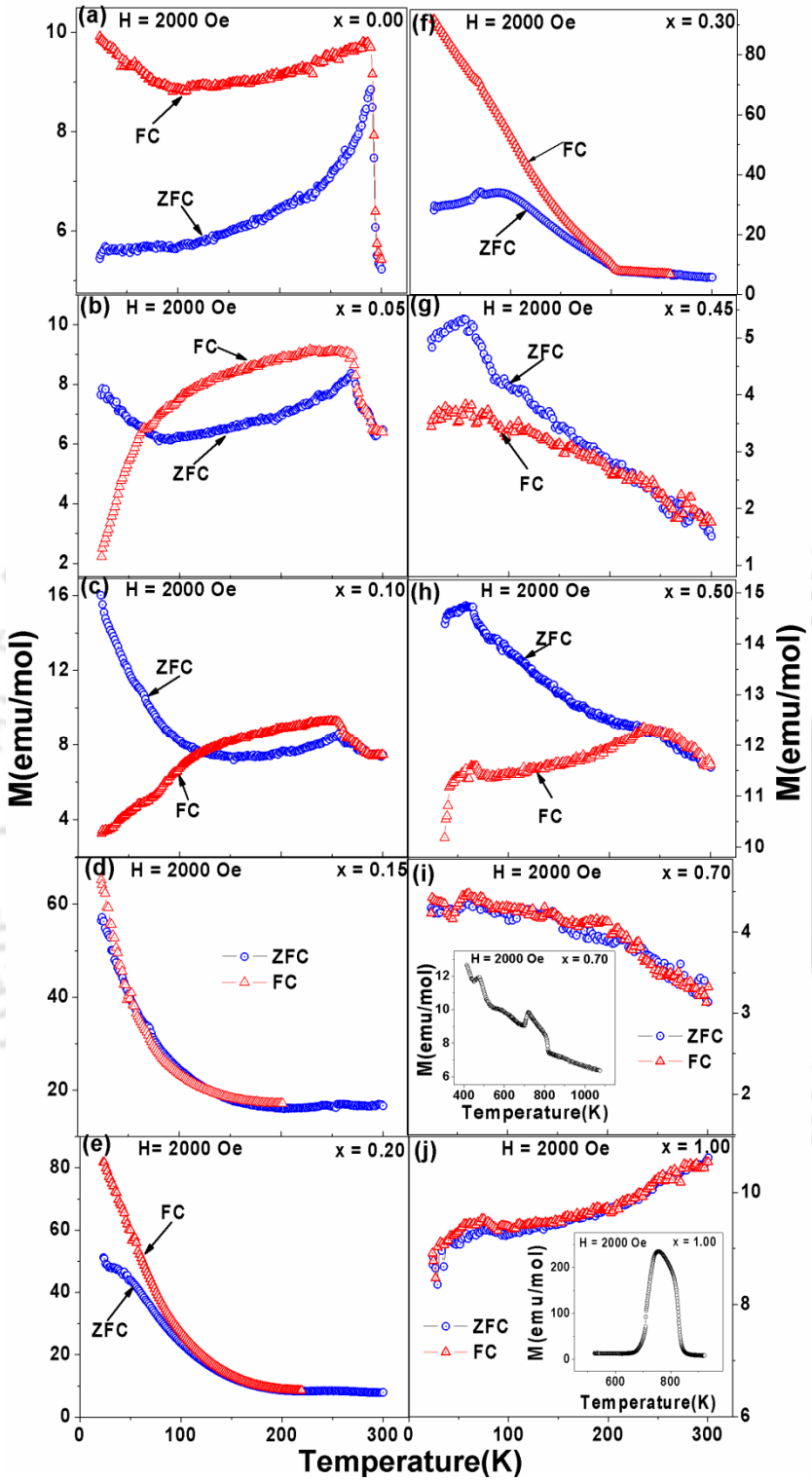

Figure 3.5: Temperature variation of magnetization for zero field cooled (ZFC) and field cooled (FC) conditions for x = 0.00, 0.05, 0.10, 0.15, 0.20, 0.30, 0.45, 0.50, 0.70 and 1.00 samples (a to j).

by crossing over the M_{ZFC} curve around 64 K. So, there is a clear tendency towards magnetization reversal (MR) even for 5 atm. % of Fe doping and similar behavior is observed for $x = 0.10$ sample. The $x = 0.15$ sample also shows a small negative irreversibility in the temperature region around 50 K to 120 K.

Both ZFC and FC magnetization values of $x = 0.20$ sample are found to increase with decrease in temperature along with a positive irreversibility ($M_{FC} > M_{ZFC}$) at $T < T_N$. Similar behavior is observed for $x = 0.30$ and 0.40 (not shown) samples but with larger irreversibility. Thus, for Fe concentrations $x = 0.20$ to 0.40, no MR tendency is observed and the irreversible magnetization is found to be relatively large. The absolute values of magnetization for these samples are found to be about one order of magnitude larger than those of samples with low level of Fe concentrations ($x \leq 0.10$). So, in the medium level of doping ($x = 0.20$ to 0.40), considerable enhancement of canted FM has been observed.

On further increasing the Fe concentration, *i.e.* for $x = 0.45$ and 0.50, the magnitude of magnetization is found to be quite small and comparable to the values of parent compound and samples with $x \leq 0.10$. Unlike the case of intermediate level of Fe concentrations ($x = 0.20$ to 0.40), here the weak FM component is found to be quite small. Again in this case, we can see a negative irreversible magnetization behavior, *i.e.* $M_{FC}(T) < M_{ZFC}(T)$ and a tendency towards MR. Even though, it exhibits negative irreversible magnetization, the temperature dependence of magnetization is found to be quite different compared to that of samples with low level of Fe concentrations. Thus, the mechanism associated with MR could be quite different for $x = 0.45$ and 0.50 samples. For $x \geq 0.60$, the antiferromagnetic to paramagnetic transition temperature is shifted to higher temperature and the AFM transition for $x = 1.00$ sample is found to be at 750 K as shown in the inset of Fig. 3.5(j). Thus, the entire set of samples can be divided into four categories, namely small Fe concentrations ($x = 0.05$ to 0.15), intermediate level of Fe concentrations ($x = 0.20$ to 0.40), half doped regions ($x = 0.40$, 0.45 and 0.50) and higher Fe concentration ($x \geq 0.60$). Since, samples of small Fe concentration and $x \simeq 0.50$ exhibit the signature of MR, we have taken up the detailed magnetization measurements under various applied magnetic fields for $x = 0.05$, 0.10, 0.15, 0.45 and 0.50 samples and their detailed analyses.

(i) Magnetization Reversal

FC *M-T* curves for *H* ranging from 50 Oe to 2000 Oe are shown in Fig. 3.6 and Fig. 3.7 for x = 0.05 and 0.10 samples. It may be noted that for the first time negative magnetization is observed even for 5 atm. % of Fe doping in $LaCrO_3$. The negative magnetization below the compensation temperature (T_{comp}) is observed up to a maximum applied field of *H* = 500 Oe and however, the trend of *M-T* curves remains same even for *H* = 2000 Oe. It suggests that no major change in the mechanism of magnetic interaction is observed with increase in *H* value rather than shifting of the entire *M-T* curve towards positive magnetization due to the field induced increase in canted FM component. The T_{comp} value is found to decrease with increase in applied field and it is found to vary from 38 K for *H* = 100 Oe to 28 K for *H* = 500 Oe. Similar to the case of x = 0.05 sample, the x = 0.10 sample also exhibits MR and the T_{comp} value is found to vary from 77 K to 51 K for the increase in *H* value from 100 Oe to 1000 Oe. Here, the MR could be observed up to *H* = 1000 Oe. So, there is an increase in T_{comp} value with increase in Fe concentration for a particular *H* value.

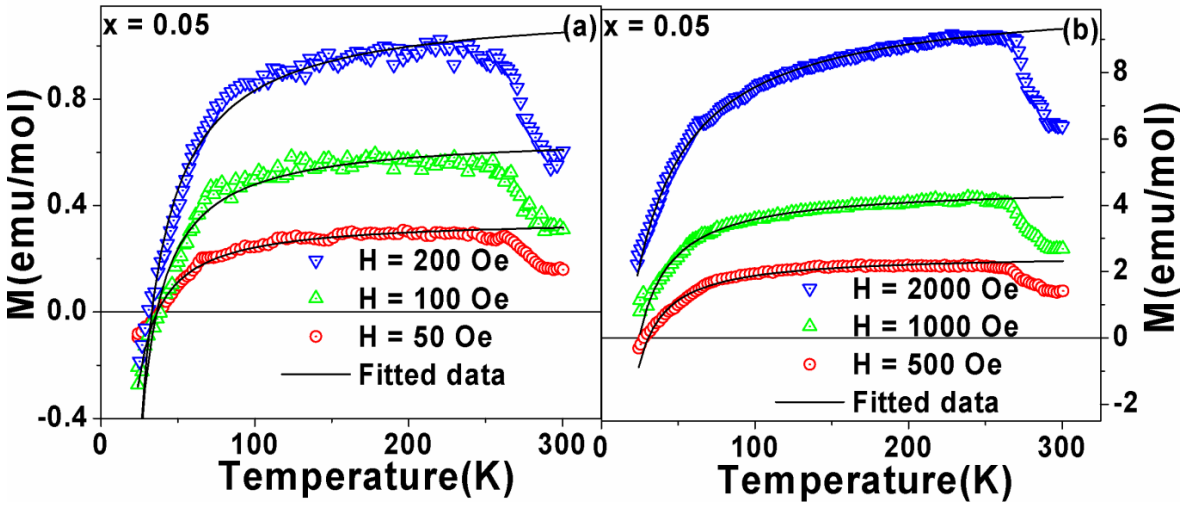

Figure 3.6: FC *M-T* curves of x = 0.05 sample for (a) *H* = 50 Oe, 100 Oe and 200 Oe and, for (b) *H* = 500 Oe, 1000 Oe and 2000 Oe.

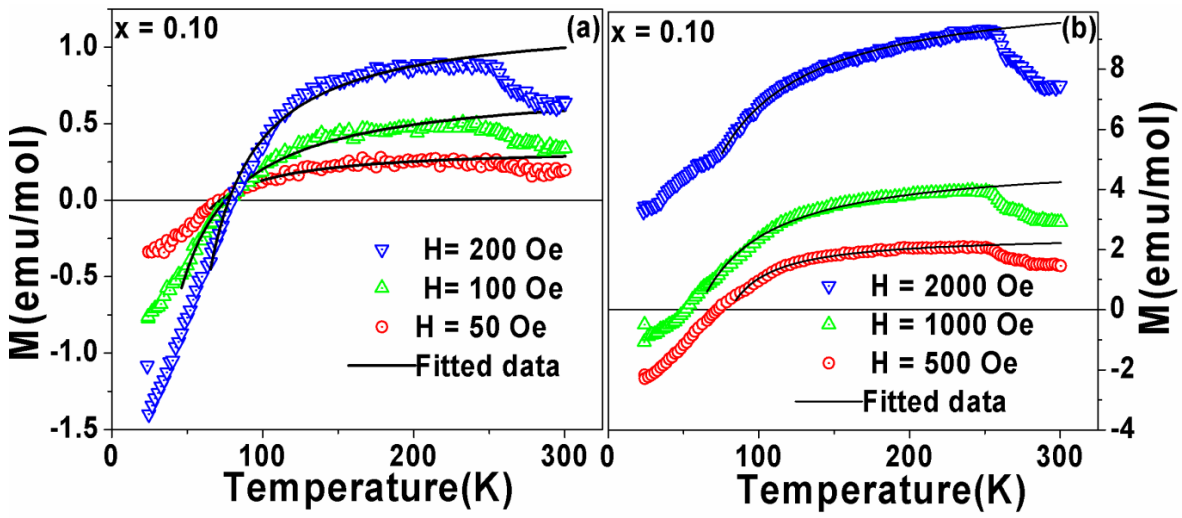

Figure 3.7: FC *M-T* curves of $x = 0.10$ sample for (a) $H = 50$ Oe, 100 Oe and 200 Oe and, for (b) $H = 500$ Oe, 1000 Oe and 2000 Oe.

In view of the absence of any known structural transition in this system at low temperature close to T_{comp}; the observed MR even for smaller concentration of Fe doping can be attributed to the competition between the paramagnetic behavior of substituted Fe^{3+} ions under the influence of predominant negative internal field due to AFM ordered Cr^{3+} ions and the weak canted FM component of Cr^{3+} ions.

Thus for $x = 0.05$ and 0.10 samples, the doped Fe ions behave like paramagnetic entities. Here, the Fe concentration is quite low such that the possibility of Fe^{3+}-O^{2-}-Fe^{3+} networks is rare. The doped Fe ions also give rise to additional canting of Cr moments. So, the FC *M-T* data were fitted to the following equation [22]

$$M = M_{Cr} + \frac{C(H + H_I)}{(T - \theta_C)} \tag{3.1}$$

Here, M is the total magnetization and M_{Cr} is the canted magnetization due to Cr^{3+} ions. H_I is the internal field and $C = x\ C_0$, where C_0 refers to the Curie constant of Fe^{3+} ions. The FC curves of $x = 0.05$ sample were fitted to equation (3.1) for $H \leq$ 2000 Oe and the fitted data along with the experimental data are shown in Fig 3.6. Similar fitting was carried out for $x =$ 0.10 sample for $H \leq 2000$ Oe as shown in Fig 3.7 The fitted data closely follow the experimental curves. The estimated values of θ_C for different H values are found to be within

± 5 K and it suggests the paramagnetic nature of doped Fe ions. However, the θ_C values for x = 0.10 sample are found to be in the range of 15 K to 35 K. It suggests the paramagnetic behavior of Fe ions in the temperature region studied along with a possible magnetic ordering between Fe ions and the canted FM component of Cr ions at low temperature. The estimated values of M_{Cr} and H_I as a function of applied field H are shown in Fig. 3.8. We can see that M_{Cr} and the magnitude of H_I increase with increase in applied field. Thus, the increase in applied field leads to an increase in the size of AFM domains and that gives to increase in H_I and M_{Cr} values.

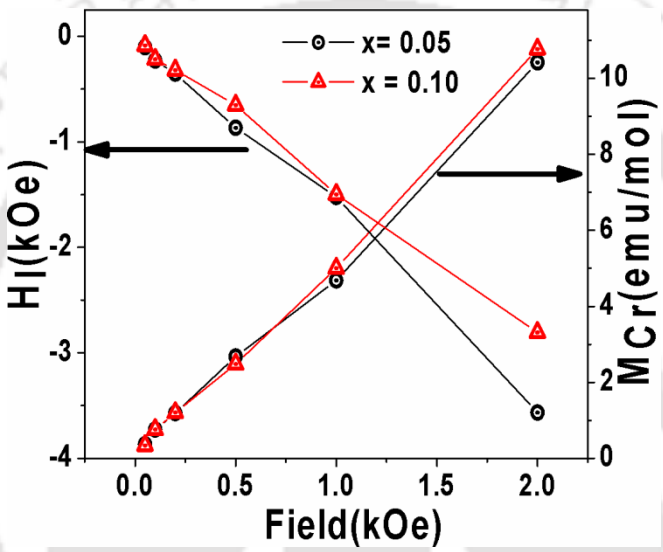

Figure 3.8: M_{Cr} and H_I as a function of applied field for x = 0.05 and 0.10 samples.

Typical M - T plots of x = 0.15 sample for H = 50 Oe, 100 Oe, 200 Oe and 500 Oe are shown in Fig. 3.9. Similar to the case of x = 0.05 and 0.10 samples, here also the MR is observed but with relatively a larger T_{comp} value of 103 K. Here, another interesting behavior of M (T) reverting back to the positive value is observed at low temperature. So, in this case, we have observed two compensation temperatures, one during the positive to negative magnetization transition upon cooling to around 100 K and another during the transition from the negative to positive magnetization value at 42 K. The above double sign reversal of magnetization is associated with a minimum magnetization (valley) at T_m = 62 K. The minimum point and the rather sharp rise in magnetization at low temperature can be attributed to either field induced magnetic ordering between the canted spin components of Cr^{3+} ions and Fe^{3+} ions or the spin reorientation of Cr^{3+} ions. The magnetization data for T >

T_m were fitted to equation (3.1) and the fitted data are shown as a solid line in Fig. 3.9. The estimated values of θ_C are found to be in the range of 60 K to 80 K depending on the magnitude of applied field. The values of H_I and M_{Cr} are found to be in the range of -285 Oe to -567 Oe and 0.3 emu/mol to 2.3 emu/mol respectively and they follow the same trend as those of x = 0.05 and 0.10 samples.

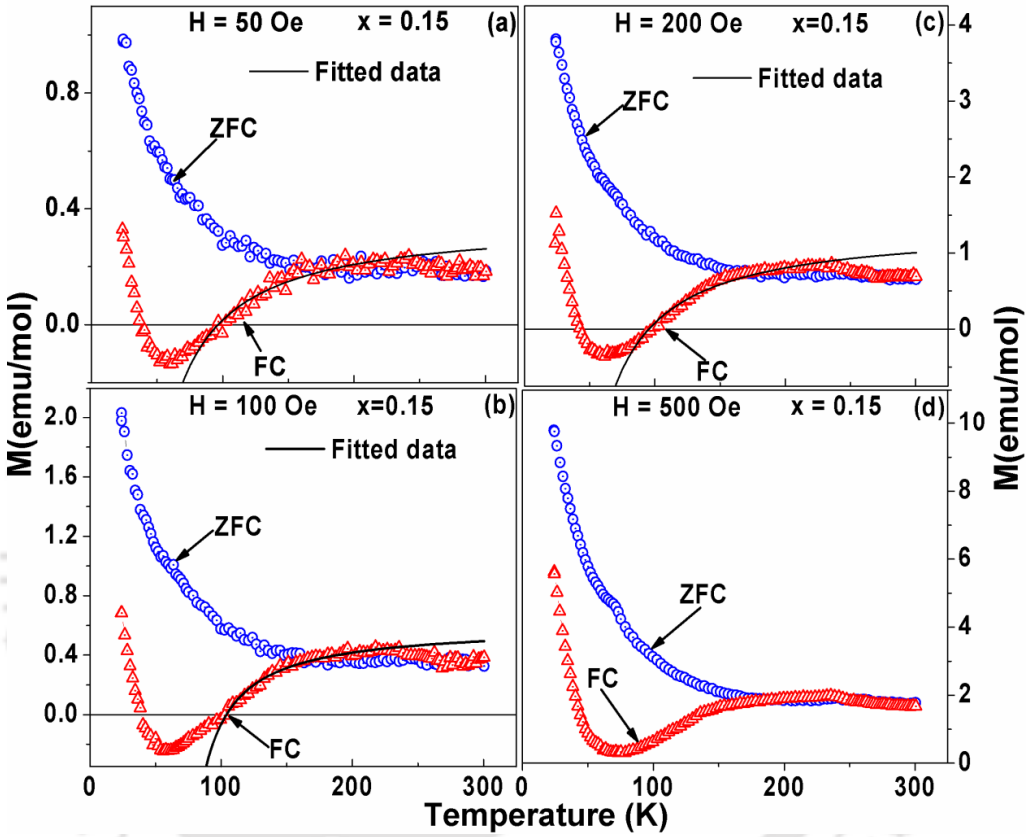

Figure 3.9: ZFC and FC *M-T* curves for x = 0.15 sample at (a) H = 50 Oe, (b) H = 100 Oe, (c) H = 200 Oe and (d) H = 500 Oe along with the fitted data.

In most of the reports on La-Cr-O based compounds, the negative magnetization has been observed either by partially or completely replacing the La ions by other magnetic rare earth ions [49, 53, 90, 92]. These magnetization data were mostly interpreted by considering the paramagnetic behavior of doped magnetic rare earth ions under the influence of negative internal field due to the AFM aligned Cr^{3+} ions. The reported T_{comp} values in $La_{0.2}Ce_{0.8}CrO_3$ [53], $La_{0.5}Pr_{0.5}CrO_3$ [92], $La_{0.5}Gd_{0.5}CrO_3$ [90] and $GdCrO_3$ [15] are 45 K, 163 K, 75 K and 130 K respectively for H = 100 Oe. In the present series of samples, the T_{comp} values are

found to be in the range of 38 K for $x = 0.05$ to 103 K for $x = 0.15$ at $H = 100$ Oe and they are mostly comparable to the values reported in literature for Lanthanum chromites. Large T_{comp} values close to 200 K and 164 K have been reported for $LaFe_{0.5}Cr_{0.5}O_3$ [93, 94] compound at $H = 1000$ Oe.

The H_I values of $La_{0.5}Pr_{0.5}CrO_3$ [49] and $GdCrO_3$ [15] were reported to be -8.5 kOe and -1.9 kOe respectively. However, Sharma *et al.* [90] have reported a moderate H_I value of -511 Oe for $H = 100$ Oe. The H_I values of $La_{1-x}Pr_xCrO_3$ [73] for $x = 0.85$ are reported to vary from 2.8 kOe to 3.0 kOe for H varying from 20 Oe to 2 kOe. The H_I values of $x = 0.05$ sample of the present series are found to vary from -230 Oe to -3.5 kOe for $H = 100$ Oe to 2000 Oe. The H_I value of the order of -3.5 kOe can be substantiated from the observed negative trend (decrease in M with a decrease in T) of FC M-T plot even for $H = 2000$ Oe. Thus, even though the doping concentration is relatively small, the tendency towards negative magnetization is found to be quite strong.

The MR is generally quantitatively estimated by determining the maximum (positive) and minimum (negative) values of magnetization *i.e.* M_{max} and M_{min}. The value of $\frac{M_{\min}}{M_{\max}}$ was reported to be 30 in $GdCrO_3$ [15] and 6 in $La_{0.5}Gd_{0.5}CrO_3$ [90] around 25 K for $H = 100$ Oe. On the other hand, its value in $La_{0.15}Pr_{0.85}CrO_3$ [73] is reported to be 300 at 5 K for $H = 20$ Oe. However, the maximum value of $\frac{M_{\min}}{M_{\max}}$ in the present set of samples is found to be around 1.6. The fractional magnetization irreversibility at a particular temperature can be quantitatively determined by using the relation $\frac{\Delta M}{M_{ZFC}} = \frac{M_{FC} - M_{ZFC}}{M_{ZFC}}$. The typical value of $\frac{\Delta M}{M_{ZFC}}$ obtained for $x = 0.10$ is found to be -2.0 for $H = 100$ Oe at 25 K. We have determined the values of $\frac{\Delta M}{M_{ZFC}}$ from the experimental data of Azad *et al.* [93] for $LaFe_{0.5}Cr_{0.5}O_3$ and Yoshii *et al.* [15] for $GdCrO_3$ and they are found to be -2.5 and -1.7 respectively. They are comparable to the result of present samples.

We have also carried out the detailed magnetization measurements on $x = 0.45$ and

0.50 samples of $LaCr_{1-x}Fe_xO_3$. Typical FC *M-T* plots for x = 0.45 are shown in Fig. 3.10 for H = 50 Oe to 500 Oe. The *M-T* plots of x = 0.50 sample are also shown in Fig. 3.11 for H = 50 Oe to 1000 Oe. We can see that they all exhibit MR. Unlike the case x = 0.05 to 0.15 samples, here the *M-T* curves are found to be almost linear in most of the temperature region. Here, the concentration of Fe ions at the Cr sites is close to 50 atm. %. So, there is a probability of Fe^{3+}-O^{2-}-Fe^{3+} networks and the corresponding AFM interaction, which is in addition to the existing AFM due to Cr^{3+}-O^{2-}-Cr^{3+} networks. So, Fe^{3+} ions in the present doping ($x \simeq 0.50$) regime cannot be treated as paramagnetic entities. The observed trend of *M-T* behavior is comparable to that reported in $LaCr_{0.5}Fe_{0.5}O_3$ [93] and $YFe_{0.5}Cr_{0.5}O_3$ [111, 113]. Azad *et al*. [93] interpreted the observed negative magnetization in $LaCr_{0.5}Fe_{0.5}O_3$ in terms of disorder in the magnetic interaction and however, no quantitative magnetization analysis was reported. Vijayanandhini *et al*. [94] have reported that the MR in $(La_{1-x/2}Bi_{x/2})Fe_{0.5}Cr_{0.5}O_3$ system was mainly due to the canting of pure $La_{1-x}Bi_xFeO_3$ and $La_{1-x}Bi_xCrO_3$ domains or clusters and their AFM interaction. Dasari *et al.* [113] explained the observed MR in $YFe_{1-x}Cr_xO_3$ (x = 0.40 and 0.50) compounds in terms of a model consisting of isotropic superexchange and Dzyaloshinsky-Moriya (DM) interactions. The MR in $BiFeO_3$-$BiMnO_3$ solid solutions was explained in terms of extrinsic origins such as, the presence of magnetic impurities or sample inhomogeneities [56]. In YVO_3 [57], the MR has been successfully explained by considering the competition between the antisymmetric DM interaction [33, 34] and the single ion anisotropy. Moreover, they have quantitatively studied the *M-T* data by fitting to the expression derived from the above DM- single ion anisotropy model.

The tilting of CrO_6/FeO_6 in the distorted perovskite structure of La(Cr, Fe)O_3 gives rise to the canted spin structure. Due to such tilting, the intermediate oxygen ion is not at the inversion center of two Cr/Fe ions and it leads to an antisymmetric interaction known as Dzyaloshinsky-Moriya (DM) interaction [33]. The form of DM interaction is $\vec{D}.(\vec{S}_1 \times \vec{S}_2)$, where $\vec{S}_1$ and $\vec{S}_2$ are the spins of two sublattices and $\vec{D}$ is the Dzyaloshinsky vector. In addition to that, the tilting of CrO_6/FeO_6 and the corresponding staggered Cr/Fe-O bonds lead to the staggering of single ion magnetic anisotropy axis. Ren *et al.* [57] have derived the expression for the net magnetization for H perpendicular to the easy axis by considering the

contributions from single ion anisotropy, DM interaction and AFM interaction.

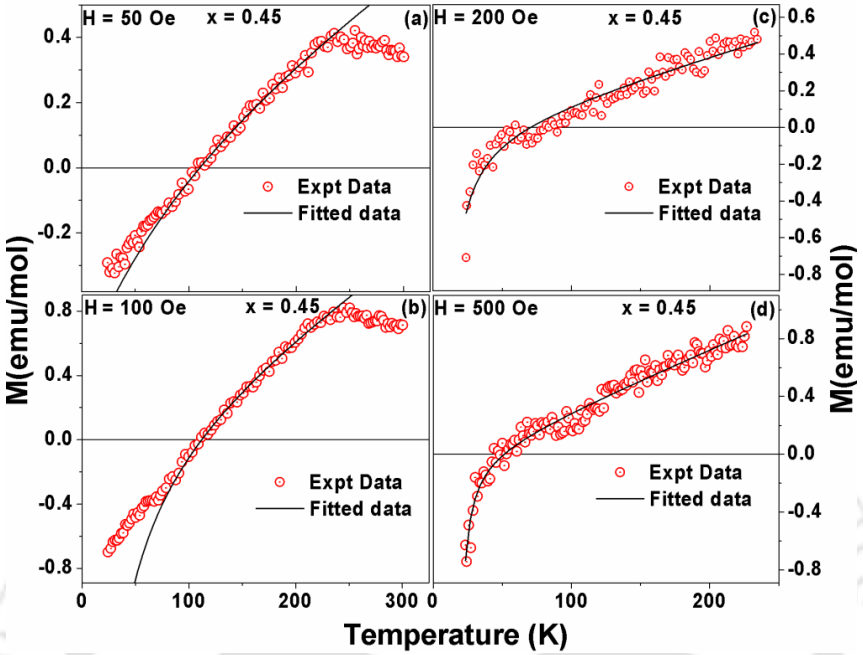

Figure 3.10: FC *M-T* curves of x = 0.45 sample for (a) H = 50 Oe, (b) H= 100 Oe, (c) H = 200 Oe and (d) H = 500 Oe. The fitted data are shown as solid line.

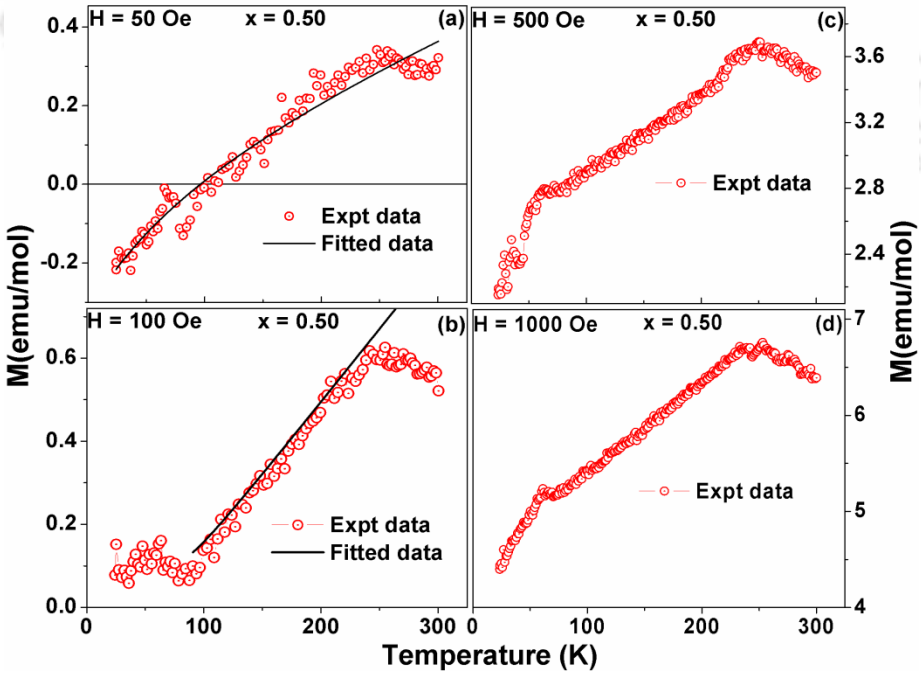

Figure 3.11: FC *M-T* curves of x = 0.50 sample for (a) H = 50 Oe, (b) H= 100 Oe, (c) H = 500 Oe and (d) H = 1000 Oe. The fitted data are shown as solid line.

The expression for the net energy of the system is given in section 1.7 (equation 1.28) and it is reproduced as follows,

$$M_{net} = 2Ng\mu_B \left|\langle S\rangle\right| \frac{S^2\xi\gamma - \gamma_D \left|\langle S\rangle\right|^2}{\left|\langle S\rangle\right|^2 + S^2\xi} \tag{3.2}$$

Here, $\left|\langle S\rangle\right| = \frac{g\mu_B S(S+1)B}{3k_B T}$ as per the mean field model. In the present work, to reduce the number of free parameters of the fit, we have assumed that $\xi \ll 1$, so that the second term in the denominator can be ignored. For polycrystalline samples having random orientation of crystallites, the expression for magnetization can be obtained as per the following integration [123] ,

$$\frac{1}{2\pi}\int_0^{\pi} M_{net} \sin\varphi d\varphi \tag{3.3}$$

Here φ is the angle of orientation H with respect to the easy axis. The FC M-T data of x = 0.45 sample could be fitted to equation (3.3). The fitted data along with the experimental data of x = 0.45 sample are shown in Fig. 3.10 for different H values. The value of T_{comp} is found to decrease from 105 K for H = 50 Oe to 50 K for H = 500 Oe. The value of γ_D for x = 0.45 sample is also found to decrease with increase in H value. The typical values of γ_D are 49×10^{-3} and 10×10^{-3} for H = 200 Oe and 500 Oe respectively. The values of $\xi\gamma$ are found to be in the range of 8.2×10^{-10} to 38×10^{-10}. Thus with increase in applied field, the DM interaction is weakened and the contribution of single ion anisotropy is enhanced. The FC magnetization of x = 0.50 sample could be also fitted to equation (3.3) and the fitted data are shown as line in Fig. 3.11. The estimated values of γ_D and $\xi\gamma$ are found to be 89×10^{-3} and 5.5×10^{-10} respectively for H = 100 Oe. No MR was observed for $H \geq$ 500 Oe. The magnetization of these samples could not be fitted to the paramagnetic model (equation (3.1)). The γ_D values of the present samples, especially for higher applied fields are found to be in the same order of magnitude (31×10^{-3}) as reported in YVO_3 single crystal [57]. However, the constant related to the single ion anisotropy, $\xi\gamma$ is found to be quite small.

The average AFM coupling constant J due to nearest neighbor spin pairs was calculated by using the measured Néel temperature T_N and the relation $J = \frac{3k_B T_N}{S(S+1)}$. These values are found to be 176 K and 186 K for x = 0.45 and 0.50 samples respectively. The total DM constant D corresponding to all nearest neighbor spin pairs was estimated using the values of γ_D and J. The estimated values of D for x = 0.45 sample are found to be -17.25 K and -3.52 K for H = 200 Oe and 500 Oe respectively. The D value corresponding to x = 0.50 sample is -33.1 K for H = 100 Oe. The corresponding D_{ij} (DM constant per spin pair) values are found to be -1.43 K and -0.29 K for x = 0.45 sample at two different fields and -2.75 K for x = 0.50 sample. They are comparable to the value (~ -0.90 K) estimated from the report of Ren *et al.* [57] for YVO_3 single crystal and the values (-0.39 K for x = 0.4 and -0.31 K for x = 0.5) reported by Dasari *et al.* [113] for $YFe_{1-x}Cr_xO_3$ compounds.

(ii) Exchange Bias:

To explore the exchange bias behavior, we have recorded the *M-H* loops of x = 0.45 and 0.50 samples in the temperature range of 25 K to 300 K under the field cooled condition with H = 5000 Oe. *M-H* loops at a few selected temperatures are shown in Fig. 3.12 and Fig. 3.13 in the expanded scale. *M-H* loops in the temperature range T < 200 K show the AFM nature. While lowering the temperature, *M-H* loops shift towards the negative field axis for both the samples. So, for both the samples we have observed negative exchange bias behavior.

The exchange bias field (H_{EB}) and the effective coercive field (H_C^{eff}) were calculated for these samples by using the relations

$$H_{EB} = (H_+ + H_-)/2 \tag{3.4}$$

$$H_c^{eff} = (H_+ - H_-)/2 \tag{3.5}$$

Here H_+ and H_- are the magnetic field values corresponding to the loop crossing the M = 0 axis during ascending and descending branches of *M-H* loop respectively.

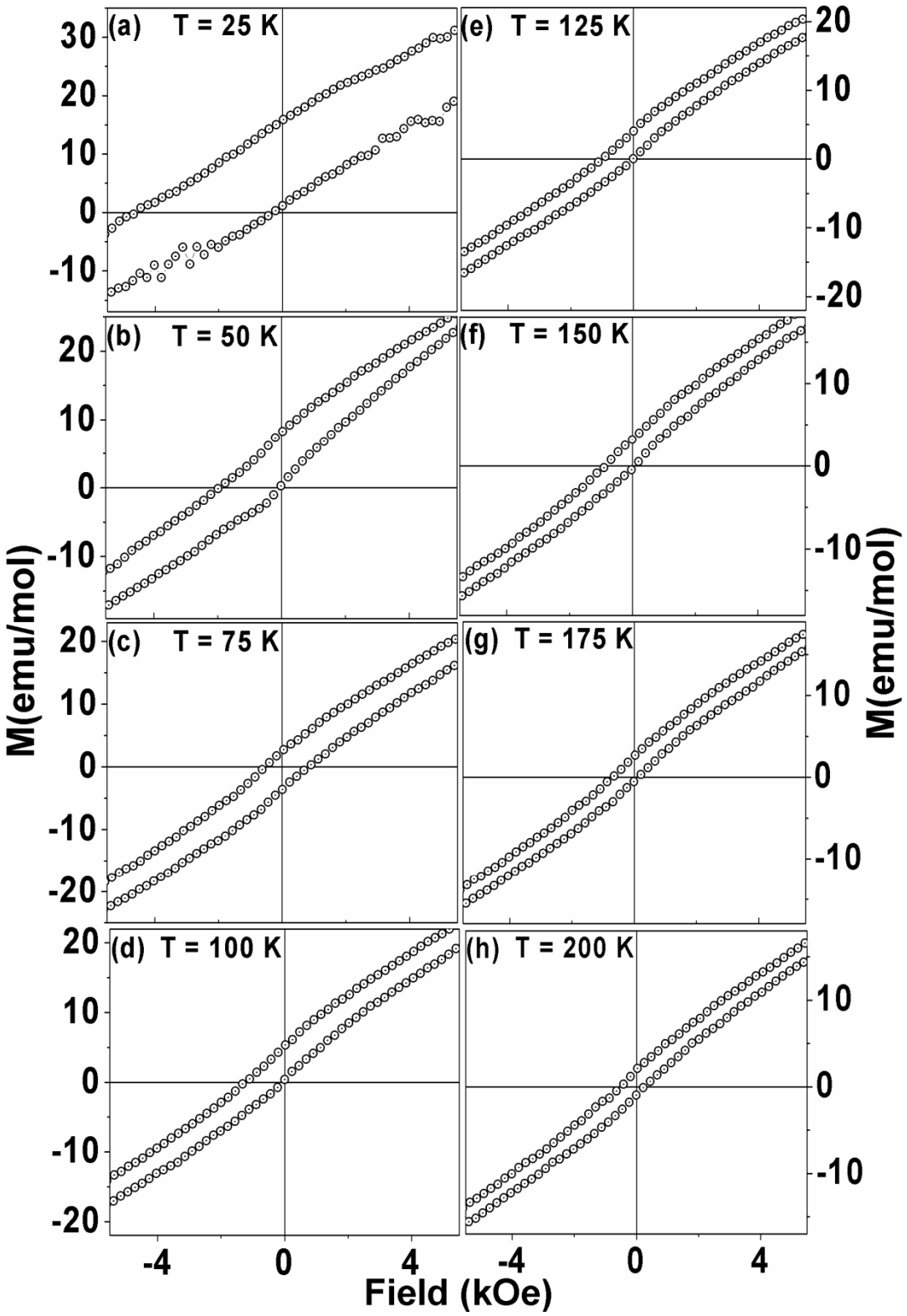

Figure 3.12: *M-H* loops of x = 0.45 sample at (a) 25 K, (b) 50 K, (c) 75 K, (d) 100 K, (e) 125 K, (f) 150 K, (g)175 K and (h) 200 K in the expanded scale.

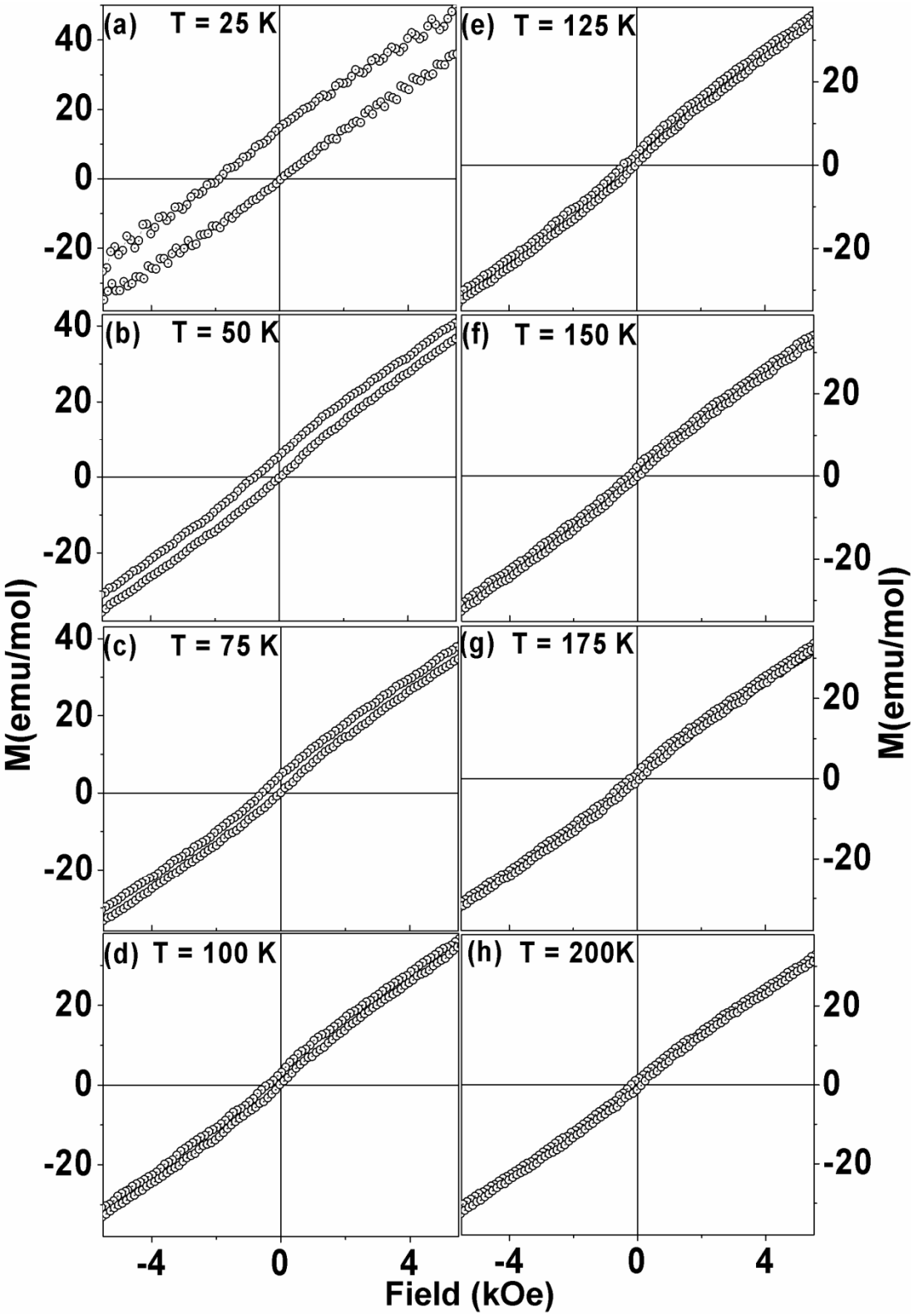

Figure 3.13: *M-H* loops of x = 0.50 sample at (a) 25 K, (b) 50 K, (c) 75 K, (d) 100 K, (e) 125 K, (f) 150 K, (g)175 K and (h) 200 K in the expanded scale.

Temperature variation of negative H_{EB} for both the samples is shown in Fig. 3.14. They show maximum H_{EB} around 25 K and as the temperature increases H_{EB} value decreases linearly. H_C^{eff} as a function of temperature is shown in Fig. 3.14 (b and d) for both the samples and they are found to decrease exponentially with increase in temperature.

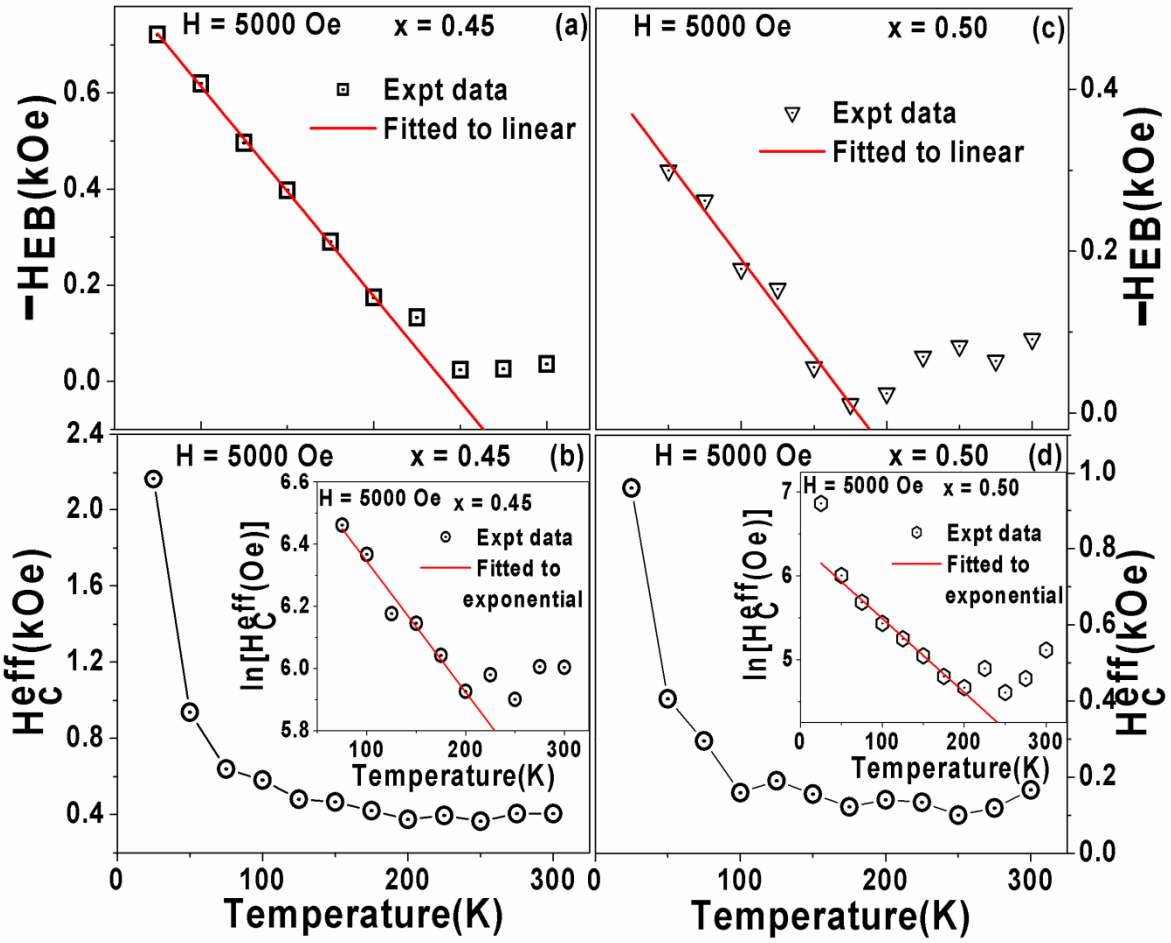

Figure 3.14: Temperature variation of H_{EB} (a and c) and H_c^{eff} (b and d) for x = 0.45 and 0.50 samples. Insets show the $\ln(H_c^{eff})$ versus T plots.

The exchange bias behavior can be explained by considering the competition between the AFM and the weak ferromagnetism due to spin canting. The presence of DM interaction and single ion anisotropy expected to contribute the spin canting. Temperature variation of H_{EB} and H_C^{eff} for x = 0.45 and 0.50 could be fitted to the following equations

$$H_{EB} = H_{EB}(0) + T_1 \times T \tag{3.6}$$

$$H_c^{eff} = H_c^{eff}(0)\exp(-T/T_2) \tag{3.7}$$

Here T_1 and T_2 are constants. Plots of H_{EB} and H_c^{eff} versus temperature for both samples were fitted to equations (3.6) and (3.7) respectively and the fitted data along are shown as solid line in Fig. 3.14. The estimated values of $H_{EB}(0)$ and $H_c^{eff}(0)$ are found to be 1 kOe and 845 Oe for $x = 0.45$ sample and, 428 Oe and 584 Oe for $x = 0.50$ samples respectively.

Typical *M-H* loops recorded for $x = 0.00$ to 0.50 samples at $T = 75$ K are shown in Fig 3.15. A paramagnetic like behavior with a linear *M-H* curve is observed for $x = 0.00$ to 0.10 samples. The $x = 0.15$ sample also exhibits similar behavior but with some minor elliptical hysteresis loop due to the presence of considerable magnetic anisotropy and canted M_{Cr}. Unlike samples with $x \leq 0.15$, the $x = 0.20$ and 0.30 samples exhibit large hysteresis and coercive field and, they can be understood in terms of disorder in the AFM interaction due to the presence of considerable Fe concentrations and associated uncompensated canted FM. Due to the presence of considerable concentration of Fe ions and the random replacement of Cr^{3+} ions by Fe^{3+} ions, the regular Cr^{3+}-O^{2-}-Cr^{3+} networks are interrupted and the uncompensated Cr^{3+} ions produce additional canted FM and large coercive field. Here, the *M* value is found to be considerably large compared to other samples. For $x = 0.45$ and 0.50 samples, the magnitude of *M* comes down due to AFM interactions in both Cr^{3+}-O^{2-}-Cr^{3+} and Fe^{3+}-O^{2-}-Fe^{3+} networks. Here, the probability of Fe^{3+}-O^{2-}-Fe^{3+} networks cannot be ruled out. In view of such small magnetization value, the competition between DM interaction and single ion anisotropy leads to MR as explained quantitatively based on equation (3.3).

In general, the MR can occur due to several reasons such as (a) core-shell structure, (b) structural transition, (c) ferrimagnetic ordering between two sublattices such that $N_1M_1 = N_2M_2$ at T_{comp} (M_1 and M_2 are sublattice magnetization and, N_1 and N_2 are the respective magnetic ion concentrations), (d) extrinsic effects like weak FM clustering or magnetic impurities, (e) paramagnetic moments under the negative internal field and (f) competition between single ion anisotropy and DM interaction, *etc*. Option (a) can be ruled out in the

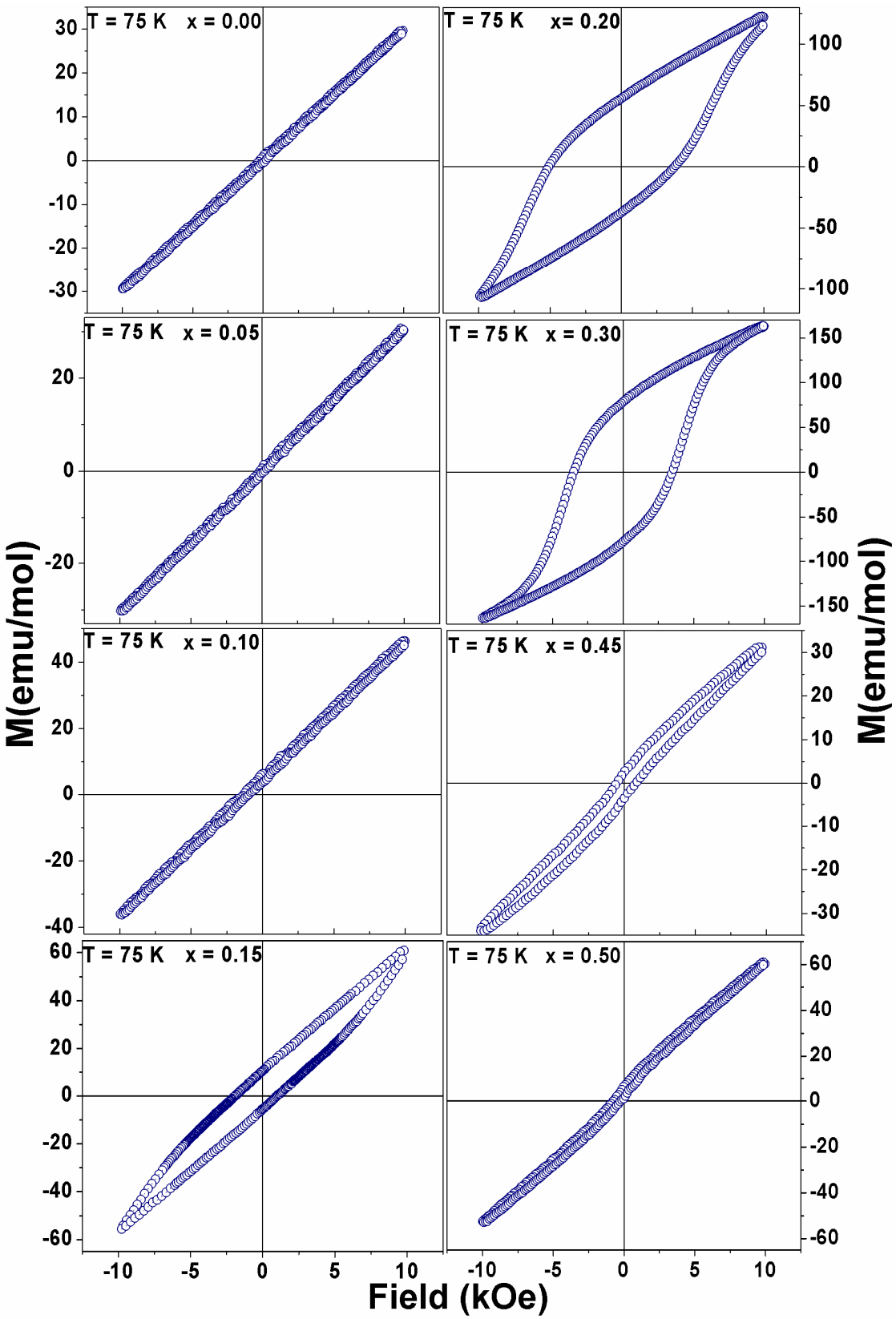

Figure 3.15: *M-H* loops at 75 K for x = 0.00 to 0.50 samples.

present series of samples, because the sizes of particles and the crystallites are not in nanometric scale. The only known structural transition in $LaCrO_3$ system is from rhombohedral to orthorhombic at around 560 K [16]. No low temperature structural transition, especially in the vicinity of T_{comp} is known and the option (b) can be eliminated. No signature of spatial and ferrimagnetic ordering of Fe^{3+} and Cr^{3+} ions was observed in the temperature region $T > T_{comp}$. In view of large difference between the magnetic moments of Fe^{3+} and Cr^{3+} ions, it is unlikely that ferrimagnetic ordering (option c) will give rise to MR especially for $x \simeq 0.50$. Such a possibility was also ruled out by Vijayanandhini *et al.* [94] in $(La_{1-x/2}Bi_{x/2})Fe_{0.5}Cr_{0.5}O_3$ system. Moreover, if it is due to ferrimagnetic ordering, one would expect considerably large spontaneous magnetization at $T << T_{comp}$ due to the difference between Fe^{3+} and Cr^{3+} moments**.** Unlike $BiFeO_3$-$BiMnO_3$ solid solutions [56], the present set of samples are known to form in single phase form with *Pbnm* space group and it is confirmed from the analysis of XRD patterns, where the lattice parameters are found to increase systematically with increase in Fe concentration x. It supports the argument of Fe ions replacing the Cr ions without any phase segregation. We have not observed any phase segregation of $LaCrO_3$ and $LaFeO_3$ from XRD analysis, if such phase segregation exists, they can be easily identified due to the considerable difference between the lattice parameters of these two phases. We have not observed any phase segregation as per the analysis of SEM micrographs and EDS spectra. If the observed MR is due to the ferromagnetic clustering induced by Fe substitution, one would expect such an effect even for the intermediate Fe concentrations (0.20 to 0.40) also, but no such behavior was observed. We have not observed any FM component at $T > T_N$. The presence of considerable magnetic moment at room temperature from the *M-T* plot for $x = 0.50$ sample can be attributed to the smearing of the AFM transition due to the presence of considerable concentration of Fe^{3+}-O^{2-}-Fe^{3+} networks at atomic levels. The canted components of magnetic moment due to such networks are taken into account in equations (3.1) and (3.2), including the components due to host Cr^{3+}-O^{2-}-Cr^{3+} networks. So, option (d) is unlikely to play a role in the present set of samples for MR.

Thus the observed MR for $x = 0.05$ to 0.15 samples is mainly due to the paramagnetic behavior of Fe ions under the influence of negative internal field arising from the AFM ordered Cr^{3+} ions. Moreover, in this composition range, the probability of having Fe^{3+}-O^{2-}-Fe^{3+} networks is quite rare. The attempt to fit the *M-T* data of $x = 0.45$ and 0.50 samples to

the paramagnetic model (equation (3.1)) did not succeed. This is understandable, because at this level of substitution Fe^{3+} ions cannot be treated as isolated paramagnetic ions. On the other hand, there is a possibility of AFM in Fe^{3+}-O^{2-}-Fe^{3+} networks in addition to the regular AFM due to Cr^{3+} ions. The experimental data of these samples could be fitted to the model, where the competition between single ion anisotropy and DM interaction is taken into account. The estimated values of DM constant are found to be reasonable. Thus, we have shown that depending upon the concentration of doped Fe ions, the mechanism of MR is found to be different.

3.2 $LaCr_{1-x}Mn_xO_3$ compounds (x = 0.0 to 1.0)

This section deals with the effect of Mn substituted at Cr site of $LaCrO_3$. The preparation, characterization and the result obtained from dc magnetization measurement along with analysis are presented.

3.2.1 Sample Preparation and Characterization

Polycrystalline samples of $LaCr_{1-x}Mn_xO_3$ for x = 0.00 to 1.00 were prepared by sol-gel route by taking high purity (99.9%) La_2O_3, $Cr(NO_3)_3.9H_2O$ and $C_4H_6MnO_4.H_2O$ as starting materials. The mixture of the above compounds dissolved in nitric acid or distilled water was converted into citrate by adding excess citric acid. It was then converted into the form of a gel by gently heating and adding ethylene glycol. The uniform precursor powder obtained from the gel was presintered at 600 ˚C for 12 h followed by final sintering in pellet form at 1100 ˚C for 24 h.

The XRD patterns recorded for the above samples are shown in Fig 3.16. XRD patterns of the prepared samples are found to be in single phase form. The XRD patterns of samples for $x \leq 0.50$ could be indexed to *Pbnm* space group with orthorhombic structure and the patterns for $x \geq 0.60$ could be indexed to $R\bar{3}c$ space group with rhombohedral structure. Typical XRD patterns along with the Rietveld refinement for x = 0.00 and 0.15 samples are shown in Fig. 3.17 and, for x = 0.70 and 1.00 samples are in Fig. 3.18.

The refined lattice parameters and unit cell volume are listed in Table 3.3. The lattice parameter c and unit cell volume are found to increase with Mn doping in orthorhombic structure as well as in rhombohedral structure because of larger ionic radii of Mn^{3+}compared to Cr^{3+} ions. Typical SEM micrographs for x = 0.00, 0.15 and 0.50 samples are shown in Fig. 3.19. The morphology of the sample is found to be uniform. The average particle size is found to be in the order of 530 nm to 660 nm. Typical EDS spectrum for x = 0.15 sample is shown in Fig. 3.19. We can see that all the elements are present. Further, the chemical compositions determined from EDS analysis are found to be comparable to the respective nominal starting compositions. The cationic ratios for a few samples are given in Table 3.4.

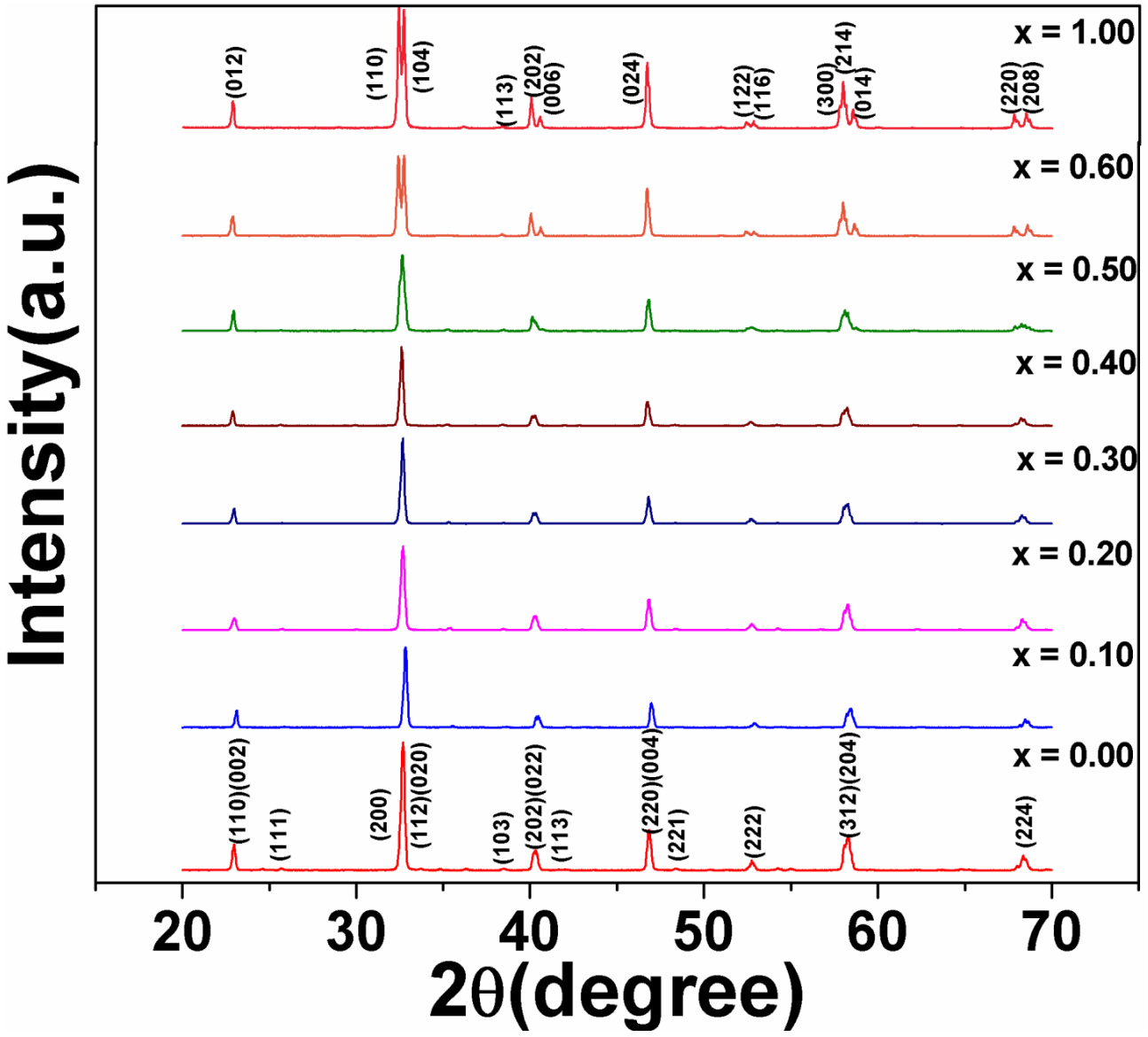

Figure 3.16: XRD patterns of $LaCr_{1-x}Mn_xO_3$ compounds for x = 0.00 to 1.00.

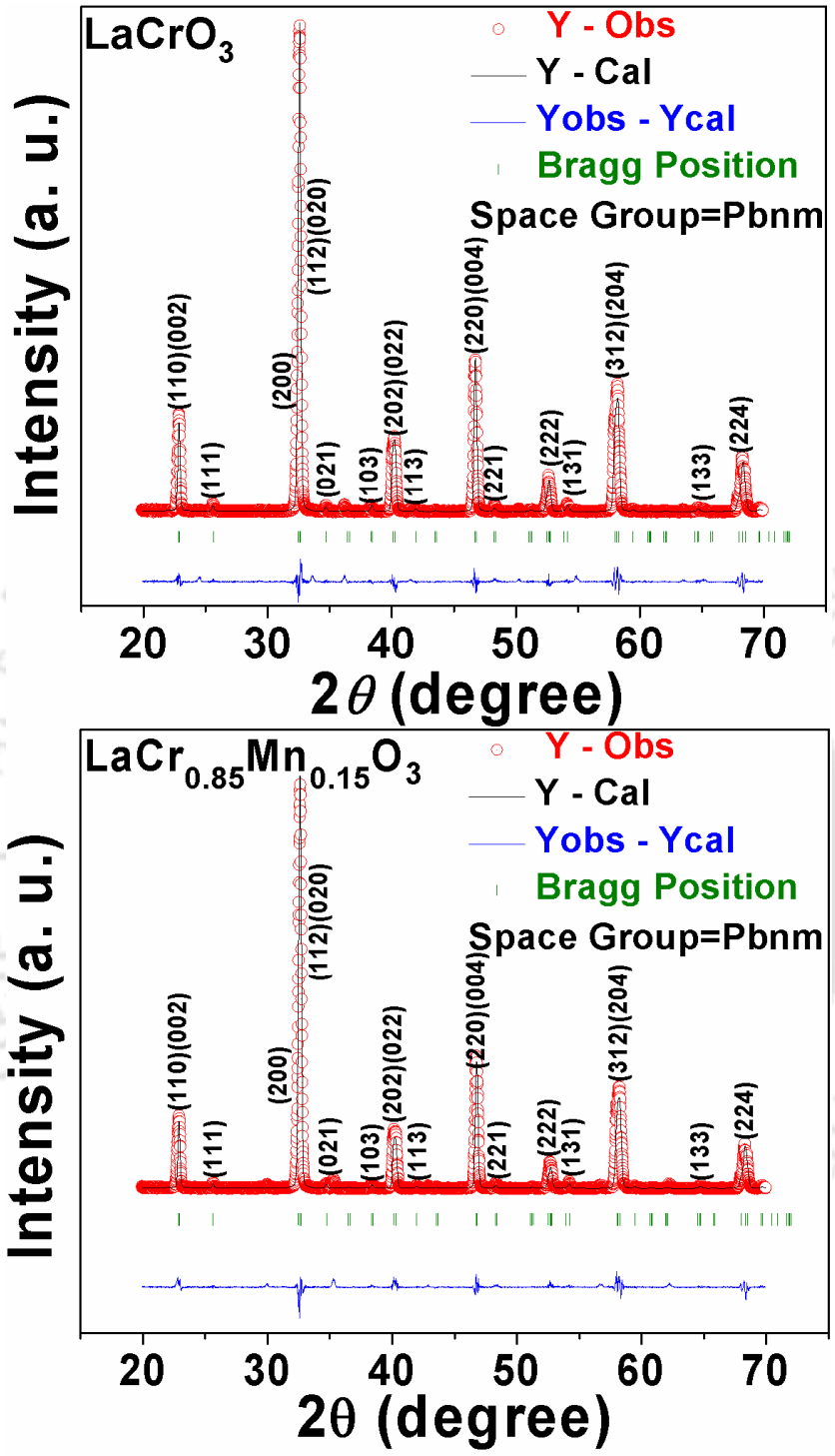

Figure 3.17: XRD patterns along with Rietveld refinement for x = 0.00 and 0.15 samples. The circles represent experimental data and solid line represents Rietveld refined data. The bottom line shows the difference between experimental and refined data. The marked 2θ positions are allowed Bragg peaks.

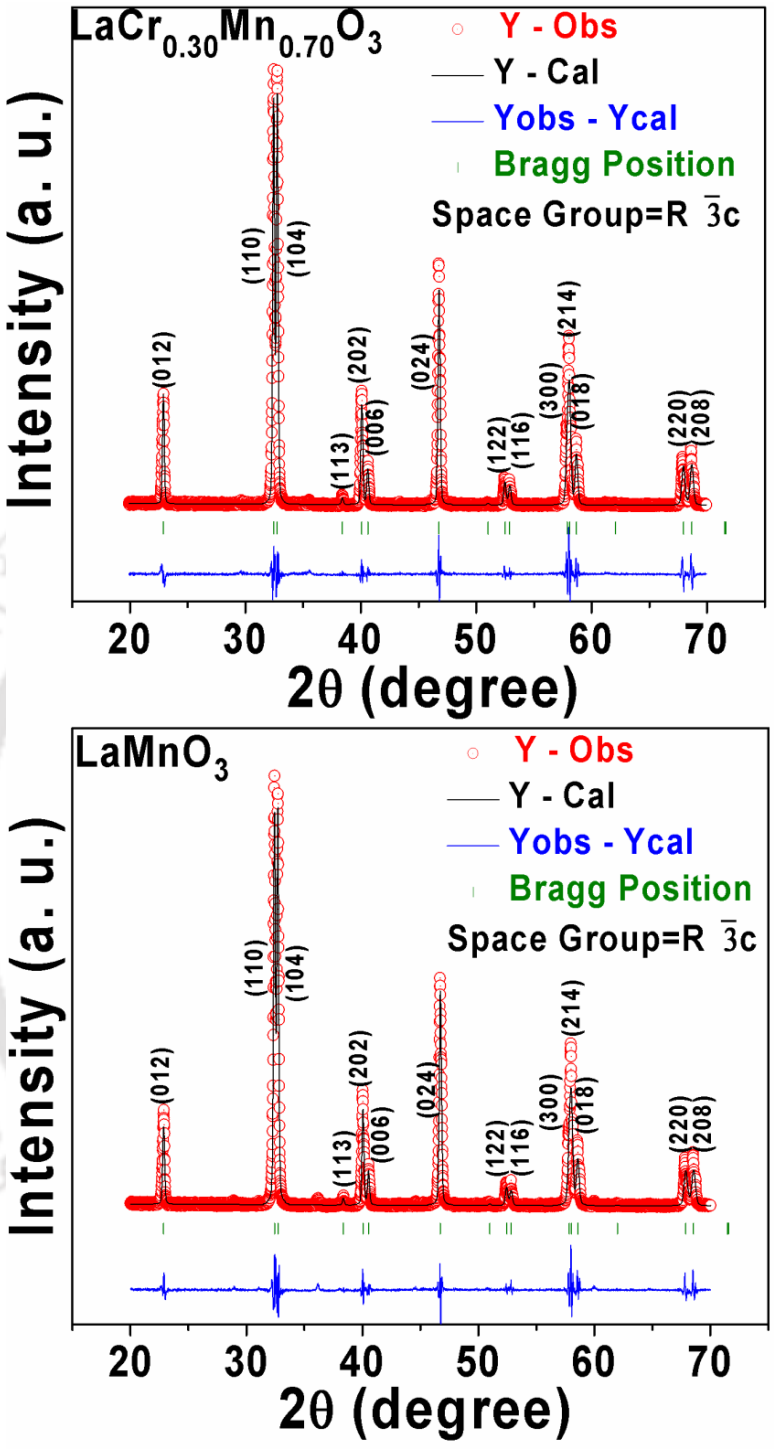

Figure 3.18: XRD patterns along with Rietveld refinement for x = 0.70 and 1.00 samples. The circles represent experimental data and solid line represents Rietveld refined data. The bottom line shows the difference between experimental and refined data. The marked 2θ positions are allowed Bragg peaks.

Table 3.3: Parameters obtained from the Rietveld analysis of XRD patterns for the samples $LaCr_{1-x}Mn_xO_3$ (0.00 to 1.00). R_F, R_{Bragg}, R_P, R_{exp} and χ^2 are the reliability factors.

Sample/ Parameters	***x* = 0.0**	***x* = 0.05**	***x* = 0.10**	***x* = 0.15**	***x* = 0.20**	***x* = 0.30**	***x* = 0.40**	***x* = 0.50**	***x* = 0.60**	***x* = 0.70**	***x* = 1.00**
Space group	*Pbnm*	*Pbnm*	*Pbnm*	*Pbnm*	*Pbnm*	*Pbnm*	*Pbnm*	*Pbnm*	$R\bar{3}c$	$R\bar{3}c$	$R\bar{3}c$
***a* (Å)**	5.5140 (0.0002)	5.5152 (0.0002)	5.5146 (0.0003)	5.5141 (0.0002)	5.5163 (0.0003)	5.5195 (0.0003)	5.5182 (0.0002)	5.5212 (0.0004)	5.5199 (0.0002)	5.5182 (0.0002)	5.5227 (0.0002)
***b* (Å)**	5.4779 (0.0002)	5.4796 (0.0002)	5.4788 (0.0002)	5.4790 (0.0002)	5.4819 (0.0003)	5.4841 (0.0003)	5.4796 (0.0002)	5.4727 (0.0004)	5.5199 (0.0002)	5.5182 (0.0002)	5.5227 (0.0002)
***c* (Å)**	7.7573 (0.0004)	7.7604 (0.0004)	7.7602 (0.0004)	7.7613 (0.0004)	7.7663 (0.0005)	7.7676 (0.0004)	7.7632 (0.0004)	7.7762 (0.0007)	13.3266 (0.0006)	13.3292 (0.0006)	13.3528 (0.0006)
***Volume* ($Å^3$)**	234.30 (0.02)	233.52 (0.02)	234.46 (0.02)	233.48 (0.02)	234.85 (0.02)	235.12 (0.02)	234.74 (0.02)	234.96 (0.03)	351.65 (0.02)	351.50 (0.02)	352.70 (0.02)
R_F (%)	3.83	4.71	5.24	4.27	4.55	4.57	4.54	8.10	2.59	2.11	2.54
R_{Bragg} (%)	4.09	4.82	5.19	3.92	3.95	4.68	3.76	8.39	2.85	2.42	2.73
R_P (%)	9.4	11.8	11.8	9.91	9.69	12.2	9.44	18.8	11.2	10.8	11.2
R_{exp} (%)	4.88	5.74	5.48	4.77	5.00	5.02	4.66	4.75	4..59	4.82	4.62
χ^2	15.1	13.8	15.1	15.1	14.0	15.5	14.1	29.9	14.5	12.5	14.1
La/Cr/Mn Occupancy	0.993 / 0.980 /0.000	0.977/ 0.937 /0.037	1.0000/ 0.897 / 0.097	0.965 /0.834 /0.134	0.919 /0.769 /0.169	0.943 /0.677 /0.277	0.950 /0.585 /0.385	0.920 /0.487 /0.487	0.949 /0.398 /0.598	0.967 /0.305 / 0.694	0.928 /0.000 /0.980

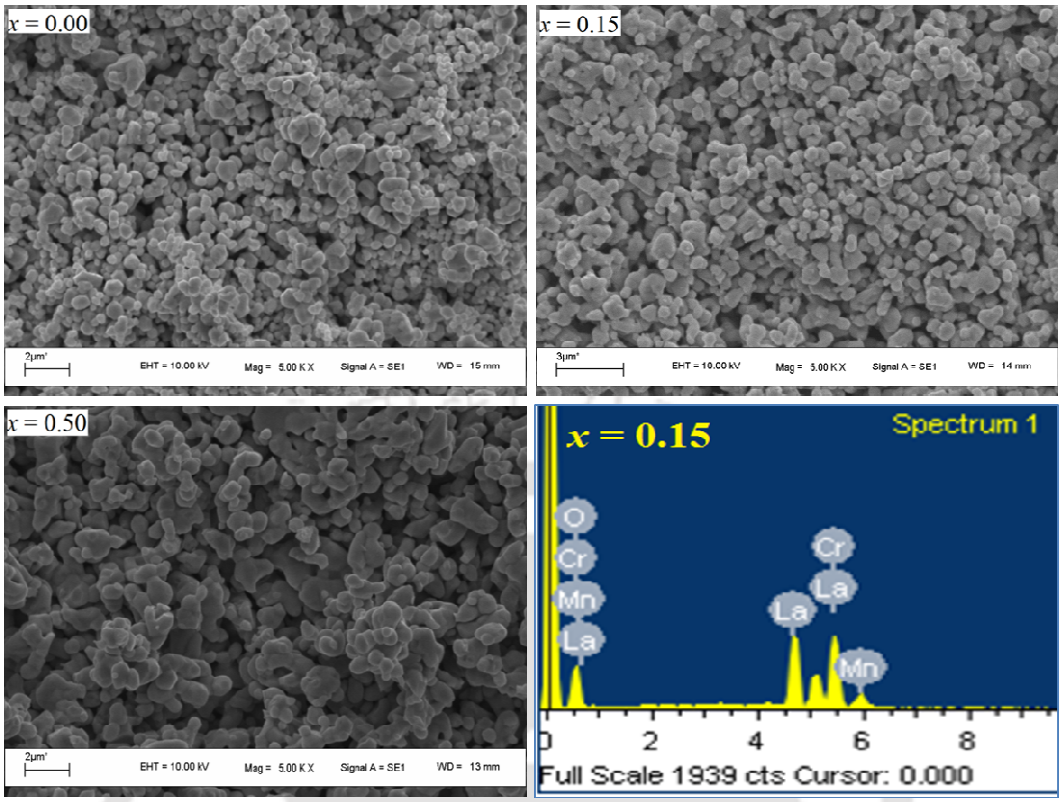

Figure 3.19: SEM images recorded for x = 0.00, 0.15 and 0.50 samples along with EDS spectrum for x = 0.15.

Table 3.4: The cationic ratio determined from EDS analysis for a few $LaCr_{1-x}Mn_xO_3$ samples.

Samples	**Calculated Cationic Ratio from EDS Analysis**		
	La	**Cr**	**Mn**
***x* = 0.00**	0.92	1.07	0.00
***x* = 0.15**	0.95	0.87	0.13
***x* = 0.20**	0.98	0.83	0.17
***x* = 0.30**	0.92	0.75	0.25
***x* = 0.40**	0.96	0.60	0.39
***x* = 0.50**	0.94	0.56	0.44
***x* = 0.70**	0.90	0.31	0.69

3.2.2 Magnetic Properties

The parent compound, $LaCrO_3$ exhibits AFM transition at T_N = 289 K followed by a weak FM signature due to spin canting and the result is comparable to the literature [83]. Magnetization (M) versus temperature (T) plots of x = 0.00, 0.05, 0.10, 0.15, 0.20, 0.30, 0.40, 0.50, 0.70 and 1.00 samples for the applied field H = 2000 Oe are shown in Fig. 3.20. Zero field cooled (ZFC) curve of x = 0.05 sample shows the presence of AFM transition at T_N = 282 K and for $T<T_N$, a weak FM component is seen similar to the case of parent compound. Around 50 K, it exhibits a sharp rise in magnetization due to a possible magnetic transition involving the interaction between Mn^{3+} and Cr^{3+} ions. Such behavior was not observed in the parent compound. The field cooled (FC) curve bifurcates from the ZFC curve at $T < T_N$ due to the enhancement of spin canted FM component of Cr^{3+} ions. A secondary rise in magnetization at T < 150 K can be seen followed by a peak. This trend can be assigned to the PM behavior of doped Mn^{3+} ions. The M value tends to decrease at $T \leq 70$ K but it is overtaken by the low temperature transition. The x = 0.10 sample behaves in a similar manner but with a difference that M value is found to be an order of magnitude larger than that of x = 0.05 sample, especially at T < 50 K. The bifurcation between ZFC and FC curves can be clearly seen from the inset of Fig. 3.20 (b) and (c).

The M-T plot of x = 0.15 sample under the FC condition shows an interesting property of magnetization reversal with a compensation temperature T_{comp} = 80 K. A minimum magnetization value of, M_{min} = -14 emu/mol is observed at T_{min} = 58 K. At $T < T_{min}$, M rises sharply towards the positive value due to the low temperature ordering. So the FC M-T curve crosses the M = 0 axis twice, giving rise to two compensation temperatures. For x = 0.20 sample, on lowering the temperature from 300 K, the FC curve bifurcates from the ZFC curve with a broad hump around 190 K (shown in inset Fig. 3.20 (e)) and for further decrease in temperature, it continuously decreases towards negative value by crossing the ZFC curve at T_{cross} = 165 K and reaching the magnetic compensation point M = 0 at T_{comp} = 139 K. Thus the FC magnetization exhibits the interesting magnetization reversal phenomenon. The minimum magnetization value is found to be -67.50 emu/mol at T_{min} = 57 K. For $T < T_{min}$, a sharp rise in M value is observed similar to that of x = 0.15. At the end of

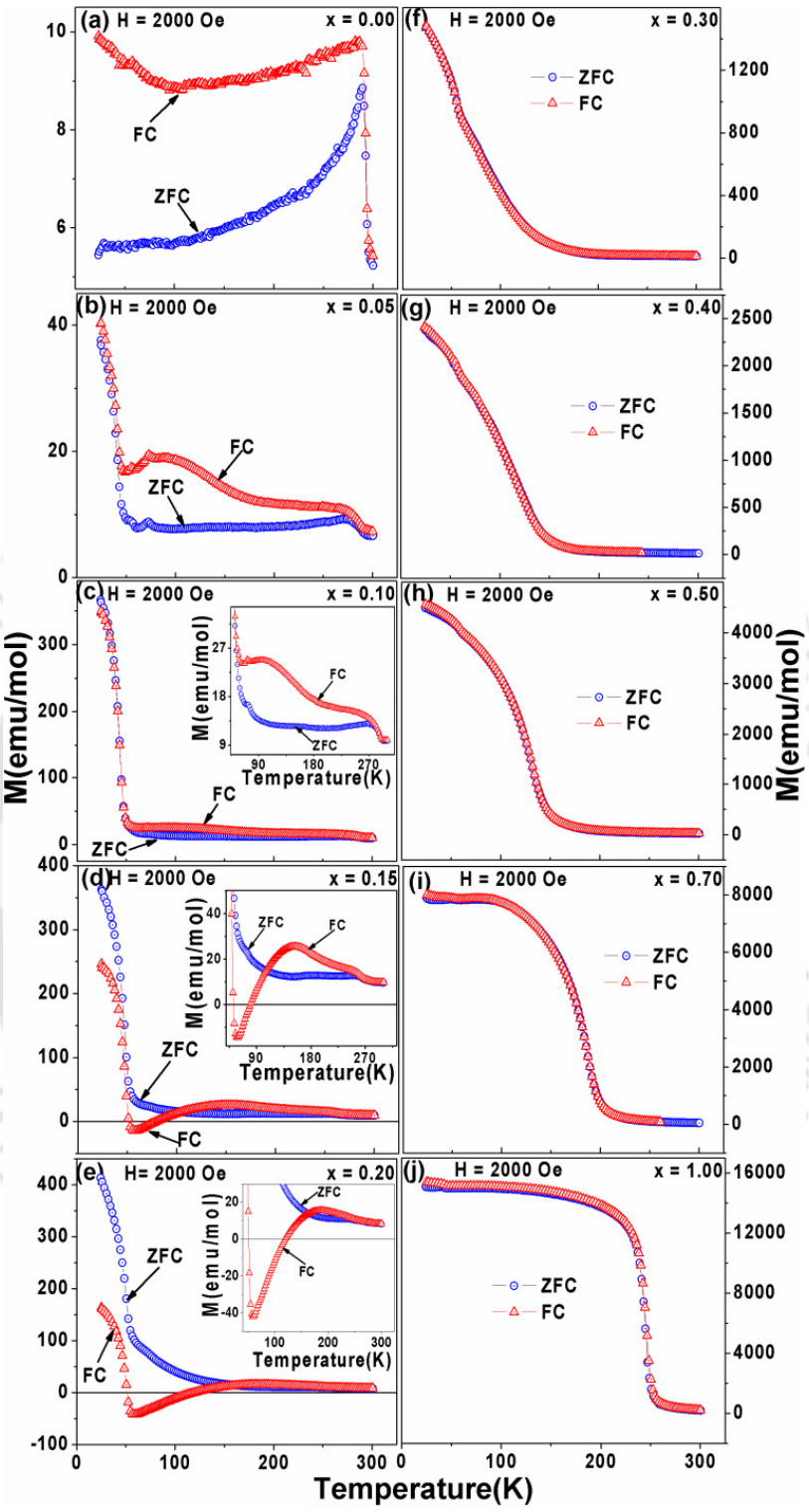

Figure 3.20: Temperature variation of magnetization for zero field cooled (ZFC) and field cooled (FC) conditions for x = 0.00, 0.05, 0.10, 0.15, 0.20, 0.30, 0.40, 0.50, 0.70 and 1.00 samples (a to j).

the low temperature transition, *M* has reverted back to positive values. Thus the FC *M-T* curve exhibits magnetic compensation at two different temperatures; one during the magnetization reversal from positive to negative values (139 K) and another during the transition from the negative to positive values (50 K).

As we increase the Mn concentration further ($x > 0.20$), we have observed the ferromagnetic transition due to the presence of Mn^{3+}-O^{2-}-Cr^{3+} and Mn^{3+}-O^{2-}-Mn^{4+} networks.

(i) Magnetization Reversal and Exchange Bias Studies in $LaCr_{1-x}Mn_xO_3$ (x = 0.15 and 0.20)

In view of the interesting magnetic property of $x = 0.15$ and 0.20 samples, we have taken up detailed *M-T* measurements under FC condition by varying the cooling field *H* from 50 Oe to 5000 Oe. Typical *M-T* plots for *H* = 200 Oe to 2000 Oe for $x = 0.15$ and 0.20 samples are shown in Fig. 3.21 and Fig. 3.22 respectively. The T_{comp} value is found to decrease with increase in *H* value and is found to be in the range of 95 K for *H* = 200 Oe to 67 K for *H* = 3000 Oe for $x = 0.15$ sample and, 147 K for *H* = 200 Oe to 120 K for *H* = 2000 Oe for $x = 0.20$ sample. No magnetization reversal was observed for *H* > 3000 Oe. The T_{comp} value is comparable to that of rare earth doped $LaCrO_3$ compounds [15, 53, 90, 92]. With increase in *H* value, the entire *M-T* curve is found to shift towards positive magnetization axis without any appreciable change in *M-T* behavior. This is due to the enhancement in the canted FM component of Cr^{3+} ions and such shifting gives rise to reduction in T_{comp} value.

The observed negative magnetization can be explained by considering the competition between the weak canted FM component of Cr^{3+} ions (M_{Cr}) and the paramagnetic behavior of doped Mn^{3+} ions under the influence of negative internal field (H_I) due to AFM ordered Cr^{3+} ions. According to this model, the measured FC magnetization (*M*) can be fitted to the equation (3.1). The fitted data are shown as solid line in Fig. 3.21 and 3.22. θ_C values are found to vary from 30 K to 40 K. The estimated values of M_{Cr} and the magnitude of H_I as a function of applied field *H* are shown in Fig. 3.23. Both M_{Cr} and negative H_I values are found to increase with increase in applied field. The size of AFM domains is expected to increase with increase in applied field and that gives rise to increase in H_I and M_{Cr} values.

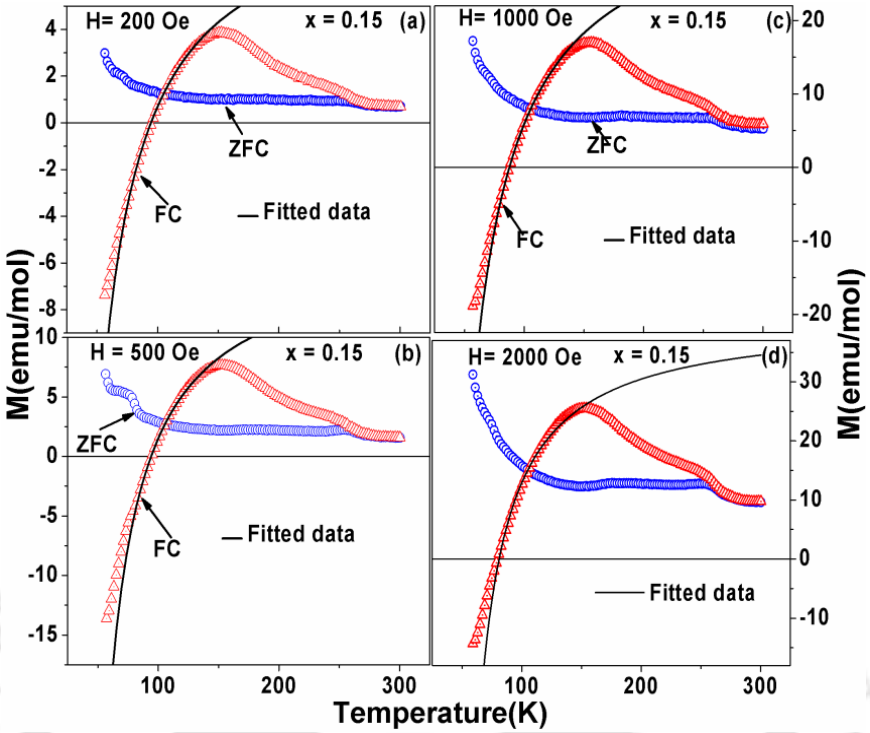

Figure 3.21: ZFC and FC *M-T* curves of $x = 0.15$ sample at (a) $H = 200$ Oe (b) $H = 500$ Oe, (c) $H = 1000$ Oe and (d) $H = 2000$ Oe.

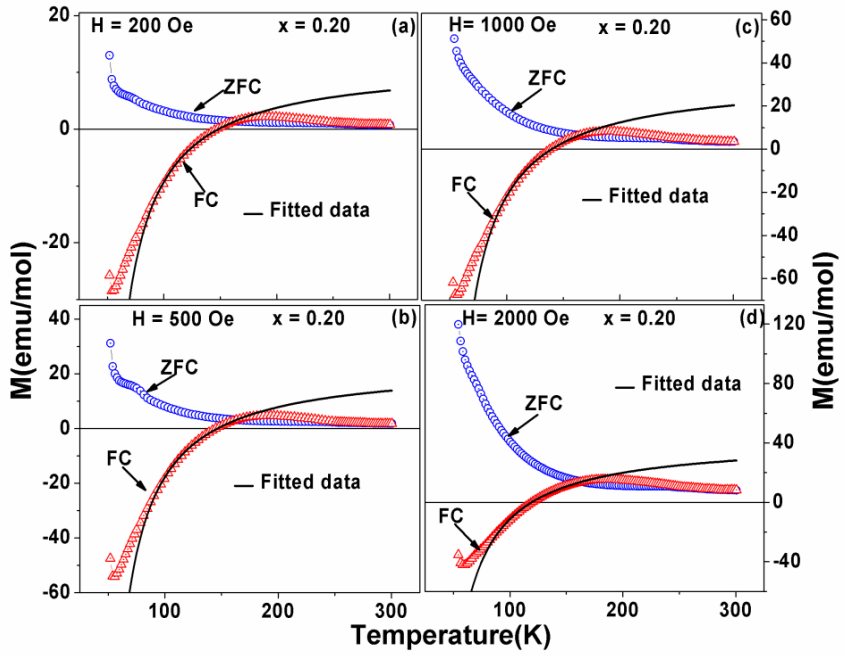

Figure 3.22: ZFC and FC *M-T* curves of $x = 0.20$ sample at (a) $H = 200$ Oe (b) $H = 500$ Oe, (c) $H = 1000$ Oe and (d) $H = 2000$ Oe.

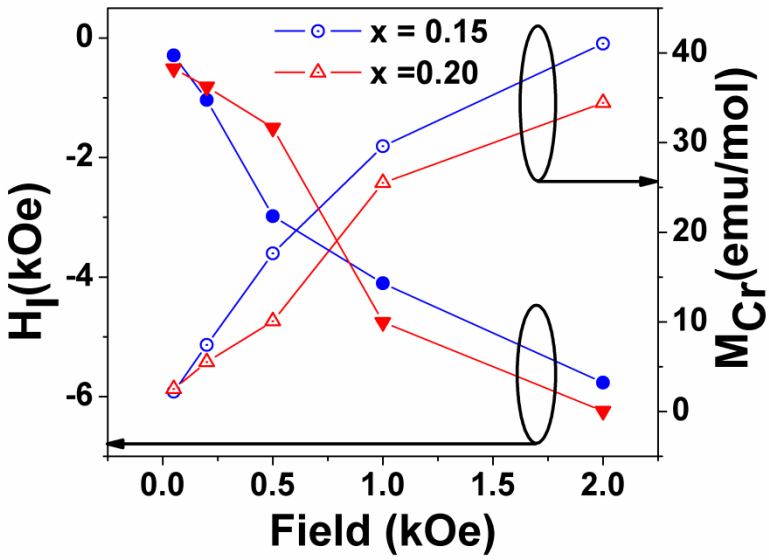

Figure 3.23: M_{Cr} and H_I as a function of applied field for x = 0.15 and 0.20 samples.

The ratio of minimum (negative) and maximum (positive) magnetization value, $\frac{M_{min}}{M_{max}}$ is found to be 2 for x = 0.15 sample at H = 200 Oe. The relative irreversible magnetization, $\frac{\Delta M}{M_{ZFC}} = \frac{M_{FC} - M_{ZFC}}{M_{ZFC}}$ was calculated and its maximum negative value is -3.7 for H = 200 Oe. These values in magnetic rare earth chromites are found to be in the range of ~ -2 to -9 [15, 90].

The observed interesting property of magnetization reversal with relatively large compensation temperature prompted us to explore the existence of exchange bias phenomenon in x = 0.15 and 0.20 samples. *M-H* loops were recorded at several temperatures after field cooling through T_N with H = 5000 Oe to the desired temperature. Representative plots of *M-H* loops at a few selected temperatures in an expanded scale for clarity are shown in Fig. 3.24 and 3.25.

The *M- H* loops of x = 0.15 sample in the temperature region T > 50 K are found to be elliptical in shape which indicate the predominant AFM nature of material with some canted FM component. At lower temperatures, the *M-H* loops are found to shift towards the positive field axis and when the temperature is increased they are found to shift in the opposite direction, *i.e.* along the negative field axis. So, there is a change in the sign of EB with

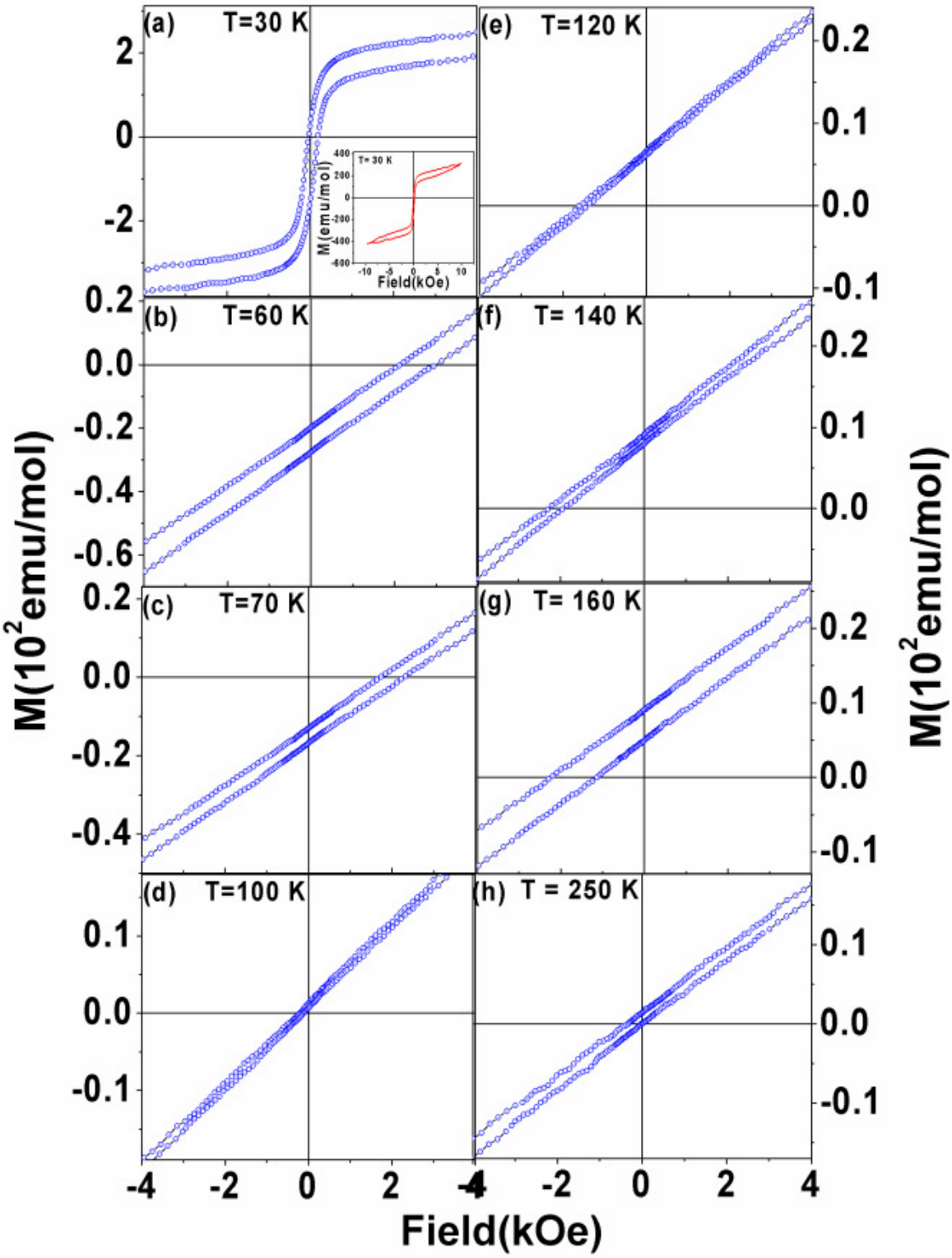

Figure 3.24: *M-H* loops of $x = 0.15$ sample at (a) 30 K, (b) 60 K, (c) 70 K, (d) 100 K, (e) 120 K, (f) 140 K, (g) 160 K and (h) 250 K.

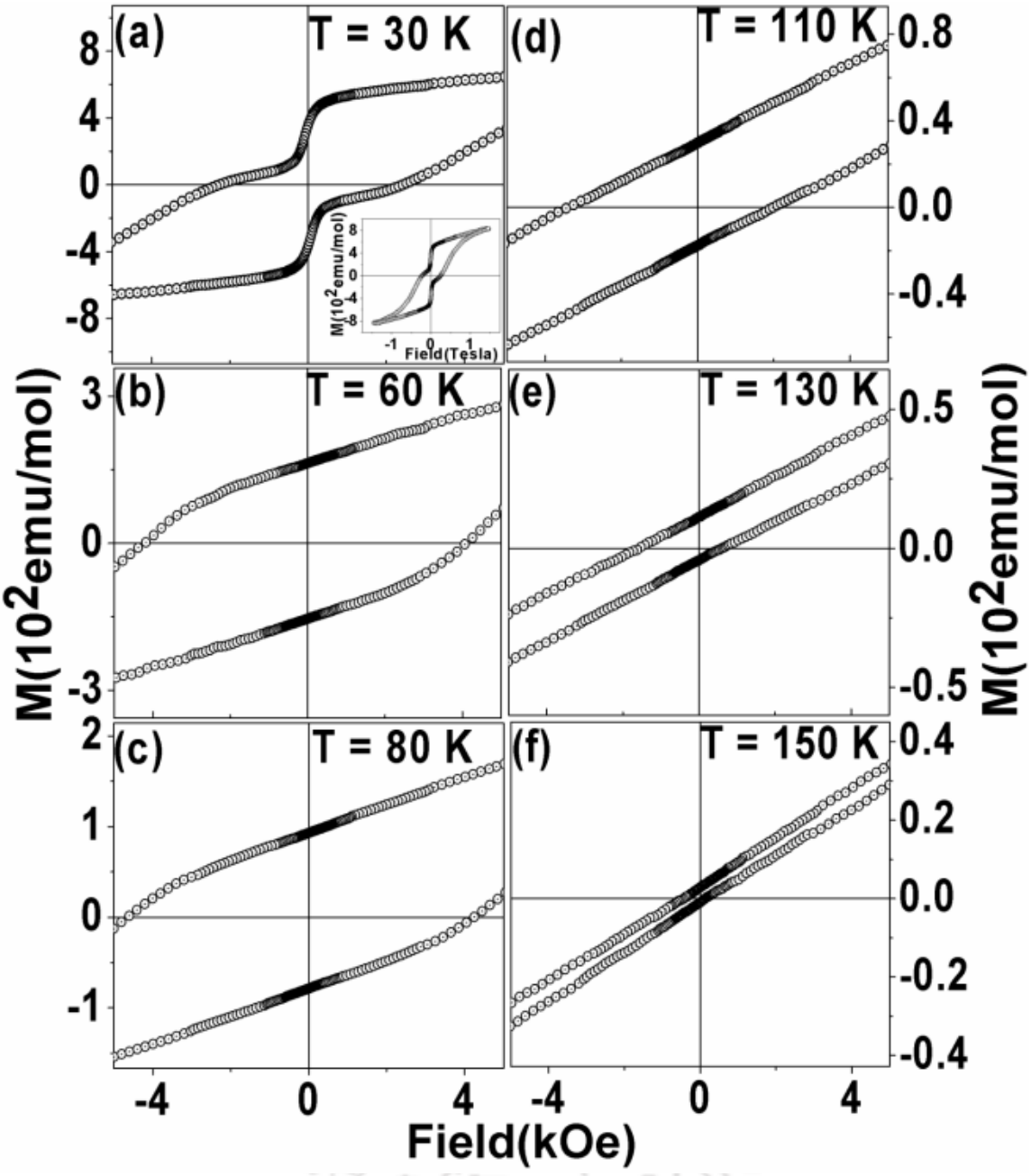

Figure 3.25: *M-H* loops of $x = 0.20$ sample at (a) 30 K, (b) 60 K, (c) 80 K, (d) 110 K, (e) 130 K and (f) 150 K.

variation in temperature. The loop at 30 K shows larger FM component as shown in Fig. 3.24 (a) and is consistent with the observed low temperature transition from *M-T* measurement. On the otherhand, the high coercivity nature of *M-H* loops of $x = 0.20$ sample indicates the presence of large canted FM component of Cr^{3+} ions. Shifting of *M-H* loops towards the

negative field axis is observed in the temperature range 50 K to 165 K. The *M-H* loop at 30 K exhibit relatively large FM component along with a step like behavior as shown in Fig. 3.25 (a) and is consistent with the observed low temperature transition in the *M-T* plot.

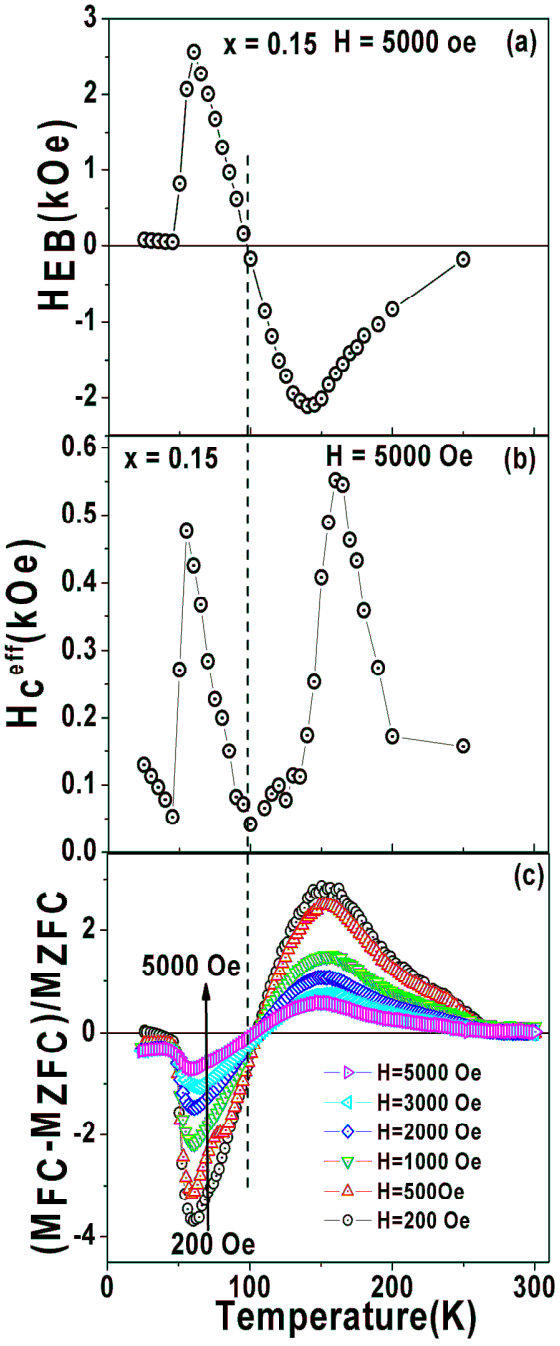

Figure 3.26: Temperature variations of (a) H_{EB}, (b) H_c^{eff} and (c) irreversible magnetization of $x = 0.15$ sample.

The values of H_{EB} and the effective coercive field (H_c^{eff}) were determined using the equations (3.4) and (3.5). The temperature dependence of H_{EB} of $x = 0.15$ sample is shown in Fig. 3.26 (a). As the temperature is lowered from T_N, negative H_{EB} is observed with its magnitude increasing with decrease in temperature and reaching a maximum negative value of H_{EB} = -2.1 kOe at T = 140 K. Thereafter, H_{EB} moves towards positive value by undergoing a sign reversal at T_{comp} and reaching a maximum positive value of 2.6 kOe at 60 K. For $T <$ 60 K, there is a sharp fall in H_{EB} to zero. The maximum H_{EB} value of the present sample is comparable to the values reported in $NdMnO_3$ [72] and $La_{0.15}Pr_{0.85}CrO_3$ [73]. Temperature variation of H_c^{eff} shows two peaks positioned on either side of T_{comp} with a minimum value at T_{comp}. The observed sign reversal of H_{EB} across T_{comp} and twin peaks of H_c^{eff} echo the reports on $Sm_{0.98}Gd_{0.02}Al_2$ [82] and $Nd_{0.75}Ho_{0.25}Al_2$ [81] intermetallic alloys, and $Co(Cr_{0.95}Fe_{0.05})_2O_4$ spinel compound [124]. For a comparison, temperature variations of irreversible magnetization $\frac{\Delta M}{M_{ZFC}}$ are shown in Fig. 3.26 (c) for different H values. All curves pass through a fixed cross over temperature T_{cross}. Positive and negative peaks are observed at $T > T_{cross}$ and $T < T_{cross}$ respectively and they coincide with negative and positive peak of H_{EB} in the respective temperature region.

The EB reversal around T_{comp} in the $x = 0.15$ sample can be explained by considering the AFM interaction between the FM component of Cr^{3+} ions (M_{Cr}) and the PM component of doped Mn^{3+} ions (M_{Mn}) under the influence of negative internal field. In the temperature region $T_{comp} < T < T_N$, M_{Cr} due to spin canting aligns along the applied field direction H while M_{Mn} aligns towards H_I but antiparallel to H as depicted in Fig. 3.27. In this temperature region, M_{Cr} dominates over M_{Mn} and the interaction between these two moments gives rise to net positive magnetization and negative exchange bias, similar to any FM/AFM interface. On the other hand, for $T < T_{comp}$, M_{Mn} dominates over M_{Cr} due to the enhanced PM moment of Mn^{3+} ions at low temperature. Even at $T < T_{comp}$, there is an AFM interaction between M_{Cr} and M_{Mn} moments but with a difference that M_{Mn} dominates over M_{Cr} and this leads to positive exchange bias. The large PM component of Mn^{3+} ions along the H_I direction can be visualized as FM domains aligned opposite to the applied field direction and in such

arrangement, larger positive field is required to bring the magnetization towards zero and positive value. So, basically the entire *M-H* loop is shifted towards positive *H* axis and hence positive exchange bias effect is seen.

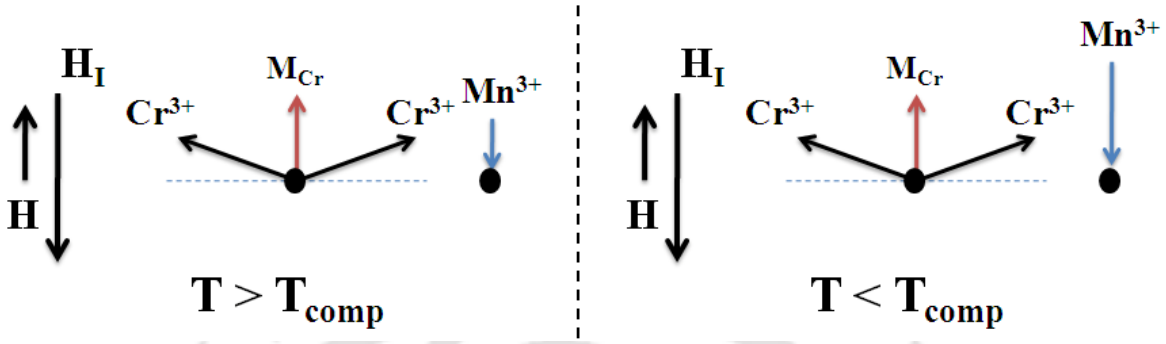

Figure 3.27: Schematic diagram of the arrangement of canted Cr^{3+} moments and the PM component of Mn^{3+} moments at $T > T_{comp}$ and $T < T_{comp}$ for $x = 0.15$ sample.

Even though, the phase reversal of H_{EB} observed in the present sample resembles the result of intermetallic compounds [81, 82], there is a subtle difference between them. In intermetallic compounds, phase reversal of H_{EB} is observed only close to T_{comp} and away from that $H_{EB} \approx 0$ and on the other hand, H_{EB} is observed for a wide temperature range in the present sample. So, the mechanism involved in the present sample is quite different. In intermetallics, reversal in the orientation of different sub components of magnetic moment of rare earth ions and conduction electron polarization gives rise to magnetization reversal. On the other hand, here no such reversal in the orientation of each component of magnetic moment is expected and it is simply one component (M_{Mn}) overtaking the other component (M_{Cr}) due to temperature variation. So, there is a gradual change in H_{EB}. Another, distinct feature observed in the present sample is, a sharp fall of H_{EB} towards zero at $T < 60$ K and this is triggered by the low temperature magnetic ordering or spin reorientation that is clearly seen in both ZFC and FC *M-T* plots. The low temperature magnetic ordering ($T < 50$ K) is likely to disturb and weaken the anisotropic exchange interaction between M_{Cr} and M_{Mn} and as a result, the exchange bias field is reduced to zero.

The observed result can be compared with the report on $NdMnO_3$ by Hong *et al.* [72]. They have studied the field induced sign reversal of H_{EB} at $T = 30$ K and 8 K. If we consider their result for a fixed field of $H = 5000$ Oe, there is a sign reversal of H_{EB} from -2.3 kOe at

30 K to +0.15 kOe at 8 K. AFM interaction between the canted FM component of Mn^{3+} ions and the FM component of Nd^{3+} ions gives rise EB and the sign reversal is induced by the long range FM ordering of Nd^{3+} ions at low temperature. Even though, Yoshii *et al.* [73] have not reported any sign reversal of H_{EB} with respect to change in temperature in $La_{0.15}Pr_{0.85}CrO_3$, the sign of H_{EB} at $T < T_{comp}$ is reported to be positive for low field cooling and is consistent with the present result. In nanoparticles, core-shell structure configuration is known to play a role in sign reversal of EB [53] and such mechanism is not applicable for the present sample.

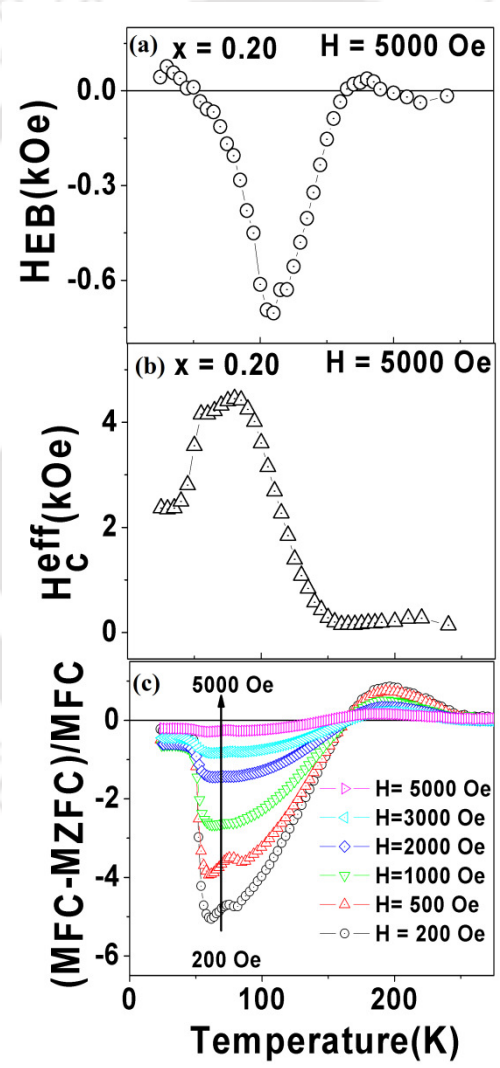

Figure 3.28: Temperature variations of (a) H_{EB}, (b) H_c^{eff} and (c) irreversible magnetization of $x = 0.20$ sample.

The temperature dependence of H_{EB} of $x = 0.20$ sample as shown in Fig. 3.28(a) exhibits a negative peak (valley) around T_V = 110 K and the corresponding H_{EB} value is -0.71 kOe. Appreciable H_{EB} values are observed only in the temperature range, 50 K < T < T_{comp}. H_c^{eff} versus temperature plot exhibits a peak at 80 K and its maximum value is found to be 4.5 kOe. However, a sharp fall in H_c^{eff} around 50 K brings down the H_c^{eff} value close to 2.4 kOe. No appreciable H_c^{eff} value is observed for $T > T_{comp}$. For comparison, we have also plotted the temperature dependence of relative irreversible magnetization $(M_{FC} - M_{ZFC})/M_{ZFC}$ for different values of applied magnetic field as shown in Fig. 3.28(c). All curves pass through a fixed cross over temperature T_{cross} = 165 K. Broad positive peak of small magnitude at $T > T_{cross}$ and negative peak at $T < T_{cross}$ are observed. At $T \leq 50$ K, the magnitude of irreversibility exhibits a sharp fall and approaches close to zero and it is due to the low temperature magnetic transition. Gradual suppression of relative irreversibility with increase in applied field can be seen.

The observed behavior of H_{EB} as a function of temperature can be explained by considering the anisotropic exchange interaction between the FM component of canted Cr^{3+} ions, (M_{Cr}) and the PM component of Mn^{3+} ions (M_{Mn}) under the influence of negative internal field. As the temperature is lowered from T_N to ~ T_{comp}, no appreciable H_{EB} value is observed, this is mainly due to a weak anisotropic exchange interaction between M_{Cr} and M_{Mn} as a result of small M_{Mn} values at higher temperature. For $T < T_{comp}$, due to the enhanced values of M_{Mn}, magnitude of H_{EB} increases with decrease in temperature and this trend continues down to ~ 110 K. On further lowering of temperature, the magnitude of H_{EB} decreases and approaches close to zero at around 50 K. This is consistent with low temperature transition observed in M-T plots (Fig. 3.20 (e)). There is a possibility that some of the Mn^{3+} ions are engaged in the long range magnetic interaction in Mn^{3+}-O^{2-}-Cr^{3+} networks and such interaction gives rise to reduction in M_{Cr} and M_{Mn} and their anisotropic exchange interaction. The temperature dependence H_c^{eff} can be also understood from the above argument. The H_{EB} value is comparable to the result of $La_{0.15}Pr_{0.85}CrO_3$ [73], where H_{EB} was observed only for $T < T_{comp}$.

(ii) Ferromagnetism in $LaCr_{1-x}Mn_xO_3$ ($x \geq 0.30$)

As depicted in Fig. 3.20, *M-T* plots of $LaCr_{1-x}Mn_xCrO_3$ samples for $x \geq 0.30$ exhibit FM behavior. The ferromagnetic T_C was determined from the plot of *dM/dT* versus *T*. Typical *dM/dT* versus *T* plots for $x = 0.50$, 0.60, 0.70 and 1.00 are shown in Fig. 3.29 where they exhibit negative peak indicating the ferromagnetic transition. The values of FM T_C for $x \geq 0.40$ samples are given in Table 3.5 and they increase with increase in Mn concentration which reflects the increase in double exchange FM interaction.

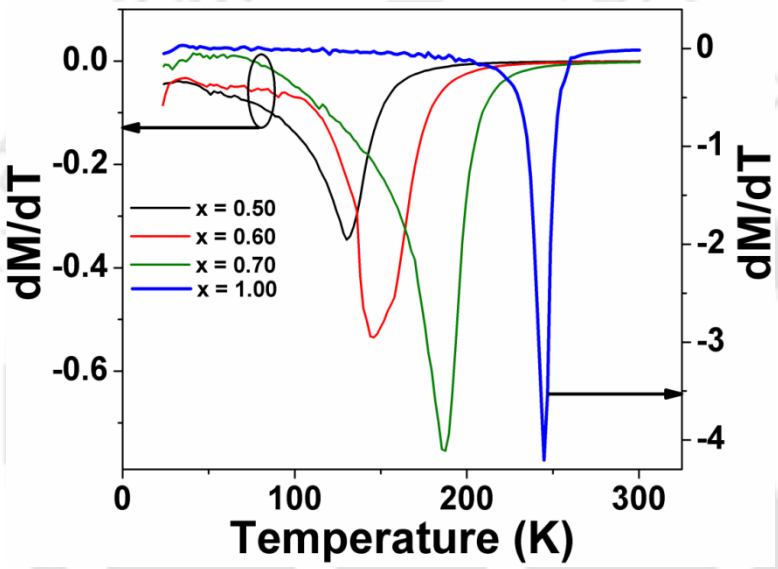

Figure 3.29: *dM/dT* versus *T* plots for $x = 0.50$, 0.60, 0.70 and 1.00 samples.

Temperature variation of inverse dc susceptibility for $x = 0.30$ to 1.00 samples are shown in Fig. 3.30. We can see the linear behavior in the paramagnetic region. The dc susceptibility in the paramagnetic region was analyzed by Curie Weiss law, $\chi = \frac{C}{(T - \theta_C)}$ for all samples except for $x = 0.30$ because the linear (paramagnetic) behavior was observed in a narrow temperature region. The Curie temperature θ_C values for $0.40 \leq x \leq 1.00$ samples are found to be positive and indicate the FM nature of transition.

The fitted data are shown as solid lines in Fig. 3.30 and they closely follow the experimental data. The difference between the T_C and θ_C are mainly due to the observed broad magnetic transition. The effective magnetic moment, μ_{eff} was determined from the

fitted values of Curie constant C by using the relation $\mu_{eff} = \sqrt{\frac{3k_B C}{N_A \mu_0 \mu_B^2}}$ and are given in Table 3.5. The effective paramagnetic moment is found to increase with increase in Mn concentration and such variation could be understood in terms of Mn^{3+} ions of paramagnetic moment 4.90 μ_B replacing the Cr^{3+} ions of paramagnetic moment 3.87 μ_B.

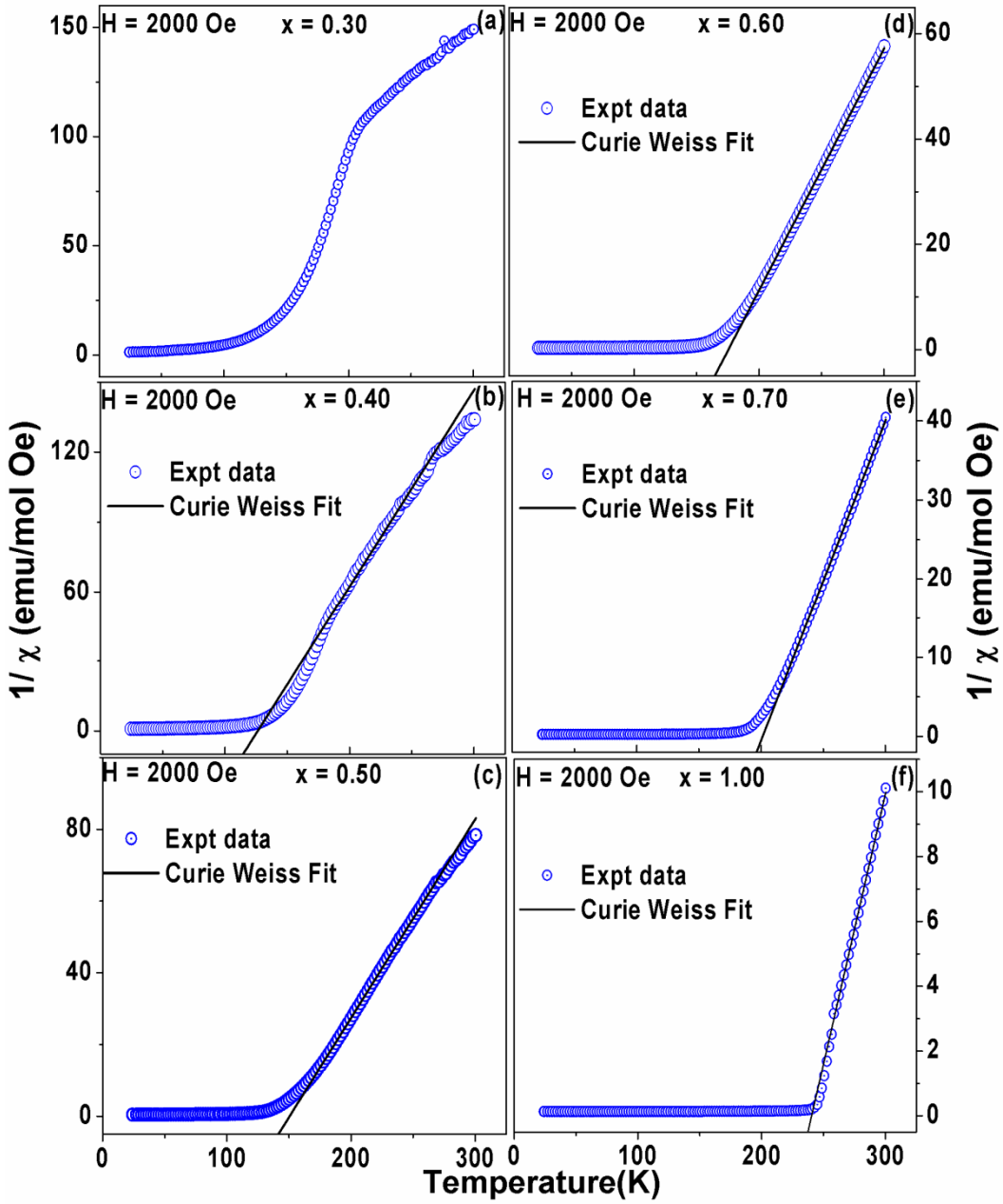

Figure 3.30: 1/ χ versus temperature for the samples (a) x = 0.30, (b) x = 0.40, (c) x = 0.50, (d) x = 0.60, (e) x = 0.70 and (f) x = 1.00 samples.

Table 3.5: Parameters obtained from the magnetization measurement of $LaCr_{1-x}Mn_xO_3$. T_C is the ferromagnetic transition temperature. θ_C (Curie temperature), C (Curie constant) and μ_{eff} (effective magnetic moment) have been obtained from the fit of Curie-Weiss law.

Samples/ Parameters	x = 0.40	x = 0.50	x = 0.60	x = 0.70	x = 1.00
T_C (K)	128 ± 2	130 ± 1	145 ± 1	186 ± 1	244 ± 1
θ_C (K)	126 ± 3	150.5 ± 0.5	175.5 ± 0.5	201.3 ± 0.9	240 ± 2
C (emu K/mol Oe)	1.18 ± 0.02	1.805 ± 0.004	2.179 ± 0.006	2.468 ± 0.001	6.008 ± 0.004
μ_{eff} (μ_B/f.u.)	3.075 ± 0.002	3.799 ± 0.005	4.174 ± 0.005	4.441 ± 0.001	6.930 ± 0.002
μ_{th} (μ_B/f.u.)	4.184	4.259	4.332	4.404	4.615
M_S (μ_B/f.u.)	0.689 ± 0.003	0.970 ± 0.002	1.275 ± 0.003	1.907 ± 0.005	3.720 ± 0.002
$M_{S.th}$ (μ_B/f.u.)	1.3	1.7	2.1	2.5	3.7

The theoretical moment, μ_{th} can be estimated by using the relation,

$$\mu_{th}^2 = (1-x)\mu_{Cr^{3+}}^2 + x[0.7\mu_{Mn^{3+}}^2 + 0.3\mu_{Mn^{4+}}^2] \quad (3.8)$$

where, x is the Mn concentration. $\mu_{Cr^{3+}}$, $\mu_{Mn^{3+}}$ and $\mu_{Mn^{4+}}$ are the theoretical magnetic moments of Cr^{3+}, Mn^{3+} and Mn^{4+} ions and their values due to spin only contribution are 3.87 μ_B, 4.90 μ_B and 3.87 μ_B respectively. Here it is assumed that 70 % of doped ions are in Mn^{3+} state and 30% are in Mn^{4+} state. The estimated μ_{th} and μ_{eff} are comparable and the slight deviation is present and that could be mainly due to the oxygen off stoichiometry or the deviation in Mn^{3+}/Mn^{4+} concentration. The experimental μ_{eff} value of x = 1.00 sample is

found to be considerably larger than that of μ_{th} as shown in Table 3.5 and it could be mainly due to the presence of some isolated FM clusters.

The *M-H* loops recorded at 25 K for x = 0.30, 0.40, 0.50, 060, 0.70 and 1.00 samples are shown in Fig. 3.31. The magnetization value is found to increase with increase in Mn concentration and the coercive field (H_C) decreases. It can be understood in terms of enhanced double exchange ferromagnetic interaction, as a result of generation of Mn^{4+} ions.

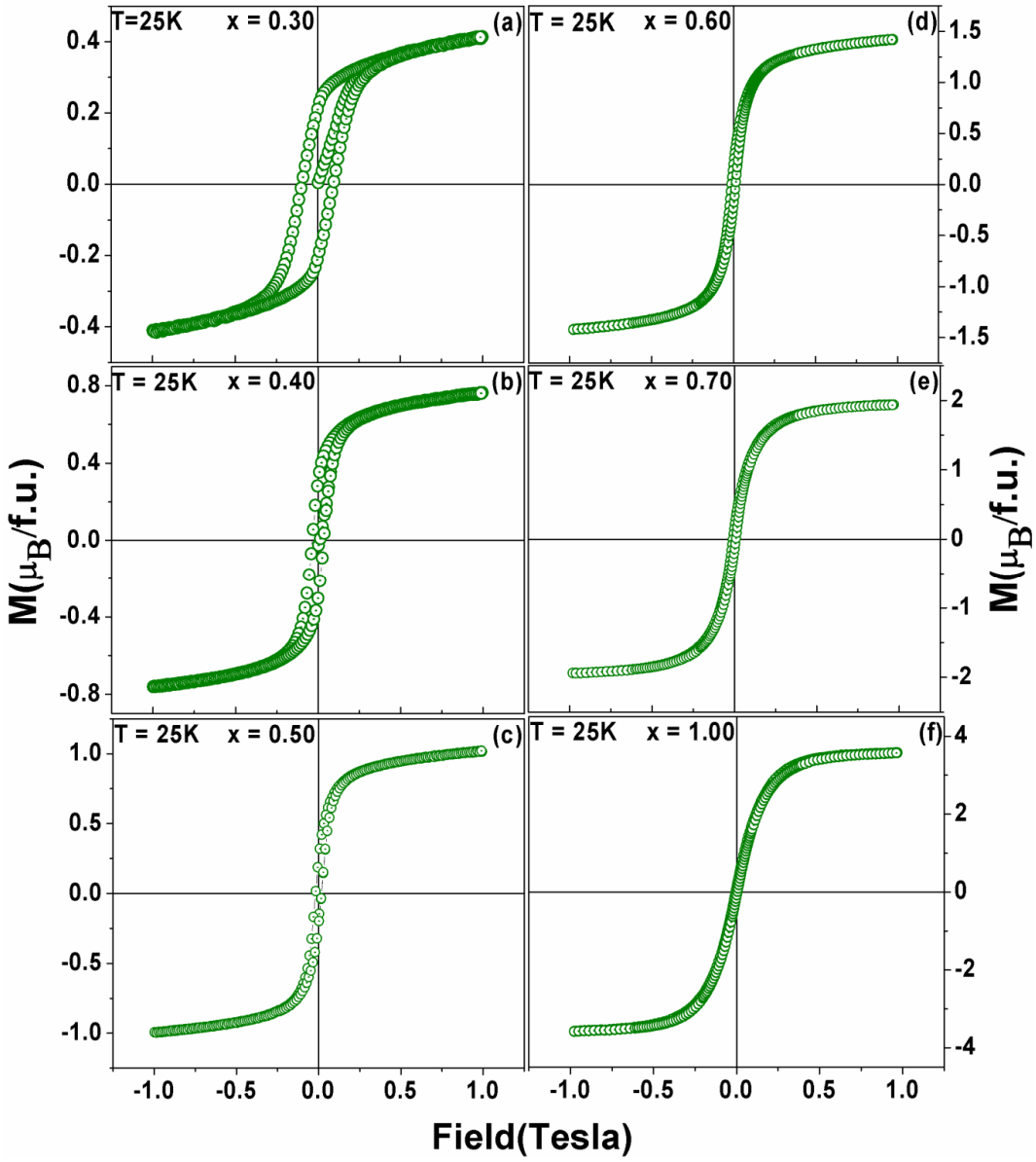

Figure 3.31: Magnetization versus magnetic field plots of the samples x = 0.30, 0.40, 0.50, 0.60, 0.70 and 1.00.

The saturation magnetization (M_S) can be calculated from the following equation [21],

$$M(H) = M_S\left[1 - \frac{a}{H} + \frac{b}{H^2}\right] + \chi_d H \qquad (3.9)$$

Where, χ_d is the high field differential susceptibility and, a and b are constants. The initial isothermal magnetization curves of x = 0.30 to 1.00 samples were fitted to equation (3.9) as shown in Fig. 3.32. The saturation magnetization values of all these samples are given in Table 3.5.

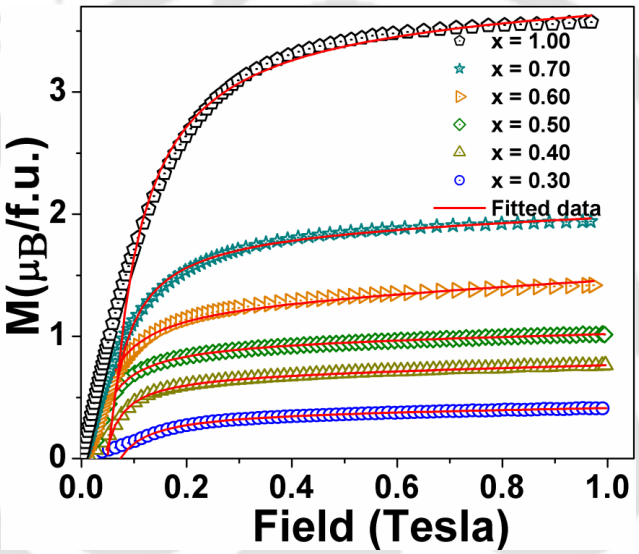

Figure 3.32: Initial *M-H* curves for x = 0.30 to 1.00 samples along with fit to equation (3.9).

The M_s value of x = 1.00 sample suggests that in this sample 70 % Mn^{3+} ions and 30 % Mn^{4+} ions are present. Except for x = 1.00 sample, the experimental M_S values are quite small compared to the expected ferromagnetic M_S value. This suggests that there is a presence of competing AFM in these samples and also due to the lack of optimum Mn^{3+}/Mn^{4+} concentrations.

3.2.3 Critical Exponent Analysis

The highest ferromagnetic T_C in the Mn doped $LaCrO_3$ was observed for x = 0.70 (other than the parent compound $LaMnO_3$). In order to understand the nature of

ferromagnetic interaction we have carried out isothermal magnetization measurement at closer temperature interval in the vicinity of FM T_C as described below and the critical exponent analysis was carried out.

The sample was cooled down to the measuring temperature in the absence of any external magnetic field. Isothermal magnetization as a function of magnetic field was measured at different temperatures with 1 K interval in the immediate vicinity of T_C, *i.e.* 170 K ≤ T ≤ 195 K and with 2 K interval outside that region. The entire critical region (160 – 205 K) was covered to see the continuous transition from FM to PM state. The effective intrinsic magnetic field $H = (H_{ext} - N_dM)$, was used for the scaling analysis. Here, N_d is the demagnetization factor and is taken as 4π/3 for spherical sample. H_{ext} is the external applied field. The isothermal magnetization curves for x = 0.70 sample in the temperature range 160 K to 205 K are shown in Fig. 3.33. A gradual transition from FM to PM state with increase in temperature can be clearly seen.

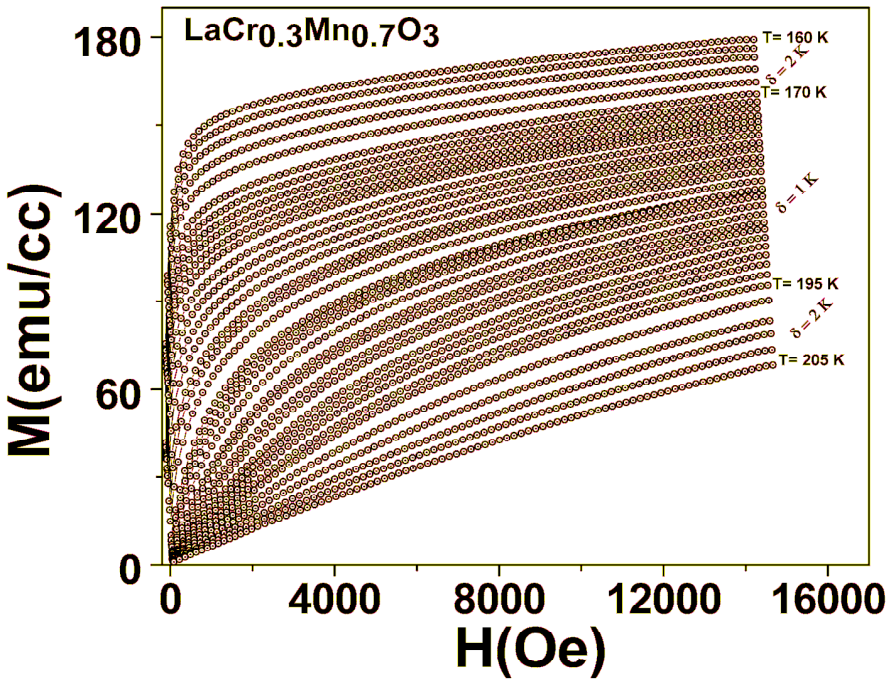

Figure 3.33 Isothermal magnetization as a function of magnetic field for x = 0.70 sample.

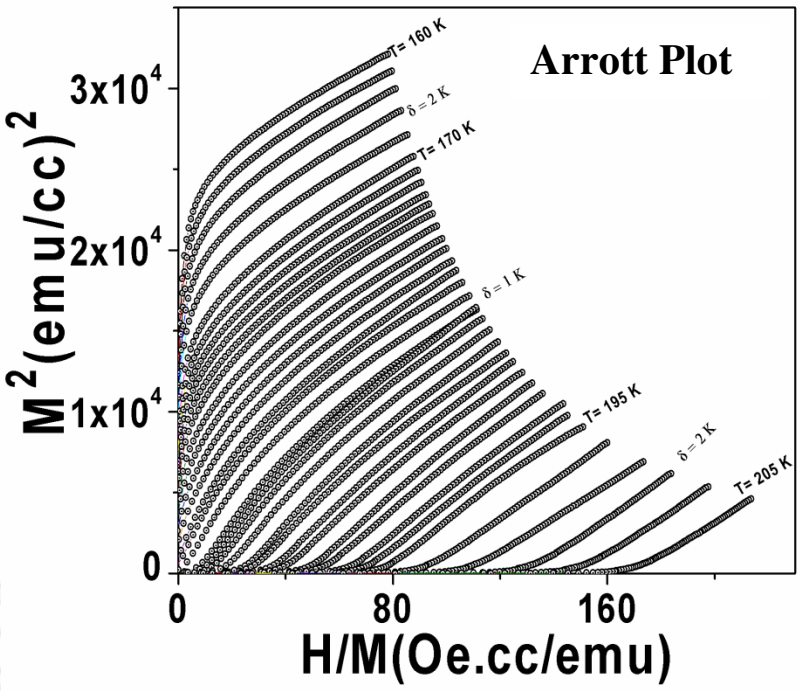

Figure 3.34: Arrott plots (M^{2} versus H/M) of $x = 0.70$ sample in the temperature range 160 K to 205 K.

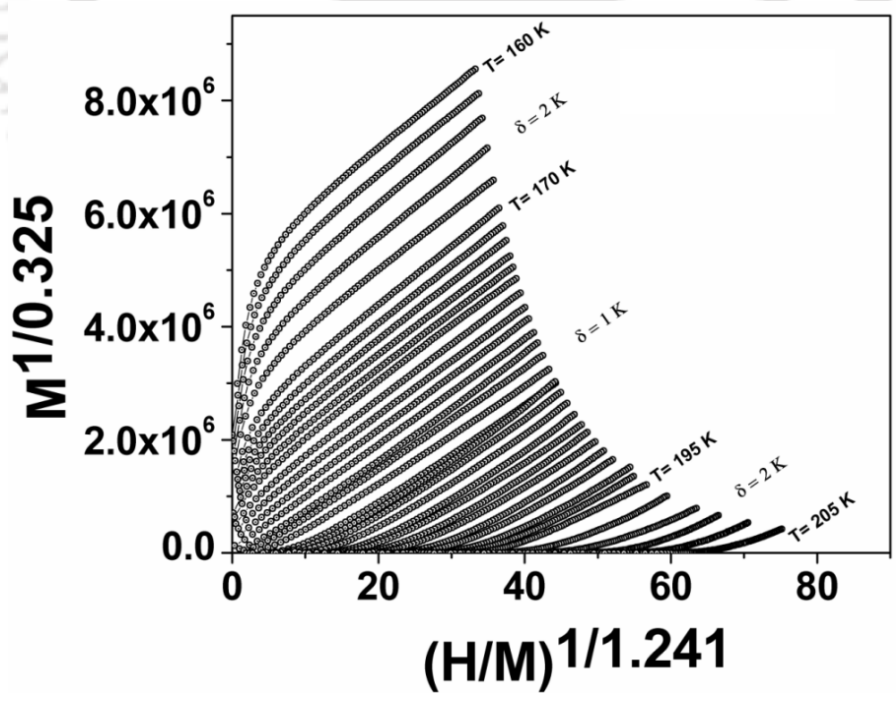

Figure 3.35: $M^{1/0.325}$ versus $H/M^{1/1.241}$ of $x = 0.70$ sample in the temperature range 160 K to 205 K by considering standard values of β and γ for 3D Ising model.

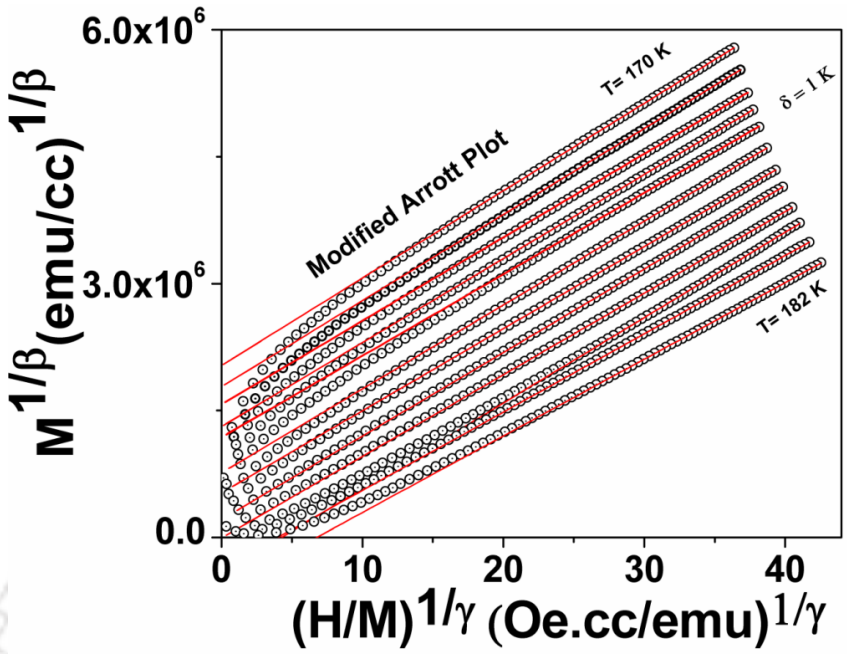

Figure 3.36: Modified Arrot plots $M^{1/\beta}$ versus $(H/M)^{1/\gamma}$ for $x = 0.70$ sample ($\beta = 0.325$ and $\gamma = 1.247$)

The isothermal magnetization data in the form of Arrott plots (M^2 versus H/M) are shown in Fig. 3.34. These plots exhibit parallel set of lines in the high field region with positive slope, confirming the second order nature of the magnetic phase transition. In order to determine the critical exponents, we have to determine the accurate values of spontaneous magnetization, $M_S\ (0, T)$ and zero field inverse susceptibility, $\chi_0^{-1}\ (0, T)$. We have obtained these values by following the modified Arrott plot (MAP) method, as described by *Kim et al.* [125]. The expression corresponding to modified Arrott plot as mentioned in equation (1.22) is reproduced here,

$$\left(\frac{H}{M}\right)^{\frac{1}{\gamma}} = \frac{(T - T_C)}{T_1} + \left(\frac{M}{M_1}\right)^{\frac{1}{\beta}} \qquad (3.10)$$

MAP plots were generated by appropriately selecting the right β and γ values, such that the plots are linear. Initially we have plotted the experimental data by choosing the Mean field (shown in Fig. 3.34), Heisenberg and Ising model's (shown in Fig. 3.35) β and γ values. Subsequently, $M_s(T)$ values were determined by extrapolating the high-field data of $M^{1/\beta}$

versus $(H/M)^{1/\gamma}$ to $(H/M)^{1/\gamma} = 0$. Similarly $\chi_0^{-1}(T)$ values were determined by extrapolating the high field data of the above curve to $M^{1/\beta} = 0$. T_C value was determined from the temperature corresponding to the $M^{1/\beta}$ versus $(H/M)^{1/\gamma}$ curve passing through the origin. The $M_s(T)$, $\chi_0^{-1}(T)$ and the isothermal magnetization at the critical temperature $M(H, T = T_C)$ follow the power law behavior with the respective critical exponents β, γ and δ as given in section 1.6 and for easy reference they (equation 1.19-1.21) are reproduced as below,

$$M_S(T) \alpha |\varepsilon|^{-\beta} \qquad \varepsilon < 0 \qquad (3.11)$$

$$\chi_0^{-1}(T) \alpha |\varepsilon|^{\gamma} \qquad \varepsilon > 0 \qquad (3.12)$$

$$M(H, T = T_C) \alpha H^{\frac{1}{\delta}} \qquad \varepsilon = 0 \qquad (3.13)$$

where, $\varepsilon = (T - T_C)/T_C$ is the reduced temperature. By plotting $ln(M_s)$ versus $ln(\varepsilon)$ for $\varepsilon < 0$, and $ln(\chi_0^{-1})$ versus $ln(\varepsilon)$ for $\varepsilon > 0$ and fitting them to linear relation as per equations. (3.11) and (3.12), a new set of β and γ values were obtained. The above process was repeated several times until consistent values of β and γ were obtained. By fitting $ln(M)$ versus $ln(H)$ data at $T = T_C$, the critical exponent δ was determined. The final set of converged β, γ and δ values are tabulated in Table 3.6. These critical exponent values are close to those values predicted by the Ising model. MAP plots using the final set of critical exponents for selected temperatures close to T_C are shown in Fig. 3.36 for $x = 0.70$. The observed linear behavior at higher field of MAP plots confirms the validity of the 3D Ising model in the present sample. The extracted values of M_S and χ_0^{-1} from the MAP for the sample are plotted as a function of temperature as shown in Fig. 3.37. The fitted data using equations (3.11) and (3.12) are shown as solid line and they follow the experimental data closely. Plots of $ln(M_S)$ versus $ln(\varepsilon)$ and $ln(\chi_0^{-1})$ versus $ln(\varepsilon)$ are shown as insets in Fig. 3.37 (a) and 3.37 (b). The isothermal M-H curves at $T = T_C$ along with theoretical fit are shown in Fig. 3.37 (c). The insets show the same data in logarithmic scale. The value of $\delta - (1+\gamma/\beta)$ is found to be -0.014, which is close to zero as per the Widom scaling relation.

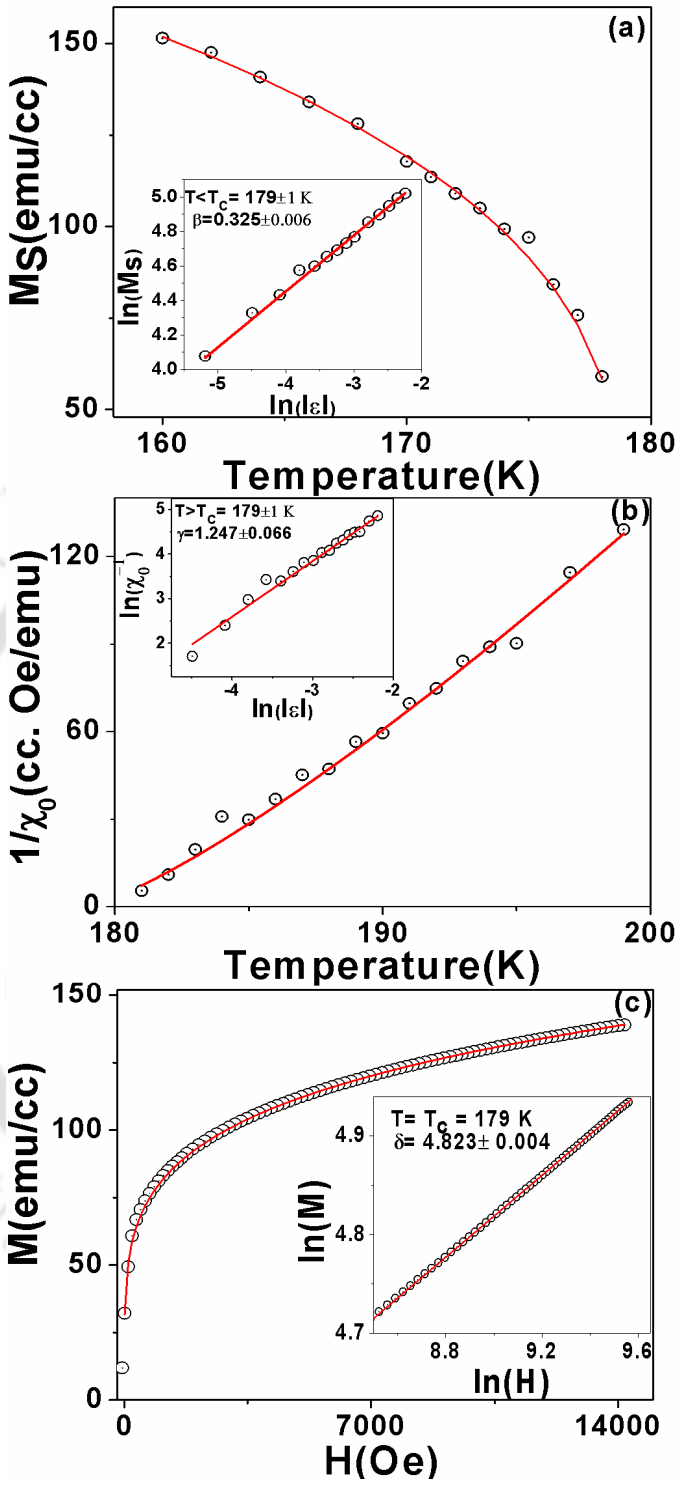

Figure 3.37: Temperature variation of (a) spontaneous magnetization (M_S (0, T)) and (b) the zero field inverse susceptibility (χ_0^{-1}) for x = 0.70 sample along with fitted data. (c) Isothermal magnetization curve at $T = T_C$ for x = 0.70 sample. Insets show the same data plotted in logarithmic scale.

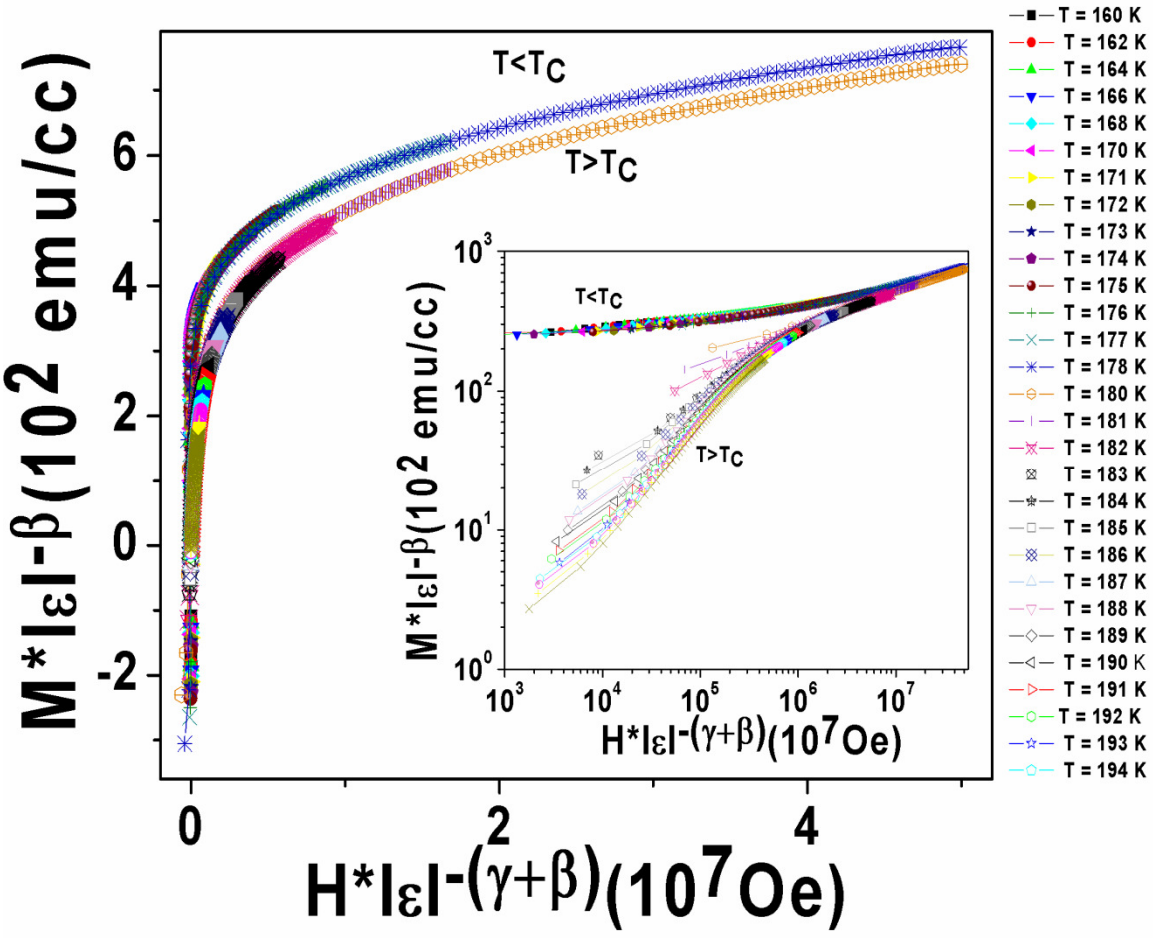

Figure 3.38: Scaling plots of $H\ |\varepsilon|^{-\beta}$ versus $H\ |\varepsilon|^{-\beta+\gamma}$ with β, γ and δ values from final iteration for $x = 0.70$ sample. Different symbol represent data taken at different temperatures. Inset shows the plots in double logarithmic scale.

The static scaling hypothesis predicts that $M(H, \varepsilon)$ is an universal function of ε and H as mentioned in equation (1.23) and for easy reference the equation is reproduced here,

$$M(H,\varepsilon)\left|\varepsilon\right|^{-\beta} = f_{\pm}(H\left|\varepsilon\right|^{-(\beta+\gamma)}) \qquad (3.14)$$

where, f_+ and f_- are regular analytical functions for $\varepsilon > 0$ and $\varepsilon < 0$, respectively. According to equation (3.14), plots of $M\ (H, \varepsilon)|\varepsilon|^{-\beta}$ versus $H|\varepsilon|^{-(\beta+\gamma)}$ would lead to universal curves, one for temperatures $T > T_C\ (\varepsilon > 0)$ and the other for $T < T_C\ (\varepsilon < 0)$. Fig. 3.38 shows the scaling plot on a linear scale and the inset shows the same data in a logarithmic scale. All the data points in the entire range of variables simply fall into two curves, depending upon the sign of

ε. This shows that the critical exponent values and T_C obtained from the present investigation are accurate.

Table 3.6: Comparison of critical parameters for double exchange ferromagnet $LaCr_{0.30}Mn_{0.70}O_3$ with values predicted for different theoretical models. The abbreviations M and PC refer magnetization and polycrystalline sample, respectively.

Material	Ref.	Technique	T_C (K)	β	γ	δ
$LaCr_{0.30}Mn_{0.70}O_3$ (PC)	This Work	Bulk M	179.0 ±0.5	0.325 ±0.006	1.247 ±0.066	4.823 ±0.004
Mean-Field Model	[39]	Theory	--	0.5	1.0	3.0
Tricritical Mean-field	[42]	Theory	--	0.25	1	5
3D Heisenberg Model	[39]	Theory	--	0.365	1.336	4.80
3D Ising Model	[39]	Theory	--	0.325	1.241	4.82

The critical exponent values for the present sample and the values predicted by the mean field model [39], tricritical mean field [42], 3D Heisenberg [39] and 3D Ising model [39] are tabulated in Table 3.6. The exponent values obtained from the analysis are close to the values predicted by 3D Ising model and it signifies the presence of strong anisotropy. The present result differs from the long range mean field model reported in manganite such as $Nd_{0.7}Sr_{0.3}MnO_3$ [126], (Nd, K)MnO_3 [127], *etc*. In manganites, continuous Mn^{3+}-O^{2-}-Mn^{4+} networks present in the long range, so long double exchange FM is fulfilled. On the otherhand, in the present sample, the Mn^{3+}-O^{2-}-Mn^{4+} networks are interrupted due to the presence of Cr^{3+} ions. This could be one of the reason for the deviation from the mean field model. Moreover, samples with $x \geq 0.6$ exhibit $R\bar{3}c$ space group, so in the rhombohedral symmetry Mn/CrO_6 octahedra are expected to align along the three fold rotational axis. Such orientation is expected to induce uniaxial anisotropy. So, the magnetic interaction exhibits strong anisotropy, thereby following the 3D Ising model.

3.3 Conclusions:

In this chapter, effect of Cr site doping in $LaCrO_3$ by using transition elements Fe and Mn has been discussed.

We have prepared single phase samples of polycrystalline $LaCr_{1-x}Fe_xO_3$ (x = 0 to 1.0). The x = 0 sample shows the AFM-PM transition without any magnetization reversal. The T_N value is found to vary from 289 K for x = 0.00 to 244 K for x = 0.15 and it can be understood in terms of weakening of AFM interaction due to random positioning of Fe ions at the site of Cr ions. For higher concentration of Fe substituted samples, AFM transition close to 750 K was observed. Negative magnetization upon field cooling under moderate magnetic fields has been observed in the composition range x = 0.05 to 0.15 and again for x = 0.45 and 0.50. The maximum compensation temperature is found to be 105 K. The mechanism of magnetization reversal is found to be quite different depending on the Fe concentration. The magnetization reversal in the composition range x = 0.05 to 0.15 could be quantitatively studied based on the paramagnetic behavior of doped Fe ions under the influence of negative internal field due to AFM ordered Cr ions. The maximum H_I value of -3.5 kOe is observed for x = 0.05 sample. The x = 0.15 sample exhibits a spin reorientation transition at around ≃ 42 K and it is found to shift towards higher temperature with increase in applied magnetic field. The magnetization reversal of x = 0.45 and 0.50 samples could be quantitatively studied based on the model, where the competition between single ion anisotropy and DM interaction is taken into account. The increase in applied field is found to weaken the DM interaction and decrease the compensation temperature. The obtained DM parameter γ_D is found to in the order of 49×10^{-3} for H = 200 Oe. Thus, we have observed negative magnetization in a wide composition range and its mechanism is found to differ depending on the doping concentration.

Single phase samples of $LaCr_{1-x}Mn_xO_3$ (x = 0.00 to 1.00) were prepared by sol-gel technique. The x = 0.15 and 0.20 samples exhibit the interesting property of magnetization reversal and exchange bias field. The magnetization reversal could be explained by considering the competition between the canted FM components of Cr^{3+} ions and the PM component of doped Mn^{3+} ions under the influence of negative internal field due to AFM

ordered Cr^{3+} ions. T_{comp} value is found to increase with increase in Mn concentration and is found to be 95 K for x = 0.15 sample and 147 K for x = 0.20 sample. As per the analysis, the maximum internal field estimated for x = 0.20 sample is to be H_I = -8.2 kOe. The presence of exchange bias field and its temperature dependence could be explained by considering the interaction between the canted FM component of Cr^{3+} ions and PM component of Mn^{3+} ions along with possible magnetic interaction in Mn^{3+}-O^{2-}-Cr^{3+} networks. Thus in x = 0.15 sample, exchange bias can be tuned from negative to positive value by varying the temperature. The presence of exchange bias field is observed in a wide temperature range. With increase in Mn concentration *i.e.* $x \geq 0.30$, ferromagnetic to paramagnetic transition was observed with the transition temperature ranging from 128 K to 244 K as per magnetization measurements. The saturation magnetization value was found to increase with increase in doping concentration.

The critical exponent behavior was analyzed for x = 0.70 sample. Isothermal magnetization was measured as a function of field in the vicinity of FM transition. They were analyzed in terms of modified Arrott plot method and the estimated values of critical exponents β = 0.325±0.006, γ = 1.247±0.066 and δ = 4.823±0.004 are found to be close to the 3D Ising model values. The observed static scaling plot clearly shows that the estimated critical exponents are accurate.

In $LaCrO_3$ series, Fe substituted (x = 0.05, 0.10, 0.15, 0.45 and 0.50) and Mn substituted (x = 0.15 and 0.20) samples show the magnetization reversal. Since magnetic moment of Fe^{3+} ion is larger than Mn^{3+} ion so even x = 0.05 sample of Fe substituted $LaCrO_3$ shows magnetization reversal. The 5 and 10 atm. % of Mn substituted samples show the low temperature transition due to the interaction between Cr^{3+} and Mn^{3+} ions but such type of behavior was not observed in Fe substituted samples except for x = 0.15 sample. The negative exchange bias behavior was observed for Fe substituted samples of compositions *i.e.* x = 0.45 and 0.50 but in Mn substituted sample (x = 0.15) shows the tunable exchange bias behavior. With increasing the concentration, Fe substituted samples show AFM transition due to the increase in Fe^{3+}-O^{2-}-Fe^{3+} networks and Mn substituted samples show the FM transition because of Cr^{3+}-O^{2-}-Mn^{3+} and Mn^{3+}-O^{2-}-Mn^{4+} networks.

Chapter 4

$NdCr_{1-x}M_xO_3$ (M = Fe and Mn) series

Chapter 4: $NdCr_{1-x}M_xO_3$ (M = Fe and Mn) series

$NdCrO_3$ is one of the interesting orthochromites having G-type antiferromagnetic (AFM) structure with Néel temperature around T_N = 219 K and in addition to that, it exhibits spin reorientation transition of Cr^{3+} ions at T_{SRT} = 35 K [99]. Substitution of Nd by La is reported to increase T_N value but reduce T_{SRT} [13]. Troyanchuk *et al.* [103] have reported magnetization reversal in $NdMn_{0.15}Cr_{0.85}O_3$ compound below 160 K. Even though there are several reports on the study of sign reversal of magnetization in $LaCrO_3$ based system by mostly carrying out the substitutions at La site using other rare earth ions [49, 92, 93], such studies in $NdCrO_3$ is limited. To our knowledge there is no systematic study in Nd (Cr, Mn)-O system as well as in Nd (Cr, Fe)-O system to investigate the magnetization reversal and exchange bias field. Since $NdCrO_3$ contains the magnetic rare earth element, it would be interesting to study the Cr site substitution using transition elements (Fe^{3+}, Mn^{3+}) having higher magnetic moment in order to easily tune the canted ferromagnetic component and investigate the exotic magnetization reversal phenomenon. So, we have prepared $NdCr_{1-x}Fe_xO_3$ (x = 0.00 to 1.00) and $NdCr_{1-x}Mn_xO_3$ (x = 0.00 to 0.70) compounds and carried out the detailed magnetization studies. We have also demonstrated the bipolar switching of magnetization by varying the applied field magnitude.

4.1 $NdCr_{1-x}Fe_xO_3$ compounds (x = 0.0 to 1.0)

This section deals with the effect of Fe substitution at Cr site of $NdCrO_3$. The preparation, characterization and the result obtained from dc magnetization measurement and analysis are presented.

4.1.1 Sample Preparation and Characterization

Polycrystalline samples of $NdCr_{1-x}Fe_xO_3$ (x = 0.00 to 1.00) were prepared by the standard sol-gel method. Nd_2O_3, $Cr(NO_3)_3.9H_2O$, $Fe(NO_3)_3.6H_2O$ having 99.9% purity were taken as starting compounds. Nd_2O_3 compound was dissolved in nitric acid and the other two were dissolved in distilled water. An excess amount of citric acid was added to convert the mixture of above nitrate solution into citrate. Ethylene glycol was added to the citrate

solution to promote the gel formation and the gel was converted into fine powder upon heating. The powder was presintered at 600 ˚C for 12 h and final sintering was done in pellet form at 1100 ˚C for 24 h.

The parent compound and all the Fe doped $NdCrO_3$ compounds are found to be in single phase form as per the XRD patterns. The XRD patterns for x = 0.00 to 1.00 are shown in Fig. 4.1. We can clearly see the shifting of (112) peak position towards lower 2θ value with increase in Fe concentration as shown in Fig. 4.2. The XRD patterns of all samples could be refined by taking *Pbnm* space group in orthorhombic cell. The typical XRD patterns along with Rietveld refinement for x = 0.15 and 0.60 samples are shown in Fig. 4.3. The room temperature lattice parameters, reliability factors and unit cell volume are given in Table 4.1. We can see that the lattice parameters increase linearly with increase in Fe concentration and this can be easily explained in terms of Fe^{3+} ions (0.645 Å) having larger ionic radii replacing the Cr^{3+} (0.615 Å) ions. Thus the doped Fe^{3+} ions indeed get substituted at Cr sites.

The morphology of all the samples has been studied by recording microstructral images using scanning electron microscope. The typical SEM micrographs for x = 0.00, 0.10 and 0.20 are shown in Fig. 4.4. The surface morphology is found to be quite uniform for all the samples. The average particle size is found to be in the range of 430 nm to 550 nm. The elemental analysis of the prepared compounds has been carried out by recording EDS spectra. Typical EDS spectrum for x = 0.30 sample is shown in Fig. 4.4. The chemical composition determined from EDS analysis is found to be comparable to the nominal starting composition. The cationic ratio for x = 0.00, 0.05, 0.30 and 0.40 samples is given in Table 4.2.

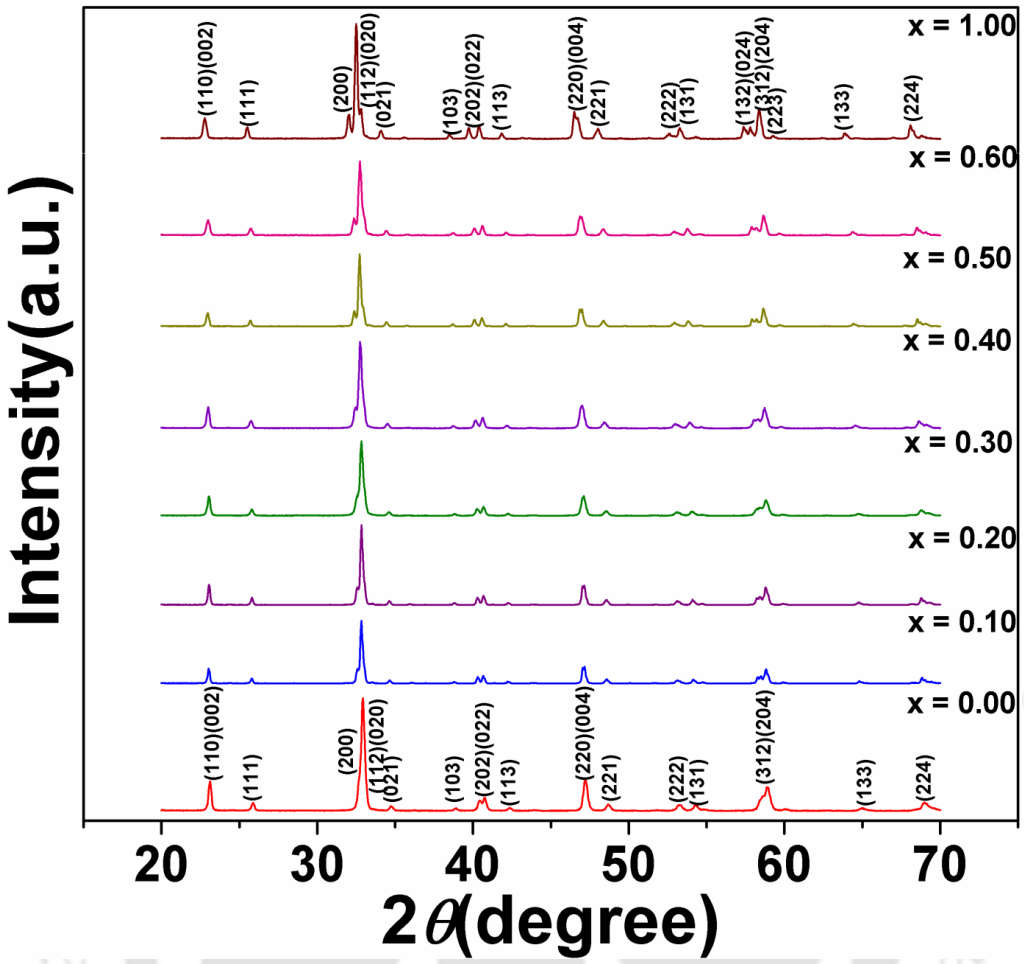

Figure 4.1: XRD patterns of $NdCr_{1-x}Fe_xO_3$ compounds for x = 0.00 to 1.00.

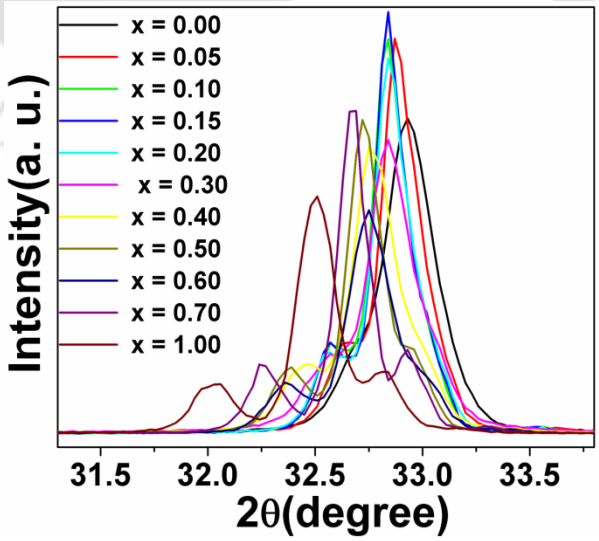

Figure 4.2: Expanded view of (112) peak of XRD patterns for $NdCr_{1-x}Fe_xO_3$ samples.

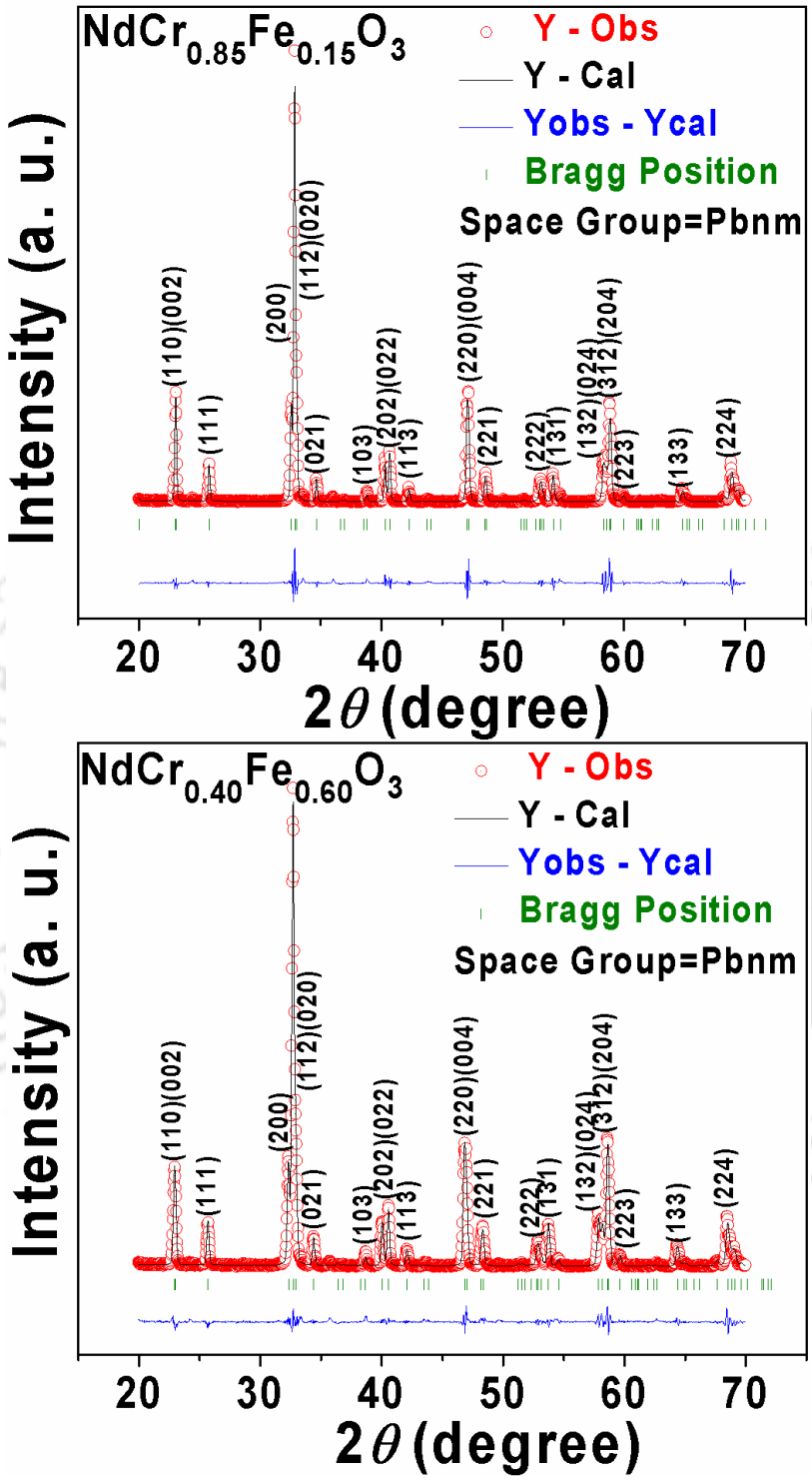

Figure 4.3: XRD patterns along with Rietveld refinement for x = 0.15 and 0.60 samples. The circles represent experimental data and solid lines represent Rietveld refined data. The bottom line shows the difference between experimental and refined data. The marked 2θ positions are allowed Bragg peaks.

Table 4.1: Parameters obtained from the Rietveld analysis of XRD patterns for the samples $NdCr_{1-x}Fe_xO_3$ (0.00 to 1.00). R_F, R_{Bragg}, R_P, R_{exp} and χ^2 are the reliability factors.

Sample/ Parameters	***x* = 0.00**	***x* = 0.05**	***x* = 0.10**	***x* = 0.15**	***x* = 0.20**	***x* = 0.30**	***x* = 0.40**	***x* = 0.50**	***x* = 0.60**	***x* = 0.70**	***x* = 1.00**
Space group	*Pbnm*	*Pbnm*	*Pbnm*	*Pbnm*	*Pbnm*	*Pbnm*	*Pbnm*	*Pbnm*	*Pbnm*	*Pbnm*	*Pbnm*
***a* (Å)**	5.4138 (0.0003)	5.4156 (0.0003)	5.4172 (0.0003)	5.4196 (0.0003)	5.4213 (0.0003)	5.4199 (0.0003)	5.4254 (0.0003)	5.4308 (0.0003)	5.4341 (0.0003)	5.4370 (0.0003)	5.4460 (0.0003)
***b* (Å)**	5.4772 (0.0003)	5.4826 (0.0003)	5.4864 (0.0003)	5.4913 (0.0003)	5.4952 (0.0003)	5.4992 (0.0003)	5.5138 (0.0003)	5.5246 (0.0003)	5.5359 (0.0003)	5.5470 (0.0003)	5.5760 (0.0003)
***c* (Å)**	7.6831 (0.0005)	7.6870 (0.0005)	7.6900 (0.0005)	7.6939 (0.0005)	7.6973 (0.0004)	7.6991 (0.0005)	7.7105 (0.0005)	7.7190 (0.0005)	7.7265 (0.0004)	7.7343 (0.0005)	7.7532 (0.0004)
***Volume* (Å^3)**	227.82 (0.02)	228.24 (0.02)	228.55 (0.02)	228.98 (0.02)	229.32 (0.02)	229.47 (0.02)	230.66 (0.02)	231.59 (0.02)	232.43 (0.02)	233.26 (0.02)	235.44 (0.02)
R_F (%)	3.90	5.08	4.79	4.86	4.77	5.00	4.48	5.60	5.02	6.04	6.11
R_{Bragg} (%)	2.71	4.29	3.86	3.87	3.28	2.96	2.86	4.57	3.24	4.76	4.32
R_P (%)	6.97	9.81	10.9	12.0	9.72	7.44	7.31	10.8	8.42	13.3	9.84
R_{exp} (%)	6.04	5.84	5.81	5.84	5.95	6.07	6.10	6.23	6.91	6.39	6.71
χ^2	4.01	6.80	7.74	8.58	6.05	3.84	3.88	6.80	4.25	8.55	5.25
Nd/Cr/Fe Occupancy	1.000 /1.000 /0.000	1.000 /0.958 /0.050	0.975 /0.898 /0.098	1.000 /0.855 /0.149	1.000 /0.807 /0.199	1.000 /0.700 /0.300	0.979 /0.597 /0.399	0.966 /0.495 /0.499	0.993 /0.398 /0.599	0.984 /0.299 /0.699	0.976 /0.000 /0.998

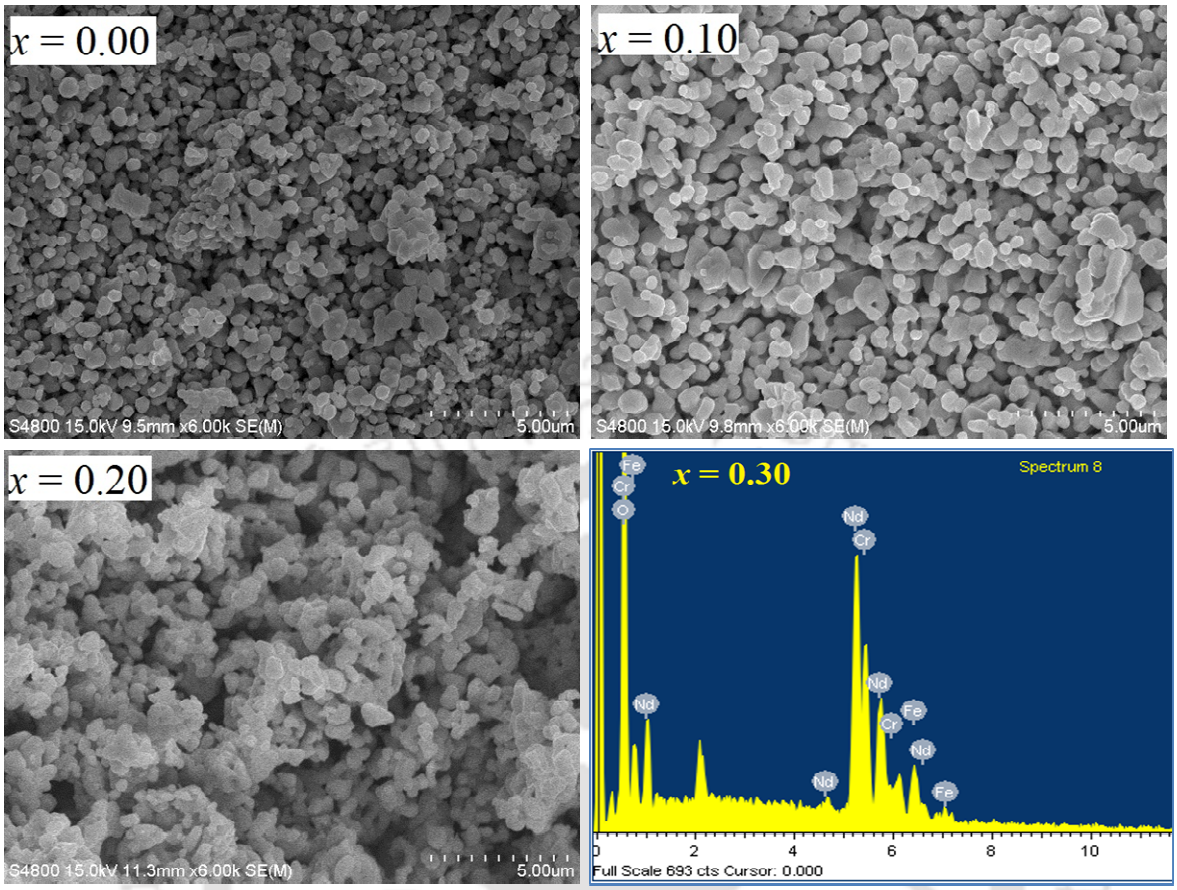

Figure 4.4: SEM images recorded for x = 0.00, 0.10 and 0.20 samples along with EDS spectrum for x = 0.30.

Table 4.2: The cationic ratio determined from EDS analysis for x = 0.00, 0.05, 0.30 and 0.40 samples.

Samples	**Calculated Cationic Ratio from EDS Analysis**		
	Nd	**Cr**	**Fe**
***x* = 0.00**	0.93	1.00	0.00
***x* = 0.05**	0.99	0.95	0.05
***x* = 0.30**	0.96	0.68	0.32
***x* = 0.40**	0.93	0.62	0.38

4.1.2 Magnetic Properties

Temperature variations of magnetization in zero field cooled (ZFC) and field cooled (FC) conditions at an applied field of H = 2 kOe are shown in Fig. 4.5. The parent compound exhibits AFM transition at T_N = 225 K followed by a secondary rise in magnetization at around 50 K due to the spin reorientation of Cr^{3+} ions. The ZFC M-T plot of x = 0.05 sample follows the trend of x = 0.00 sample but with a reduced T_N of 219 K. Under FC condition, magnetic irreversibility is observed at $T < T_N$ in the form of a broad peak and for further decrease in temperature, magnetization decreases towards negative values by crossing over the ZFC magnetization curve at T_{cross} = 163 K and passing through magnetic compensation (M = 0) at T_{comp} = 102 K. A minimum magnetization (maximum negative value) of M_{min} = -2.45 emu/mol is observed at T_{min} = 80 K. On further decrease in temperature a sharp rise in magnetization towards positive value is observed at $T_{SRT} \simeq$ 60 K. M-T plots of other samples with higher Fe concentration $0.1 \leq x \leq 0.2$ also show similar behavior but with enhanced T_{comp} values. Moreover, the broad peak observed in the vicinity of T_N is found to diminish with increase in Fe concentration due to the widening of negative magnetization region. T_{comp} value is found to vary from 102 K for x = 0.05 to 169 K for x = 0.15 at H = 2 kOe. The maximum negative magnetization value for x = 0.10 and 0.15 samples is found to be about one order of magnitude larger than that of x = 0.05 sample. The T_{comp} value for x = 0.20 sample is found to be smaller than that of x = 0.15 sample and this can be understood in terms of lack of contribution of all the doped Fe ions for magnetization reversal and some of the Fe ions are possibly engaged in long range AFM interaction in Fe^{3+}-O^{2-}-Fe^{3+} networks. Such networks are possible especially for $x \geq 0.20$.

For $x \geq 0.30$ samples, the magnetization behavior is found to be quite different. They exhibit positive irreversible magnetization, *i.e.* $M_{FC} > M_{ZFC}$. With increase in Fe concentration, the AFM transition is found to shift towards higher temperature and T_N value is found to vary from 210 K for x = 0.30 sample to 670 K for x = 1.00 sample (inset of Fig. 4.5 (j)) due to increase in Fe^{3+}-O^{2-}-Fe^{3+} networks. Spin reorientation like transition was observed in x = 0.60, 0.70 and 1.00 samples along with a broad hump as shown in Fig. 4.5. The hump is found to shift from 250 K for x = 0.60 to 150 K for x = 1.00, due to the possible increase in Nd^{3+}-Fe^{3+} interactions.

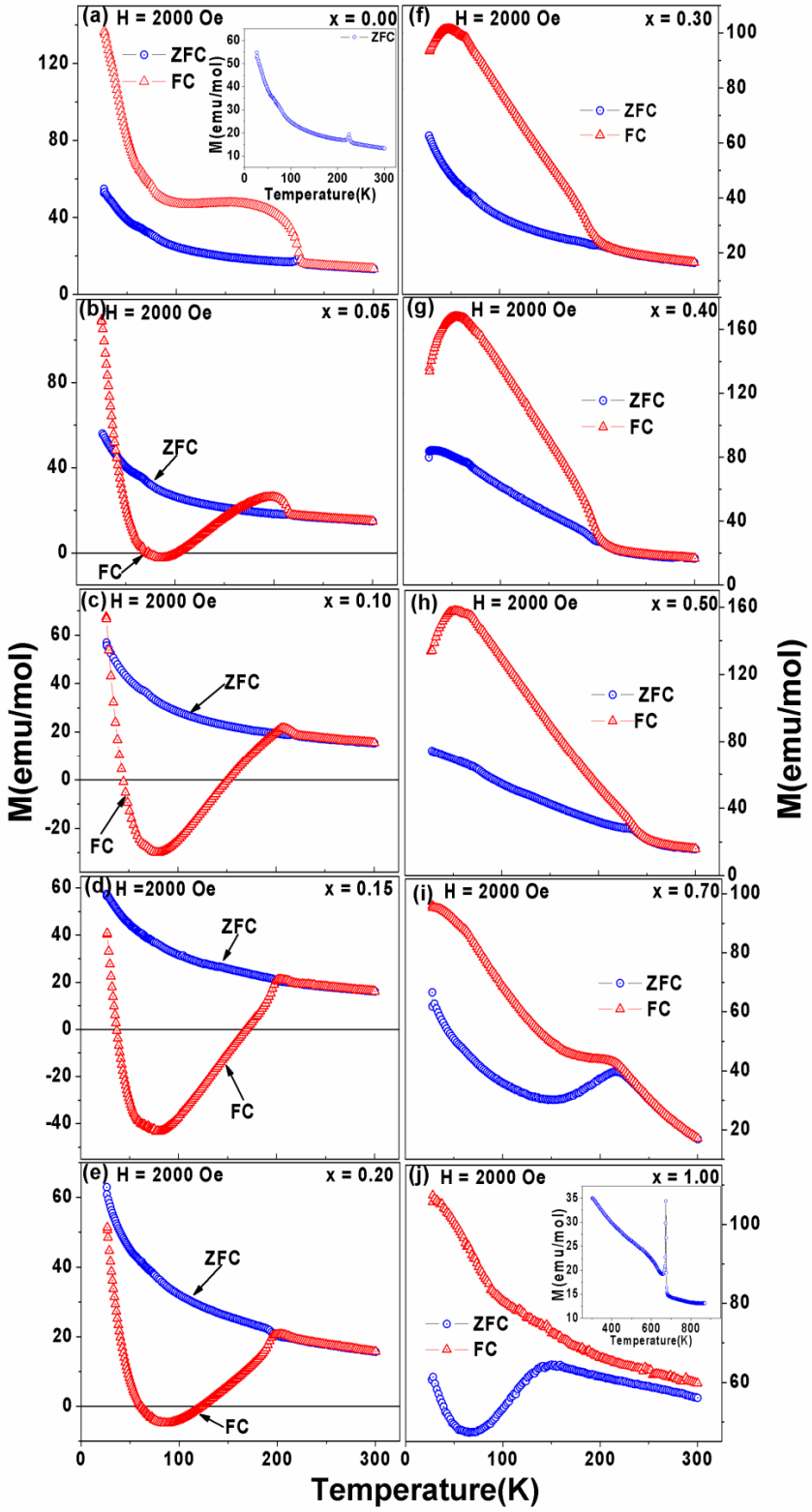

Figure 4.5: Magnetization versus temperature plots in ZFC and FC conditions for x = 0.00 to 1.00 samples

(i) Magnetization Reversal

To understand the MR phenomenon, we have recorded *M-T* curves for x = 0.05 to 0.20 samples at different applied fields in the range 50 Oe to 5000 Oe. They are shown in Figs. 4.6 and 4.7 for H = 200 Oe to 2000 Oe. Prominent negative magnetization is observed for all these samples especially for low applied field. The magnitude of negative magnetization is found to decrease with increase in applied field and correspondingly the T_{comp} value also decreases as shown in Fig. 4.8. No MR was observed for $H \geq 2000$ Oe for x = 0.05 and 0.20 samples and $H \geq 5000$ Oe for x = 0.10 and 0.15 samples. For x = 0.05 and 0.10 samples at H = 200 Oe, additional magnetic compensation is observed at low temperature *i.e.* at T'_{comp} = 41 K and 31 K respectively. Similarly, larger T_{comp} values of 252 K and 230 K were reported in other orthochromites containing magnetic rare earth ions, *i.e.* $SmCr_{0.5}Fe_{0.5}O_3$ [110] and $La_{0.15}Pr_{0.85}CrO_3$ [73] respectively.

The competition between the weak ferromagnetic component of canted Cr^{3+} ions and the paramagnetic moments of Nd^{3+} and Fe^{3+} ions under the influence of the negative internal magnetic field due to the AFM ordered Cr^{3+} ions gives rise to the magnetization reversal. According to this model [22],

$$M = M_{Cr} + \frac{C(H + H_I)}{(T - \theta_C)} \qquad (4.1)$$

where, M_{Cr} is the canted FM component of Cr^{3+} ions, H_I is the internal magnetic field and C is the Curie constant. The FC *M-T* curves were fitted to the above equation for $H \leq 2000$ Oe and the fitted data are shown as solid line in Figs. 4.6 and 4.7. The estimated θ_C values for x = 0.05 sample is found to be in the range of - 40 K to - 65 K depending on the applied field. These values for x = 0.10, 0.15 and 0.20 are found to be in the range of -119 to -139 K, -98K to -167K and -162K to -176K respectively. Plots of $-H_I$ and M_{Cr} as a function of H are shown in Fig. 4.9. H_I and M_{Cr} values are found to almost saturate for $H \geq 0.5$ kOe, however for x = 0.15 sample, they increase linearly.

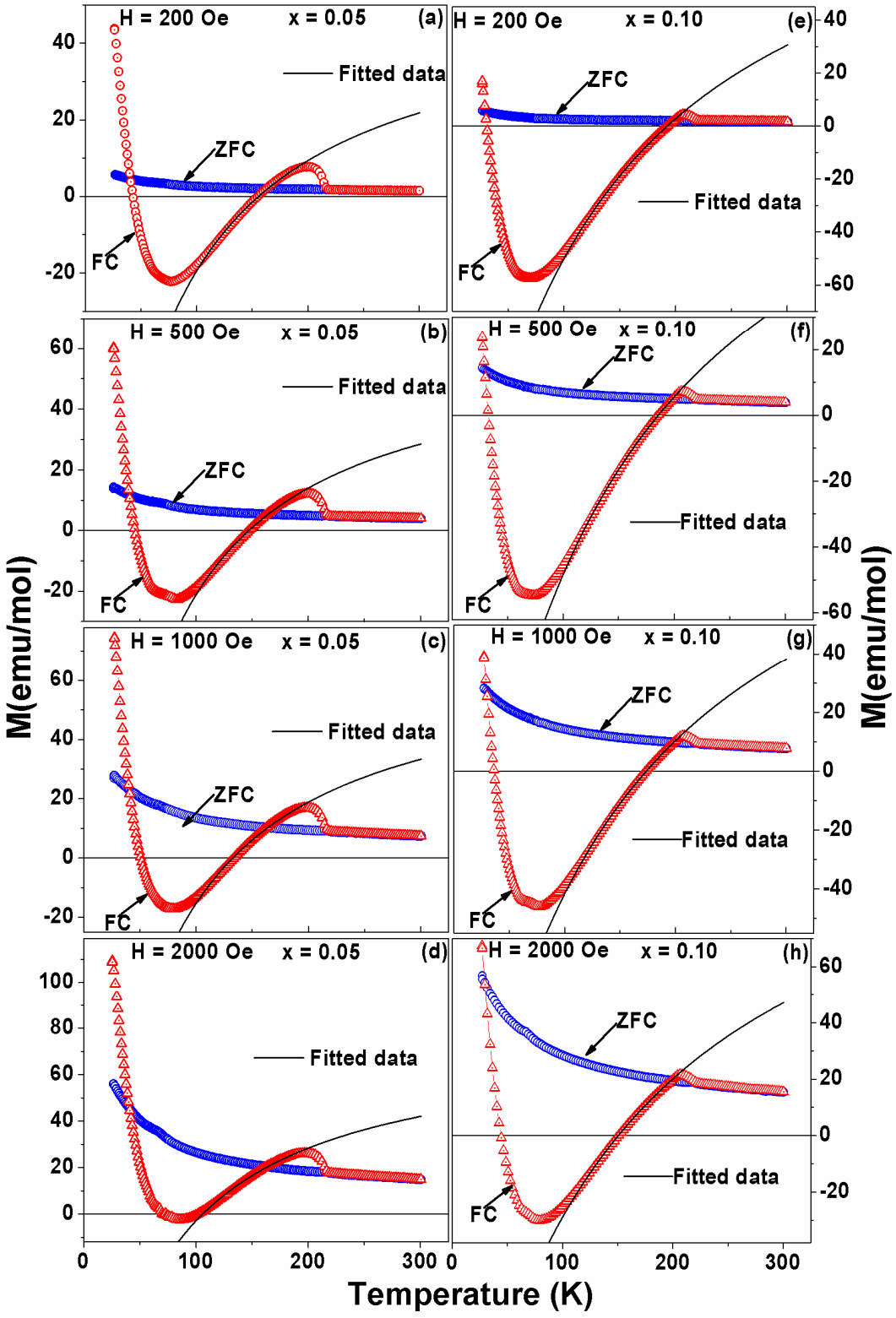

Figure 4.6: ZFC and FC *M-T* curves of x = 0.05 and 0.10 samples at H = 200 Oe, 500 Oe, 1000 Oe and 2000 Oe along with fitted data.

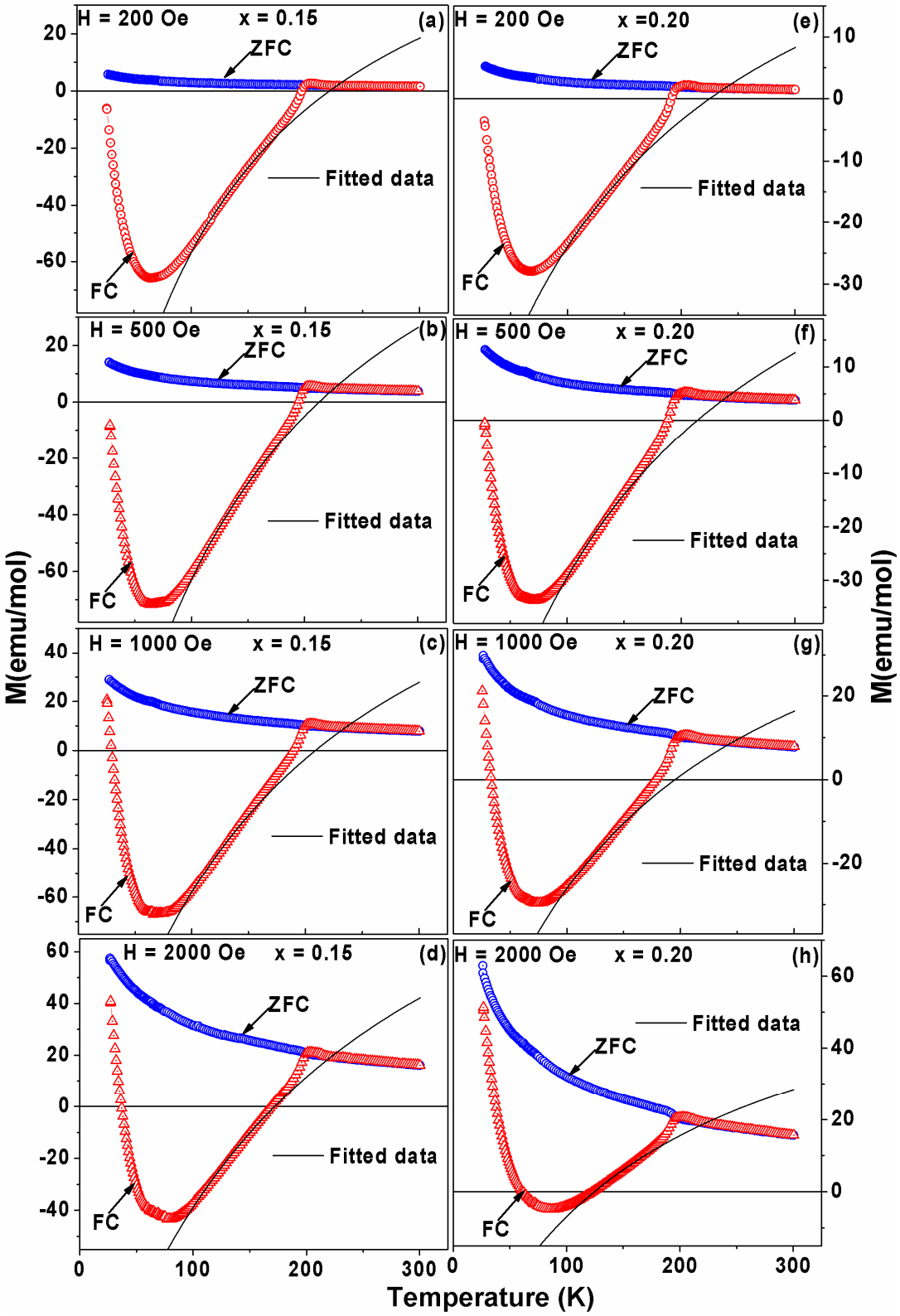

Figure 4.7: ZFC and FC *M-T* curves of x = 0.15 and 0.20 samples at H = 200 Oe, 500 Oe, 1000 Oe and 2000 Oe along with fitted data.

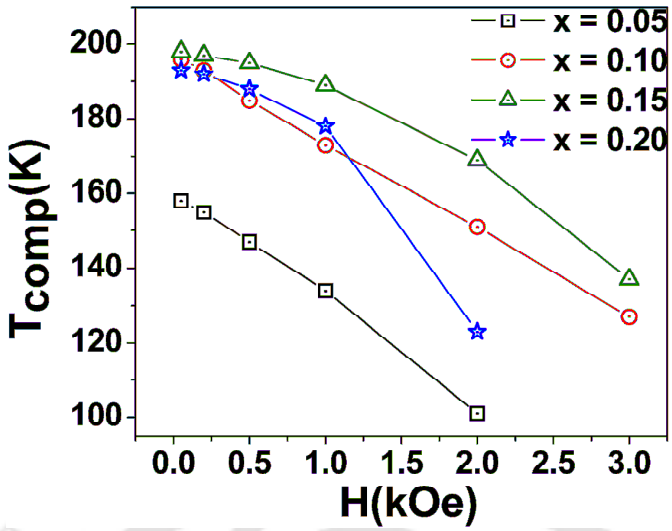

Figure 4.8: T_{comp} as a function of applied magnetic field.

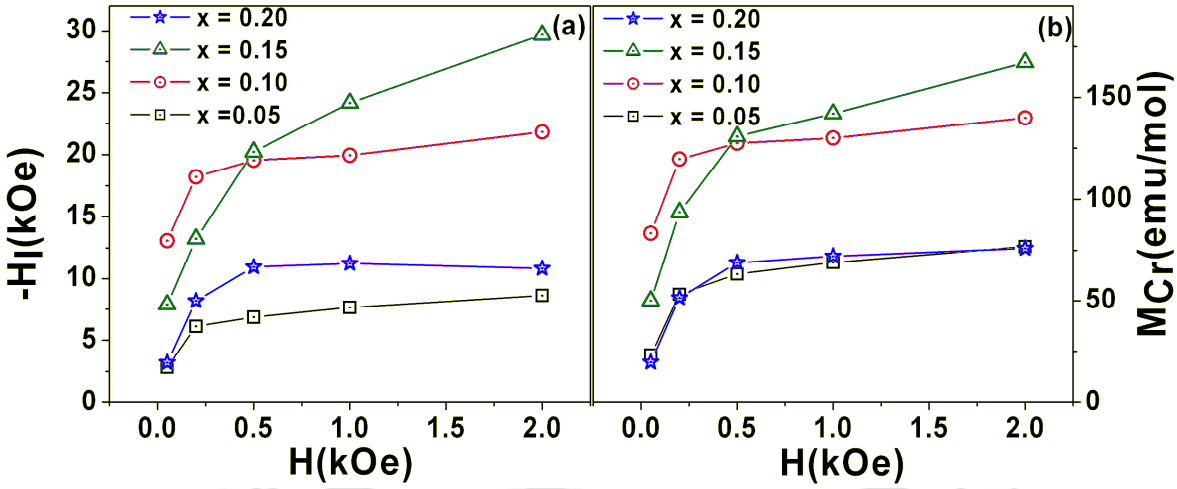

Figure 4.9: (a) $-H_I$ and (b) M_{Cr} as a function of applied field for $NdCr_{1-x}Fe_xO_3$ samples.

Bipolar switching of magnetization at T = 100 K for x = 0.05, 0.10, 0.15 and 0.20 samples are shown in Fig. 4.10. Here, the samples were initially FC to 100 K through T_N by applying H = 200 Oe. By keeping the temperature fixed H was increased from 200 Oe to 4000 Oe and then decreased to 200 Oe for x = 0.05 and 0.20 samples. Such a field variation flips the magnetization from negative to positive and back to negative. Subsequent cycling of the fields between the above two values give rise to reproducible magnetization reversal. Thus by varying the magnitude of positive applied field, bipolar switching of magnetization

can be achieved. Similar type of switching behavior is also observed for x = 0.10 and 0.15 samples for H = 200 Oe to 7000 Oe.

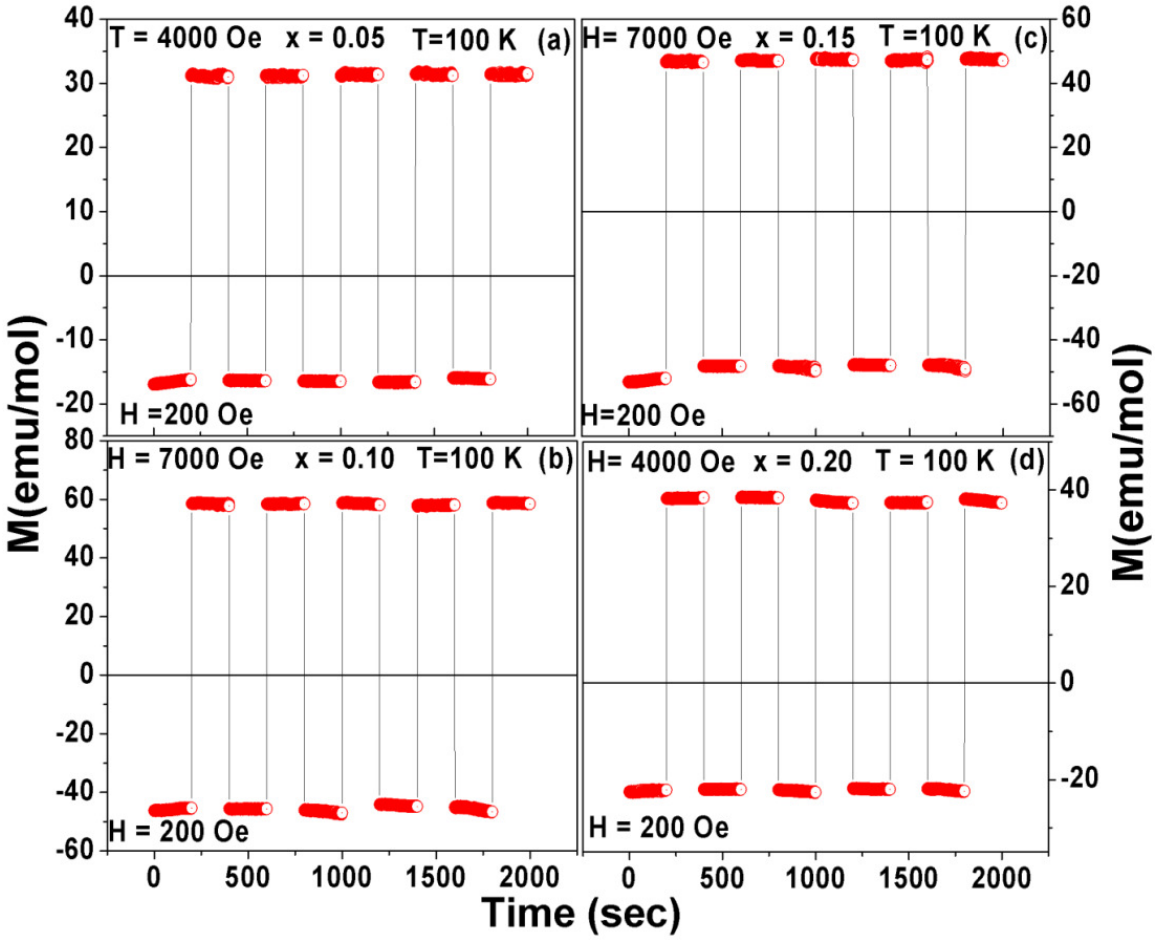

Figure 4.10: Bipolar switching of magnetization for x = 0.05 to x = 0.20 samples at T = 100 K (a to d).

(ii) Exchange Bias

In order to study the exchange bias behavior, *M-H* loops were recorded under FC condition (H = 5000 Oe) in the temperature range 30 K to 220 K at 5 K interval. Typical *M-H* loops for x = 0.05, 0.10, 0.15 and 0.20 samples in expanded scale are shown in Fig. 4.11, 4.12, 4.13 and 4.14 respectively at selected temperatures.

For x = 0.05 sample, as the sample is cooled from T_N, the *M-H* loops are found to shift towards negative field axis and for further cooling, the centre of *M-H* loop approaches

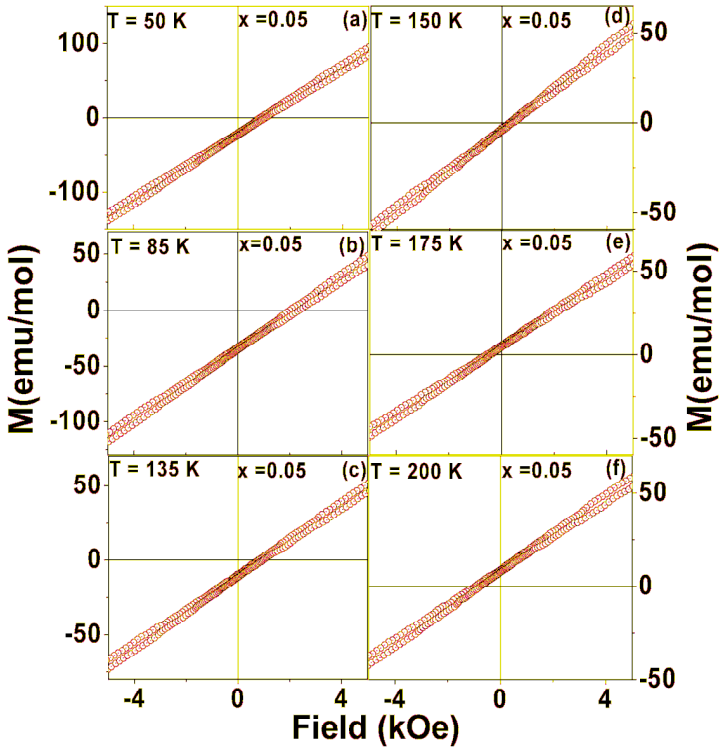

Figure 4.11: *M-H* loops recorded at different temperatures for x = 0.05 sample in the expanded scale.

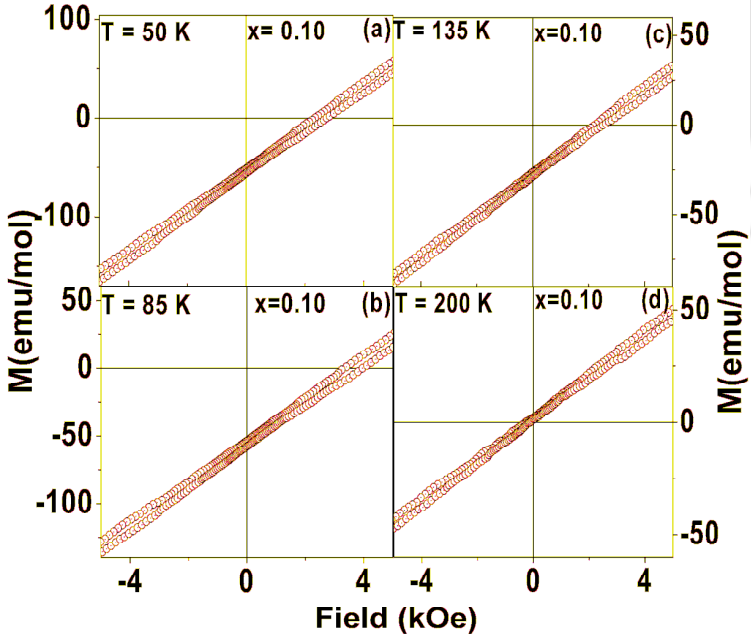

Figure 4.12: *M-H* loops recorded at different temperatures for x = 0.10 sample in the expanded scale.

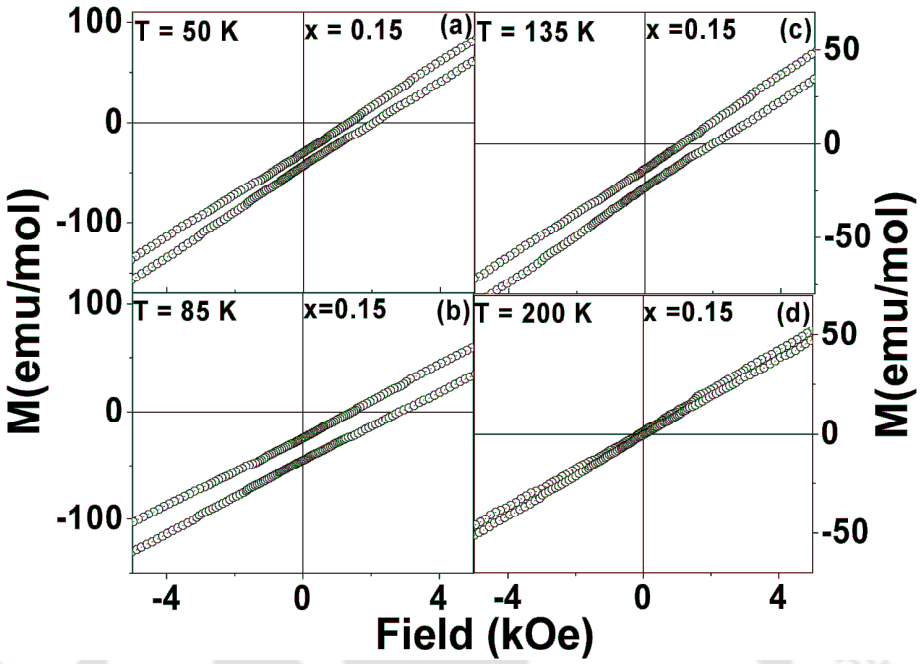

Figure 4.13: *M-H* loops recorded at different temperatures for x = 0.15 sample in the expanded scale.

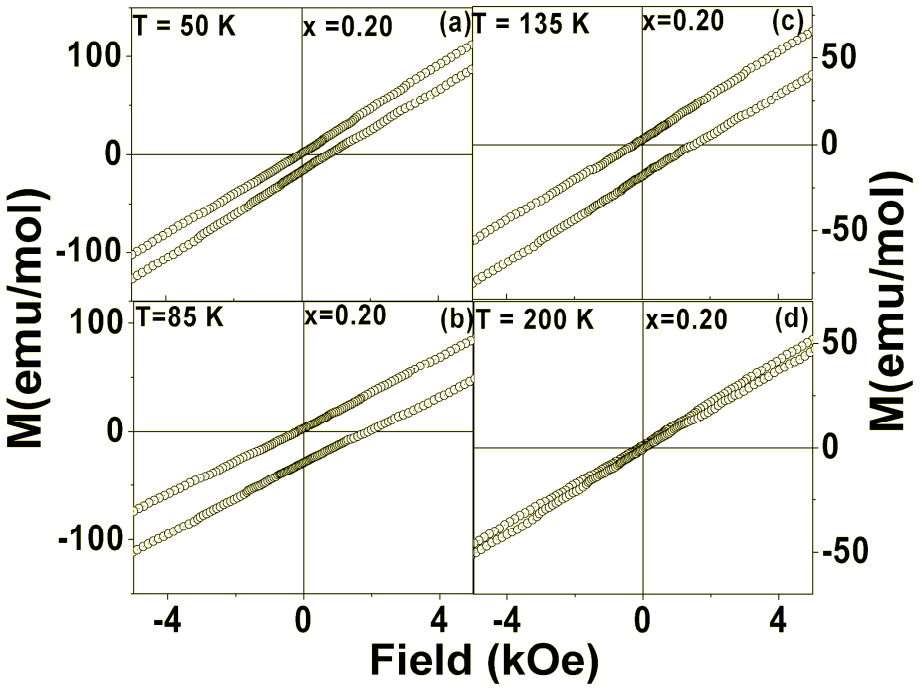

Figure 4.14: *M-H* loops recorded at different temperatures for x = 0.20 sample in the expanded scale.

towards origin. For $T \leq 150$ K, the loops are found to shift towards positive field axis. Thus the present sample exhibits exchange bias field that can be tuned by varying the temperature. Similar behavior is observed for $x = 0.10$ sample but the shifting in negative field axis is noticed only in a narrow temperature range close to T_N. *M-H* loops of $x = 0.15$ and 0.20 samples also show shifting of the loop but mostly along the positive *H* axis.

The exchange bias field was determined using the relation $H_{EB} = (H_+ + H_-)/2$ where H_+ and H_- are the field values corresponding to $M = 0$ at ascending and descending branches of the *M-H* loop respectively. Fig. 4.15(a) shows H_{EB} versus temperature plot for $x = 0.05$ sample. As the temperature is decreased from T_N, H_{EB} decreases towards negative value and approaches a maximum negative value of - 0.85 kOe at 200 K. For further decrease in temperature, H_{EB} increases towards positive values and approaches $H_{EB} = 0$ axis at $T \simeq T_{comp}$ = 160 K. For $T < T_{comp}$, a broad positive peak is observed at $T_P = 85$ K with a maximum positive H_{EB} value of + 2.17 kOe. Here T_P is found to be close to the temperature at which maximum negative magnetization was observed in the *M-T* plot (see Fig. 4.5). For $T < T_P$, the H_{EB} values fall towards negative value by crossing the $H_{EB} = 0$ axis for the second time at $T \simeq T'_{comp} = 40$ K. Unlike $x = 0.05$ sample, $x = 0.10$ sample exhibits positive H_{EB} values in a wide temperature range below T_N with a peak value of H_{EB} = 3.65 kOe at 85 K. Small negative H_{EB} values are observed in a narrow temperature range close to T_N. Similar behavior is observed for $x = 0.15$ and 0.20 samples as shown in Fig. 4.15. The observed maximum H_{EB} value is comparable to that reported in $La_{0.15}Pr_{0.85}CrO_3$ [73], $NdMnO_3$ [72] and $La_{0.8}Ce_{0.2}CrO_3$ [53] compounds.

For a comparison, temperature variations of $\Delta M/M_{ZFC}$ are shown in Fig. 4.16 for different *H* values, where ΔM is the difference between the FC (M_{FC}) and ZFC (M_{ZFC}) magnetization at a particular magnetic field. All curves pass through the temperature axis at a particular temperature known as T_{cross}. A large negative peak at $T < T_{cross}$ is observed for all the samples and in addition to that a small positive peak is observed at $T > T_{cross}$ especially for $x = 0.05$ and $x = 0.10$ samples. These peaks coincide with respective positive and negative peaks of H_{EB} versus *T* plots.

The observed H_{EB} and its temperature dependence can be explained by considering

the exchange anisotropy between the ferromagnetic components of Cr^{3+} ions (M_{Cr}) and the paramagnetic moments of Nd^{3+} and Fe^{3+} ions (M_{Nd}+M_{Fe}) under the negative internal field. The negative peak observed in the temperature range $T_{comp} < T < T_N$ especially for x = 0.05 sample is due to the dominant M_{Cr} aligned along the field direction compared to M_{Nd}+M_{Fe} which are aligned along H_I *i.e.* opposite to the direction of applied field. On the other hand, for $T < T_{comp}$, H_{EB} shows a broad positive peak because M_{Nd}+M_{Fe} dominates over the M_{Cr} component. The dominant behavior of M_{Nd}+M_{Fe} at low temperature is consistent with

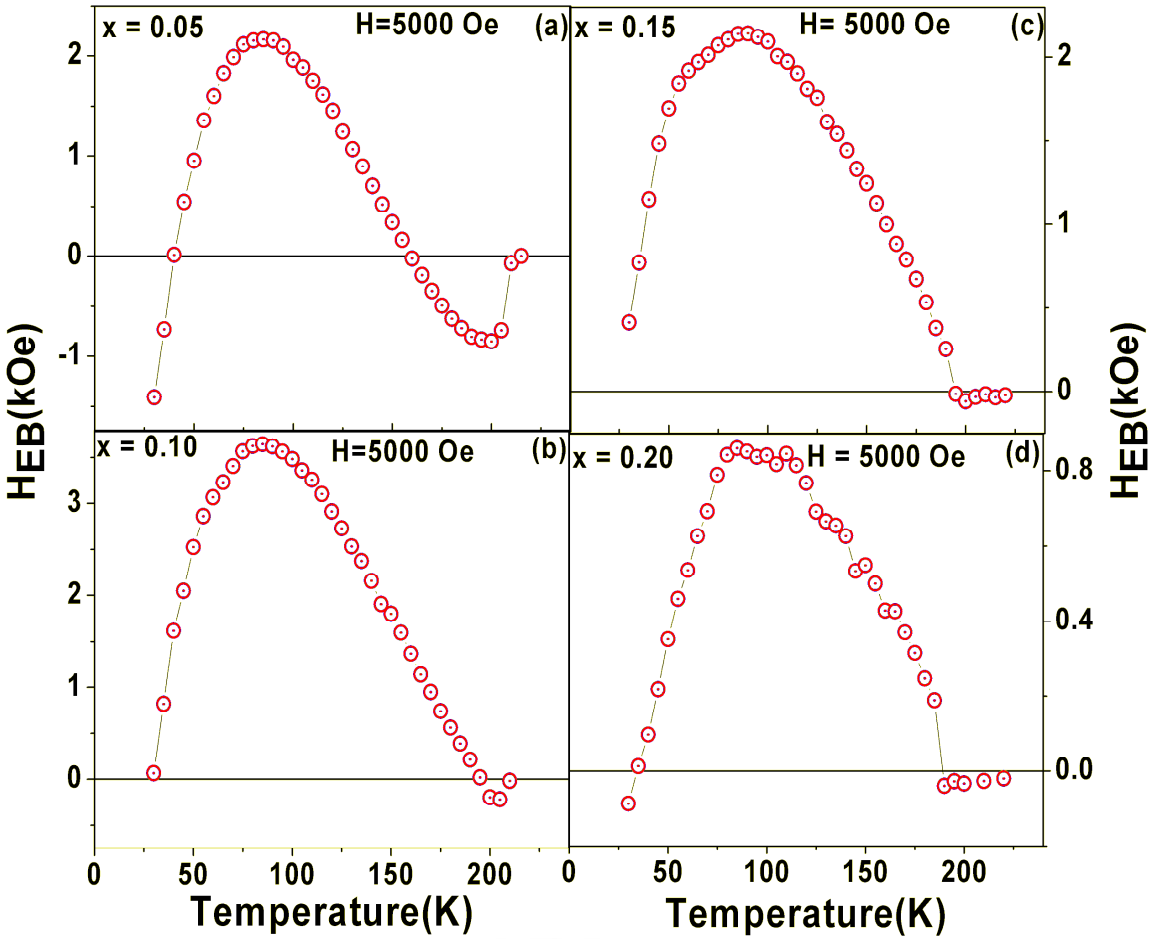

Figure 4.15: Temperature variation of H_{EB} for (a) x = 0.05, (b) x = 0.10, (c) x = 0.15 and (d) x = 0.20 samples.

general temperature dependence of paramagnetic moment. The H_{EB} behavior of x = 0.10 sample can be also understood based on the above argument; however in this sample negative H_{EB} is observed for a very narrow temperature range and it is mainly due to the

enhanced T_{comp} value, which is quite close to T_N. The observation of only positive H_{EB} values for x = 0.15 and 0.20 sample is due to the larger contribution of M_{Nd}+M_{Fe} as a result of higher concentration of Fe doping and the corresponding larger T_{comp} value quite close to T_N.

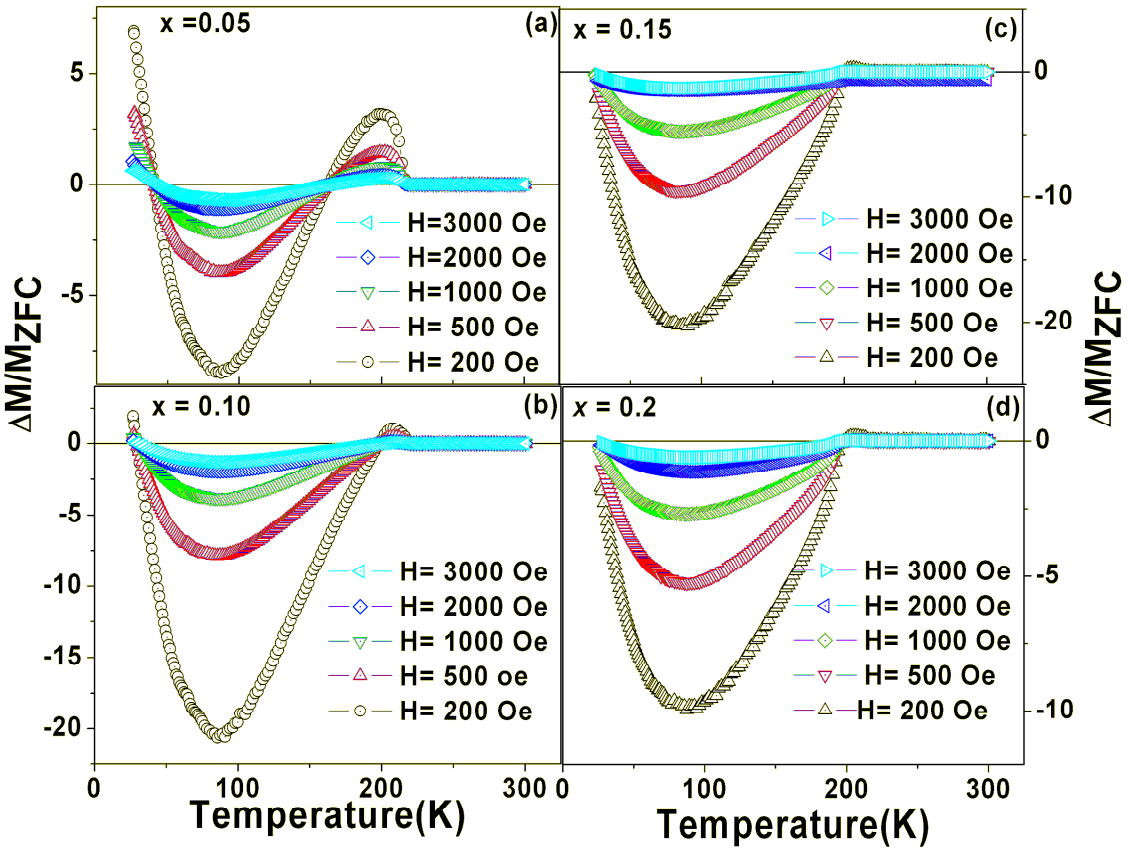

Figure 4.16: Temperature variation of relative irreversible magnetization for (a) x = 0.05, (b) x = 0.10, (c) x = 0.15 and (d) x = 0.20 samples.

The sign reversal of H_{EB} especially for x = 0.05 and 0.10 and its mechanism is discussed. Such a sign reversal of H_{EB} has been reported in other orthochromites [53, 73, 109] and intermetallic compounds [81, 82]; however its mechanism is found to differ depending on the nature of the sample and its microstructure. EB was explained by considering various models such as core shell structure [53], competition between the DM interaction and single ion magnetic anisotropy [112], unidirectional magnetic anisotropy due to DM interaction [109] and antiparallel coupling between the magnetic spins of Cr^{3+} ions and rare earth ions [73]. Sign reversal of different sub components of magnetic moment of rare earth ions and conduction electron polarization is reported to contribute EB and its sign

reversal in intermetallic compounds [81, 82]. Since we are not dealing with nano-particles, core shell structure is unlikely to play a role in the present set of samples. Because of the presence of considerable paramagnetic moment, the present data could not be fitted to the model involving the competition between DM interaction and single ion anisotropy [57]. The measured *M-T* data could be fitted to the model containing the canted FM component of Cr^{3+} ions and paramagnetic moments of Fe^{3+} and Nd^{3+} ions. H_{EB} is explained in terms of exchange anisotropy between M_{Cr} and M_{Nd}+M_{Fe} and its sign reversal is due to one component overtaking the other as the temperature is varied.

4.2 $NdCr_{1-x}Mn_xO_3$ compounds (x = 0.0 to 0.7)

This section deals with the effect of Mn substitution at Cr site of $NdCrO_3$. The preparation, characterization and the result obtained from dc magnetization along with the analysis are presented.

4.2.1 Sample Preparation and Characterization

Polycrystalline samples of $NdCr_{1-x}Mn_xO_3$ (x = 0.00 - 0.70) were prepared by the standard sol-gel route. Nd_2O_3, $Cr(NO_3)_3.9H_2O$ and $C_4H_6MnO_4.4H_2O$ were taken as starting compounds. All these compounds after dissolving in nitric acid or distilled water were converted into citrate by adding citric acid. By adding ethylene glycol the solution was converted into gel form. The precursor powder obtained from the gel was presintered at 600 ˚C for 12 h and the final sintering was done at 1100 ˚C for 24 h.

The XRD patterns recorded for the above samples are shown in Fig 4.17. The XRD patterns of the prepared samples are found to be in single phase form. They were refined by Rietveld technique [120] using *Pbnm* space group *i.e.* in orthorhombic structure. Typical XRD patterns along with the Rietveld refinement for x = 0.15 and 0.60 samples are shown in Fig. 4.18.

The refined lattice parameters and unit cell volume are listed in Table 4.3. The lattice parameter b and the unit cell volume are found to increase systematically with Mn doping except an anomaly for x = 0.50 sample. Typical SEM micrographs for x = 0.05, 0.10 and 0.15 samples are shown in Fig. 4.19. The morphology of the sample is found to be uniform. The average particle size is found to be in the order of 430 nm to 650 nm. Typical EDS spectrum for x = 0.15 sample is shown in Fig. 4.19. We can see that all the elements are present. Further, the chemical compositions determined from EDS analysis are comparable to the nominal starting compositions of the prepared materials. The cationic ratios for x = 0.00, 0.05, 0.10 and 0.15 samples are given in Table 4.4.

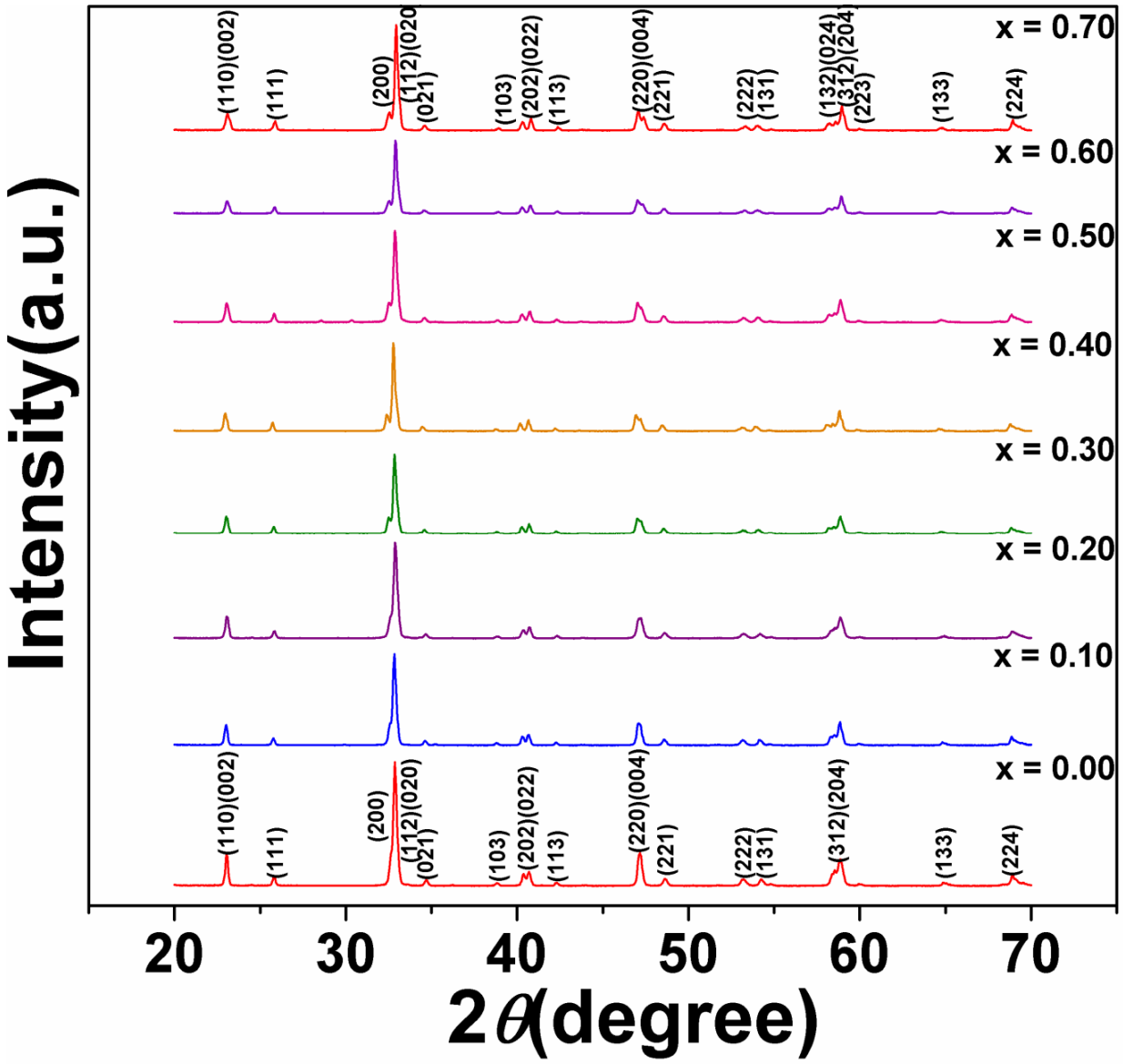

Figure 4.17: XRD patterns of $NdCr_{1-x}Mn_xO_3$ compounds for x = 0.00 to 0.70

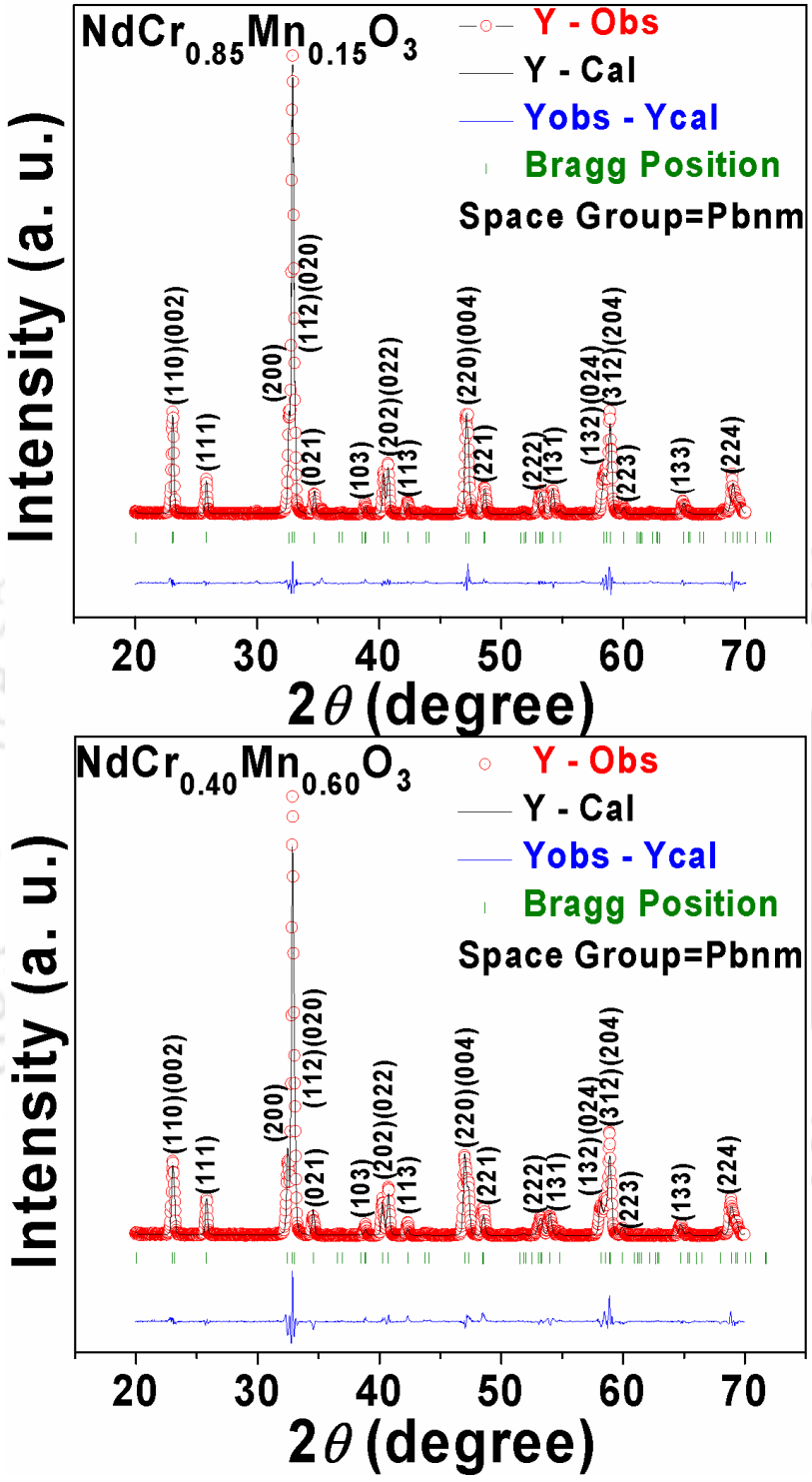

Figure 4.18: XRD patterns along with Rietveld refinement for x = 0.15 and 0.60 samples. The circles represent experimental data and solid line represents Rietveld refined data. The bottom line shows the difference between experimental and refined data. The marked 2θ positions are allowed Bragg peaks.

Table 4.3: Parameters obtained from the Rietveld analysis of XRD patterns for the samples $NdCr_{1-x}Mn_xO_3$ (0.00 to 0.70). R_F, R_{Bragg}, R_P, R_{exp} and χ^2 are the reliability factors.

Sample/ Parameters	***x* = 0.00**	***x* = 0.05**	***x* = 0.10**	***x* = 0.15**	***x* = 0.20**	***x* = 0.30**	***x* = 0.40**	***x* = 0.50**	***x* = 0.60**	***x* = 0.70**
Space group	*Pbnm*	*Pbnm*	*Pbnm*	*Pbnm*	*Pbnm*	*Pbnm*	*Pbnm*	*Pbnm*	*Pbnm*	*Pbnm*
***a* (Å)**	5.4138 (0.0003)	5.4134 (0.0003)	5.4133 (0.0003)	5.4154 (0.0003)	5.4164 (0.0003)	5.4162 (0.0003)	5.4149 0.0003)	5.4128 (0.0003)	5.4166 (0.0003)	5.4169 (0.0003)
***b* (Å)**	5.4772 (0.0003)	5.4771 (0.0003)	5.4814 (0.0003)	5.4860 (0.0003)	5.4880 (0.0003)	5.4993 (0.0003)	5.5073 (0.0003)	5.5287 (0.0003)	5.5104 (0.0003)	5.5135 (0.0004)
***c* (Å)**	7.6831 (0.0005)	7.6780 (0.0005)	7.6787 (0.0004)	7.6808 (0.0004)	7.6799 (0.0005)	7.6814 (0.0004)	7.6810 (0.0004)	7.6742 (0.0005)	7.6799 (0.0005)	7.6768 (0.0005)
***Volume* (Å^3)**	227.82 (0.02)	227.65 (0.02)	227.85 (0.02)	228.19 (0.02)	228.28 (0.02)	228.79 (0.02)	229.06 (0.02)	229.65 (0.02)	229.23 (0.02)	229.28 (0.02)
R_F (%)	3.90	4.54	4.99	4.73	4.97	5.66	4.86	6.16	6.23	6.10
R_{Bragg} (%)	2.71	3.17	3.19	2.98	3.14	3.26	4.67	6.02	5.76	5.73
R_P (%)	6.97	7.34	8.04	8.40	8.06	8.47	10.2	14.8	11.6	12.1
R_{exp} (%)	6.04	6.22	6.06	5.94	5.98	5.89	5.94	6.32	6.38	6.72
χ^2	4.01	3.71	4.79	5.18	4.66	4.92	5.95	9.15	6.14	5.88
Nd/Cr/Mn Occupancy	1.000 /1.000 /0.000	0.970 /0.941 /0.049	0.970 /0.895 /0.099	0.981 /0.850 /0.149	0.996 /0.802 /0.198	0.990 /0.703 /0.297	0.989 /0.602 /0.398	0.972 /0.499 /0.499	0.956 /0.399 /0.599	0.959 /0.299 0.699

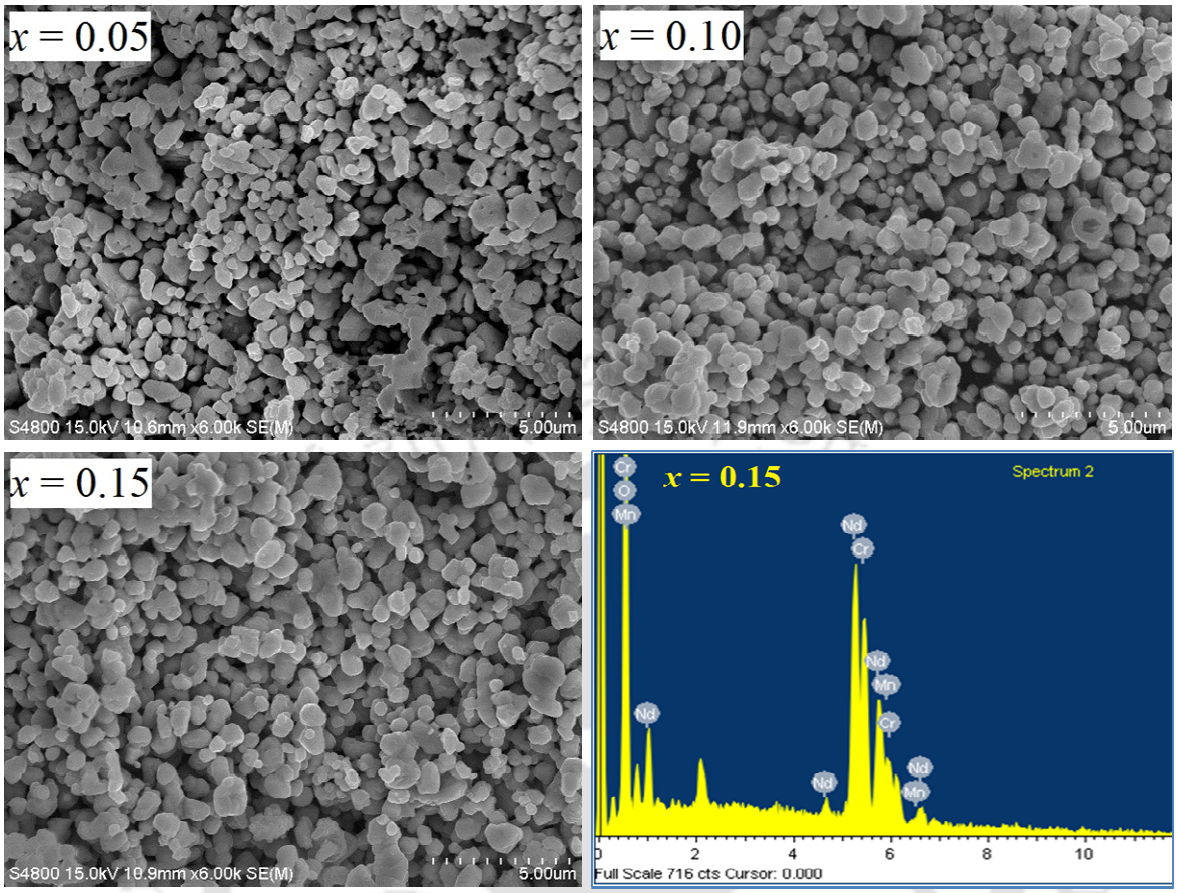

Figure 4.19: SEM images recorded for x = 0.05, 0.10 and 0.15 samples along with EDS spectrum for x = 0.15.

Table 4.4: The cationic ratio determined from EDS analysis for x = 0.00, 0.05, 0.10 and 0.15 samples.

Samples	**Calculated Cationic Ratio from EDS Analysis**		
	Nd	**Cr**	**Mn**
***x* = 0.00**	0.93	1.00	0.00
***x* = 0.05**	0.92	0.92	0.07
***x* = 0.10**	0.89	0.88	0.11
***x* = 0.15**	0.96	0.83	0.16

4.2.2 Magnetic Properties

Magnetization (M) versus temperature (T) plots in zero field cooled (ZFC) and field cooled (FC) conditions at applied field H = 2000 Oe are shown in Fig. 4.20 for x = 0.00, 0.05, 0.10, 0.15, 0.20, 0.30, 0.40, 0.50, 0.60 and 0.70 samples. The ZFC magnetization of x = 0.00 sample shows a tiny sharp peak at T_N = 223 K indicating the AFM transition as shown in the inset of Fig. 4.20 (a). For $T < T_N$, M is found to increase with typical paramagnetic behavior and it can be understood in terms of contribution from Nd ions. The FC data show large irreversibility for $T < T_N$. M increases quite sharply reaching a plateau at $T < T_N$. The plateau persists down to around 100 K and beyond that a secondary rise in magnetization is observed due to spin reorientation of Cr^{3+} ions [99]. The M-T behavior of x = 0.05 sample follows the trend of x = 0.00 sample but with a smaller T_N value of 213 K. Moreover, upon reaching a peak value of about 45 emu/mol, the FC magnetization decreases with decrease in temperature and this trend continues down to 100 K. On further decrease in temperature a sharp rise in magnetization is observed at $T_{SRT} \cong$ 50 K. In x = 0.10 sample, an appreciable positive irreversibility is observed only over a temperature range of T_N to 110 K and beyond that, the FC magnetization is found to fall below (crossover) the ZFC magnetization value. The crossover temperature is increased to 150 K for x = 0.15 sample. For x = 0.20 sample, the entire FC magnetization values for $T < T_N$ are found to be lower than those of ZFC magnetization. So, it exhibits tendency towards MR.

With increase in doping concentration, the ZFC magnetization value is found to increase monotonously due to the reduction in AFM interaction in Cr^{3+}-O^{2-}-Cr^{3+} networks. The T_N value is found to decrease from 223 K for x = 0 to 196 K for x = 0.15. The x = 0.30 sample shows a different behavior compared to lower doped samples. Both ZFC and FC M-T curves almost merge without any considerable irreversibility. No signature of low temperature spin reorientation transition is observed. Moreover the magnitude of magnetization is about five times greater than that of other low doped ($x \leq 0.20$) samples. So, it shows the presence of ferromagnetic contribution. For further increase in Mn concentration beyond x = 0.30, monotonous increase in ferromagnetic transition temperature, magnitude of magnetization and the sharpness of FM transition is observed. Thus samples in the composition range $0.40 \leq x \leq 0.70$ exhibit FM transition due to double exchange

ferromagnetic interaction in possible Cr^{3+}-O^{2-} -Mn^{3+} and Mn^{3+}-O^{2-}-Mn^{4+} networks.

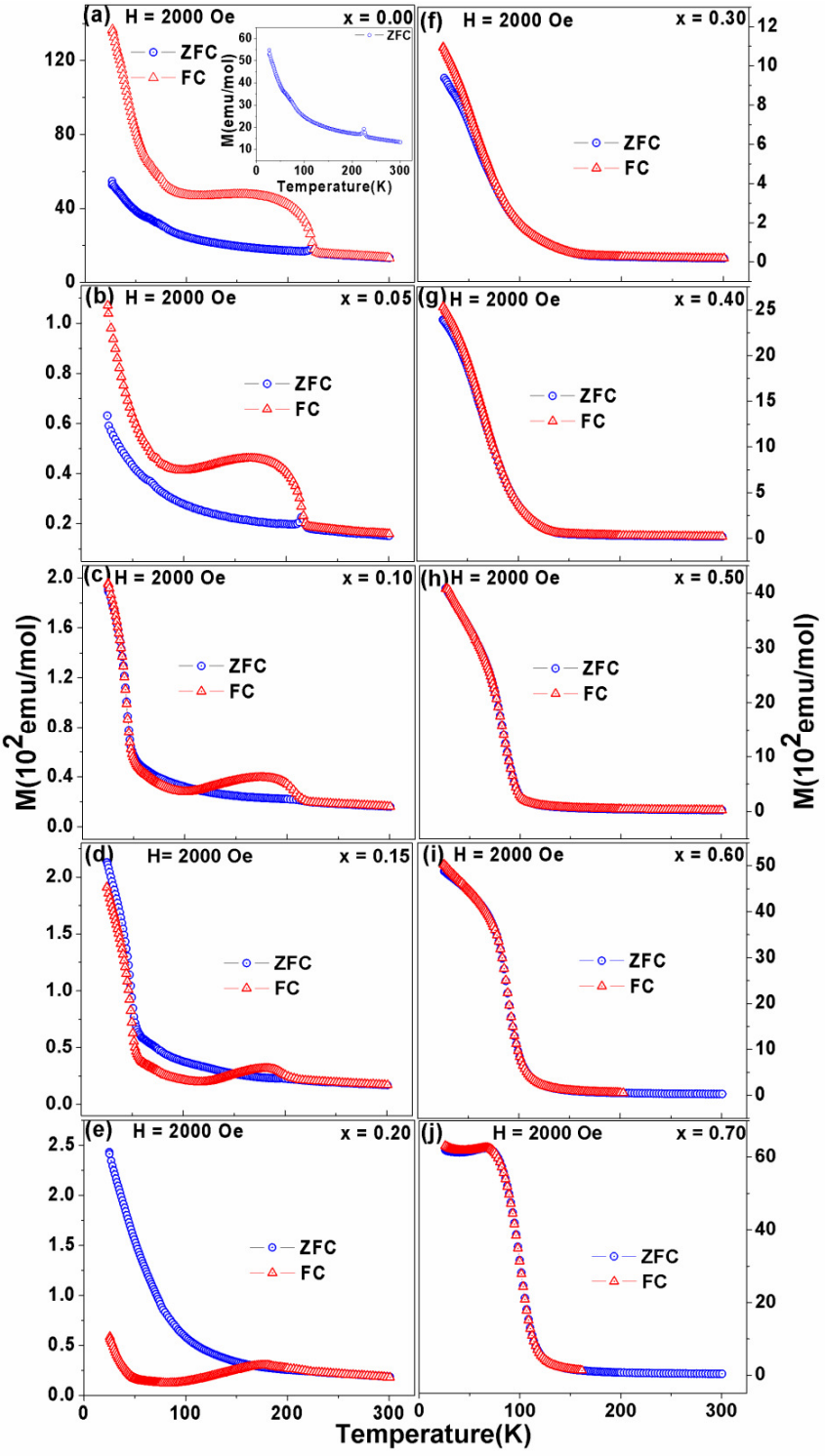

Figure 4.20: Temperature variation of magnetization in ZFC and FC conditions for x = 0.00 to 0.70 samples.

(i) Magnetization Reversal

In view of the observed magnetization crossover and tendency towards magnetization reversal in x = 0.10, 0.15 and 0.20 samples, we have carried out systematic *M-T* measurements for different applied fields ranging from 50 Oe to 2000 Oe. The magnetization reversal is observed up to a magnetic field of H = 200 Oe for x = 0.10 sample and beyond this field the *M-T* curve is shifted to positive magnetization without changing the trend of *M-T* plot. The FC curve crosses the temperature axis twice leading to two compensation temperatures as shown in Fig. 4.21. With increase in H, the T_{comp} value decreases from 110 K for 50 Oe to 103 K for 200 Oe. Similarly, for x = 0.15 sample, T_{comp} varies from 147 K at 50 Oe to 133 K at 500 Oe and the MR is observed up to H = 500 Oe as shown in Fig. 4.22. On the other hand, for x = 0.20 sample, only one compensation temperature is observed *i.e.* below T_{comp}, M continues to go towards more negative value down to the lowest measured temperature as shown in Fig. 4.23. The maximum negative magnetization value of this sample is found to be 10 times larger than that of x = 0.10 and 0.15 samples. As H increases, T_{comp} decreases from 157 K at H = 50 Oe to 128 K at H =1000 Oe. For $H \geq$ 2000 Oe, the *M-T* curve is shifted to positive magnetization direction. With increase in Mn concentration, T_{comp} value is found to increase.

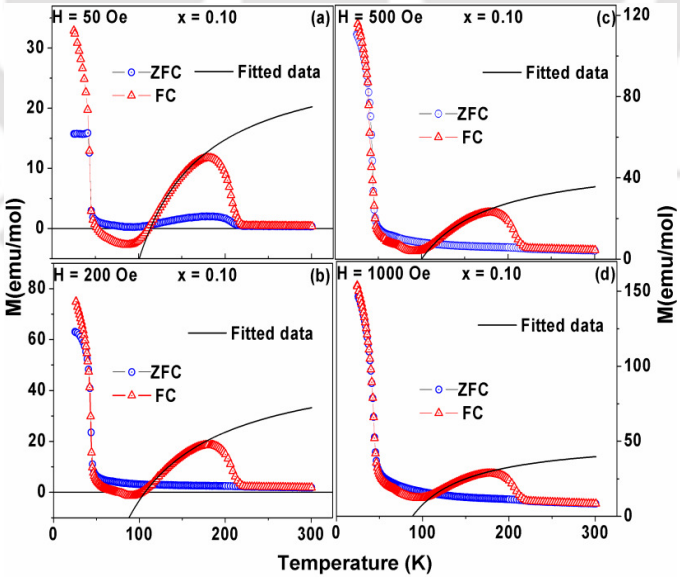

Figure 4.21: ZFC and FC curves of x = 0.10 sample at H = 50 Oe, 200 Oe, 500 Oe and 1000 Oe along with fitted data.

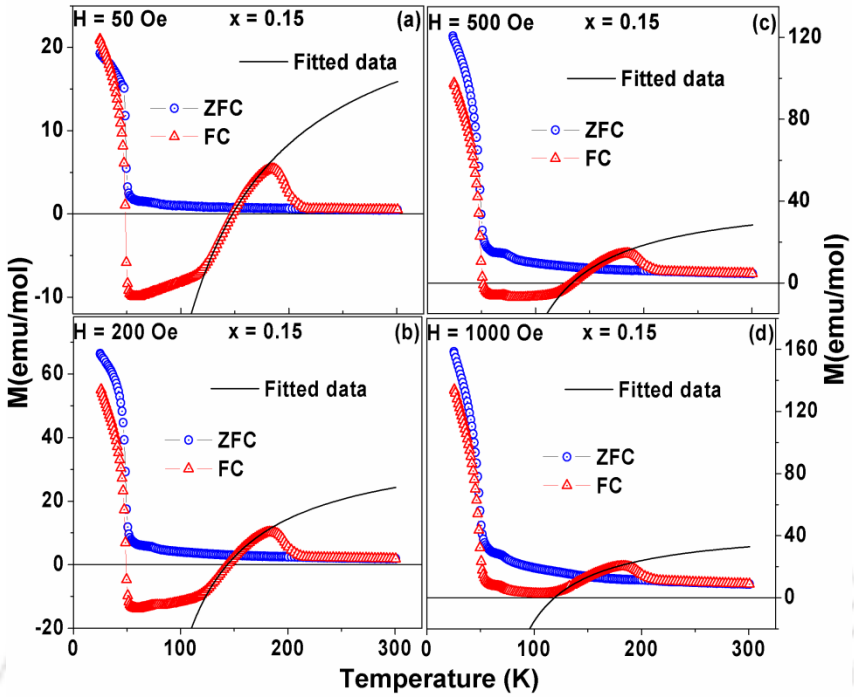

Figure 4.22: ZFC and FC curves of $x = 0.15$ sample at $H = 50$ Oe, 200 Oe, 500 Oe and 1000 Oe along with fitted data.

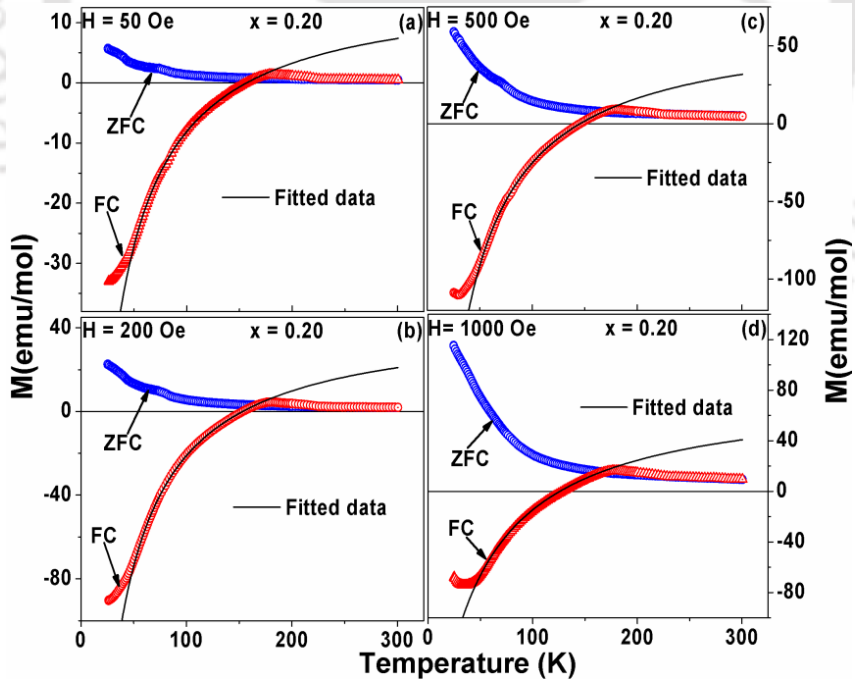

Figure 4.23: ZFC and FC curves of $x = 0.20$ sample at $H = 50$ Oe, 200 Oe, 500 Oe and 1000 Oe along with fitted data.

For low concentration of Mn, the possibility of Mn^{3+}-O^{2-}-Mn^{3+} networks and their interaction is very rare, so, we have considered both Nd and Mn ions are paramagnetic entities. The competition between the weak FM component of Cr^{3+} moment and the paramagnetic moments of Mn^{3+} and Nd^{3+} under the influence of negative internal magnetic field of AFM ordered Cr^{3+} ions gives rise to the magnetization reversal. So, the experimental data were analyzed as per the above model and hence following the equation (4.1). The FC curves of x = 0.10 to 0.20 samples were fitted to equation (4.1) for $H \leq 1000$ Oe. The fitted data of x = 0.10, 0.15 and x = 0.20 samples closely follow the experimental curve as shown in Figs. 4.21, 4.22 and 4.23 respectively. The estimated θ_C value is found to be around 40 K for x = 0.10 and 0.15 samples. Magnitudes of both H_I and M_{Cr} are found to increase with applied field as shown in Fig. 4.24. Similar behavior is observed for x = 0.20 sample and they are found to be in the range of H_I = -1.2 kOe to -6.9 kOe and M_{Cr} = 16.2 emu/mol to 78.8 emu/mol for the applied field H = 50 Oe to 1000 Oe. The obtained H_I values for these samples are comparable to the result of $GdCrO_3$ [15] and $La_{1-x}Pr_xCrO_3$ [73] compounds. With increase in applied field, the AFM domain size is also expected to increases and this gives rise to increase in H_I and M_{Cr} values.

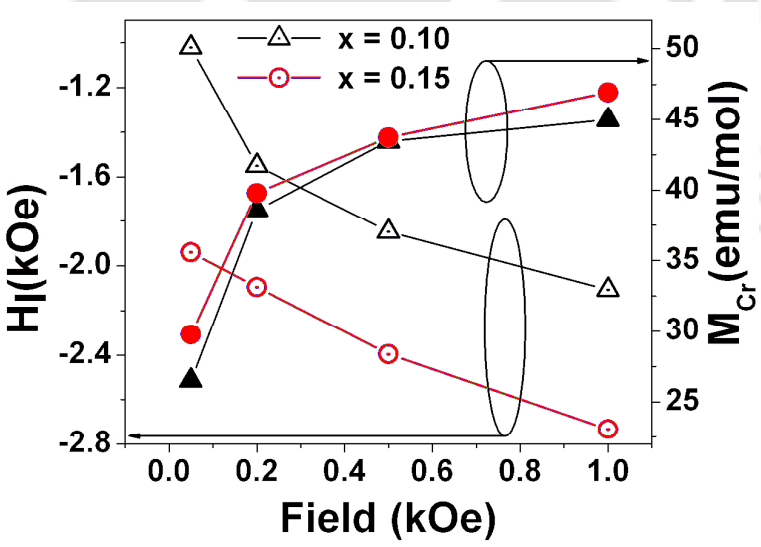

Figure 4.24: M_{Cr} and H_I as a function of applied field for x = 0.10 (triangles) and 0.15 (circles) samples.

Thus with increase in Mn concentration, the net paramagnetic moment increases as a result, we see the increase in T_{comp} values for a fixed H value. For x = 0.20, a large negative

magnetization is observed due to the enhanced paramagnetic moment and simultaneous decrease in M_{Cr}. We have not observed the spin reorientation transition for H = 200 Oe; however for a large applied field of the order of H_I, the presence of spin reorientation transition is seen as shown in Fig. 4.20 (e).

We can estimate the extend of MR by considering the maximum (positive) magnetization and minimum (negative) magnetization *i.e.* M_{max} and M_{min}. The maximum value of M_{min}/M_{max} is found to be 24 for x = 0.20 sample at H = 200 Oe. It is reported to be 30 for $GdCrO_3$ [15] and 40 for $La_{0.5}Pr_{0.5}CrO_3$ [49]. The fractional magnetization irreversibility at a particular temperature can be calculated by using the relation $\Delta M/M_{ZFC} = (M_{FC} - M_{ZFC})/M_{ZFC}$. The value of $\Delta M/M_{ZFC}$ for x = 0.20 sample at 50 K is found to be -9.4 for H = 50 Oe. It is found to be in the range of -2 to -9 in magnetic rare earth orthochromites [15, 90].

To clearly demonstrate the MR below T_{comp}, typical bipolar switching of magnetization for x = 0.15 and x = 0.20 samples are shown in Fig. 4.25. Samples were cooled in the presence of an applied field of H = 200 Oe and then H was increased to 3000 Oe to switch the magnetization to positive value and the subsequent variation of field in the range 200 Oe to 3000 Oe produces the reversible and reproducible magnetization switching.

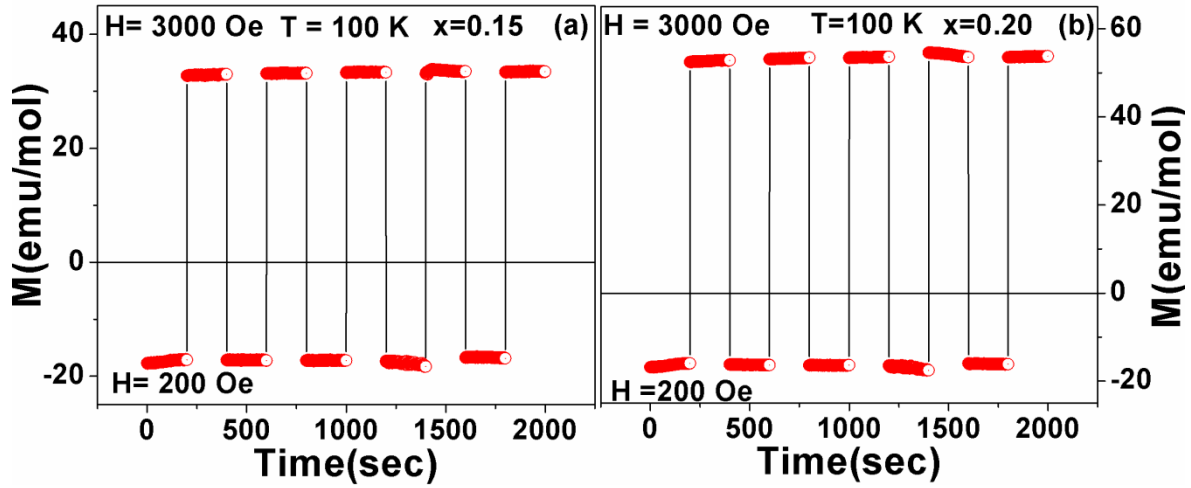

Figure 4.25: Bipolar switching of magnetization at 100 K for (a) x = 0.15 and (b) x = 0.20 samples.

Similar magnetization switching was observed for x = 0.10 sample but for a smaller applied field range of 50 Oe to 500 Oe. This phenomenon can be useful in device application such as magnetic data storage, nonvolatile magnetic memory *etc* [128].

(ii) Change in Magnetic Entropy

In order to understand the magnetic properties in the vicinity of T_{SRT}, we have estimated the change in magnetic entropy as per the following relation [129],

$$\Delta S = \int_0^H \frac{\partial M}{\partial T} dH$$

We have calculated the ΔS values from isothermal magnetization curve of different applied magnetic fields. Plots of $-\Delta S$ versus temperature for x = 0.10 and 0.15 samples at three different H values are shown in Fig. 4.26.

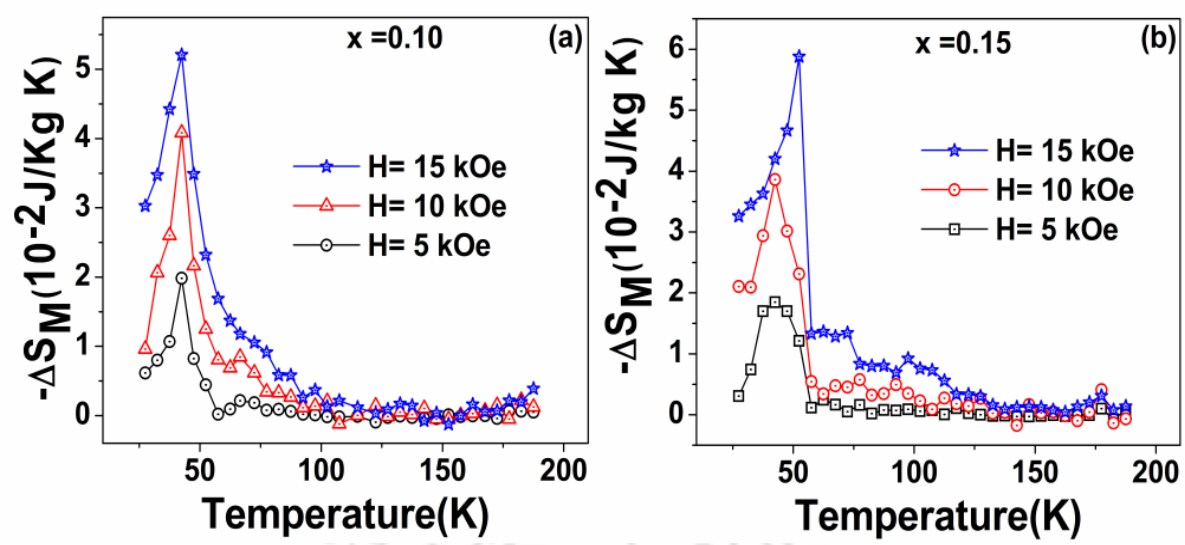

Figure 4.26: Plots of change in entropy (-Δ*S*) versus *T* for *x* = 0.10 and 0.15 samples for different applied field.

We can see a positive peak at around T_{SRT} and it depicts that the spin reorientation is associated with weak ferromagnetic transition. Shifting of peak to higher temperature with increasing in H is observed and similar shifting was reported in $TmCrO_3$ [109] and $DyCrO_3$ [130] compounds. However they have carried out the measurement up to H = 4 T and large shifting was reported for H = 4 T. The maximum value of $-\Delta S$ in the present series of sample

is quite small compared to that of $TmCrO_3$ and $DyCrO_3$ and it is due to the smaller magnetization observed in the present series. The smaller magnetization in $NdCrO_3$ is due to the smaller magnetic moment of Nd^{3+} (3.63 μ_B) ions compared to Tm^{3+} (7.57 μ_B) and Dy^{3+} (10.63 μ_B), and moreover the ionic size of rare earth ions play a crucial role. The larger ionic radius of Nd^{3+} (0.983 Å) ions compared to Dy^{3+} (0.912 Å) and Tm^{3+} (0.88 Å) ions gives rise to smaller lattice distortion and hence smaller values of canted FM component.

(iii) Exchange Bias

To explore exchange bias behavior, we have recorded *M-H* loops in the temperature range of 25 K - 200 K after cooling the samples under the field of 5000 Oe for x = 0.10, 0.15 and 0.20. Typical *M-H* loops at a few selected temperatures for x = 0.10, 0.15 and 0.20 samples are shown in Figs. 4.27, 4.28 and 4.29 respectively. The *M-H* loops at low temperature, especially in the temperature range 50 K < T < 150 K are found to shift towards positive field axis but as the temperature is raised towards T_N, the loops are found to shift towards negative field axis.

The exchange bias field H_{EB} was determined using the relation $H_{EB} = (H_+ + H_-)/2$ *i.e.* similar to that described in section 4.1.2. The variation of H_{EB} with T for x = 0.10, 0.15 and 0.20 samples are shown in Fig. 4.30. H_{EB} versus T plots exhibit asymmetric sinusoidal like behavior with a positive peak at low temperature and a negative peak at higher temperature. The peak values of H_{EB} for x = 0.10 sample are -1.6 kOe and + 0.39 kOe at 175 K and 85 K respectively. With increase in doping concentration, the negative peak is found to be suppressed and positive H_{EB} values are observed for a wider temperature range. The observed H_{EB} values are comparable to those of $NdMnO_3$ [72] and $La_{0.15}Pr_{0.85}CrO_3$ [73]. The trend of H_{EB} for x = 0.10 and 0.15 samples are comparable to intermetallic alloys such as $Sm_{0.98}Gd_{0.02}Al_2$ [82] and $Nd_{0.75}Ho_{0.25}Al_2$ [81]. For a comparison, temperature variation of $\Delta M/M_{ZFC}$ are shown in Fig. 4.31 for different H values. All curves pass through the temperature axis at a particular temperature known as T_{cross}. A negative peak at $T < T_{cross}$ is observed for all the samples and in addition to that a positive peak is observed at $T > T_{cross}$. These peaks coincide with the positive and negative peaks of H_{EB} versus T plots.

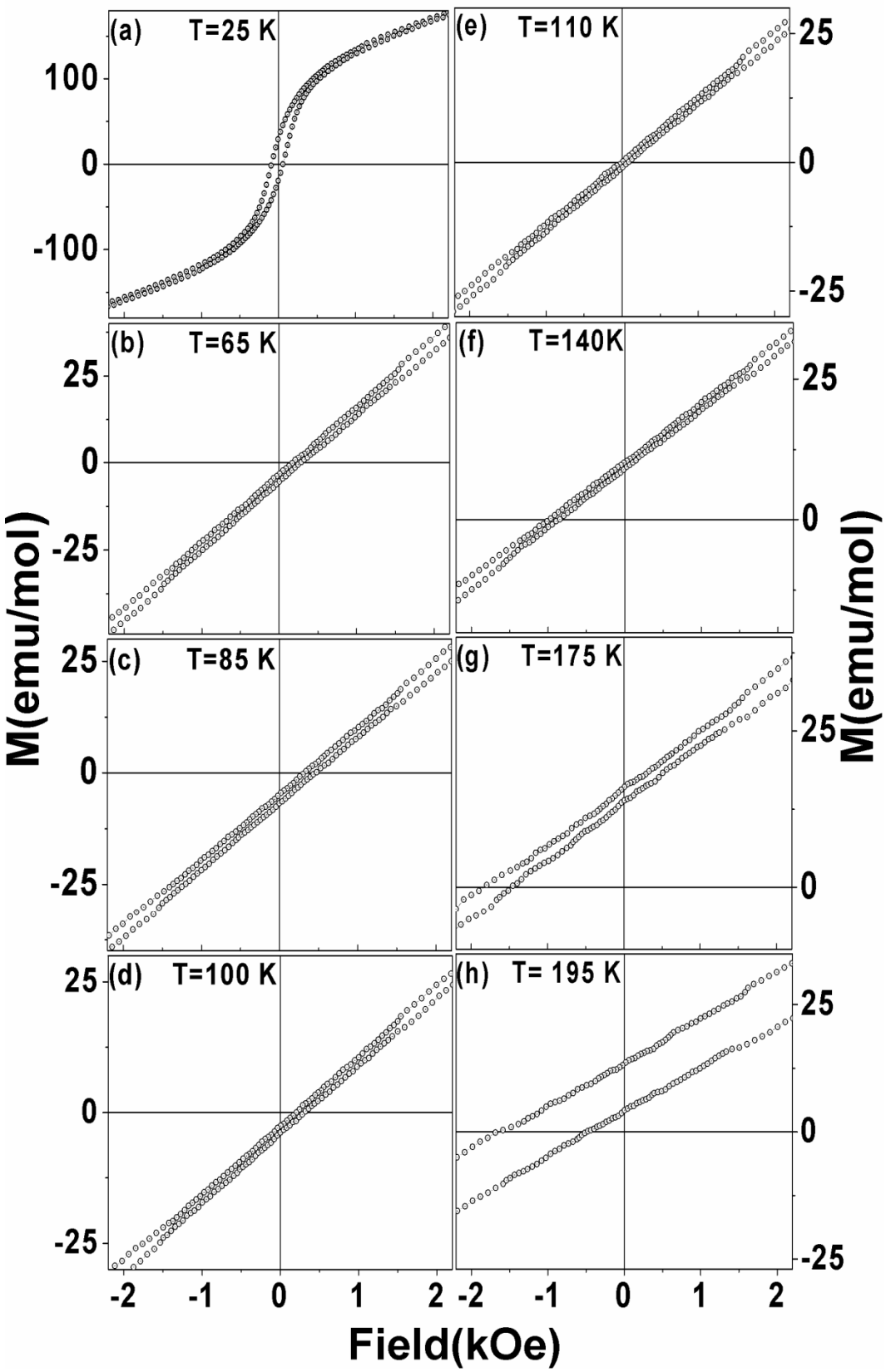

Figure 4.27: *M-H* loops of $x = 0.10$ sample at different temperatures in expanded scale.

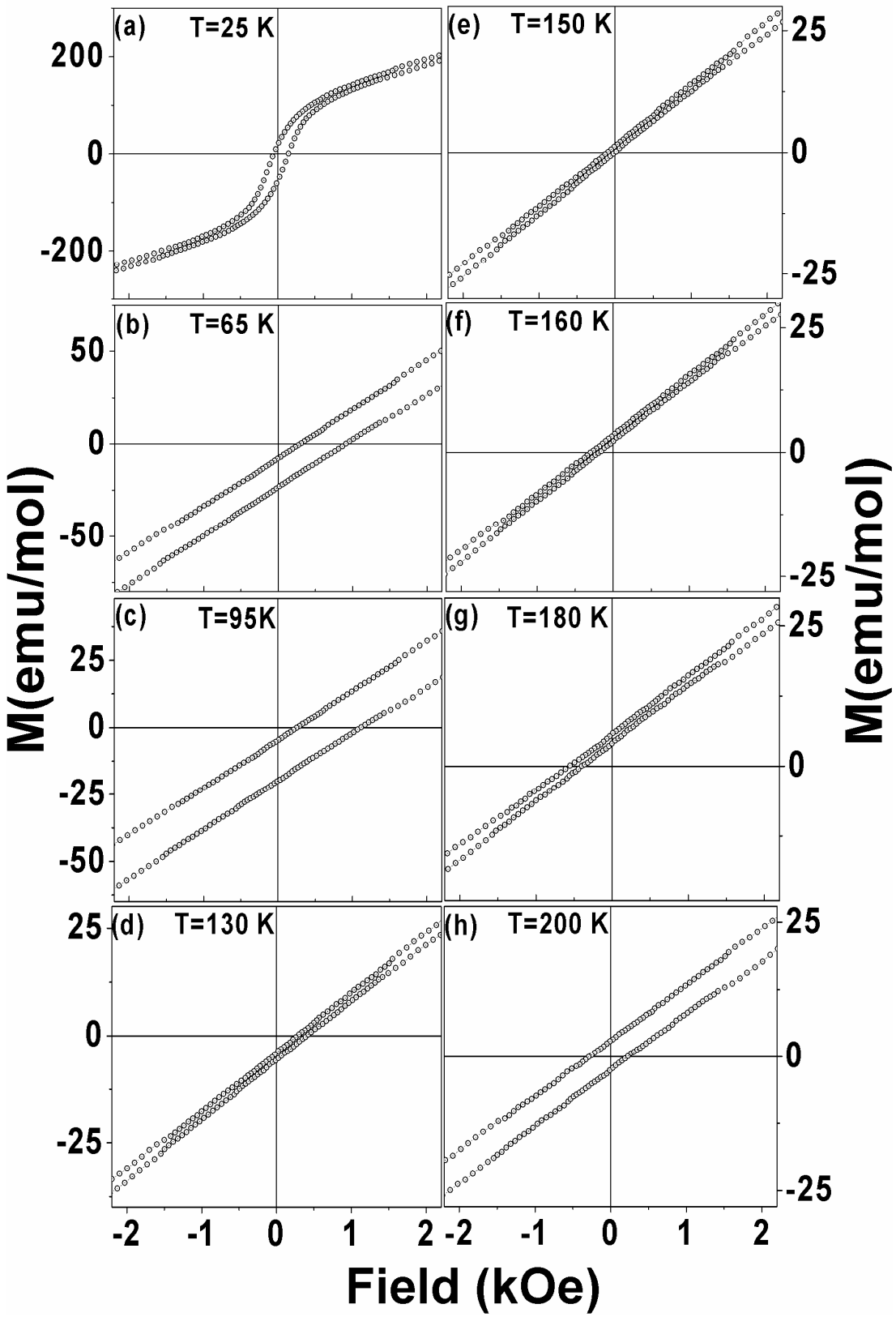

Figure 4.28: *M-H* loops of $x = 0.15$ sample at different temperatures in expanded scale.

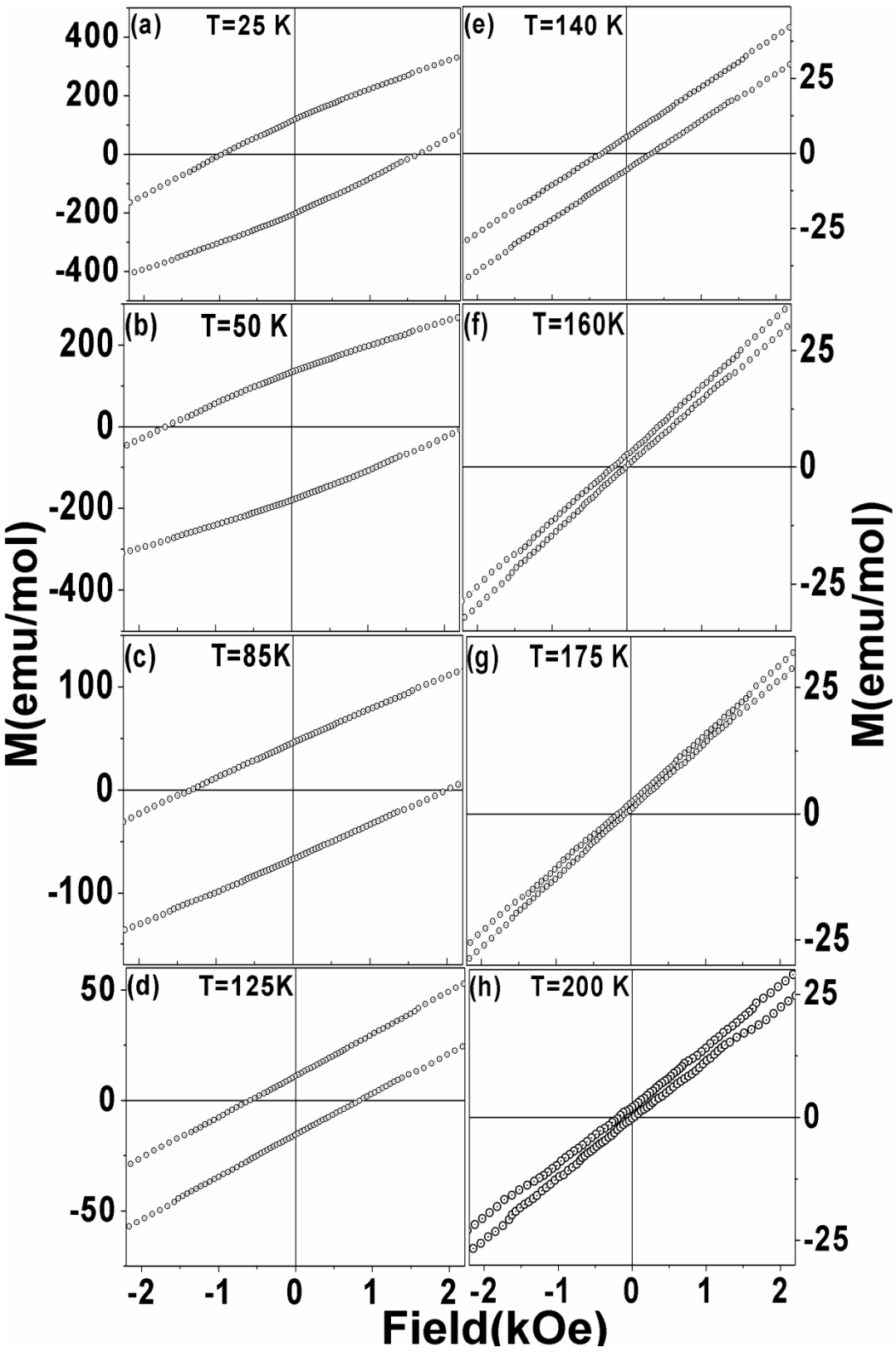

Figure 4.29: *M-H* loops of $x = 0.20$ sample at different temperatures in expanded scale.

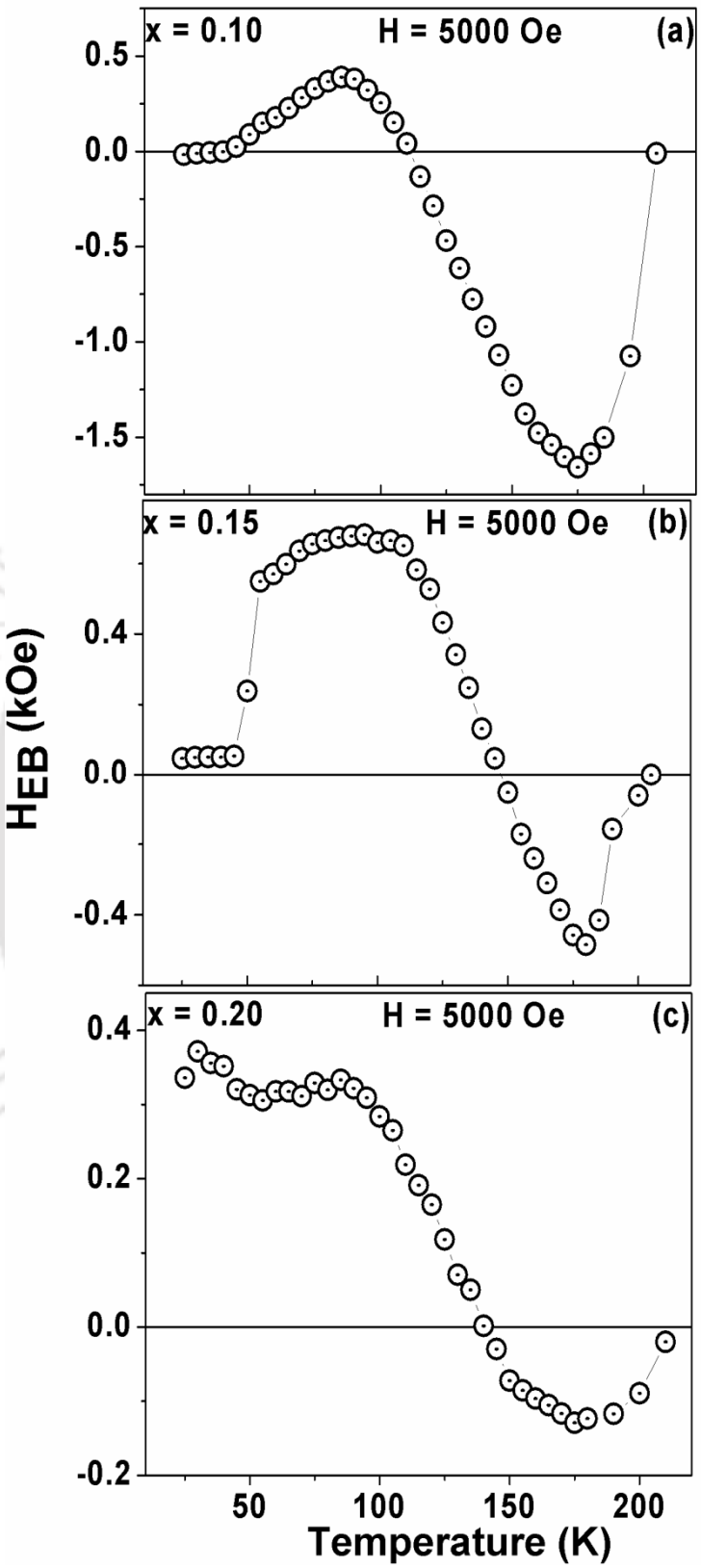

Figure 4.30: H_{EB} versus T plots for (a) $x = 0.10$, (b) $x = 0.15$ and (c) $x = 0.20$ samples.

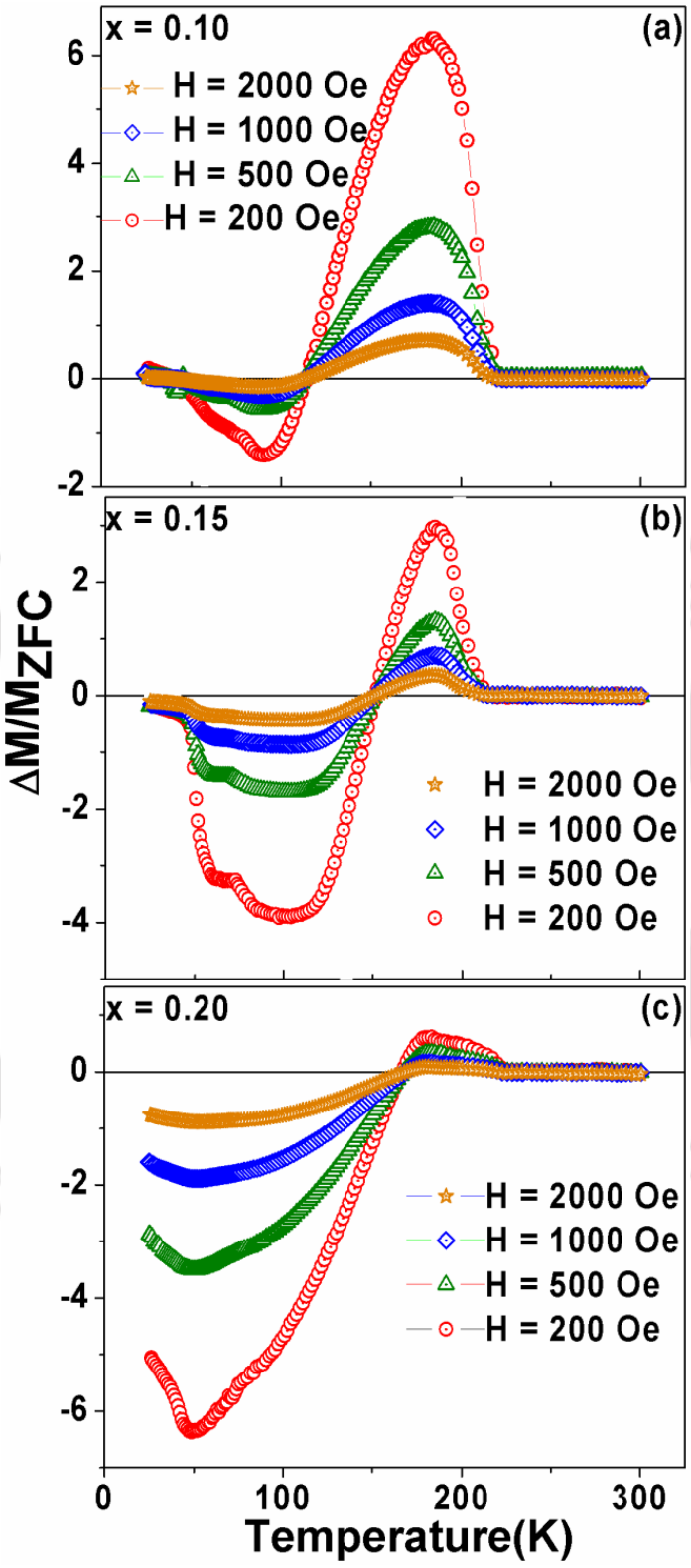

Figure 4.31: Irreversible magnetization versus temperature plots for (a) $x = 0.10$, (b) $x = 0.15$ and (c) $x = 0.20$ samples.

The observed tunable exchange bias of these samples can be explained by considering the antiferromagnetic interaction between the ferromagnetic component of Cr^{3+} ions (M_{Cr}) and the paramagnetic component of Nd^{3+} ions and the doped Mn^{3+} ions ($M_{Nd} + M_{Mn}$) under the influence of negative internal field. In the temperature region $T_{comp} < T < T_N$, M_{Cr} dominates over the $M_{Nd} + M_{Mn}$ and the net magnetization is found to be positive and the exchange bias is found to be negative. Below T_{comp}, $M_{Nd} + M_{Mn}$ dominates over M_{Cr} and it gives rise to negative magnetization and positive exchange bias. For $T < 50$ K, presence of weak ferromagnetic interaction reduces the strength of anisotropic exchange interaction between M_{Cr} and $M_{Nd} + M_{Mn}$ and that brings down the exchange bias field close to zero for $x = 0.10$ and 0.15 samples. On the other hand, non-zero H_{EB} is observed for $x = 0.20$ sample due to the absence of low temperature ferromagnetic like transition, especially under FC condition for $H \leq 1000$ Oe.

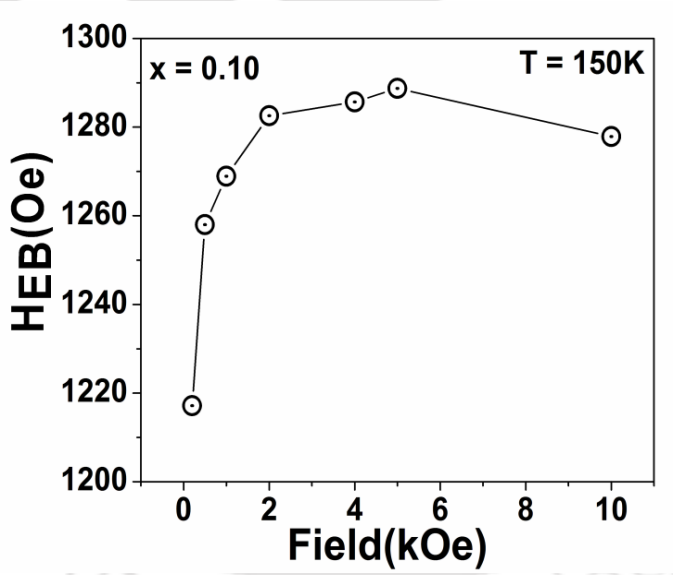

Figure 4.32: The cooling field dependence H_{EB} for $x = 0.10$ sample.

We have also studied the cooling field dependence of H_{EB} for $x = 0.10$ sample by cooling the sample from 300 K to 25 K under different applied field of 200 Oe $\leq H \leq$ 10 kOe. The cooling field variation of H_{EB} at 150 K is shown in Fig. 4.32. The H_{EB} value increases with increase in cooling field up to 6 kOe after that it starts to decrease. For low cooling fields, all M_{Cr} cannot saturate in the direction of applied field so the exchange anisotropy is expected to be weak and hence H_{EB} is small. As H increases, M_{Cr} increases and it leads to

increase in exchange anisotropy and as a result H_{EB} also increases. This trend continues until the saturation of M_{Cr}, which is observed at $H \simeq 6$ kOe. For further increase in H value, H_{EB} decrease due to possible magnetic interaction between M_{Cr} and M_{Nd}+M_{Mn}. Similar behavior was reported on bulk charge ordered and cluster glass manganites [63, 67] and phase separated cobalites [69].

In general EB is possible due to the presence of core-shell like structure, spin glass/cluster glass/low temperature freezing phase, bilayer/multilayer structure, minor loop effect and antiferromagnetic coupling between the two magnetic components. The present samples are bulk in nature so core- shell structure model is not applicable for these samples and moreover we are not dealing with layered structure. We have observed low temperature upturn in the *M-T* plot for x = 0.10 and 0.15 samples due to the Cr^{3+} spin reorientation and we have not observed any freezing phase. If the observed EB is due to the minor loop effect, then we would not have observed the trend shown in Fig. 4.32. So, the observed H_{EB} is due to the AFM coupling between the canted Cr^{3+} ions and the PM moment of Nd^{3+} and Mn^{3+} ions.

As per the *M-T* plots of $NdCr_{1-x}Mn_xO_3$ samples for $x \geq 0.30$ we have observed FM like transition. In order to further explore the nature of transition, we have plotted inverse magnetic susceptibility obtained from magnetization as a function of temperature measured at H = 2000 Oe. The plots of $1/\chi$ versus T for x = 0.30, 0.40, 0.50 and 0.70 are shown in Fig. 4.33. We can see that they exhibit linear behavior in the paramagnetic region. These data in the paramagnetic region were analyzed by fitting to Curie-Weiss Law, $\chi = \frac{C}{(T-\theta_c)}$. The estimated values of Curie temperature θ_c are given in Table 4.5 for x = 0.30 to 0.70. These θ_c values signify that increase in Mn concentration strengthens the ferromagnetic interaction especially for $x \geq 0.4$. The ferromagnetic interaction in Cr^{3+}-O^{2-}-Mn^{3+} and Mn^{3+}-O^{2-}- Mn^{4+} networks through double exchange interaction is expected to be responsible for the above ordering. The effective magnetic moment μ_{eff} was calculated from the fitted value of C by using the relation $\mu_{eff} = \sqrt{3k_BC/N_A\mu_0\mu_B^2}$. The μ_{eff} values for x = 0.30, 0.40, 0.50, 0.60 and 0.70 samples are given in Table 4.5. With increase in Mn concentration, μ_{eff} value is also increases. The μ_{eff} values obtained from the analysis of experimental data can be compared with the theoretical effective magnetic moment μ_{th}. By taking into account magnetic moment

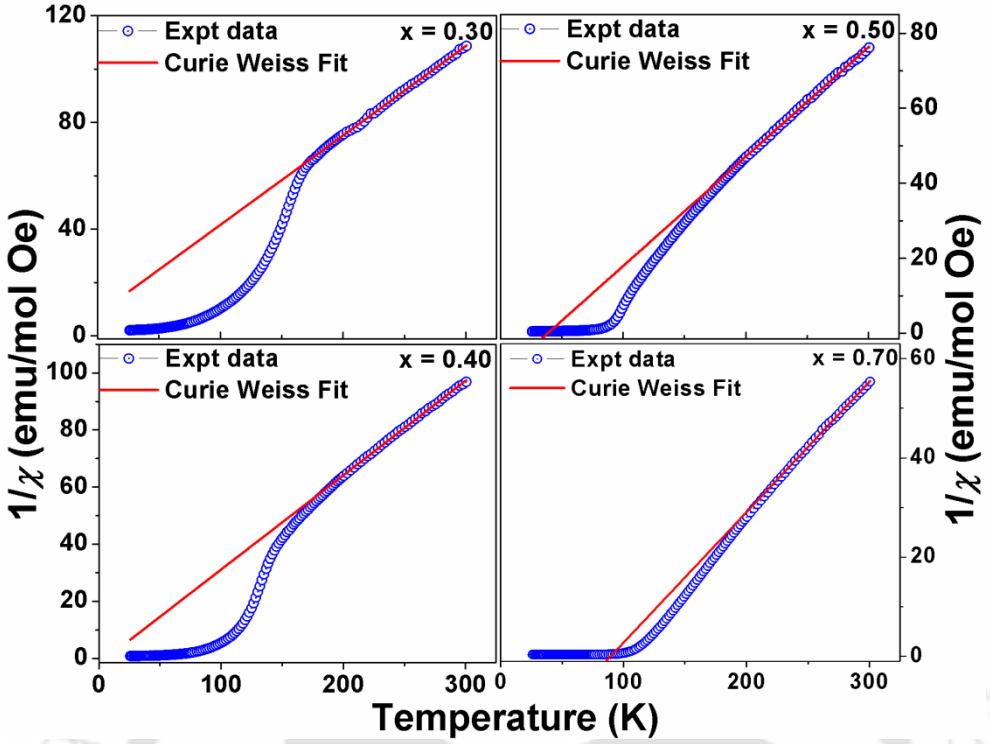

Figure 4.33: $1/\chi$ versus temperature for the samples x = 0.30, 0.40, 0.50 and 0.70. Solid lines represent fit to the Curie-Weiss Law.

contribution from Nd^{3+}, Cr^{3+}, Mn^{3+} ions, μ_{th} can be calculated as $\mu_{th} = \sqrt{x_1\mu_1^2 + x_2\mu_2^2 + x_3\mu_3^2}$, where x_1, x_2 and x_3 are the fractional concentration of Nd^{3+}, Cr^{3+} and Mn^{3+} ions per formula unit. μ_1, μ_2 and μ_3 are the theoretical magnetic moments of Nd^{3+}, Cr^{3+} and Mn^{3+} ions and their values due to spin only contribution are 3.63 μ_B, 3.87 μ_B and 4.9 μ_B respectively. Eventhough, presence of small Mn^{4+} concentration is expected, it is difficult to estimate Mn^{3+}/Mn^{4+} ratio, so for the approximate estimation of μ_{th} only the moment due to Mn^{3+} is taken into account. Even though magnetic transitions are observed at $T < 150$ K for $x \geq 0.3$, there is a possibility of Cr^{3+}-O^{2-}-Cr^{3+} networks which order AFM at higher temperature, thereby affecting the Curie-Weiss Law fit in the paramagnetic region. The probability of Cr^{3+}-O^{2-}-Cr^{3+} networks is calculated by using the relation [131] $P(n,x) = [6!/n!(6-n)!]x^n(1-x)^{6-n}$. The probability of Cr^{3+} ions to have one Cr^{3+} nearest neighbor for the doping concentration x = 0.3, 0.4, 0.5, 0.60 and 0.70 are found to be P(1, 0.30) = 0.3, P(1, 0.40) = 0.2, P(1, 0.50) = 0.09, P(1, 0.60) = 0.03 and P(1, 0.70) = 0.01 . By assuming that such networks interact antiferromagnetically

and do not contribute to μ_{eff}, the theoretical values were recalculated and the values are found to be mostly comparable to experimental values.

Table 4.5: Parameters obtained from the magnetization measurement of $NdCr_{1-x}Mn_xO_3$. T_C is the ferromagnetic transition temperature. θ_C (Curie temperature), C (Curie constant) and μ_{eff} (effective magnetic moment) have been obtained from the Curie –Weiss law.

Samples/ Parameters	***x* = 0.30**	***x* = 0.40**	***x* = 0.50**	***x* = 0.60**	***x* = 0.70**
T_C **(K)**	55±2	66±2	83±2	88±2	100±1
θ_C **(K)**	-24 ± 1	5.7±0.9	38.5±0.5	62±3	89±2
***C* (emu K/mol Oe)**	2.98±0.01	3.03±0.01	3.43±0.02	3.58±0.04	3.80±0.03
μ_{eff} **(μ_B/f.u.)**	4.885±0.015	4.921±0.008	5.241±0.018	5.318±0.029	5.514±0.018
μ_{th} **(μ_B/f.u.)**	5.55	5.63	5.71	5.79	5.87

Typical *M-H* loops for x = 0.00 to 0.70 samples at T = 75 K are shown in Fig. 4.34. The parent compound and x = 0.05 sample show the linear behavior due to the presence of dominant antiferromagnetic interaction. But x = 0.10 to 0.20 samples show the elliptical loop which signifies the presence of weak canted ferromagnetism. Surprisingly, we have seen a large hysteresis loop for x = 0.30 sample along with large coercive field (H_C = 2.5 kOe) because of the presence of considerable FM component in addition to the competing antiferromagnetic interaction. However, for $x \geq 0.40$, a long range FM behavior is observed with the spontaneous magnetization and reduced coercive field, similar to that of double exchange ferromagnetic materials [132]. The magnitude of magnetization is found to increase with Mn concentration and they indicate the presence of ferromagnetic interaction due to the Cr^{3+}-O^{2-}-Mn^{3+} and Mn^{3+}-O^{2-}-Mn^{4+} networks.

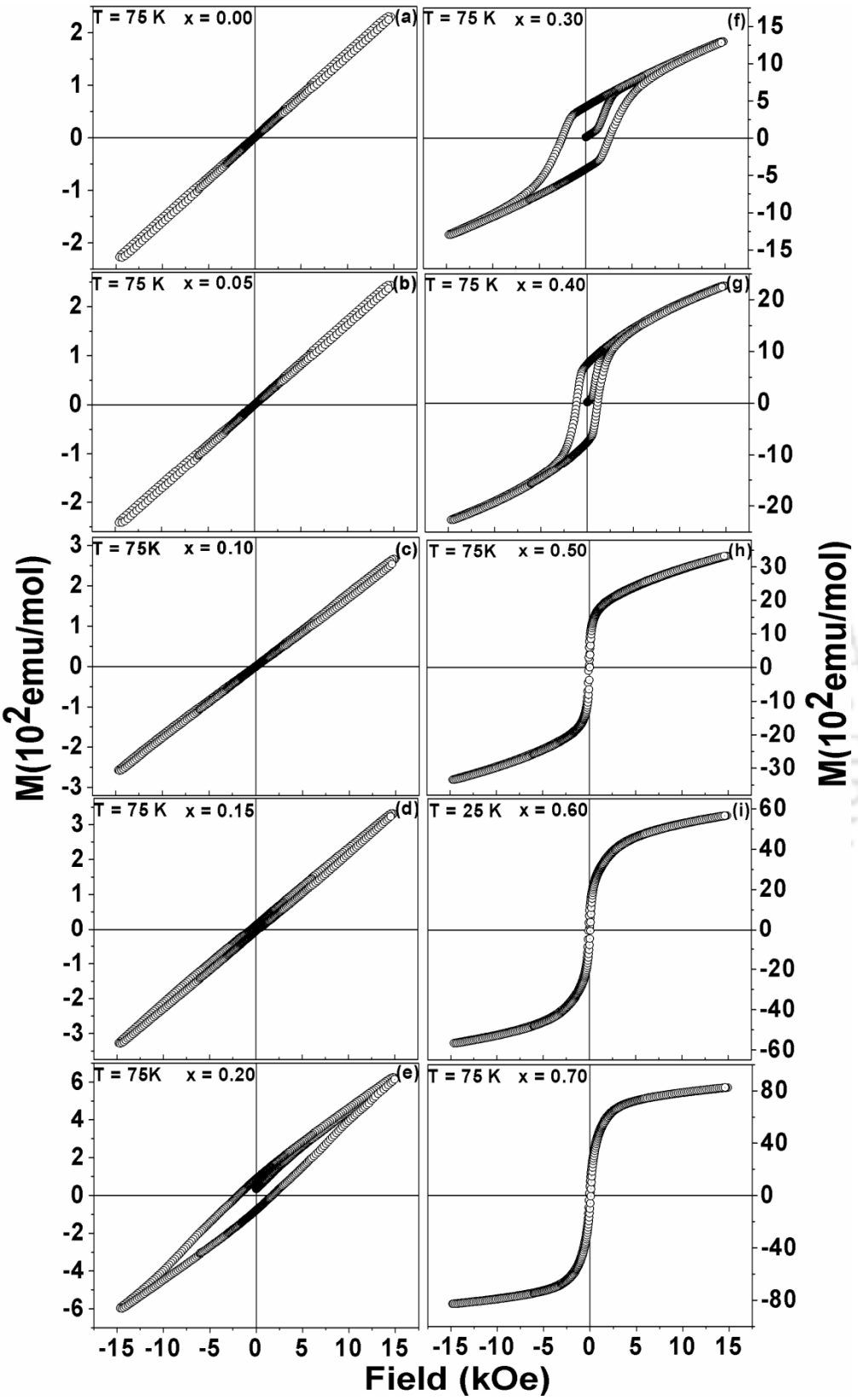

Figure 4.34: *M-H* loops of x = 0.00 to 0.70 samples at T = 75 K.

4.3 Conclusions

The effect of Fe and Mn substitutions at Cr site of the parent compound $NdCrO_3$ has been studied in this chapter.

Polycrystalline samples of $NdCr_{1-x}Fe_xO_3$ (x = 0.00 to 1.00) were prepared by sol-gel method and they are found to crystallize in orthorhombic structure with *Pbnm* space group. The lattice parameters increase systematically with Fe concentration. Magnetization reversal has been observed even for 5 atm % of Fe doping and this phenomenon persists upto x = 0.20. The magnetic compensation temperature is found to increase with increase in Fe concentration and its maximum value is 198 K for x = 0.15 sample. The magnetization reversal is explained by considering the competition between the canted FM component of Cr^{3+} ions and the paramagnetic moments of Fe^{3+} and Nd^{3+} in negative internal field. The maximum H_I value is found to be - 29.6 kOe for x = 0.15 sample. Tunable exchange bias field has been observed due to the exchange anisotropy between the above two components of magnetic moment. The sign reversal of H_{EB} is observed due to the switching of domination of one component over the other in different temperature region. The maximum H_{EB} value is found to be 3.65 kOe for x = 0.10 sample. With increase in Fe concentration, AFM transition was found to shift towards higher temperature due to the Fe^{3+}-O^{2-}-Fe^{3+} networks.

Magnetic properties of $NdCr_{1-x}Mn_xO_3$ (x = 0.00 to 0.70) compounds have been studied. Magnetization reversal has been observed for x = 0.10, 0.15 and 0.20 samples and the maximum compensation temperature is found to be 157 K for x = 0.20 sample. The temperature dependence of magnetization under FC condition has been analyzed by considering the competition between the canted FM component of Cr^{3+} ions and the paramagnetic moments of Mn^{3+} and Nd^{3+} under the influence of negative internal magnetic field of AFM ordered Cr^{3+} ions. The maximum H_I value is found to be - 6.9 kOe for x = 0.20 sample. We have demonstrated the bipolar switching of magnetization by varying the applied field and temperature. *M-H* loops recorded under field cooled conditions show the presence of exchange bias phenomenon. Tunable positive and negative exchange bias fields have been observed and they are explained in terms of antiferromagnetic interaction between the

ferromagnetic component of Cr^{3+} ions (M_{Cr}) and the paramagnetic component of Nd^{3+} ions and the doped Mn^{3+} ions ($M_{Nd} + M_{Mn}$) under the influence of negative internal field. With increase in doping concentration, positive exchange bias field is observed for a wider temperature range. For $0.40 \leq x \leq 0.70$ samples, the ferromagnetic T_C is found to increase from 66 K for $x = 0.40$ sample to 100 K for $x = 0.70$ sample due to the Cr^{3+}-O^{2-}-Mn^{3+} and Mn^{3+}-O^{2-}-Mn^{4+} networks.

In $NdCrO_3$ series, the magnetization reversal was observed for Fe substituted (x = 0.05, 0.10, 0.15 and 0.20) samples as well as Mn substituted samples (x = 0.10, 0.15 and 0.20). The negative magnetization value and the compensation temperature of Fe substituted $NdCrO_3$ samples are found to be larger than the Mn substituted samples because of higher magnetic moment of Fe^{3+} ion compared to Mn^{3+} ion. Mn substituted samples show the clear positive and negative H_{EB} behavior but Fe substituted samples mostly show positive H_{EB} values with an exception for x = 0.05 sample due to the presence of relatively large paramagnetic moment and hence T_{comp} approaching close to T_N. Higher concentration of Mn substitution ($x \geq 0.4$) is found to promote double exchange FM interaction, on the other hand higher Fe concentration promotes AFM interaction.

Chapter 5

$La_{1-x}Ce_xCrO_3$ series

Chapter 5: $La_{1-x}Ce_x CrO_3$ series

Perovskite compounds containing either Cr^{3+} or Mn^{4+} ions exhibit G-type antiferromagnetic (AFM) structure. The isoelectronic configuration of three *3d* electrons in both Cr^{3+} and Mn^{4+} ions has prompted the study of possible double exchange ferromagnetism (FM) in mixed valent Cr ion networks [14, 87]. Alkaline earth (Ca, Sr) doped $LaCrO_3$ is known to exhibit reduction in T_N value along with low temperature transitions especially for Sr doping [5, 6]. A few groups have studied the electron doping in perovskite orthochromites by substituting tetravalent elements in place of La. Yang *et al.* [87] reported FM transition at T_C = 105 K along with AFM transition around 282 K in $La_{0.7}Te_{0.3}CrO_3$. Predominant AFM behavior in $La_{1-x}Ce_xCrO_3$ for x up to 0.2 and decrease in T_N values from 282 K to 257 K with increase in Ce concentration have been reported [88, 89]. Moreover they have observed large irreversibility between zero field cooled (ZFC) and field cooled (FC) magnetization curves. Typically the ionic radius of tetravalent ions is less than that of the trivalent rare earth ions that form the perovskite structure. There is a problem of segregation of CeO_2 impurity in Ce doped $LaCrO_3$. Tetravalent doping would be very significant because it is expected to introduce the mixed valence of Cr^{3+}/Cr^{2+} ions. The nature of magnetic interaction in Ce doped $LaCrO_3$ is yet to be understood. In the present chapter, we report the preparation of single phase samples of Ce doped $LaCrO_3$ by sol-gel route and study of their crystal structure and magnetic properties.

5.1 Sample Preparation and Characterization

Polycrystalline samples of $La_{1-x}Ce_xCrO_3$ (x = 0.0 to 0.2) were prepared by the standard sol-gel route. La_2O_3, $Cr(NO_3)_3.9H_2O$ and $Ce(NO_3)_3.6H_2O$ compounds were taken as starting materials. The precursor obtained from the sol-gel was presintered at 600 ˚C for 12 h followed by final sintering in pellet form at 1350 ˚C for 36 h.

All the Ce doped $LaCrO_3$ compounds are found to be in single phase form as per the XRD patterns. The XRD patterns for x = 0.00 to 0.20 are shown in Fig. 5.1. The XRD patterns could be refined by taking *Pbnm* space group in orthorhombic cell. The typical XRD pattern along with Rietveld refinement for x = 0.05 and 0.20 samples are shown in Fig. 5.2.

The room temperature lattice parameters, reliability factors and unit cell volume are given in Table 5.1. The lattice parameter *c* and unit cell volume are found to decrease with increase in Ce concentration upto $x = 0.10$ and this is consistent with Ce^{4+} ions substituting the La ions. For $x \geq 0.15$ samples, no systematic variation was observed due to the possible oxygen off stoichiometry.

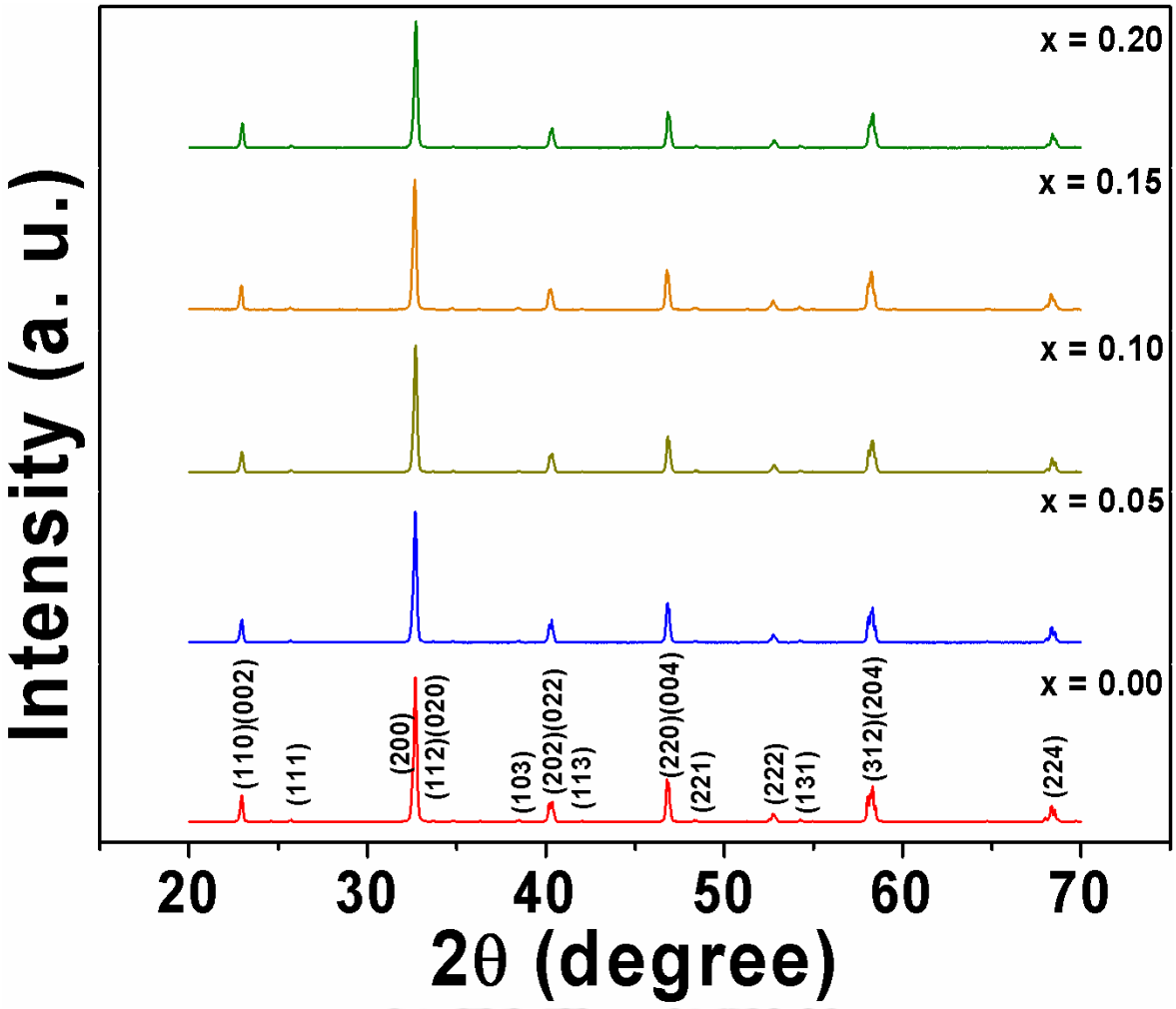

Figure 5.1: XRD patterns of $La_{1-x}Ce_xCrO_3$ samples for $x = 0.00$ to 0.20.

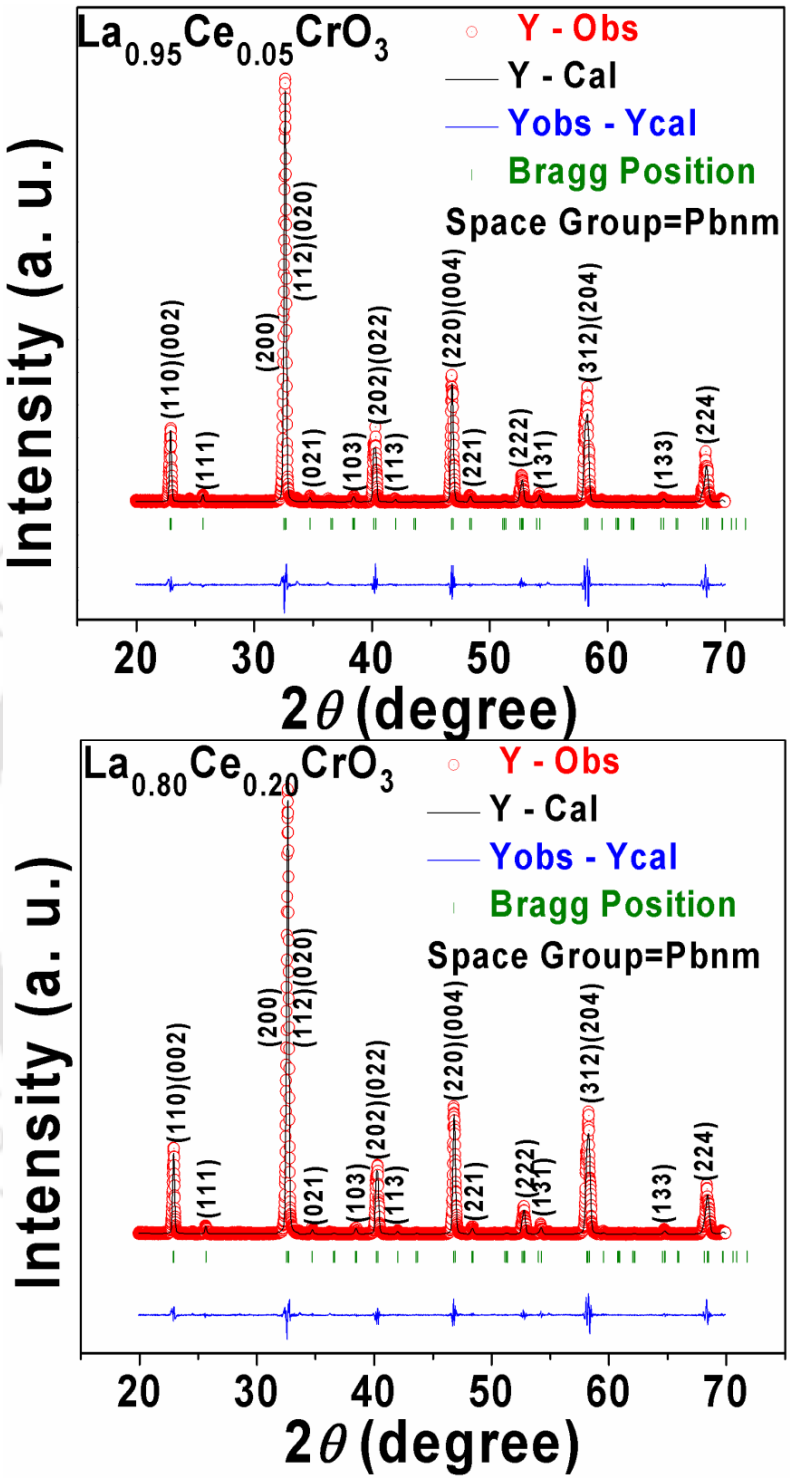

Figure 5.2: XRD patterns along with Rietveld refinement for $x = 0.05$ and 0.20 samples. The circle represents experimental data and solid line represents Rietveld refined data. The bottom line shows the difference between experimental and refined data. The marked 2θ positions are allowed Bragg peaks.

Table 5.1: Parameters obtained from the Rietveld analysis of XRD patterns for the samples $La_{1-x}Ce_xCrO_3$ (0.00 to 0.20). R_F, R_{Bragg}, R_P, R_{exp} and χ^2 are the reliability factors.

Sample/ Parameters	***x* = 0.00**	***x* = 0.05**	***x* = 0.10**	***x* = 0.15**	***x* = 0.20**
Space group	*Pbnm*	*Pbnm*	*Pbnm*	*Pbnm*	*Pbnm*
***a* (Å)**	5.5131 (0.0002)	5.5092 (0.0002)	5.5066 (0.0002)	5.5070 (0.0002)	5.5057 (0.0002)
***b* (Å)**	5.4767 (0.0002)	5.4766 (0.0002)	5.4757 (0.0002)	5.4776 (0.0002)	5.4779 (0.0002)
***c* (Å)**	7.7554 (0.0004)	7.7537 (0.0004)	7.7514 (0.0004)	7.7535 (0.0003)	7.7524 (0.0003)
***Volume* ($Å^3$)**	234.16 (0.01)	233.94 (0.01)	233.72 (0.01)	233.89(0.01)	233.81 (0.01)
R_F (%)	3.72	4.00	3.57	3.44	3.08
R_{Bragg} (%)	3.70	4.50	3.56	3.76	3.42
R_P (%)	10.4	11.6	10.0	9.55	9.59
R_{exp} (%)	4.59	4.77	4.58	4.69	4.70
χ^2	14.7	14.8	14.3	12.9	12.4
La/Ce/Cr Occupancy	0.982 /0.000 / 0.980	0.934 / 0.034 / 0.973	0.886 /0.086 / 0.988	0.823 /0.123 /0.936	0.800 / 0.200 /0.987

The morphology of all the samples has been studied by recording microstructral images using scanning electron microscope. The typical SEM micrographs for x = 0.15 and 0.20 samples are shown in Fig. 5.3. The surface morphology is found to be quite uniform for all the samples. The average particle size is found to be in the order of 420 nm to 550 nm. The elemental analysis of the prepared compounds has been carried out by recording EDS spectra. Typical EDS spectra for x = 0.10 and 0.15 samples are shown in Fig. 5.3. The chemical composition determined from the EDS analysis is found to be comparable to the nominal starting composition. The cationic ratio for a few samples is given in Table 5.2.

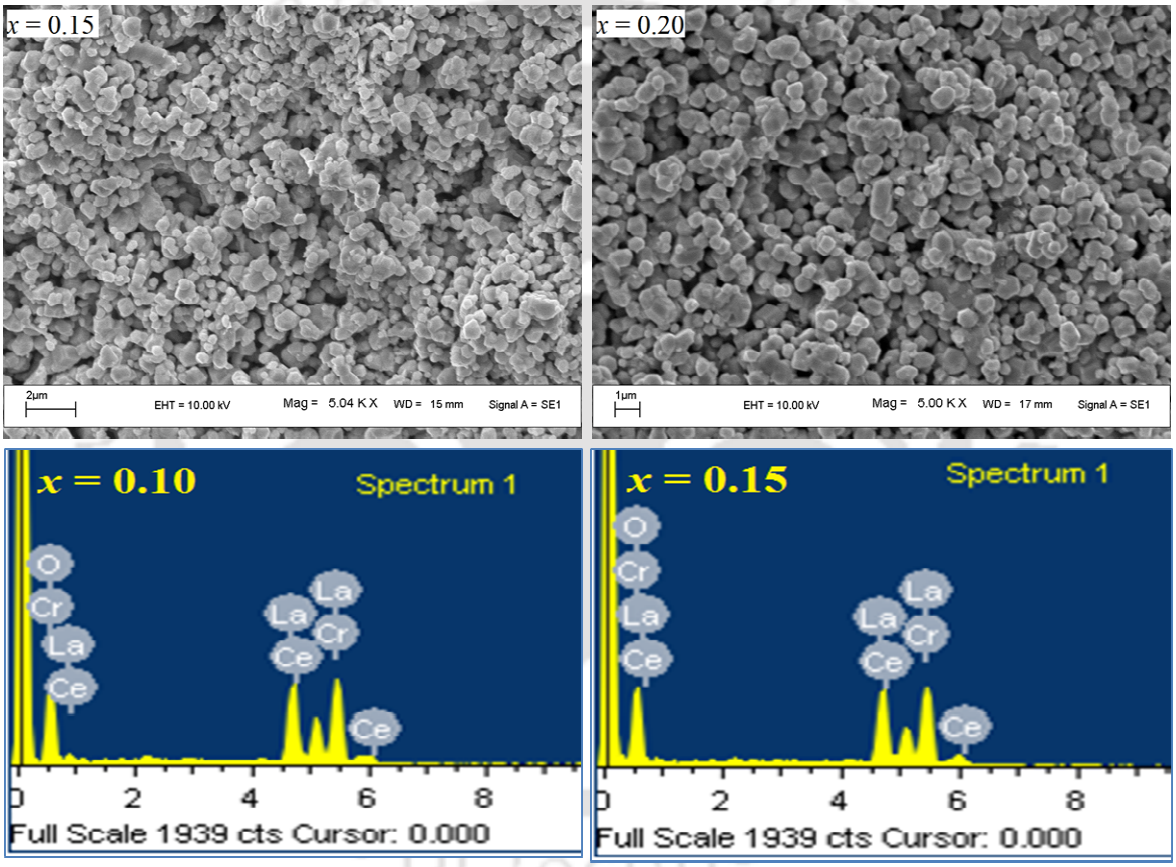

Figure 5.3: SEM images recorded for x = 0.15 and 0.20 samples along with EDS spectra for x = 0.10 and 0.15 samples.

Table 5.2: The cationic ratio determined from EDS analysis for x = 0.00, 0.10, 0.15 and 0.20 samples.

Samples	Calculated Cationic Ratio from EDS Analysis		
	La	**Ce**	**Cr**
***x* = 0.00**	0.92	0.00	1.07
***x* = 0.10**	0.89	0.11	0.88
***x* = 0.15**	0.86	0.13	0.91
***x* = 0.20**	0.75	0.25	0.90

5.2 Magnetic Properties

Temperature (T) variation of magnetization (M) plots in ZFC and FC conditions are shown in Fig. 5.4. The parent compound exhibits AFM transition at 291 K followed by monotonous decrease in magnetization with decrease in temperature (not shown). The ZFC M-T plot of x = 0.05 sample exhibits an AFM transition at 288 K followed by a low temperature transition with a peak like structure at T_c' = 40 K as shown in Fig. 5.4 (a). The FC magnetization exhibits large irreversibility, especially at $T \leq 40$ K, *i.e.* below the low temperature transition. Thus, in addition to the regular AFM transition due to Cr^{3+}-O^{2-}-Cr^{3+} networks, additional magnetic transition is observed in Ce doped samples. Similar behaviour of AFM transition followed by low temperature transition is observed for x = 0.10 and 0.15 samples; however, the T_N values are found to decrease and T_c' values are found to increase sharply with increase in Ce concentration. For x = 0.20 both T_c' and T_N merge such that the low temperature transition could not be seen. Presence of magnetic irreversibility is seen as the sample is cooled below T_N; however for $T < T_c'$, the irreversibility is found to be quite large. The T_N values are found to vary from 291K for x = 0 to 280 K for x = 0.2 and the T_c' increases from 40 K for x = 0.05 to 135 K for x = 0.15. Thus, with increase in Ce

concentration T_c' value increases and approaches close to T_N and as a result of that, the onset of large low temperature irreversibility is also found to shift towards higher temperature approaching close to T_N. The increase in Ce concentration is expected to promote the concentration of Cr^{2+} ions and this contributes to Cr^{2+}-O^{2-}-Cr^{3+} networks. Such networks are likely to facilitate double exchange ferromagnetic (DE-FM) interaction. However, no long range DE-FM is observed. Various factors such as deviation of Cr^{2+}-O^{2-}-Cr^{3+} bond angle from 180°, lack of overlapping between e_g band of Cr ions and O-2*p* ions, could contribute to such weak FM. However when the sample is cooled under magnetic field, the FM phase is expected to be energetically favorable and the enhanced magnetization is observed. We have also recorded the resistivity versus temperature data for all samples but there is no signature of metal insulator transition which confirms that no long range DE-FM interaction exists.

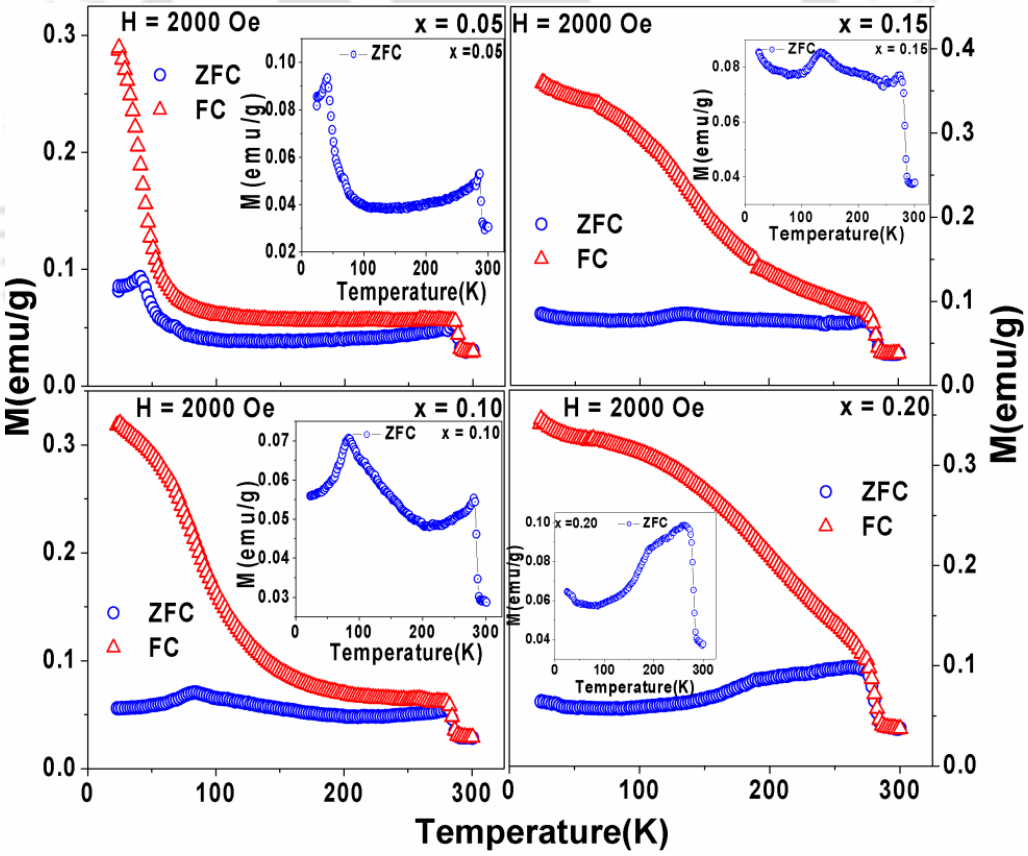

Figure 5.4: *M-T* plots of x = 0.05, 0.10, 0.15 and 0.20 samples in ZFC and FC conditions at H = 2000 Oe. For clarity ZFC plots are reproduced in the inset.

Typical *M-H* loops at selected temperatures T = 75 K, 100 K and 150 K are shown in Fig. 5.5 for the doped samples x = 0.05, 0.10, 0.15 and 0.20. The *M-H* loops at 150 K (Fig 5.5(c)) show FM like behavior with large coercivity and considerable remanent magnetization for x = 0.15 and 0.20 samples; however at the same temperature x = 0.05 and 0.10 samples exhibit just a linear behavior. This can be understood by comparing the *M-T* plots, where the T_c' values for x = 0.05 and 0.10 samples are quite low (< 150 K). So, the observed FM like behavior can be attributed to the low temperature transition and not simply due to the canted component of Cr^{3+} ions engaged in AFM interaction. *M-H* loops at 100 K show the FM behavior especially for samples with $x \geq 0.10$. The observation of large coercivity for each doped sample can be understood in terms of competition between DE-FM and the long range AFM interaction. Temperature variation of coercive field H_c exhibits broad peak especially for $x \geq 0.15$ samples as shown in Fig. 5.5 (d). The peak temperature decreases with decrease in doping concentration. For x = 0.05 and 0.10 samples, complete peak could not be seen because of low T_c' values. The onset of rise in H_c value with decrease in temperature is found to coincide with the onset of weak FM transition. So, it clearly

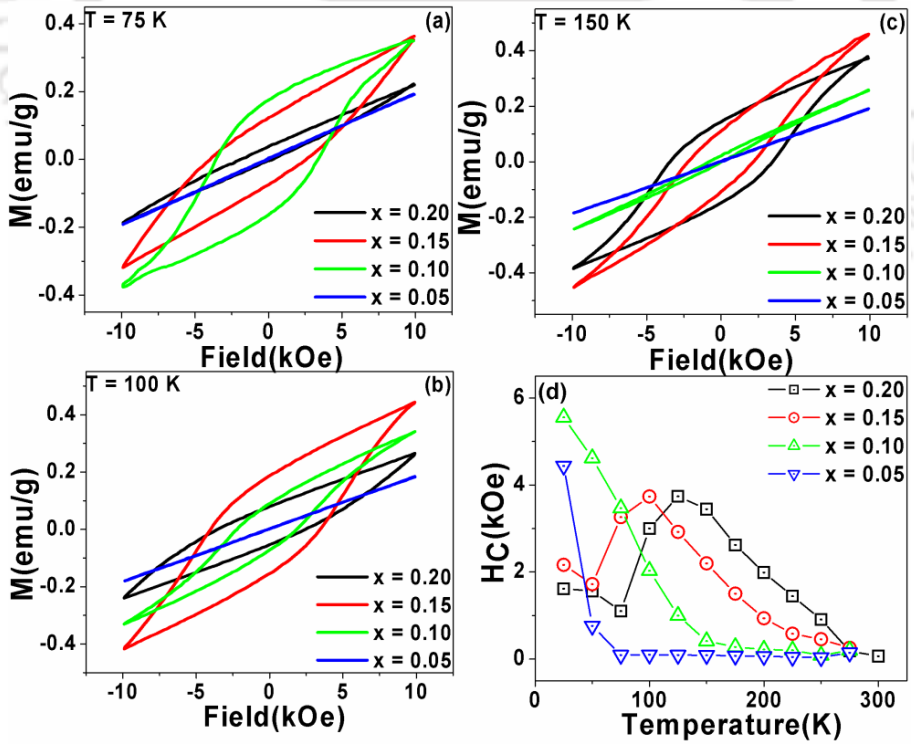

Figure 5.5: *M-H* loops at (a) 75 K, (b) 100 K, (c) 150 K and (d) H_C versus T plots of x = 0.05, 0.10, 0.15 and 0.20 samples.

demonstrates the presence of competing magnetic interaction that gives rise to magnetic hysteresis and large coercivity. All the *M-H* loops were recorded for the maximum applied field of 10 kOe and we have not observed any magnetization saturation. The absence of magnetization saturation may lead to the underestimation of H_C values to some extent.

The observed large coercivity can be in principle due to various factors such as magnetic impurity phases, lattice distortion or defect induced spin canting and short range ferromagnetic interaction. In the present series of samples, we have not observed any impurity phase and the lattice parameters are found to vary systematically with doped Ce concentration upto $x = 0.10$ samples. If the observed result is due to purely spin canting, one would observe such behavior as soon as the temperature is lowered below the Néel temperature and on the other hand such behavior is observed only close to T_c' values. So, the low temperature FM transition and its competition with long range AFM gives rise to magnetic hysteresis and large coercivity.

5.3 Conclusions

We have prepared single phase $La_{1-x}Ce_xCrO_3$ ($x = 0$ to 0.2) samples. The samples are found to crystallize in *Pbnm* space group *i.e.* with orthorhombic crystal structure. A decrease in unit cell volume is observed with increase in Ce concentration upto $x = 0.10$ due to the substitution of smaller Ce^{4+} ions for La ions. Systematic decrease in AFM Néel temperature and increase in short range FM transition temperature were observed with increase in Ce concentration. Thus, Ce doping gives rise to short range double exchange FM interaction in Cr^{2+}-O^{2-}-Cr^{3+} networks. All doped samples exhibit FM like hysteresis loop but without any saturation at $T < T_c'$. The observed large coercivity and irreversibility are explained in terms of competing magnetic interaction. Temperature dependence of coercive field exhibits broad peak and the peak temperature was found to increase with Ce concentration.

Chapter 6

Conclusions

Chapter 6: Conclusions

The summary of results and discussion from structural and magnetization studies carried out in Fe and Mn substituted $LaCrO_3$ and $NdCrO_3$ series at Cr site and Ce substituted $LaCrO_3$ at La site is presented in this chapter.

Fe substituted $LaCrO_3$ series *i.e.* $LaCr_{1-x}Fe_xO_3$ (x = 0.00 to 1.00) compounds have been prepared in single phase form and they are found to crystallize in orthorhombic structure. With increase in Fe concentration, lattice parameters and unit cell volume increase and it is explained on the basis of replacement of Cr^{3+} ions by Fe^{3+} ions having larger ionic size. Mn substituted $LaCrO_3$ samples have been also prepared in single phase form and the structural transition from orthorhombic to rhombohedral symmetry has been observed with increase in Mn concentration beyond x = 0.50.

Temperature variation of magnetization of the parent compound, $LaCrO_3$ exhibits a peak around 289 K and it is due to the AFM ordering of Cr^{3+} ions. *M-H* loop measurements, at low temperature show paramagnetic like behavior with a linear *M-H* curve. In Fe substituted $LaCrO_3$ samples, an interesting phenomenon of magnetization reversal (MR) has been observed for x = 0.05 to 0.15 samples and the magnetic compensation temperature *i.e.* T_{comp} was found to increase from 38 K to 103 K. Ferromagnetic like behavior with a large coercive field of the order of 0.5 T was observed in the intermediate composition range of x = 0.20 to 0.40. However, for x = 0.45 and 0.50 samples, the magnetization reversal was again observed with T_{comp} ~ 105 K. For further increase in Fe concentration, the AFM transition was found to shift towards higher temperature due to the increase in Fe^{3+}-O^{2-}-Fe^{3+} networks.

In order to investigate the magnetization reversal behavior, x = 0.05, 0.10, 0.15, 0.45 and 0.50 samples of $LaCr_{1-x}Fe_xO_3$ series were taken up for the detailed *M-T* measurements under FC condition by varying the cooling field from 50 to 5000 Oe. The magnetization reversal was observed upto a threshold magnetic field and it was found to vary from sample to sample. The maximum threshold field of 1000 Oe was observed for x = 0.05, 0.10 and 0.45 samples. As the cooling field is increased, the entire *M-T* curves are found to shift towards positive magnetization axis due to the enhanced canted FM. The mechanism of magnetization reversal for low Fe concentrations (x = 0.05 to 0.15) is basically due to the

paramagnetic behavior of doped Fe ions under the influence of negative internal field arising from the antiferromagnetically ordered Cr^{3+} ions. They have been quantitatively explained by fitting the measured FC *M-T* data to the relation $M = M_{Cr} + \frac{C(H+H_I)}{(T-\theta_C)}$ by taking the canted FM component of Cr^{3+} ions as M_{Cr} and the internal field due to AFM ordered Cr^{3+} ions as H_I. The value of maximum negative internal field, H_I was estimated to be -3.5 kOe. On the other hand, the mechanism of magnetization reversal for x = 0.45 and 0.50 samples is found to be quite different. They could be quantitatively analyzed based on the model, where the competition between single ion anisotropy and Dzyaloshinsky-Moriya interaction is taken into account. *M-H* loops of x = 0.45 and 0.50 samples show the shifting along the field axis. Such shifting is attributed to the exchange bias behavior and the corresponding exchange bias field, H_{EB} was determined. The maximum H_{EB} value is 0.93 kOe. The presence of exchange bias in x = 0.45 and 0.50 samples is due to the presence of competing weak FM arising out of spin canting and the AFM.

In Mn doped $LaCrO_3$, x = 0.05 and 0.10 samples show the AFM transition along with a low temperature magnetic transition around 50 K due to the possible magnetic interaction between Mn^{3+} and Cr^{3+} ions. The role of spin reorientation for the above transition cannot be ruled out. The x = 0.15 and 0.20 samples exhibit magnetization reversal and the magnetic compensation temperature T_{comp} is found to increase from 95 K for x = 0.15 to 147 K for x = 0.20.

The competition between the magnetic moment due to the canted ferromagnetic component of Cr^{3+} ions and the paramagnetic component of doped Mn^{3+} ions under the negative internal field gives rise to the magnetization reversal in x = 0.15 and 0.20 samples. The maximum internal magnetic field H_I was found to be -6.9 kOe for x = 0.15 sample and -8.2 kOe for x = 0.20 sample.

To understand the exchange bias behavior around the compensation temperature, we have recorded *M-H* loops at several temperatures under field cooled condition with H = 5000 Oe. Negative and positive values of exchange bias field (H_{EB}) having sign reversal around T_{comp} have been observed for x = 0.15 sample. On the other hand, x = 0.20 sample shows the negative exchange bias behavior. The value of H_{EB} could be tuned from -2.1 kOe to +2.6 kOe

with change in temperature for x = 0.15 sample and on the otherhand maximum negative exchange bias field for x = 0.20 was found to -0.71 kOe. The observed exchange bias behavior can be explained by considering the anisotropic exchange interaction between the FM components of canted Cr^{3+} ions and the PM component of Mn^{3+} ions under the influence of negative internal field. For $x \geq 0.30$, FM was observed and the T_C value was found to increase from 128 K for x = 0.40 sample to 244 K for x = 1.00 due to the presence of Cr^{3+}-O^{2-}-Mn^{3+} and Mn^{3+}-O^{2-}-Mn^{4+} networks. The M_S value is found to increase with increase in doping concentration *i.e.*, 0.69 μ_B/f.u for x = 0.40 to 3.72 μ_B/f.u for x = 1.00. The dc susceptibility in the paramagnetic region could be fitted to Curie Weiss law and the effective magnetic moment μ_{eff} was estimated. The value of μ_{eff} is found to increase with increase in doping concentration.

The critical exponent behavior of $LaCr_{0.30}Mn_{0.70}O_3$ sample was studied by measuring the isothermal magnetization in the vicinity of T_C. The critical exponents β, γ and δ corresponding to the spontaneous magnetization, initial susceptibility and isothermal magnetization were determined by analyzing the magnetization data in terms of modified Arrott plot method. The estimated values of critical exponents, *i.e.*, β = 0.325±0.006, γ = 1.247±0.066, and δ = 4.832±0.004 are found to be close to the 3D Ising model values. The present sample exhibits rhombohedral crystal structure where the Mn/CrO_6 octahedra are expected to align along the three fold rotational symmetric axis. Such orientation is expected to induce uniaxial anisotropy for magnetization and it gives rise to 3D Ising type of magnetic interaction. So, the critical exponents follow the 3D Ising model. The lack of long range, *i.e.* mean field model can be understood due to the possible interruption of Mn^{3+}-O^{2-}-Mn^{4+} networks by the presence of a few Cr ions that do not take part in double exchange interaction. The critical exponent values are found to be consistent with the Widom scaling relation and the universal scaling hypothesis.

The phase diagrams of Fe and Mn substituted $LaCrO_3$ are shown in Fig. 6.1 and Fig. 6.2 respectively. From the phase diagram of Fe substituted samples we can see the multiple magnetic behaviors such as magnetization reversal (MR), AFM and FM. Rich magnetic properties are seen in $LaCr_{1-x}Fe_xO_3$ system especially for $x \leq 0.5$. For $x \cong 0.5$, PM to AFM transition followed by magnetization reversal (MR) has been observed. In the composition

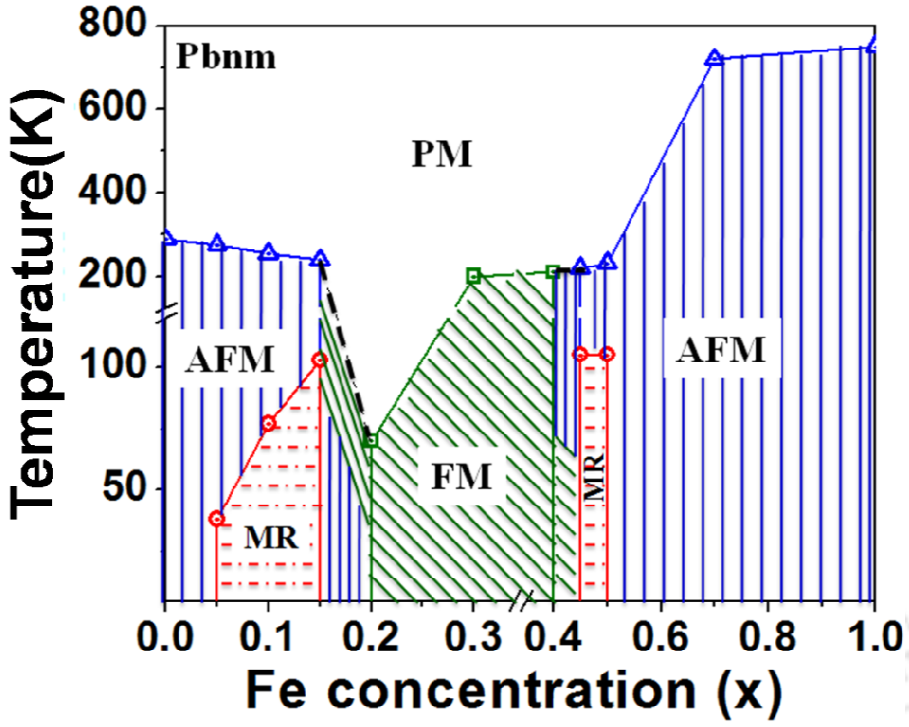

Figure 6.1: Phase diagram of $LaCr_{1-x}Fe_xO_3$ (x = 0.00-1.00). Triangle represents T_N, square represents FM T_C and circle represents T_{comp}.

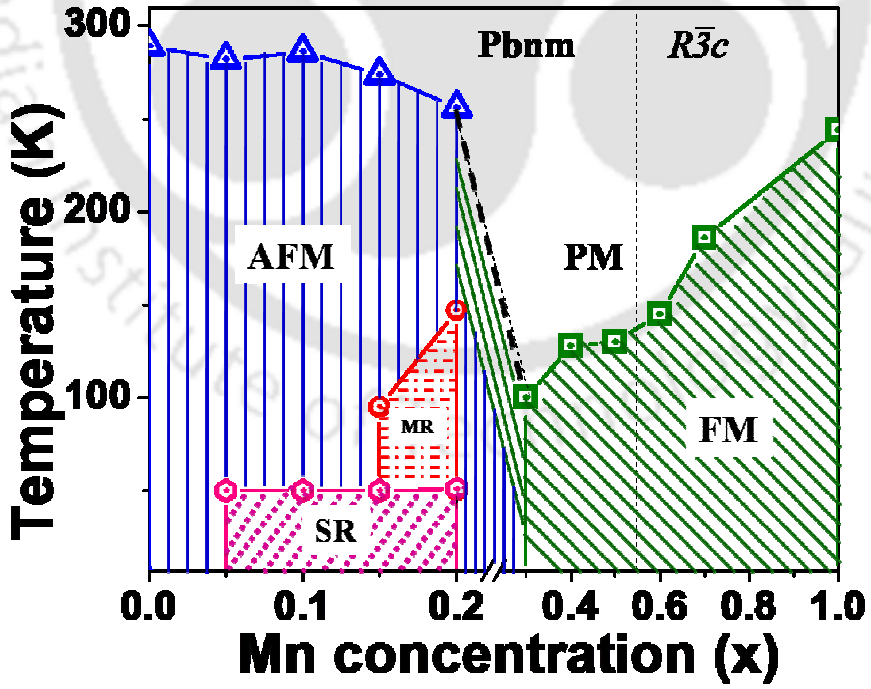

Figure 6.2: Phase diagram of $LaCr_{1-x}Mn_xO_3$ (x = 0.00-1.00). Triangle represents T_N, square represents FM T_C, circle represents T_{comp} and pentagone represents T_{SRT}.

range x = 0.2 to 0.4, mostly PM to FM transition has been observed. For $x \leq 0.2$, PM, AFM and MR behaviors have been observed with decrease in temperature. In the entire composition range the structure remains orthorhombic with *Pbnm* space group. However, from the phase diagram of Mn substituted samples, we can see the structural transition from orthorhombic to rhombohedral with increase in Mn concentration. These samples exhibit magnetization reversal (MR), spin reorientation (SR), AFM and FM behaviors. Unlike the Fe substituted series, here the MR is observed only for a narrow composition range. Moreover spin reorientation like transition is observed at $T < 50$ K in the composition range x = 0.05 to 0.20. Another interesting behavior is the observed FM in a wide composition range $x \geq 0.4$.

In both Fe and Mn substituted $LaCrO_3$, the magnetization reversal was observed. In Fe substituted series, MR was observed even for x = 0.05 while in Mn substituted series, it was observed only for $x \geq 0.15$. This is mainly due to the higher magnetic moment of Fe^{3+} (5.9 μ_B) ions compared to Mn^{3+} (4.9 μ_B) in high spin states. Moreover, if we compare the same doping concentration say x = 0.15, Fe substituted series shows the higher T_{comp} value of 103 K compared to the Mn substituted series. So, the observed negative magnetization and T_{comp} values are consistent with the paramagnetic model. Large T_{comp} value of 147 K is observed in x = 0.2 sample of Mn doped series, while the Fe doped series for the same composition did not show any MR due to the possible AFM in Fe^{3+}-O^{2-}-Fe^{3+} networks.

Polycrystalline samples of $NdCr_{1-x}M_xO_3$ (M = Fe and Mn) have been prepared. All of these samples are found to be in single phase form. X-ray diffraction patterns could be refined by using *Pbnm* space group. The lattice parameters and unit cell volume are found to increase with Fe doping. In Mn doped samples, increase in lattice parameter *b* and unit cell volume has been observed.

In Fe substituted $NdCrO_3$ compounds *i.e.* $NdCr_{1-x}Fe_xO_3$ (x = 0.00 to 1.00), temperature variation of magnetization measurements show the interesting magnetic behavior such as antiferromagnetic transition, magnetization reversal and spin reorientation transition. The magnetization reversal and tunable exchange bias behavior are observed for x = 0.05, 0.10, 0.15 and 0.20 samples. The magnetic compensation temperature is found to increase from 158 K for x = 0.05 to 198 K for x = 0.15 sample. With increase in Fe concentration, AFM transition is shifted to higher temperature and the T_N for $NdFeO_3$ is

found at 670 K. The observed magnetization reversal is explained by considering the competition between the weak ferromagnetic component of Cr^{3+} ions and the paramagnetic component of Nd^{3+} and Fe^{3+} ions under the influence of negative internal field. The maximum H_I value is found to be -29.6 kOe for x = 0.15 sample. The exchange anisotropy between the above two components of magnetic moments give rise to positive and negative exchange bias fields. The sign reversal of exchange bias field also coincides with T_{comp}. The maximum H_{EB} value is found to be 3.65 kOe for x = 0.10 sample. Bipolar switching of magnetization is demonstrated at $T < T_{comp}$ by just varying the magnitude of positive magnetic field.

Polycrystalline samples of $NdCr_{1-x}Mn_xO_3$ (x = 0.00 to 0.70) were prepared by sol-gel method. The x = 0.00 and 0.05 samples exhibit antiferromagnetic transition along spin reorientation of Cr^{3+} ions. Samples in the composition range, x = 0.10 to 0.20 exhibit magnetization reversal and the magnetic compensation temperature T_{comp} is found to increase from 110 K to 157 K with increase in Mn concentration. The magnetization reversal behavior is explained by considering paramagnetic moments of Nd^{3+} and Mn^{3+} ions under the influence of negative internal magnetic field and the canted ferromagnetic component of Cr^{3+} ions. Bipolar switching of magnetization is observed for x = 0.10 to 0.20 samples by varying either the applied field H = 200 Oe to 3000 Oe or temperature through T_{comp}. Also magneto caloric effect is observed for these samples. Tunable exchange bias behavior was observed for x = 0.10 to 0.20 samples, and the value of exchange bias field, H_{EB}, could be tuned from -1.6 kOe to +0.39 kOe for x = 0.10 sample. The origin of exchange bias is explained by considering the antiferromagnetic interaction between ferromagnetic component of Cr^{3+} ions and the paramagnetic components of Nd^{3+} and Mn^{3+} ions. Samples with $x \geq 0.3$ show the ferromagnetic behavior due to the double exchange interaction in Cr^{3+}-O^{2-}-Mn^{3+} and Mn^{3+}-O^{2-}-Mn^{4+} networks. The paramagnetic susceptibility of $x \geq 0.30$ samples could be fitted to Curie Weiss law and the estimated μ_{eff} value for each sample is smaller than that of theoretical value and this can be attributed to the presence of short range AFM interaction in some of Cr^{3+}-O^{2-}-Cr^{3+} networks in the temperature region of the fit.

The phase diagram of Fe and Mn substituted $NdCrO_3$ samples are shown in Figs. 6.3 and 6.4 respectively. From the phase diagram of Fe substituted $NdCrO_3$ samples we can see

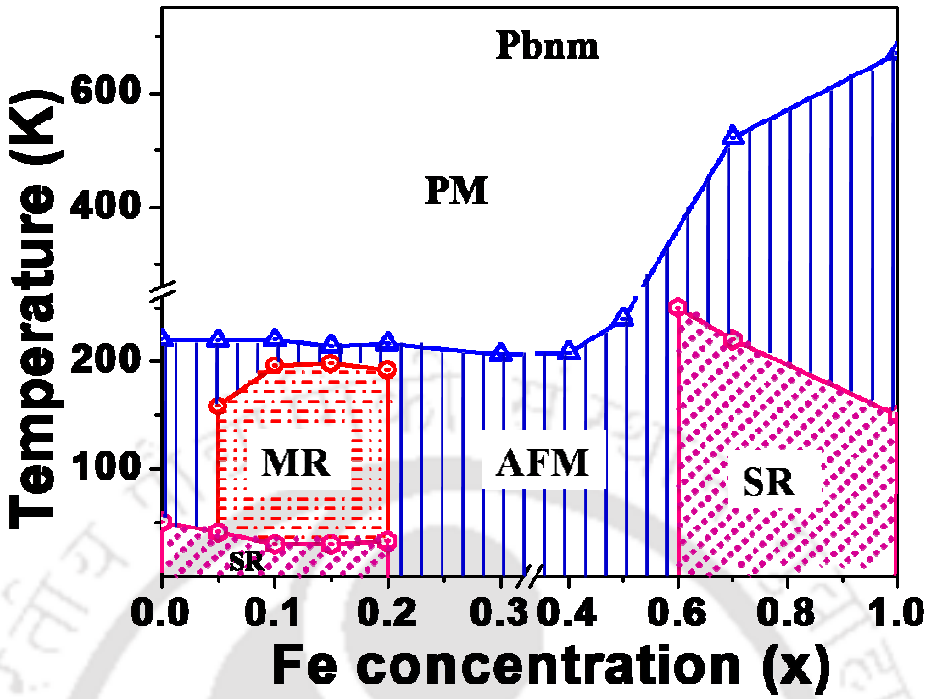

Figure 6.3: Phase diagram of $NdCr_{1-x}Fe_xO_3$ (x = 0.00 – 1.00). Triangle represents T_N, square represents FM T_C, circle represents T_{comp} and pentagone represents T_{SRT}.

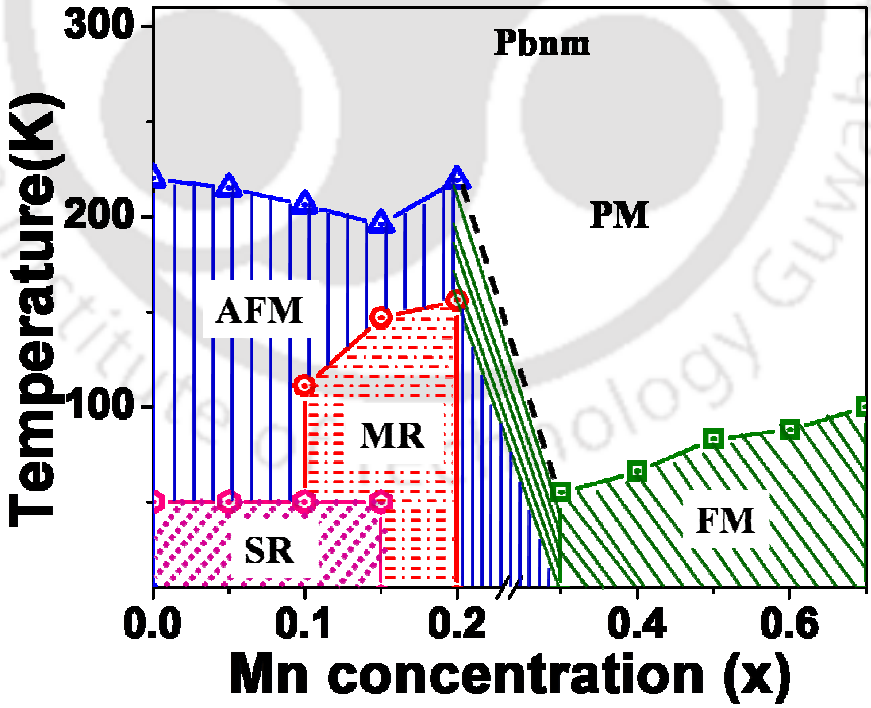

Figure 6.4: Phase diagram of $NdCr_{1-x}Mn_xO_3$ (x = 0.00 – 0.70). Triangle represents T_N, square represents FM T_C, circle represents T_{comp} and pentagone represents T_{SRT}.

that all sample exhibits AFM to PM transition with increase in temperature. The MR was observed for x = 0.05 to 0.20 samples and the SR was observed in a wide composition range. On the other hand, from the phase diagram of Mn substituted $NdCrO_3$ depicts AFM to PM transition for $0.00 \leq x \leq 0.20$ and FM to PM for $0.30 \leq x \leq 0.70$ samples. MR was observed for x = 0.10 to 0.20 samples and x = 0.00 to 0.15 samples exhibit SR behavior.

In $NdCrO_3$ series, the magnetization reversal was observed both for Fe substitution (x = 0.05, 0.10, 0.15 and 0.20) and Mn substitution (x = 0.10, 0.15 and 0.20) at Cr site. For a particular doping concentration of either Fe or Mn, the negative magnetization value is found to be larger in $NdCrO_3$ series compared to that of $LaCrO_3$. It is mainly due to the presence of magnetic rare earth of Nd^{3+} ion in $NdCrO_3$. The negative magnetization value and the compensation temperature of Fe substituted $NdCrO_3$ samples are found to be larger than the Mn substituted samples because of higher magnetic moment of Fe^{3+} ion compared to Mn^{3+} ion.

Single phase $La_{1-x}Ce_xCrO_3$ (x = 0 to 0.2) samples were prepared by sol-gel method. The samples are found to crystallize in *Pbnm* space group *i.e.* with orthorhombic crystal structure. A decrease in unit cell volume is observed with increase in Ce concentration upto x = 0.10 due to the substitution of smaller Ce^{4+} ions for La ions. Systematic decrease in AFM Néel temperature and increase in short range FM transition temperature were observed with increase in Ce concentration. Thus, Ce doping gives rise to short range double exchange FM interaction in Cr^{2+}-O^{2-}-Cr^{3+} networks. All doped samples exhibit FM like hysteresis loop but without any saturation at $T < T_C'$. The observed large coercivity and irreversibility are explained in terms of competing magnetic interaction. Temperature dependence of coercive field exhibits broad peak and the peak temperature was found to increase with Ce concentration.

Thus in this thesis work, we have studied the magnetic properties of two orthochromites series: one with non-magnetic rare earth ion $LaCrO_3$ and another with magnetic rare earth ion $NdCrO_3$. The Cr site substitution with other transition elements such as Fe and Mn gives rise to the development of interesting magnetization reversal and tunable exchange bias behavior. Most of the magnetic data could be quantitatively interpreted with the help of existing theoretical models.

Future Scope of Studies

The above series can be taken up for further studies and the further scope of studies is listed below

- Neutron powder diffraction studies at different temperatures in both zero field cooled and field cooled condition would shed light on the nature of magnetic structure and the origin of spin reorientation like transition at low temperature.
- To carry out the magnetization study by extending the maximum applied field upto ~ 5 T to further understand the exchange bias behavior.
- Study of magnetocaloric effect from the detailed magnetization measurements.
- Study of role of particle size effects in magnetization reversal and exchange bias by preparing the above samples in nanoparticles form.
- Preparation of the above samples in thin film form to study the effect of lattice strain in magnetization reversal and exchange bias phenomenon.
- Study of dielectric properties to look for possible mutiferroic properties in the above series.
- Study of electrical conductivity and magneto-conductivity to understand the electrical transport.
- Attempt to study the critical exponents behavior of samples exhibiting weak ferromagnetic behavior.

References

[1] A. Fert, P. Grünberg, A. Barthélémy, F. Petroff, W. Zinn, J. Magn. Magn. Mater., **140–144, Part 1** (1995) 1.

[2] C.N.R. Rao, B. Raveau, Colossal Magnetoresistance, Charge Ordering and Related Properties of Manganese Oxides, World Scientific, Singapore (1998).

[3] R. von Helmolt, J. Wecker, B. Holzapfel, L. Schultz, K. Samwer, Phys. Rev. Lett., **71** (1993) 2331.

[4] H. Ohno, Science, **281** (1998) 951.

[5] K. Tezuka, Y. Hinatsu, A. Nakamura, T. Inami, Y. Shimojo, Y. Morii, J. Solid State Chem., **141** (1998) 404.

[6] J.J. Neumeier, H. Terashita, Phys.Rev. B, **70** (2004) 214435.

[7] J. Nogues, I.K. Schuller, J. Magn. Magn. Mater., **192** (1999) 203.

[8] C. Tsang, R.E. Fontana, T. Lin, D.E. Heim, V.S. Speriosu, B.A. Gurney, M.L. Williams, IEEE Trans. Magn., **30** (1994) 3801.

[9] I.L. Prejbeanu, M. Kerekes, R.C. Sousa, H. Sibuet, O. Redon, B. Dieny, J.P. Nozieres, J. Phys.: Condens. Matter, **19** (2007) 165218.

[10] T. Hughes, K. O'Grady, H. Laidler, R.W. Chantrell, J. Magn. Magn. Mater., **235** (2001) 329.

[11] Y.T. Chen, S.U. Jen, Y.D. Yao, J.M. Wu, J.H. Liao, T.B. Wu, J. Alloys Compd., **448** (2008) 59.

[12] V.M. Goldschmidt, Geochemistry, Oxford University Press, London (1958).

[13] Y. Du, Z.X. Cheng, X.-L. Wang, S.X. Dou, J. Appl. Phys., **108** (2010) 093914 .

[14] W.C. Koehler, E.O. Wollan, J. Phys. Chem. Solids **2**(1957) 100.

[15] K. Yoshii, J. Solid State Chem., **159** (2001) 204.

[16] C.P. Khattak, D.E. Cox, Matter. Res. Bull., **12** (1977) 463.

[17] M. Tseggai, P. Nordblad, R. Tellgren, H. Rundlof, G. Andre, F. Bouree, J. Alloys Compd., **457** (2008) 532.

[18] Y. Tokura, Science, **288** (2000) 462.

[19] S. Blundell, Magnetism in Condensed Matter, Oxford University press (2001).

[20] A.H. Morrish, The Physical Principle of Magnetism, IEEE press (2001).

[21] B.D. Cullity, D.G. Graham, Introduction to Magnetic Material, IEEE press (2009).

[22] A.H. Cooke, D.M. Martin, M.R. Wells, J. Phys. C: Solid State Phys., **7** (1974) 3133.

[23] H. Kramers, Physica, **1** (1934) 182.

[24] J.C. Slater, Quart. Progr. Rep. M. I. T. July 15,1; Oct. 15, 1 (1953).

[25] J.B. Goodenough, A.L. Loeb, Phys. Rev., **98** (1955) 391.

[26] J.B. Goodenough, Phys. Rev., **100** (1955) 564.

[27] J. Kanamori, J. Phys. Chem. Solids, **10** (1959) 87.

[28] C. Zener, Phys. Rev., **81** (1951) 440.

[29] C. Zener, Phys. Rev., **82** (1951) 403.

[30] P.W. Anderson, H. Hasegawa, Phys. Rev., **100** (1955) 675.

[31] L. Néel, Ann. Phys., **4** (1949) 249.

[32] Y.-Y. Li, Phys. Rev., **101** (1956) 1450.

[33] I.Dzyaloshinsky, J. Phys. Chem. Solids, **4** (1958) 241.

[34] T. Moriya, Phys. Rev., **120** (1960) 91.

[35] W.H. Meiklejohn, C.P. Bean, Phys. Rev., **102** (1956) 1413.

[36] L.D. Landau, Phys. Z. Sowjetunion, **11** (1937) 26.

[37] A. Arrott, Phys. Rev., **108** (1957) 1394.

[38] S.K. Banerjee, Phys. Lett., **12** (1964) 16.

[39] H.E. Stanley, Introduction to Phase Transition and Critical Phenomena, Oxford University Press, New York (1971).

[40] A. Arrott, J.E. Noakes, Phys. Rev. Lett., **19** (1967) 786.

[41] R.V. Chamberlin, Nature, **408** (2000) 337.

[42] K. Huang, Statistical Mechanics, Wiley, New York (1987).

[43] B. Widom, J.Chem. Phys., **43** (1965) 3898.

[44] M.S. Green, M. Vicentini-Missoni, J.M.H.L. Sengers, Phys. Rev. Lett., **18** (1967) 1113.

[45] P. Weiss, R. Forrer, Ann. Phys. (Paris), **5** (1926) 153.

[46] L. Néel, Ann. Phys., **3** (1948) 137.

[47] Y. Ren, T.T.M. Palstra, D.I. Khomskii, E. Pellegrin, A.A. Nugroho, A.A. Menovsky, G.A. Sawatzky, Nature, **396** (1998) 441.

[48] H.C. Nguyen, J.B. Goodenough, Phys.Rev. B, **52** (1995) 324.

[49] K. Yoshii, A. Nakamura, Y. Ishii, Y. Morii, J. Solid State Chem., **162** (2001) 84.

[50] V.A. Khomchenko, I.O. Troyanchuk, R. Szymczak, H. Szymczak, J. Mater. Sci., **43** (2008) 5662.

[51] H. Adachi, H. Ino, Nature, **401** (1999) 148.

[52] N. Menyuk, K. Dwight, D.G. Wickham, Phys. Rev. Lett, **4** (1960) 119.

[53] P.K. Manna, S.M. Yusuf, R. Shukla, A.K. Tyagi, Appl. Phys. Lett., **96** (2010) 242508.

[54] P. Bordet, C. Chaillout, M. Marezio, Q. Huang, A. Santoro, S.W. Cheong, H. Takagi, C.S. Oglesby, B. Batlogg, J. Solid State Chem., **106** (1993) 253.

[55] A.V. Mahajan, D.C. Johnston, D.R. Torgeson, F. Borsa, Phys. Rev. B, **46** (1992) 10966.

[56] A.A. Belik, Inorg. Chem., **52** (2013) 2015.

[57] Y. Ren, T.T.M. Palstra, D.I. Khomskii, A.A. Nugroho, A.A. Menovsky, G.A. Sawatzky, Phys.Rev. B, **62** (2000) 6577.

[58] W.H. Meiklejohn, C.P. Bean, Phys. Rev., **105** (1957) 904.

[59] R.L. Stamps, J. Phys. D: Appl. Phys., **33** (2000) R247.

[60] J. Nogués, J. Sort, V. Langlais, V. Skumryev, S. Suriñach, J.S. Muñoz, M.D. Baró, Phys. Rep., **422** (2005) 65.

[61] S. Giri, M. Patra, S. Majumdar, J. Phys.: Condens. Matter, **23** (2011) 073201.

[62] J.C.S. Kools, IEEE Trans. Magn., **32** (1996) 3165.

[63] D. Niebieskikwiat, M.B. Salamon, Phys.Rev. B, **72** (2005) 174422.

[64] T. Qian, G. Li, T. Zhang, T.F. Zhou, X.Q. Xiang, X.W. Kang, X.G. Li, Appl. Phys. Lett., **90** (2007) 012503.

[65] X.H. Huang, J.F. Ding, G.Q. Zhang, Y. Hou, Y.P. Yao, X.G. Li, Phys.Rev. B, **78** (2008) 224408.

[66] S.K. Giri, A. Poddar, T.K. Nath, J. Appl. Phys., **112** (2012) 113903.

[67] M. Patra, K. De, S. Majumdar, S. Giri, Eur. Phys. J. B, **58** (2007) 367.

[68] S. Karmakar, S. Taran, E. Bose, B.K. Chaudhuri, C.P. Sun, C.L. Huang, H.D. Yang, Phys.Rev. B, **77** (2008) 144409.

[69] Y.-k. Tang, Y. Sun, Z.-h. Cheng, Phys.Rev. B, **73** (2006) 174419.

[70] J. Nogues, D. Lederman, T.J. Moran, I.K. Schuller, Phys. Rev. Lett., **76** (1996) 4624.

[71] R.P. Singh, C.V. Tomy, A.K. Grover, Appl. Phys. Lett., **97** (2010) 182505.

[72] F. Hong, Z. Cheng, J. Wang, X. Wang, S. Dou, Appl. Phys. Lett., **101** (2012) 102411.

[73] K. Yoshii, Appl. Phys. Lett., **99** (2011) 142501.

[74] P.D. Kulkarni, S.K. Dhar, A. Provino, P. Manfrinetti, A.K. Grover, Phys. Rev. B, **82** (2010) 144411.

[75] E.W. Gorter, J.A. Schulkes, Phys. Rev., **90** (1953) 487.

[76] S.-i. Ohkoshi, T. Iyoda, A. Fujishima, K. Hashimoto, Phys.Rev. B, **56** (1997) 11642.

[77] S.-i. Ohkoshi, Y. Abe, A. Fujishima, K. Hashimoto, Phys. Rev. Lett., **82** (1999) 1285.

[78] H. Kageyama, D.I. Khomskii, R.Z. Levitin, A.N. Vasil'ev, Phys.Rev. B, **67** (2003) 224422.

[79] H. Kageyama, D.I. Khomskii, R.Z. Levitin, M.M. Markina, T. Okuyama, T. Uchimoto, A.N. Vasil'ev, J. Magn. Magn. Mater., **262** (2003) 445.

[80] S.M. Yusuf, A. Kumar, J.V. Yakhmi, Appl. Phys. Lett., **95** (2009) 182506.

[81] P.D. Kulkarni, A. Thamizhavel, V.C. Rakhecha, A.K. Nigam, P.L. Paulose, S. Ramakrishnan, A.K. Grover, Eur. Phys. Lett., **86** (2009) 47003.

[82] S. Venkatesh, U. Vaidya, V.C. Rakhecha, S. Ramakrishnan, A.K. Grover, J. Phys.: Condens. Matter, **22** (2010) 496002.

[83] G.H. Jonker, Physica, **22** (1956) 707.

[84] K. Ueda, H. Tabata, T. Kawai, Science, **280** (1998) 1064.

[85] N. Sakai, H. Fjellvag, B.C. Hauback, J. Solid State Chem., **121** (1996) 202.

[86] G.A. Alvarez, X.L. Wang, G. Peleckis, S.X. Dou, J. Appl. Phys., **103** (2008) 07B916.

[87] J. Yang, Y.Q. Ma, B.C. Zhao, R.L. Zhang, W.H. Song, Y.P. Sun, Phys. Lett. A, **346** (2005) 217.

[88] E. Winkler, M.T. Causa, J.J. Neumeier, S.B. Oseroff, J. Magn. Magn. Mater., **310** (2007) e959.

[89] R. Shukla, J. Manjanna, A. Bera, S.M. Yusuf, A.K. Tyagi, Inorg. Chem., **48** (2009) 11691.

[90] N. Sharma, B.K. Srivastava, A. Krishnamurthy, A.K. Nigam, Solid State Sci., **12** (2010) 1464.

[91] K.R. Chakraborty, A. Das, S.M. Yusuf, P.S.R. Krishna, A.K. Tyagi, J. Magn. Magn. Mater., **301** (2006) 74.

[92] K. Yoshii, A. Nakamura, J. Solid State Chem., **155** (2000) 447.

[93] A.K. Azad, A. Mellergard, S.-G. Eriksson, S.A. Ivanovb, S.M. Yunus, F. Lindberg, G. Svensson, R. Mathieu, Mater. Res. Bull., **40** (2005) 1633.

[94] K.Vijayanandhini, C. Simon, V. Pralong, Y. Breard, V. Caignaert, B. Raveau, P. Mandal, A. Sundaresan, C. N. Rao, J. Phys.: Condens. Matter, **21** (2009) 486002.

[95] L.W. Zhang, G. Feng, H. Liang, B.S. Cao, Z. Meihong, Y.G. Zhao, J. Magn. Magn. Mater., **219** (2000) 236.

[96] Y. Sun, W. Tong, X. Xu, Y. Zhang, Phys. Rev. B, **63** (2001) 174438.

[97] L. Morales, R. Allub, B. Alascio, A. Butera, A. Caneiro, Phys. Rev. B, **72** (2005) 132413.

[98] A. Jaiswal, R. Das, K. Vivekanand, T. Maity, P.M. Abraham, S. Adyanthaya, P. Poddar, J. Appl. Phys., **107** (2010) 013912.

[99] R.M. Hornreich, J. Magn. Magn. Mater., **7** (1978) 280.

[100] R.M. Hornreich, Y. Komet, B.M. Wanklyn, Solid State Commu., **11** (1972) 969.

[101] G.G. Artem'ev, A.M. Kadomtseva, V.N. Milov, M.M. Lukina, A.A. Mukhin, J. Magn. Magn. Mater., **140-144** (1995) 2157.

[102] F. Bartolome, J. Bartolome, M. Castro, J.J. Melero, Phys.Rev. B, **62** (2000) 1058.

[103] I.O. Troyanchuk, M.V. Bushinsky, N.V. Pushkarev, N.Y. Bespalaya, Phys. Solid State, **46** (2004) 1878.

[104] M. Liu, Y. Shen, Y. Ji, T. He, J. Alloys Compd., **461** (2008) 628.

[105] B. Samantaray, S. Ravi, A. Das, S.K. Srivastava, J. Appl. Phys., **110** (2011) 093906 .

[106] T. Tamaki, K. Tsushima, Y. Yamaguchi, Physica **86-88B** (1977) 923.

[107] G. Gorodetsky, S. Shaft, A. Shaulof, B.M. Wanklyn, B. Sharon, I. Yaeger, AIP Conf. Proc., **29** (1976) 449.

[108] Y. Su, J. Zhang, Z. Feng, L. Li, B. Li, Y. Zhou, Z. Chen, S. Cao, J. Appl. Phys., **108** (2010) 013905.

[109] K. Yoshii, Mater. Res. Bull., **47** (2012) 3243.

[110] L.H. Yin, Y. Liu, S.G. Tan, B.C. Zhao, J.M. Dai, W.H. Song, Y.P. Sun, Mater. Res. Bull., **48** (2013) 4016.

[111] J. Mao, Y. Sui, X. Zhang, Y. Su, X. Wang, Z. Liu, Y. Wang, R. Zhu, Y. Wang, W. Liu, J. Tang, Appl. Phys. Lett., **98** (2011) 192510.

[112] J. Mao, Y. Sui, X. Zhang, X. Wang, Y. Su, Z. Liu, Y. Wang, R. Zhu, Y. Wang, W. Liu, X. Liu, Solid State Comm., **151** (2011) 1982.

[113] N. Dasari, P. Mandal, A. Sundaresan, N.S.Vidhyadhiraja, Eur. Phys. Lett., **99** (2012) 17008.

[114] N. Shirakawa, M.Ishikawa, Jpn. J. Appl. Phys., **30** (1991) L755.

[115] Y. Kimishima, S. Nishida, T. Mizuno, Y. Ichiyanagi, M. Uehara, Solid State Commun., **122** (2002) 519.

[116] Y. Kimishima, Y. Ichiyanagi, K. Shimizu, T. Mizuno, J. Magn. Magn. Mater., **210** (2000) 244.

[117] Y. Kimishima, M. Uehara, T. Saitoh, Solid State Commun., **133** (2005) 559.

[118] L.D. Tung, M.R. Lees, G. Balakrishnan, D. McK. Paul, Phys.Rev. B, **75** (2007) 104404.

[119] S.-J.L. Kang, Sintering, Densification, Grain Growth and Microstructure, Elsevier (2005).

[120] R.A. Young, "The Rietveld Method" International Union of Crystallography, New York, Oxford University (1996).

[121] S. Foner, Rev. Sci. Instr., **30** (1959) 548.

[122] N.Q. Minh, J.Am. Ceram. Soc, **76** (1993) 563.

[123] E. Lima Jr, T.B. Martins, H.R. Rechenberg, G.F. Goya, C. Cavelius, R. Rapalaviciute, S. Hao, S. Mathur, J.Magn.Magn. Mater., **320** (2008) 622.

[124] R. Padam, S. Pandya, S. Ravi, A.K. Nigam, S. Ramakrishnan, A.K. Grover, D. Pal, Appl. Phys. Lett., **102** (2013) 112412.

[125] D. Kim, B.L. Zink, F. Hellman, J.M.D. Coey, Phys. Rev. B, **65** (2002) 214424.

[126] R. Venkatesh, M. Pattabiraman, S. Angappane, G. Rangarajan, K. Sethupathi, J. Karatha, M. Fecioru-Morariu, R.M. Ghadimi, G. Guntherodt, Phys. Rev. B, **75** (2007) 224415.

[127] B. Samantaray, S. Ravi, A. Perumal, J. Magn. Magn. Mater., **322** (2010) 3391.

[128] P. Mandal, A. Sundaresan, C.N.R. Rao, A. Iyo, P.M. Shirage, Y. Tanaka, C. Simon, V. Pralong, O.I. Lebedev, V. Caignaert, B. Raveau, Phys. Rev. B, **82** (2010) 100416.

[129] M.-H. Phan, S.-C. Yu, J.Magn.Magn. Mater., **308** (2007) 325.

[130] A. McDannald, L. Kuna, M. Jain, J. Appl. Phys., **114** (2013) 113904.

[131] T.S. Zhao, W.X. Xianyu, B.H. Li, Z.N. Qian, J. Alloys Compd., **459** (2008) 29.

[132] Y. Tokura, Colossal magneto-resistive Oxides, Gordon and Breach Science Publishers (2000).

Publications/Communications in International Journals

From Thesis Work

1. Sign reversal of magnetization and tunable exchange bias field in $NdCr_{1-x}Fe_xO_3$ (x = 0.05 -0.20)

   Tribedi Bora and S. Ravi, *Journal of Magnetism and Magnetic Materials* (Accepted in 2015)

2. Sign reversal of magnetization and ferromagnetism in $NdCr_{1-x}Mn_xO_3$ (x = 0 to 0.50)

   Tribedi Bora and S. Ravi, *Journal of Superconductivity and Novel Magnetism,* **28** (2015) 869.

3. Bipolar switching of magnetization and tunable exchange bias in $NdCr_{1-x}Mn_xO_3$ (x = 0.0 -0.30)

   Tribedi Bora and S. Ravi, *Journal of Applied Physics,* **116 (**2014) 063901**.**

4. Effect of Ce doping on the magnetic properties of $LaCrO_3$

   Tribedi Bora and S. Ravi, *Physica B: Condensed Matter,* **448** (2014) 233.

5. Negative magnetization and the tunable exchange bias field in $LaCr_{0.8}Mn_{0.2}O_3$

   Tribedi Bora and S. Ravi, *Journal of Magnetism and Magnetic Materials,* **358** (2014) 208.

6. Sign reversal of magnetization and exchange bias field in $LaC_{r0.85}Mn_{0.15}O_3$

   Tribedi Bora and S. Ravi, *Journal of Applied Physics,* **114** (2013) 183902.

7. Study of magnetization reversal in $LaCr_{1-x}Fe_xO_3$ compounds

   Tribedi Bora and S. Ravi, *Journal of Applied Physics,* **114** (2013) 033906.

8. Antiferromagnetism and the effect of exchange bias in $LaCr_{1-x}Fe_xO_3$ (x = 0.40 to 0.60)

   Tribedi Bora, P. Saravanan and S. Ravi, *Journal of Superconductivity and Novel Magnetism, **26*** (2013) 1645.

Other Related Work

1. Ferromagnetism and bound magnetic polaron behavior in $(In_{1-x}Co_x)_2O_3$
   Tribedi Bora, B. Samantaray, S. Mohanty and S. Ravi, *IEEE Transaction in Magnetics,* **47** (2011) 10.
2. Study of exchange bias and training effect in $NiCr_2O_4$
   Junmoni Barman, **Tribedi Bora** and S. Ravi, *Journal of Magnetism and Magnetic* **385** (2015) 93.

Conference Papers:

1. Structural, optical and magnetic properties of Nd0.7Sr0.3MnO3 thin films
   Ranganadha Gopalrao Tanguturi, **Tribedi Bora**, Seenipandian Ravi and Dobbidi Pamu, *Physics Procedia*, **54** (2015) 70.
2. Magnetic, electrical and optical properties of $Nd_{0.85}K_{0.15}MnO_3$ thin film
   Tribedi Bora, A. Nandy, R. K. Bhuyan, D. Pamu and S. Ravi, *Advanced Nanomaterials and Nanotechnology Springer Proceeding in Physics,* **143** (2013) 449.
3. Preparation and characterization of $Nd_{0.85}K_{0.15}MnO_3$ thin film
   Tribedi Bora, A. Nandy, B. Samantaray, R. K. Bhuyan, D. Pamu and S. Ravi, *AIP Conference. Proceeding,* **1447** (2012) 1119.
4. Preparation and characterization of charged ordered $Nd_{0.80}Na_{0.20}MnO_3$ Thin Films
   A. Nandy, **Tribedi Bora**, B. Samantaray, R. K. Bhuyan, D. Pamu and S. Ravi, *AIP Conference Proceeding,* **1447** (2012) 1117.

Papers Published in Refereed Conferences Proceeding and Presented in National/ International Conferences:

1. Sign reversal of magnetization and ferromagnetism in $NdCr_{1-x}Mn_xCrO_3$ (x = 0 -0.5)
   Tribedi Bora and S. Ravi, Presented in 4th International Conference on Superconductivity and Magnetism (ICSM 2014), April 2014, Antalya, Turkey**.**
2. Negative magnetization on $LaCr_{0.8}Mn_{0.2}O_3$ compounds
   Tribedi Bora and S. Ravi, Presented in International Conference on Magnetic Materials and Applications (MAGMA 2013), December 2013, IIT Guwahati, India.
3. Effect of Ce doping on the magnetic properties of $LaCrO_3$
   Tribedi Bora and S. Ravi, Presented in International Conference on Magnetic Materials and Applications (MAGMA 2013), December 2013, IIT Guwahati, India.
4. Antiferromagnetism and effect of exchange bias in $LaCr_{1-x}Fe_xO_3$ (x = 0.4 to 0.6)
   Tribedi Bora, P. Saravanan and S. Ravi, Presented in International conference on Superconductivity and Magnetism (ICSM 2012), May 2012, Ankara University, Turkey.
5. Suppression of ferromagnetism in nanocrystalline $Nd_{0.8}K_{0.2}MnO_3$
   Tribedi Bora, B. Roy and S. Ravi, Presented in International conference on Superconductivity and Magnetism (ICSM 2012), May 2012, Ankara University, Turkey.
6. Preparation and characterization of $Nd_{0.85}K_{0.15}MnO_3$ Thin film
   Tribedi Bora, A. Nandy, B. Samantaray, R. K. Bhuyan, D. Pamu and S. Ravi, Presented in 56th DAE-Solid State Physics Symposium (DAE 2012), Dec 2012, SRM University, Tamil Nadu, India.
7. Magnetic, electrical and optical properties of $Nd_{0.85}K_{0.15}MnO_3$ thin film
   Tribedi Bora, A. Nandy, R. K. Bhuyan, D. Pamu and S. Ravi, Presented in International Conference on Advance Nanomaterials and Nanotechnology (ICANN 2011), Dec 2011, IIT Guwahati, India
8. Ferromagnetism and bound magnetic polaron behavior in $In_{1-x}Co_xO_3$
   Tribedi Bora, B. Samantaray, S. Mohanty and S. Ravi, Presented in ASIA International Magnetic Conference (INTERMAG 2011), April 2011, Taipei, Taiwan.

9. Synthesis and study of magnetic properties in Co doped In_2O_3

Tribedi Bora and S. Ravi, Presented in National Conference on Magnetic Materials and Applications (MAGMA 2011), Jan 2011, S.N. Bose National Centre for Basic Science, Kolkata, India.